Western Australian School of Mines
Department of Exploration Geophysics

Volumetric Interpretation of 3D Hard Rock Seismic Data

Muhammad Shahadat Hossain

This thesis is presented for the Degree of
Doctor of Philosophy
of
Curtin University

May 2016

Declaration

To the best of my knowledge and belief this thesis contains no material previously published by any other person except where due acknowledgment has been made.

This thesis contains no material which has been accepted for the award of any other degree or diploma in any university.

Signature: …….

Date: ……23 August 2017……..

Mother o' Mine

If I were hanged on the highest hill,
Mother o' mine, O mother o' mine!
I know whose love would follow me still,
Mother o' mine, O mother o' mine!

If I were drowned in the deepest sea,
Mother o' mine, O mother o' mine!
I know whose tears would come down to me,
Mother o' mine, O mother o' mine!

If I were damned of body and soul,
I know whose prayers would make me whole,
Mother o' mine, O mother o' mine!

— *Rudyard Kipling, 1865 - 1936*

Abstract

Seismic methods are not utilised in mineral exploration in accordance with their exceptional imaging power, primarily because of their high cost compared to the conventional gravity, magnetic and electrical methods. High acoustic velocities, low impedance contrasts, an abundance of fractures and complex geological structures make seismic imaging much more difficult in hard rock environments. Moreover, hard rock seismic interpretation does not deploy all the sophisticated tools developed for the oil industry to delineate complex geological structures despite the fact that only seismic is capable of resolving targets beyond 500 m deep. Seismic methods can indeed render high-resolution images of the subsurface structures and are capable of delineating exploration targets 2 km deep or more. Consequentially, seismic reflection methods should gain widespread acceptance as a valuable tool in mineral exploration. The research presented here tests the potential of seismic volumetric interpretation approach for an improved targeting of excessively complex ore-bodies from the 3D seismic data collected over a copper-gold mining project in Hillside, South Australia; a nickel-copper-platinum group elements mine in Kevitsa, northern Finland and a gold mine in Cracow, Queensland.

A detailed 3D high-resolution seismic investigation coupled with physical property measurements of the core samples were undertaken to delineate subvertical to vertical structures over an excessively complex Iron Oxide-Copper-Gold deposit at Hillside, South Australia. The 3D seismic volumetric interpretation signifies that the area is characterised by numerous north-south trending, subvertical faults that may have acted as the mineralisation pathways. Previous geological studies have also confirmed that these subvertical structures are associated with the host rocks in the area. Seismic attribute analysis was utilised to delineate these structures. Most of the stratigraphic attributes did not perform optimally; however, innovative interpretation workflows, such as ant-tracking provided very encouraging results. The comparison of the interpretation results and industry supplied geological information showed excellent agreement.

The second case study aimed at the delineation of subvertical structures from a 3D seismic dataset collected over a Ni-Cu-PGE mine in Kevitsa, northern Finland. The

seismic data combined with borehole logs utilised ant-tracking workflow to enhance the detection of significant structures in the top 600 m. The interpretation results were coupled with borehole data and physical property modelling.

The final case study involved volumetric interpretation of a 3D seismic volume acquired from the Cracow gold field in Queensland, Australia to delineate subvertical faults (>70°) within which the mineralisation is confined. Ant-tracking was employed on an edge-detected seismic dataset to extract the fault network that hosts gold mineralisation. Facies modelling was performed using the lithological logs upscaled from 457 boreholes. Faults encountered in the boreholes were used to appraise the accuracy of the ant-tracking result. The discontinuities extracted by the ant-tracking workflow demonstrates excellent agreement with the facies boundaries and the fault detected in the boreholes.

All three case studies were able to justify to some extent that presumed limitations of seismic data in hard rock environments can be relaxed through the application of volumetric interpretation methods, which can successfully delineate steeply dipping structures associated with mineralisation in diverse geological settings. The approach adopted in this research is therefore of general applicability to hard rock characterisation and mineral exploration.

Acknowledgements

I would like to express my sincere gratitude to my advisor Associate Professor Dr Milovan Urosevic for providing me with an opportunity to carry out my research as a DET CRC Project 3.1 PhD Student. I am most grateful to him for spending his valuable time to review my thesis and for providing helpful feedback, without which the completion of this thesis would not have been possible.

It gives me immense pleasure to thank the members of my advisory panel, Dr Maxim Lebedev, Dr Anton Kepic, Dr Andrej Bóna and Dr Roman Pevzner for their support, meticulous suggestions and astute criticism in times of need.

I am indebted to Rex Minerals Ltd for allowing me to use the 3D seismic, density, and petrophysical data from Hillside, South Australia and for their immense support during the field trips.

I am grateful to HiSeis Pty Ltd and First Quantum Minerals Ltd for allowing me to use their 3D seismic dataset and borehole logs from the Kevitsa area in Finland as a case study.

I am indebted to HiSeis Pty Ltd and Evolution Mining for granting me the permission to use their 3D seismic dataset and borehole lithological logs from Cracow area in Queensland as a case study.

I am obliged to the DET CRC and Curtin University for the Scholarships awarded to me.

I would like to thank Schlumberger Limited, Paradigm and dGB Earth Sciences for the software packages under their university programmes. Special thanks go to Mr Adrien Bisset and Mr Jacob Smith at GeoTeric for providing me a complementary GeoTeric license for seven months. I am grateful to Dr Andrew Squelch for introducing them to me.

Special thanks go to Andrew Pethick and Jai Kinkela (HiSeis Pty Ltd) for proofreading parts of the thesis. Their helpful comments made this thesis more readable.

I would like to thank our departmental administrative officers Ms Deirdre Hollingsworth and Mrs Lynda Bergey and the research secretaries Miss Zuzzanna Kuklinski and Miss Nichole Sik for their support throughout my endeavour at Curtin.

I would like to thank my colleagues and friends, especially Javad, Felix, Kevin, Lei, Thong, George, Aziz, Hosni, Mateus, Pouya, Ida, Conny, Dmitry and Evans for their support and encouragements.

I am mostly indebted to my family for their unconditional support, love and encouragement. I honestly have no words to express the gratitude I feel towards my wife Zulfia Tazin and two sons Zeroun Sabir and Zohan Sabir who have stayed by my side and patiently supported me in all the ups and downs I had to go through to complete this thesis.

This work has been supported by the Deep Exploration Technologies Cooperative Research Centre and the CHDG whose activities are funded by the Australian Government's Cooperative Research Centre Programme. This is DET CRC Document 2017/1030.

Table of contents

Abstract vii

Acknowledgements ix

Table of contents xi

Table of figures xv

List of tables xxvii

1. Introduction 1

1.1. Prologue *1*

1.2. Early application of seismics in mineral exploration *3*

1.3. Current status of mineral exploration *4*

1.4. Objectives and challenges *6*

1.5. Thesis structure *7*

2. Mineral resources of Australia and Finland 9

2.1. Australian mineral resources *9*

2.2. Finnish mineral resources *11*

2.3. Classification of ore deposits *14*

2.3.1. Porphyry deposits 14

2.3.2. Iron Oxide-Copper-Gold deposits 21

2.3.3. Banded Iron Formations 23

2.3.4. Volcanogenic Massive Sulphide deposits 25

2.3.5. Orogenic gold deposits 27

2.3.6. Mississippi Valley-type deposits 30

2.3.7. Unconformity-type Uranium deposits 33

3. Seismic reflection exploration in hard rock environments 35

3.1. Introduction *35*

3.2. Seismic reflectivity of the hard rock media *35*

3.3. Seismic resolution *40*
3.4. Seismic interpretation *43*
3.5. 2D and 3D seismic interpretation strategies *44*
3.6. Pitfalls in interpretation of hard rock seismic data *45*
3.7. Seismic attributes *48*
3.8. 3D seismic visualisation techniques *49*

4. Case study: Hillside copper–gold mine, South Australia 51
4.1. Introduction *51*
4.2. Geological setting *53*
4.3. Physical property data analysis *56*
4.4. Seismic data acquisition and processing *63*
4.5. Seismic volumetric interpretation *70*
4.5.1. Seismic attribute analysis 71
4.5.2. Fault detection 76
4.6. Summary *82*

5. Case study: Kevitsa nickel–copper–platinum group elements mine, northern Finland 85
5.1. Introduction *85*
5.2. Geological setting *87*
5.3. Seismic data acquisition and processing *92*
5.4. Seismic volumetric interpretation *97*
5.4.1. Seismic horizon extraction 98
5.4.2. Seismic attribute analysis 100
5.4.3. Fault detection 107
5.4.4. Physical property modelling 109
5.4.4.1. P-wave velocity 110
5.4.4.2. Density 114
5.4.4.3. Copper and Nickel 117
5.5. Summary *127*

6. Case study: Cracow gold mine, Queensland 129
6.1. Introduction *129*

6.2. Geological Setting *130*
6.3. Seismic data acquisition *133*
6.4. Seismic volumetric interpretation *136*
6.4.1. Seismic attribute analysis 138
6.4.2. Fault detection 143
6.4.3. Property modelling 146
6.5. Summary *151*

7. Discussion and conclusions 153
7.1. Discussion *154*
7.1.1. Case study: Hillside copper-gold mine, South Australia 154
7.1.2. Case study: Kevitsa nickel-copper-platinum group elements mine, Finland 156
7.1.3. Case study: Cracow gold mine, Queensland 157
7.2. Conclusions *158*

Bibliography 161

Appendices 185
Appendix I *185*
Appendix II *213*

Table of figures

Figure 1-1: Depths of mineral discoveries (excluding bulk minerals, and limited to Moderate, Major and Giant deposits only) in Australia during 1950-2000 (Schodde 2012). Major is > 1 million Oz of Au, > 100 kt of Ni, > 1 Mt of Cu. Giant is > 5 Mt Cu-equivalent; and Supergiant > 25 Mt Cu-equivalent. Satellite deposits supply ore to a central mill within and existing mining camp (Schodde and Guj 2012). 2

Figure 1-2: The pre-production lead-time for Australian greenfield and brownfield mineral discoveries (Schodde and Guj 2012). 5

Figure 2-1: Locations of current operating mines of identified mineral resources in Australia (Data Source: Australian Mines Atlas, January 2014). 10

Figure 2-2: Locations of the major mineral deposits found in Finland (Reproduced with the permission of Geological Survey of Finland. All rights reserved.) 12

Figure 2-3: Worldwide locations of porphyry copper systems (Sillitoe 2010). 15

Figure 2-4: The 25 largest porphyry deposits identified by ages. (A) Giant copper deposits. (B) Giant gold deposits (Cooke et al. 2005). 16

Figure 2-5: The geological relationship between different types of porphyry deposits and their host rocks as well as the temporal sequences (Sillitoe 2010). 20

Figure 2-6: Worldwide distribution of the Proterozoic Iron-Oxide (Cu-U-REE-Au) deposits (Hitzman et al. 1992). 21

Figure 2-7: The diversity of Iron Oxide-Copper-Gold deposits settings. The thickness of the arrows indicates the relative contribution of various fluids (Chen 2013). 22

Figure 2-8: Models of Banded Iron Formations deposition. (a) The traditional model of BIF deposition by chemical reaction between hydrothermal dissolved Fe^{2+} and oxygen generated by microorganisms. (b) Photo-oxidation of abiotic Fe^{2+} by ultraviolet light in anoxic ocean water. (c) Fe^{2+} oxidation by anoxygenic microbial organisms (Posth et al. 2011). 24

Figure 2-9: Worldwide distribution of seafloor hydrothermal systems and related mineral deposits (Jamieson et al. 2014).....25

Figure 2-10: Cross-section through a typically active volcanogenic massive sulphide mound on the seafloor. Mixing of cold seawater with the ascending high-temperature hydrothermal fluids results in the precipitation of massive sulphide minerals and formation of chimneys and mounts on or below the seafloor. Py=pyrite, Cpy=chalcopyrite, Sp=sphalerite, Po=pyrrhotite, Gn=Galena, Anh=anhydrite and Ba=barite (Jamieson et al. 2014). 26

Figure 2-11: A series of simplified sketches showing the formation of orogenic lode-gold deposits (Goldfarb et al. 2001). 29

Figure 2-12: Worldwide distribution of Mississippi Valley-type (MVT) deposits. BHT=Broken Hill-type, MVT=Mississippi Valley-type, SEDEX=Sedimentary exhalative, and VHMS=Volcanic-hosted massive sulphides (Paradis et al. 2007).....31

Figure 2-13: Illustration showing a favourable tectonic setting for Mississippi Valley-type (MVT) deposition. (a) early stage of collision and the formation of foreland basin, extensional domain, and forebulge. (b) favourable hydrological conditions for MVT deposition (Leach et al. 2010). 32

Figure 3-1: P-wave velocity vs. density at 200 MPa confining pressure for common hard rocks. The constant acoustic impedance for felsic and mafic rocks are shown as dotted lines. The minimum reflection coefficient R=0.06 required to produce strong reflection is superimposed for reference (Salisbury et al. 2003).....38

Figure 3-2: Relationship between S-wave velocity and density at 200 MPa confining pressure and at room temperature for common hard rocks. Lines of constant acoustic impedance are shown as dotted lines for reference (Salisbury et al. 2003). 39

Figure 3-3: Definition of the Fresnel zone AA' (Yilmaz 2001).....42

Figure 4-1: The regional geology of northern Yorke Peninsula shows the location of the Hillside deposit (red) on the east coast (modified after Conor et al. 2010, with the permission of PGC Publishing). 54

Figure 4-2: (a) Gravity anomaly map of the eastern Yorke Peninsula exhibits the location of Hillside deposit (Conor et al. 2010). (b) Residual magnetic anomaly map of the Hillside Cu-Au mining project area (Conor et al. 2010). The location of boreholes and interpreted mineralised zones are shown on the map..... 55

Figure 4-3: Core samples from the HDD-044 borehole (Tray length is 1 m and core diameter is approximately 45 mm). 56

Figure 4-4: (a) P-wave velocity, (b) S-wave velocity, (c) density and (d) magnetic susceptibility distributions of the measured core samples..... 58

Figure 4-5: P-wave velocity vs. density measured from the core samples suggesting clustering of main lithological units. Dashed lines represent lines of constant impedance in m/s kg/m^3. The minimum reflection coefficient R=0.06 required to produce strong reflection (Salisbury et al. 2003) is superimposed for reference..... 59

Figure 4-6: P-wave velocity (Vp)-density fields for sulphide ores and silicate host rocks adopted from Salisbury et al. (1996) were used to categorise samples from Hillside. Ores: py=pyrite, cpy=chalcopyrite, sph=sphalerite, po=pyrrhotite. Silicate rocks along Nafe-Drake curve: F=felsic, M=mafic, UM=ultramafic, SED=sediments, SERP=serpentinite, c=carbonate, g=gangue. The lines of constant acoustic impedance (Z) for felsic and mafic rocks are illustrated as dashed lines. 60

Figure 4-7: The empirical distribution function (empirical CDF) calculated from the (a) P-wave velocity, (b) density, and (c) acoustic impedance of the analysed core samples..... 61

Figure 4-8: The density distribution of the measured core samples extracted from the supplied database. 62

Figure 4-9: (a) The density cube extracted from the supplied database. The density data were filtered according to the range for mineralised rocks from the petrophysical data analysis (>3000 kg/m^3). (b) The filtered distribution corresponds to the high-magnetic anomaly zones on the residual magnetic anomaly map of Hillside in Figure 4-2 (b). 63

Figure 4-10: The location of the Hillside 3D seismic survey. Red and blue dots in the inset represent shot points and receiver locations respectively. 64

Figure 4-11: The solar panels were used to top up the batteries to increase effective shooting time.....64

Figure 4-12: 375 kg free-fall weight drop was carried by a skid-steer to navigate to each shot point by a spotter.....65

Figure 4-13: Actual CMP folds as achieved after 2575 shots. 66

Figure 4-14: A raw 3D shot gather from Hillside seismic data 66

Figure 4-15: The velocity model employed in time-to-depth conversion of the Hillside 3D seismic dataset. 68

Figure 4-16: Amplitude display of the depth-converted PSTM volume from Hillside 3D seismic survey. 72

Figure 4-17: The dip attribute computed along inline N6174262 (V.E. 0.5 X). 73

Figure 4-18: Azimuth attribute calculated along inline N6174262 (V.E. 0.5 X). The sigma value (window) 3 was chosen in X, Y, and Z direction for principal component of the azimuth attribute computation. 73

Figure 4-19 : (a) Amplitude display along inline 6174262 from the Hillside seismic volume, (b) structurally smoothed volume used as the input for variance attribute calculation, and (c) variance attribute display along inline 6174262 N. A smoothing operator of 10 samples was selected to reduce the noise. A plane confidence threshold of 0.7 was used for dip correction. 74

Figure 4-20: (a) Fracture density calculated from a maximum curvature volume using a radius of 100 m. Red colour indicates areas with high density fractures along inline 6174262 N (V.E. 0.5 X), horizontal slices at (b) 100 m below the Australian Height Datum, and (c) 200 m below the Australian Height Datum.....75

Figure 4-21: A flowchart exhibits the steps of FaultApp workflow (Courtesy: GeoTeric user's manual 2015). *76*

Figure 4-22: A flowchart demonstrates the steps of Schlumberger Petrel's ant-tracking workflow (modified after Schlumberger 2014) *77*

Figure 4-23: A horizontal slice of the ant-tracked volume placed on an inline section of the amplitude volume shows the comparison of the faults detected from the seismic data. *78*

Figure 4-24: Horizontal slice at 220 m below the datum shows the faults detected using (a) FaultApp workflow, and (b) ant–tracking workflow. *79*

Figure 4-25: *Multi-attribute horizontal slice at 175 m below the datum shows the faults extracted from the Hillside 3D seismic volume (view from north). A geological cross-section supplied by Rex Minerals Ltd placed as the vertical section along 6174200 N to display the correlation between the geological interpretation and ant-tracking. The geologists of Rex Minerals Ltd constructed the cross-section from the borehole information. The top regolith is shown as orange colour, granite as red, gabbro as blue, metasediment as green and the shear zones as black.* *80*

Figure 4-26: Fault network extracted for the top 200 m from the ant-tracked volume is placed against a geological cross-section along 6174200 N. (a) Viewing towards south from above and (b) viewing towards south from below. *81*

Figure 4-27: Fault volume extracted for the top 500 m from the ant-tracked volume by applying a transparency threshold of 0.5 to the data (Hossain et al. 2015b). *82*

Figure 5-1: The Geologic map of the Kevitsa Ni-Cu-PGE deposit, showing the location of the 3D seismic survey (boxed area). White lines show the location of the open-pit mine and its extension. Thick black lines represent the Kevitsa 2D seismic survey lines E2, E3, E4, and E5. The location of the drill hole KV28 is shown as a red dot (Malehmir et al. 2014). Red dashed lines (AA' and BB') show approximate locations of the geological cross-section shown in Figure 5-2. ..... *88*

Figure 5-2: Schematic geological cross-sections along southwest-northeast (AA') and southeast-northwest (BB') demonstrate the shape of the Kevitsa intrusion and fault systems (Koivisto et al. 2012). *90*

Figure 5-3: Regional lineaments interpreted from total magnetic field data. Rose diagram shows the major orientations, NW-SE and SW-NE (Lindqvist 2014). *91*

Figure 5-4: Regional lineaments interpreted from topographic hillshade map. Rose diagram shows two major orientations NNW-SSE and SSW-NNE. Aerial photograph shows the location of the Kevitsa open-pit (Lindqvist 2014). *91*

Figure 5-5: Actual CMP fold map achieved after 3300 shots. Higher fold (red) is due to extra source and receiver lines (Courtesy: HiSeis Pty Ltd). The areas in black were inaccessible during data acquisition. *93*

Figure 5-6: Estimated regolith thickness at the survey area (Ziramov et al. 2015)....94

Figure 5-7: Basic steps used in the 3D PSTM in 2014 (Ziramov et al. 2015). *96*

Figure 5-8: Amplitude display of the Kevitsa seismic data along inline 130 to compare between 2014 and 2010 processing methods. Black arrows point to the areas with improved signal to noise ratio. *96*

Figure 5-9: (a) Amplitude display of the Kevitsa seismic data, (b) Continuity attribute projected over the amplitude data to enhance lateral continuity of the reflection events, and (c) horizons picked from the Kevitsa seismic data. *99*

Figure 5-10: The PSTM cube was cropped to remove the padded areas with low signal-to-noise ratio. *100*

Figure 5-11: The cropped seismic cube employed in attribute analysis. *101*

Figure 5-12: The working principal of 3D edge enhancement for a single pixel (Schlumberger 2014). *102*

Figure 5-13: A 3D edged enhancement attribute on a vertical section along ENE-WSW direction shows the major stratigraphic boundaries in Kevitsa. *102*

Figure 5-14: (a) Dip illumination attribute displayed on a horizontal slice reveals major stratigraphy of the area. The result displays an excellent agreement with the bedrock geology of the area shown in Figure 5-1. (b) Dip illumination projected over 3D edge enhancement along inline 151 illustrates the major stratigraphic boundaries. 103

Figure 5-15: The principal component of the local structural dip attribute computed from the Kevitsa seismic data. Horizontal slices at (a) 200 m below the datum, and (b) 300 m below the datum demonstrate the variation in dip magnitude at different depths. 104

Figure 5-16: The principal component of the local structural azimuth volume calculated from the Kevitsa seismic data. Horizontal slices at (a) 200 m below the datum, and (b) 300 m below the datum demonstrate the changes in azimuth at different depths. 105

Figure 5-17: RMS amplitude map at (a) 200 m below the datum and (b) 300 m below the datum computed from the Kevitsa seismic volume. 105

Figure 5-18: Variance attribute (edge method) was computed from the Kevitsa seismic data using a smoothing operator of 20 to reduce the noise in vertical direction. The default plane confidence threshold of 0.75 was used for dip correction. 106

Figure 5-19: Fault events detected from the Kevitsa seismic volume using Schlumberger Petrel's Ant-tracking workflow (Hossain et al. 2015a). 107

Figure 5-20: A 3D representation of the fault events extracted from the ant-tracked volume. 108

Figure 5-21: Ant-tracking exhibited poor performance at the upper part of the data due to low signal to noise ratio. 108

Figure 5-22: 3D block model of the Kevitsa structural grid employed in the physical property modelling. 109

Figure 5-23: 13 boreholes with Vp (m/s) were upscaled to the grid for property modelling. Red ellipse indicates the boundary of the Kevitsa pit. 111

Figure 5-24: P-wave velocity (m/s) model from 13 borehole logs after 25 simulations. Continuous data were generated using Sequential Gaussian Simulation (stochastic) and a Gaussian variogram calculated from the boreholes. 112

Figure 5-25: Location of the P-velocity cross-sections along NNW-SSE (a-a') and SSW-NNE (b-b') directions. Blue ellipse marks the boundary of the Kevitsa pit. 112

Figure 5-26: Cross-section of the upscaled P-velocity model (a) along NNW-SSE (a-a') direction, (b) along SSW-NNE (b-b') direction, and (c) a horizontal slice show P-wave velocity (m/s) distribution in Kevitsa. The areas where metasediments and metavolcanic rocks are dominant, demonstrate lower P-velocity. Gabbro-rich areas shows higher P-velocity distribution.....113

Figure 5-27: 74 boreholes with density (kg/m^3) were upscaled to the grid for property modelling. Red ellipse marks the boundary of the Kevitsa pit. 114

Figure 5-28: Density (kg/m3) model after 25 simulations from 74 borehole logs upscaled to the grid. Continuous data were generated using Sequential Gaussian Simulation (stochastic) algorithm and a Gaussian variogram calculated from boreholes. 115

Figure 5-29: Cross-section of the upscaled density model (a) along NNW-SSE (a-a') direction), (b) along SSW-NNE (b-b') direction, and (c) a horizontal slice show density (kg/m^3) distribution in Kevitsa. The areas where metasediments and metavolcanic rocks are dominant, demonstrate lower density values. Olivine pyroxenite-rich areas within Kevitsa pit show highest density distribution in the area.....116

Figure 5-30: 242 boreholes with Cu (wt.%) and Ni (wt.%) logs were upscaled to the grid for property modelling. Red ellipse marks the boundary of the Kevitsa pit. 117

Figure 5-31: Cu (wt.%) model of the Kevitsa area created from 242 borehole logs. 118

Figure 5-32: Cross-section of the upscaled Cu model (a) along NNW-SSE (a-a') direction), (b) along SSW-NNE (b-b') direction, and (c) a horizontal slice show that minable Cu-grade (0.41 wt.%) is located within the Kevitsa pit area. 119

Figure 5-33: (a) Plan view of the estimated minable Cu-grade using 0.41 wt.% cut-off limit. Red ellipse marks the boundary of the Kevitsa pit. (b) Minable Cu-grade volume using 0.41 wt.% cut-off limit. 120

Figure 5-34: Ni (wt.%) model of the Kevitsa area simulated from the borehole data. 121

Figure 5-35: Cross-section of the upscaled Ni model (a) along NNW-SSE (a-a') direction, (b) along SSW-NNE (b-b') direction, and (c) a horizontal slice show that minable Ni-grade (0.3 wt.%) is located within the Kevitsa pit area. 122

Figure 5-36: (a) Plan view of the estimated minable Ni-grade using 0.3 wt.% cut-off limit. Red ellipse marks the boundary of the Kevitsa pit. (b) Minable Ni-grade volume using 0.3 wt.% cut-off limit. 123

Figure 5-37: Exact seismic amplitudes from the Kevitsa seismic volume was upscaled to grid resolution. 124

Figure 5-38: Cross-section of the upscaled seismic model (a) along NNW-SSE (a-a') direction, (b)along SSW-NNE (b-b') direction, and (c) a horizontal slice show the distribution of upscaled exact amplitude. 125

Figure 5-39: Minable Cu-grade (0.41 wt.%) volume was projected over the Kevitsa seismic data to identify the correlation between seismic data and Cu-ore. 126

Figure 5-40: Minable Ni-grade (0.3 wt.%) volume was projected over the Kevitsa seismic data to identify the correlation between seismic data and Ni-ore. 127

Figure 6-1: Location map of Cracow (Courtesy: Google)..... 131

Figure 6-2: Geology of the Cracow gold field area showing the faults, veins, dykes and alterations. Polygons with red colour fill show pit outlines. Green colour-filled polygon

shows the location of the 3D seismic survey. Inset map shows the location of Cracow in southeast Queensland (modified after Micklethwaite 2009). 132

Figure 6-3: The prestack time-migrated seismic data acquired at Cracow in 2014 by HiSeis Pty Ltd. 134

Figure 6-4: (a) The cropped and preconditioned prestack time-migrated seismic volume employed in seismic attribute analysis and fault detection. (b) The seismic cube before cropping and conditioning, and (c) the seismic cube after cropping and conditioning. 137

Figure 6-5: (a) Instantaneous phase attribute exposes the subvertical faults along crossline 95, (b) cosine of phase attribute along crossline 95 also supports the fact that the study area is characterised by an abundance of subvertical faults. 139

Figure 6-6: Semblance attribute demonstrates zones of low coherency.....140

Figure 6-7: Consistent dip attribute along a horizontal slice at 0 m Australian Height Datum showing (a) inline dip and (b) crossline dip. 140

Figure 6-8: Residual dip on a horizontal slice at 0 m Australian Height Datum highlights the areas of uncertainty in the dip estimation where the data is discontinuous due to the presence of faults or low signal-to-noise ratio. 141

Figure 6-9: (a) Minimum similarity attribute on a vertical section along crossline 95 highlights areas with potential faults. (b) Maximum similarity attribute along the same crossline shows the areas with consistent signals. 142

Figure 6-10: Laplacian edge enhancement filter preserves edges, thereby, highlights the areas with potential faults.....143

Figure 6-11: (a) Faults detected from the Cracow seismic volume using Schlumberger Petrel's ant-tracking workflow. The grey events indicate discontinuities detected from the seismic data. Red dots are the faults detected in the borehole during drilling. Ant-tracking result shows an excellent agreement with the faults detected during drilling. (b) A plan view of the ant-tracked faults from the Cracow seismic data. 144

Figure 6-12: Comparison of ant-tracking result with the interpretation of (Micklethwaite 2009). *145*

Figure 6-13: Comparison of ant-tracking results with the quartz vein lode map provided in (Evolution Mining 2014). *146*

Figure 6-14: Zone logs created from 457 boreholes were upscaled to the grid to create a facies model. *147*

Figure 6-15: Facies model of Cracow was constructed by interpolating the upscaled zone logs from 457 boreholes using a Gaussian variogram calculated from the upscaled property. *147*

Figure 6-16: Projection of the fault network extracted from the edge-detected seismic data over the facies model. The discontinuities demonstrate a moderate correlation with the lithological boundaries of the facies model. *148*

Figure 6-17: Comparison of ant-tracking, facies model and faults encountered in the borehole on a horizontal slice at 200 m above the Australian Height Datum. *149*

Figure 6-18: Comparison of ant-tracking, facies model and faults encountered in the borehole on a horizontal slice at the Australian Height Datum. *149*

Figure 6-19: Comparison of ant-tracking, facies model and faults encountered in the borehole on a horizontal slice at 140 m below the Australian Height Datum. *150*

Figure 6-20: Comparison of ant-tracking, facies model and faults encountered in the borehole on a horizontal slice at 300 m below the Australian Height Datum. *150*

List of tables

Table 2-1: The 25 largest gold-rich porphyry copper deposits, ranked on contained gold (Cooke et al. 2005). 17

Table 3-1: Acoustic properties of common igneous and metamorphic rocks at 200 MPa pressure and at room temperature (Salisbury et al. 2003). 37

Table 4-1: Measured, indicated and inferred mineral resources summary of Hillside Cu-Au Mining Project - May 2015 (Rex Minerals Ltd 2015). 52

Table 4-2: Ore reserve at Hillside - May 2015 (Rex Minerals Ltd 2015). 52

Table 4-3: Data acquisition parameters for Hillside 3D seismic survey. 67

Table 4-4: Processing steps applied on the Hillside 3D seismic data 69

Table 4-5: Statistics for the Hillside 3D seismic dataset 71

Table 5-1: Total production in 2013 from the Ni-Cu-PGE mine in Kevitsa (First Quantum Minerals Ltd 2015). 86

Table 5-2: The estimated mineral resources in the Kevitsa mine – 31 December 2013 (First Quantum Minerals Ltd 2015). 86

Table 5-3: The estimated mineral reserves in Kevitsa – 31 December 2013 (First Quantum Minerals Ltd 2015). 87

Table 5-4: Reflection seismic data acquisition parameters for Kevitsa 3D conducted in 2010 (Courtesy: HiSeis Pty Ltd; Malehmir et al. 2014). 95

Table 5-5: Survey details of the Kevitsa 3D seismic volume 97

Table 5-6: Details for the Kevitsa structural grid 110

Table 6-1: December 2015 quarter production from the Cracow mining project (Evolution Mining 2016). 130

Table 6-2: 3D Seismic data acquisition parameters for Cracow (Courtesy: HiSeis Pty Ltd) *133*

Table 6-3: Statistics for the Cracow 3D prestack time-migrated seismic volume *135*

Table 6-4: Conditioning steps used to prepare the data for edge detection *136*

1. Introduction

1.1. Prologue

Mining, alongside agriculture, is one of human's earliest activities, fundamentally contributing to the development and continuation of modern civilisation (Bell and Donnelly 2006). The dependency of mining upon ancient civilisations is evidenced by the terms "the Stone Age", "the Bronze Age", and "the Iron Age", which implies increasing complexity of extraction techniques over time. The oldest known mine is the Lion Cave in Switzerland and has a radiocarbon age of about 43,000 years (Bell and Donnelly 2006).

Earth's crust hosts rocks of various geologic ages and origins and thus has different lithological compositions (Rudnick and Fountain 1995; Taylor and McLennan 1985). As a result, they differ in physical properties such as magnetic susceptibility, thermal conductivity, electrical resistivity, density, and elastic properties (Taylor and McLennan 1985). Based on these properties the well-known geophysical methods have been developed. The principal purpose of geophysical investigations is to identify anomalous physical properties in the subsurface (Taylor and McLennan 1985).

Figure 1-1 exhibits the depths of the major mineral discoveries between 1950 and 2010 in Australia. The plot portrays an increasing trend towards the depths of mineral discovery inferring that near-surface deposits have already been explored to a great extent. Therefore, faster, cheaper and better deep exploration techniques are essential to sustain the future needs (Salisbury and Snyder 2007). The conventional exploration tools used for mineral exploration are gravity, magnetic, electrical, electromagnetic, geological field mapping and drilling. Gravity, electrical, electromagnetic and magnetic methods are incapable of resolving exploration targets beyond 500 m deep, whereas seismic reflection methods can be used to render images of the subsurface geologic structures and sometimes can successfully delineate ore-bodies at depths more than one kilometre (Malehmir *et al.* 2012b; Salisbury and Snyder 2007). Consequentially, the seismic reflection method can potentially become an essential tool to delineate subsurface structures hosting ore-bodies (Malehmir *et al.* 2012b; Salisbury and Snyder 2007; Urosevic *et al.* 2012).

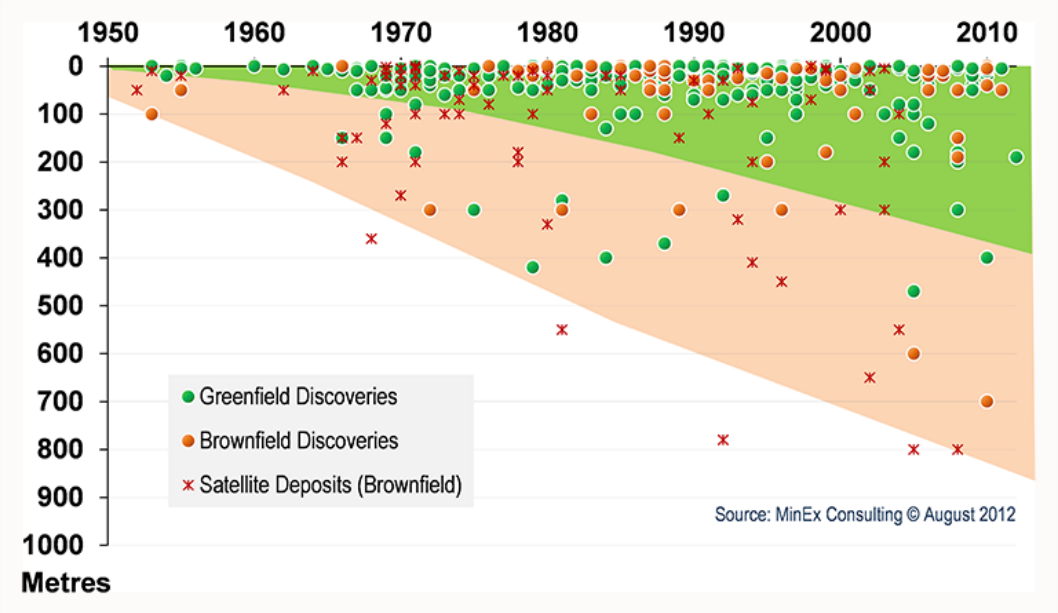

Figure 1-1: Depths of mineral discoveries (excluding bulk minerals, and limited to Moderate, Major and Giant deposits only) in Australia during 1950-2000 (Schodde 2012). Major is > 1 million Oz of Au, > 100 kt of Ni, > 1 Mt of Cu. Giant is > 5 Mt Cu-equivalent; and Supergiant > 25 Mt Cu-equivalent. Satellite deposits supply ore to a central mill within and existing mining camp (Schodde and Guj 2012).

Seismic reflection method has been utilised in sedimentary environments with great success to explore petroleum resources since 1960s. Despite being successful in sedimentary environments, seismic methods are not widely employed in mineral exploration. The main reason is the expenditures of seismic surveys compared to the conventional gravity, electrical, electromagnetic and magnetic methods. Solutions towards improving low signal-to-noise ratio and resolving the lack of prominent marker horizons within hard rock environments need to be pursued to popularise seismic reflection methods in mineral exploration (L'Heureux *et al.* 2005). In hard rock settings, the intrinsic heterogeneity of the media hosting mineral systems scatters seismic signals, thus obscuring the desired target (L'Heureux *et al.* 2005).

Hard rock comprises of igneous and metamorphic rocks, and often have very complex geological structures, including a high number of subvertical faults, fractures, shear zones, granitic intrusions, alterations, and rugged topography. The presence of weathered regolith overburden may cause attenuation of seismic signals by distorting, scattering, and absorbing seismic energy. The often-small contrast in elastic properties

of hard rocks results in a low seismic reflectivity and presents challenge to seismic data processing and interpretation.

1.2. Early application of seismics in mineral exploration

In the 1970s and 1980s, many seismic experiments have been conducted employing seismic imaging methods in hard rock environments. The possibility of observing reflections from the boundaries within crystalline rocks was discussed by Noponen *et al.* (1979). Noponen *et al.* (1979) concluded that the acoustic impedance contrast of most mafic rocks and high-density ores against felsic rocks would generate discernible reflections. Mair and Green (1981) conducted a high-resolution seismic reflection survey across the central region of an Archaean granitic pluton to investigate the use of plutonic rock bodies for the disposal of radioactive waste material. Reed (1993) provided a comprehensive review of mineral exploration using seismic reflection methods. Cosma *et al.* (2001) conducted Vertical Seismic Profile (VSP) surveys to detect fracture zones in the crystalline bedrock for a potential nuclear waste disposal-site selection in south-west Finland. Juhlin and Stephens (2006) successfully used reflection seismic and borehole data to investigate site feasibility for the disposal of highly radioactive nuclear waste in Sweden.

A 3D seismic reflection survey for mineral exploration in hard rock environments was first carried out in South Africa in 1987 (Campbell and Crotty 1990; Campbell 1994; Malehmir *et al.* 2012b; 2012a; Manzi *et al.* 2012b). In 1995, a 3D seismic reflection survey was conducted in the Sudbury complex to explore a Ni-Cu deposit (Malehmir *et al.* 2012b; Milkereit *et al.* 1996; Milkereit *et al.* 2000b).

In Canada, Nordanda Inc. (currently known as Xstrata) carried out numerous 2D and 3D seismic reflection surveys for deep exploration (>1500 m) during 1996-2000. In Canada, a 3D seismic reflection survey was conducted for the first time in the western part of the Bathurst mining camp of the Halfmile Lake area to delineate a blind massive sulphide deposit at 1.2 km depth (Bellefleur *et al.* 2004; Kukkonen *et al.* 2011; Malehmir and Bellefleur 2009; Malehmir *et al.* 2012b; Matthews 2002).

Geoscience Australia is extensively experienced in land seismic surveying within regional Australia and has collected about 15,000 km of land crustal seismic reflection

data and numerous 2D seismic reflection profiles (Malehmir *et al.* 2012b). In Australia, particularly in Western Australia, seismic reflection methods have been utilised on many occasions to explore mineral deposits. Greenhalgh *et al.* (2000) conducted research on the use of cross-hole and VSP to delineate mineralisation and rock structures at the Kambalda nickel mines. In 2002, Urosevic *et al.* (2007) reprocessed and reinterpreted several low and high-resolution seismic lines from the Kambalda area for gold exploration. In 2004, Urosevic et al. (2005; 2007) started an experimental programme to collect high-resolution seismic reflection data over six gold-bearing deposits at the depth range of 100-1500 m. This project was able to shatter the preconceived idea that seismic reflection methods do not produce relevant information for mineral exploration in Australian hard rock environments (Hossain *et al.* 2013). Their success has initiated a high-resolution seismic data acquisition project in 2004 to collect about 150 km of 2D seismic data within Australia (Urosevic *et al.* 2005).

Numerous 3D seismic reflection surveys have been conducted for mineral exploration in Western Australia for Independent Group, Consolidated Minerals, BHPB Nickel West, Mincor, Weebo Well (Poseidon Nickel), Spotted Qual (Newexco), Oxiana 3D (MMG), Pilbara region (Rio Tinto), and Ranger (ERA) (Hossain *et al.* 2013; Malehmir *et al.* 2012b). Several 3D seismic surveys were able to delineate nickel deposits in the Kambalda region (Malehmir *et al.* 2012b; Urosevic and Kepic 2008; Urosevic *et al.* 2012).

1.3. Current status of mineral exploration

The population growth and rapid urbanisation have created an unprecedented demand for minerals and metals. The historical record demonstrates that the overall discovery rate increased during the 1950s and 1960s, peaked in the 1980s and then began to fall during the 1980s and 1990s (Blain 2000). Most mineral production at present is two to three orders of magnitude higher than a century ago.

The sustainability of mining relies on the discovery of new mineral deposits. Greenfield exploration is crucial to the steady growth of the mining industry. The development of new drilling technologies and a combination of geological, geophysical and geochemical exploration methods are essential for the discovery of new economic mineral resources. Schodde (2011, 2012) revealed that the new discoveries of large,

near-surface deposits are becoming increasingly rare and the near-surface reserves of zinc, copper, gold, and other minerals are in decline. As a result, the current trend of mineral discoveries is shifting toward greater depths.

Major mineral deposits are discovered during the greenfield exploration stage because of their dimensions and distinct signatures (Schodde 2011). It has been discerned that extensive exploration operations and continuous research in the brownfield areas can result in significant discoveries.

The advantages of brownfield exploration are that the existing infrastructures allow rapid development and production of the new mine site. Schodde (2011) and Schodde and Guj (2012) have demonstrated that brownfield explorations take 25% less time from the discovery moment to production compared to greenfield explorations. Figure 1-2 illustrates that the pre-production lead-time for the Australian brownfield mineral discoveries tends to be quicker than the greenfield discoveries.

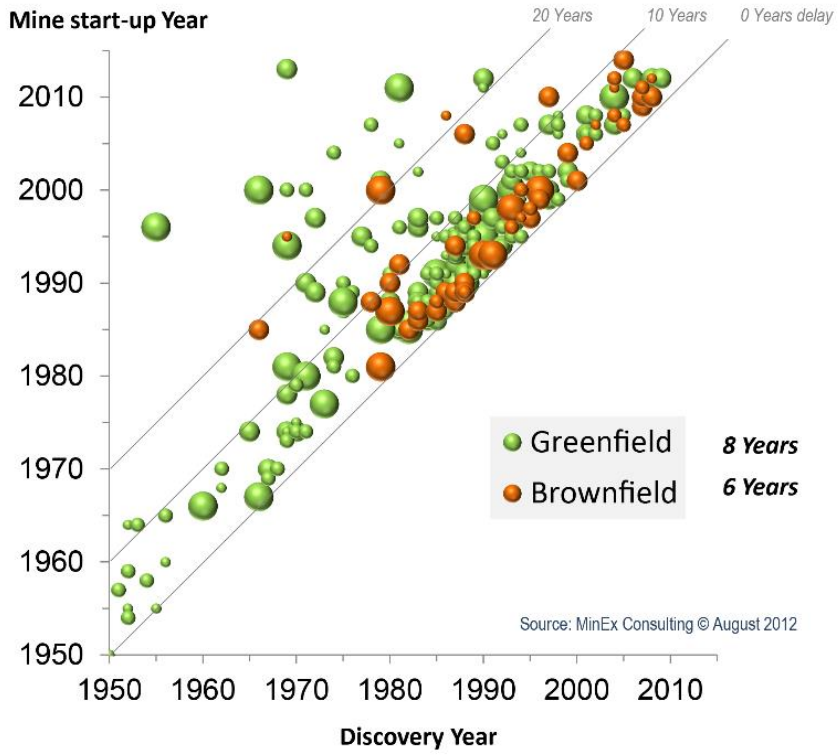

Figure 1-2: The pre-production lead-time for Australian greenfield and brownfield mineral discoveries (Schodde and Guj 2012).

The sustainable supply of mineral resources depends on understanding the origin and formation processes of ore deposits, successful execution of geological, geochemical and geophysical surveys, and mapping of subsurface structures. Future development of the mining industry relies on the discovery of new major deposits and exploration for deeper deposits.

1.4. Objectives and challenges

The primary aims of this research are to determine the feasibility and efficacy of high-resolution surface seismic reflection methods to image deep structures in hard rock environments and improve mapping of deep ore-bodies using 3D seismic data combined with seismic volumetric interpretation. Complex geological settings and industry-specific exploration standards have made these objectives challenging. To overcome the challenges, further developments and improvement in seismic acquisition, data processing and analysis, and interpretation are obligatory. Hard rock environments are often characterised by subvertical structures that are difficult to image using surface seismic methods because the reflected waves often do not reach the surface. The abundance of subvertical to vertical faults, fractures, shear zones and often the presence of regolith overburden causes attenuation of seismic signals by distorting, scattering and absorbing the energy. There is often a lack of acoustic impedance contrast and consequently, low reflectivity and low imaging clarity, complex lateral velocity variations, which results in a reduced interpretability and reduced resolving power of the method. All these difficulties mentioned above make hard rock seismic imaging and analysis a challenge.

The volumetric interpretation of seismic data attempts to compensate for some of these shortfalls by employing seismic attribute analysis that lies at the core of this research and represents a significant and new approach for seismic interpretation within the hard rock environment. For perspective, ant-tracking is a very popular workflow in the petroleum industry to delineate subvertical structures; it has, to our knowledge, never been adopted to the hard rock seismic data until this research. The results presented suggest that the hard rock seismic interpretation has much more to offer than is the current practice in the industry.

1.5. Thesis structure

This thesis is divided into seven chapters. The introductory chapter provides a brief review of the current trend in hard rock mineral exploration, the challenges and the advantages of seismic reflection methods in hard rock mineral exploration. The research objectives and challenges are summarised in this chapter.

Chapter 2 overviews economic mineral deposits found in Australia and Finland followed by the classification of ore deposits and a brief description of each class. The origin, occurrences and geological setting of each ore types are also discussed in this chapter.

Chapter 3 discusses the basic concepts of seismic reflection method relevant to hard rock environments. The conventional and attribute-based seismic volumetric interpretation methods, 2D and 3D interpretation strategies, pitfalls in the interpretation of hard rock seismic data and 3D visualisation techniques are also discussed in this chapter.

Chapter 4 includes a case study from the Hillside copper-gold mining project in South Australia. This chapter discusses the geological setting of the survey area followed by acquisition, processing and interpretation of the seismic data.

Chapter 5 deals with the second case study from the Kevitsa nickel-copper-platinum group elements mine in northern Finland. A brief overview of the geological setting of the study area is presented at the beginning of the chapter. The seismic acquisition, processing steps and seismic volumetric interpretation techniques and property modelling employing boreholes logs are discussed afterwards.

Chapter 6 overviews the final case study from the Cracow gold mine in Queensland, Australia. This case study is based on a consultancy work done for HiSeis Pty Ltd, leading to a report entitled, "*The application of edge enhancement attributes to detect and characterise high order structures for the direct interest of gold exploration in Cracow, Queensland*". This chapter briefly discusses the geology of the study area followed by the interpretation of fault network and lithological modelling. The chapter is concluded by comparing the ant-tracking result with faults detected in the boreholes.

The discussion and conclusions are outlined in Chapter 7.

A full list of references cited is provided at the end of the thesis using a slightly modified version of the Chicago Manual of Style 16th Edition provided by the Curtin University library.

Permissions to use Figures and tables from previously published books and articles are provided in the Appendix I. Physical property data measured from the core samples from Hillside mine are provided in Appendix II.

2. Mineral resources of Australia and Finland

2.1. Australian mineral resources

The mineral industry is a major contributor to the Australian economy (Hughes 1990). According to 1301.0–Year Book Australia, 2012, the mining sector represents 7% of Gross Domestic Product (GDP); incorporating mining services, the total value of the mining industry during 2009 and 2010 was 8.4% of GDP. Australia is one of the biggest key producers of mineral commodities. In 2012, Australia's Economic Demonstrated Resources (EDR) for iron ore, gold, nickel, lead, rutile, zircon, uranium and zinc were the world's largest (McKay *et al.* 2014). Copper, bauxite, black coal, silver, recoverable brown coal, cobalt, ilmenite, lithium, manganese, magnesite, niobium, tantalum, tungsten and vanadium are all ranked in the top six worldwide (McKay *et al.* 2014).

Australia's EDR of gold increased about 8% (~750 tonnes) in 2012 to 9909 tonnes (McKay *et al.* 2014). It is the world's largest gold producer by country, with about 18% of the estimated total production. In 2012, Western Australia dominated the national gold production (43%), an increase of about 240 tonnes from 2011 (McKay *et al.* 2014).

In 2012, Australia's EDR for iron ore increased to 44650 Mt (18%). Western Australia produced ~91% of Australia's EDR and the majority of which was in the Pilbara region (McKay *et al.* 2014).

Australia ranked second in the worldwide in bauxite production (6281 Mt in 2012) behind the Republic of Guinea and ahead of Brazil, Jamaica, Vietnam and Indonesia (McKay *et al.* 2014). In 2012, Australia was the second largest producer of alumina and the fifth largest producer of aluminium (McKay *et al.* 2014). The estimated recoverable black coal EDR of Australia in 2012 was 61082 Mt, an increase of 6% from 2011 (McKay *et al.* 2014).

In 2012, Australia's EDR of lithium boosted by 50%, ranking it third largest globally; magnesite summed up to 330 Mt, which was about 4% of the global resources, Copper rose by 4 Mt to 91.1 Mt, an increase of 5% (McKay *et al.* 2014). After Chile (28%)

Australia has the second largest economic resources of copper (13%) and 68% of the national total of EDR is located in the Olympic Dam of South Australia (McKay *et al.* 2014).

However, in 2012, the EDR of diamonds, lead, nickel, silver, brown coal, ilmenite, cobalt, phosphate rock, manganese, tantalum, rutile, uranium and zinc decreased (McKay *et al.* 2014). Figure 2-1 depicts the locations of the currently operating mines of Australian identified mineral resources (last updated January 2014).

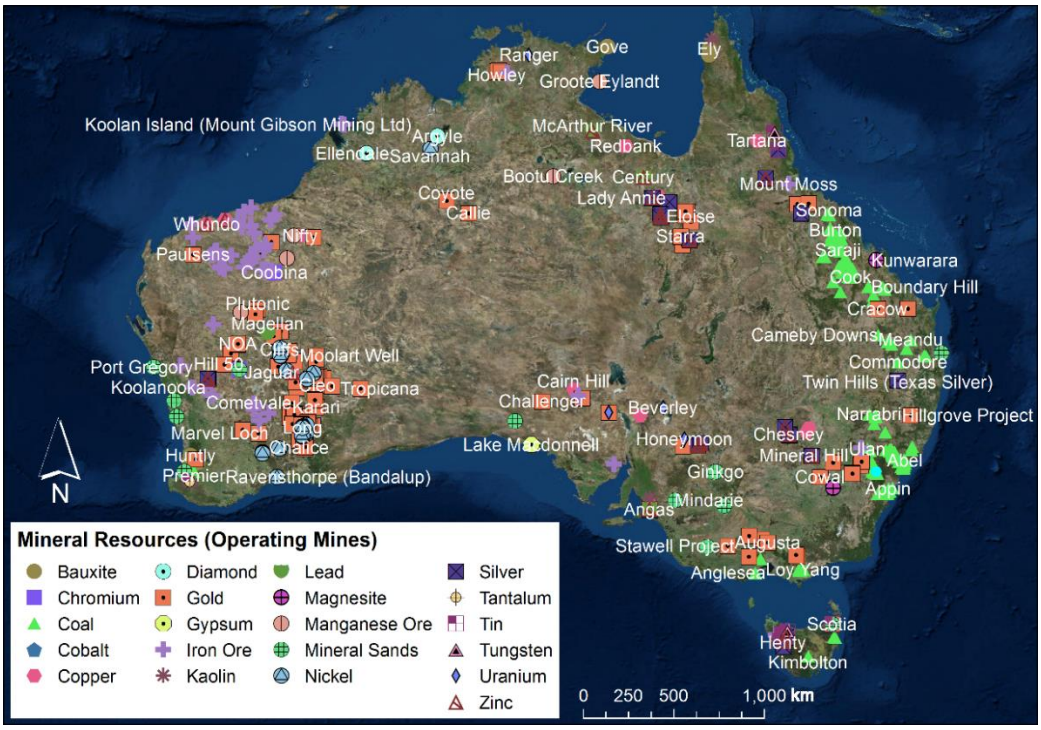

Figure 2-1: Locations of current operating mines of identified mineral resources in Australia (Data Source: Australian Mines Atlas, January 2014).

Australia's economic mineral deposits occur in a great variety of geological conditions. Such diverseness in depositional conditions exists due to the complex interaction of several mechanisms: i) presence of ore-component source, ii) transport mechanism, iii) precipitation and accumulation of the components on site, and iv) appropriate settings for mineral preservation (Tertyshnikov 2014).

2.2. Finnish mineral resources

Finland has a long history of mineral exploration; the history of mining in Finland dates back to 1540 when iron ore mining began (Bowie *et al.* 1978). There are about 270 metal mines in operation, and the total output has been 250 million tonnes of ores (Perez 2014). The country's metal industry includes mining of copper, nickel, lead, zinc, cobalt as well as chromium, vanadium and iron (Bowie *et al.* 1978; Eerola 2013; Perez 2014). The major industrial minerals are carbonates, apatite and talc (Perez 2014).

State-owned companies entirely operated the mining industry in Finland until 1990s (Eerola 2013). During the 90s, Finland joined the European Union that opened the door for foreign companies to explore for diamonds and gold. With the increase in metal prices, some foreign companies started to invest in mining and exploration of several commodities in Finland (Eerola 2013). Finland produces mostly base metals, gold, and platinum-group metals, as well as industrial minerals (Perez 2014). The metal mining industry in Finland is experiencing a boom, and the mined volumes have exceeded previous records (Tuusjärvi *et al.* 2014). Finland was ranked highest in the "Fraser Institute's 2012/2013 survey for mining companies" (Tuusjärvi *et al.* 2014; Wilson and Cervantes 2013). In 2012, copper concentrate production was increased by 118%, gold by 27.8%, silver by 84.9%, nickel by 26.6% and feldspar by 64% (Perez 2014).

The expansion of the Finnish mining industry began with the discovery of Precambrian Outokumpu Copper deposit in 1910 (Peltola 1978). Before closing down, the Outokumpu mine (1913-1988) produced 25.8 Mt of ores with 3.8% Cu, 0.8 ppm Au, 8.9 ppm Ag, 0.12% Ni, 1.07% Zn, and 0.24% Co (Geological Survey of Finland 2014). Serpentinite massifs with dolomite rims, skarn and quartz rocks comprise the 1.96 Ga old Outokumpu rock assemblage (Geological Survey of Finland 2014). A few other Outokumpu-type copper deposits were discovered in Finland much later. Copper deposits in Finland consist of a heterogeneous group of Palaeoproterozoic ores that also contain other base metals (Zn, Co and Ni) and some precious metals e.g., Au, Ag (Geological Survey of Finland 2014). Figure 2-2 shows the locations of primary commodities found in Finland.

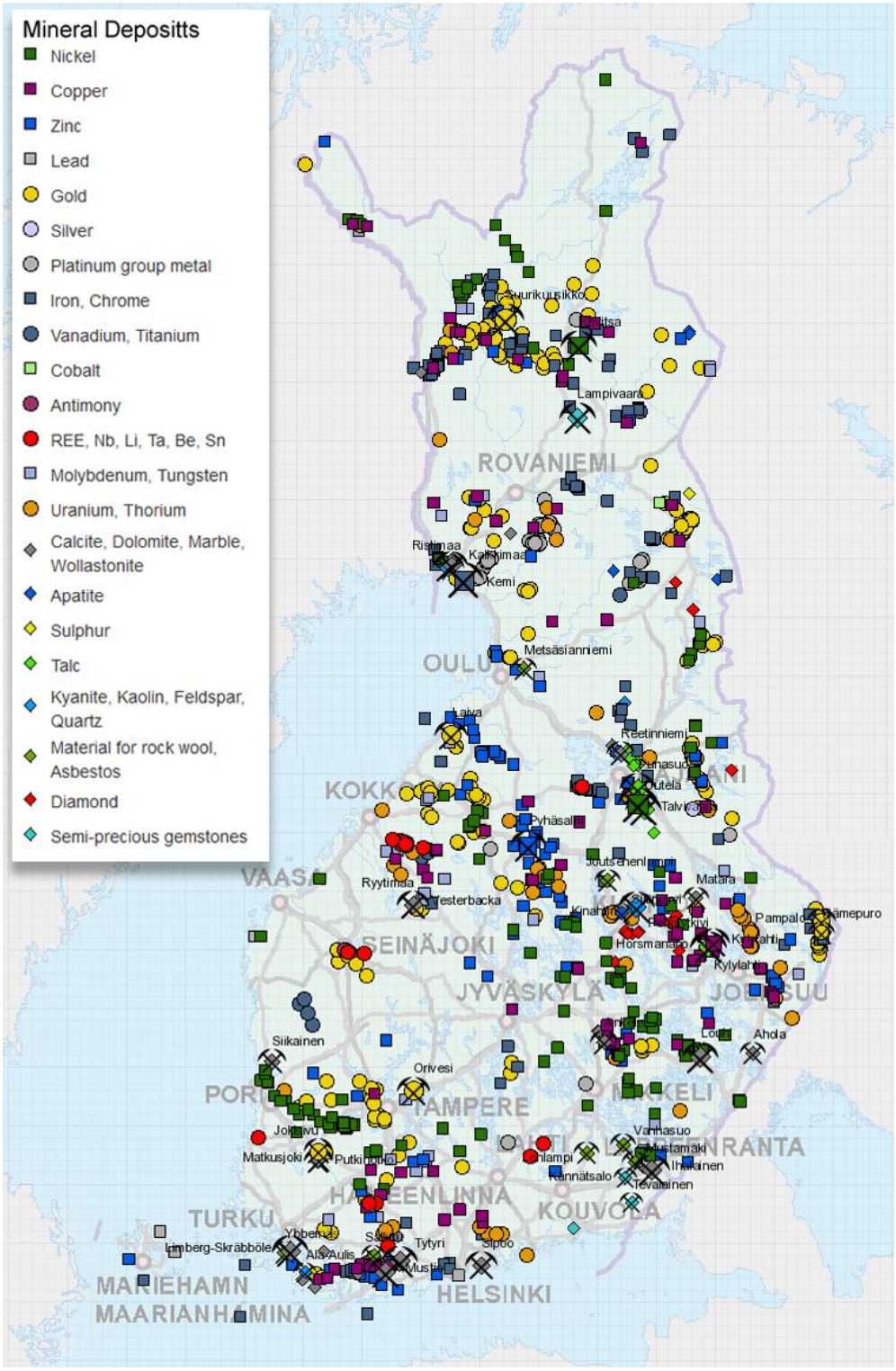

Figure 2-2: Locations of the major mineral deposits found in Finland (Reproduced with the permission of Geological Survey of Finland. All rights reserved.)

In central Finnish Lapland, many early Proterozoic layered intrusions contain Platinum-Group Elements (PGE) enriched mineralised zones (Gervilla and Kojonen 2002). Some deposits also contain sulphides due to the mixing of highly differentiated silicate melts and new pulses of primitive mafic-ultramafic melt (Gervilla and Kojonen 2002; Halkoaho *et al.* 1990). Mutanen *et al.* (1988) and Mutanen (1997) argued that PGE in the Koitelainen and Keivitsa-Satovaara complexes take place in melt-solution Cl complexes. They also suggested that the PGE concentration occurred by the breakdown of such complexes due to crystallisation of primary, cumulus or postcumulus chlorapatite, Cl-rich hornblende and Cl-rich biotite.

The formation of Diamonds occurs at lithospheric depths beyond 150 km (Kennedy and Kennedy 1976). Kimberlite-hosted mantle peridotite xenoliths in eastern Finland indicate that the thickness of the lithosphere is at least 240 km (Kukkonen and Peltonen 1999). Diamondiferous pipes, i.e., Terskii kimberlites in the Kola region, Kostamuksha (lamproite), Archangelsk pipes (Group I and II kimberlites), and Kemozero (kimberlite) confirm that the lithosphere is very thick and extended over a large area (Beard *et al.* 2000; Mahotkin and Skinner 1998). In the northeastern Finland, the known kimberlites occur at the edge of the Archean Craton near Kuopio and Kaavi. The mineralogy includes abundant microcrysts of olivine, picroilmenite, Cr-diopside, pyrope garnet, olivine phenocrysts, microphenocrysts of picroilmenite, perovskite, kinoshitalite mica and spinel in a calcite-serpentine matrix (O'Brien and Tyni 1999).

In Finland, both Archaean and Proterozoic domains in all possible geological settings of the igneous-metamorphic terrains host gold deposits (Eilu 2015; Niiranen *et al.* 2015). The major gold provinces are the Archaean greenstone belts in eastern Finland, the Palaeoproterozoic Svecofennian schist belts in central and southern Finland and the Palaeoprotezoic Karelian greenstone belts in Lapland (Eilu *et al.* 2003; Niiranen *et al.* 2015). Most gold occurrences in Finland are related to orogenic mesothermal mineralisation (Kellaway 2013). Other genetic types include skarn or FeOx-Cu-Au, metamorphosed epithermal, intrusion-related, palaeoplacer and placer deposits (Kellaway 2013).

Finland has a long history of nickel exploration. The Palaeoproterozoic orogenic deposits (Svecofennian) is considered as the primary exploration targets (Loukola-Ruskeeniemi and Sorjonen-Ward 1997). Several potential Ni deposits are hosted in the

Kotalahti and Vammala Nickel belts in central and southern Finland (Fiorentini *et al.* 2010).

The Platinum Group Elements are exclusively confined to an east-west trending 300 km long Tornio-Näränkävaara belt in northern Finland (Alapieti 2005). Uranium, Zinc, and industrial minerals and rocks have also been explored to some extent in Finland.

2.3. Classification of ore deposits

The classification of ore deposits is established through several criteria, e.g., mineral content, shape and size of the deposit, host rocks or the genesis of the deposit. There is considerable debate among geologists about the exact genesis of most mineral deposits. However, a classification based on the physical description of a deposit coincides with the classification based on Genesis (Evans 1993).

Ore deposits are categorised into two general groups: i) syngenetic and ii) epigenetic. Syngenetic deposits form during the formation of the enclosing rock and are associated with specific stratigraphic formation, whereas, epigenetic minerals form much later than the enclosing rocks in the form of veins, stocks, lenses and pipes that cut through the rocks (Hughes 1990). A general overview of the most economically significant mineral deposits is provided in the following sections.

2.3.1. Porphyry deposits

Porphyry deposits are large, low-grade and usually associated with an intrusive porphyritic body(Clark 2014). It is the biggest source of copper in the world and a significant host of gold, silver, and molybdenum (Cooke *et al.* 2005; Evans 1993). The porphyry deposits most commonly occur in continental and oceanic arcs of Tertiary and Quaternary age (Cooke *et al.* 2005; Evans 1993). Figure 2-3 shows the worldwide distribution of porphyry copper deposits.

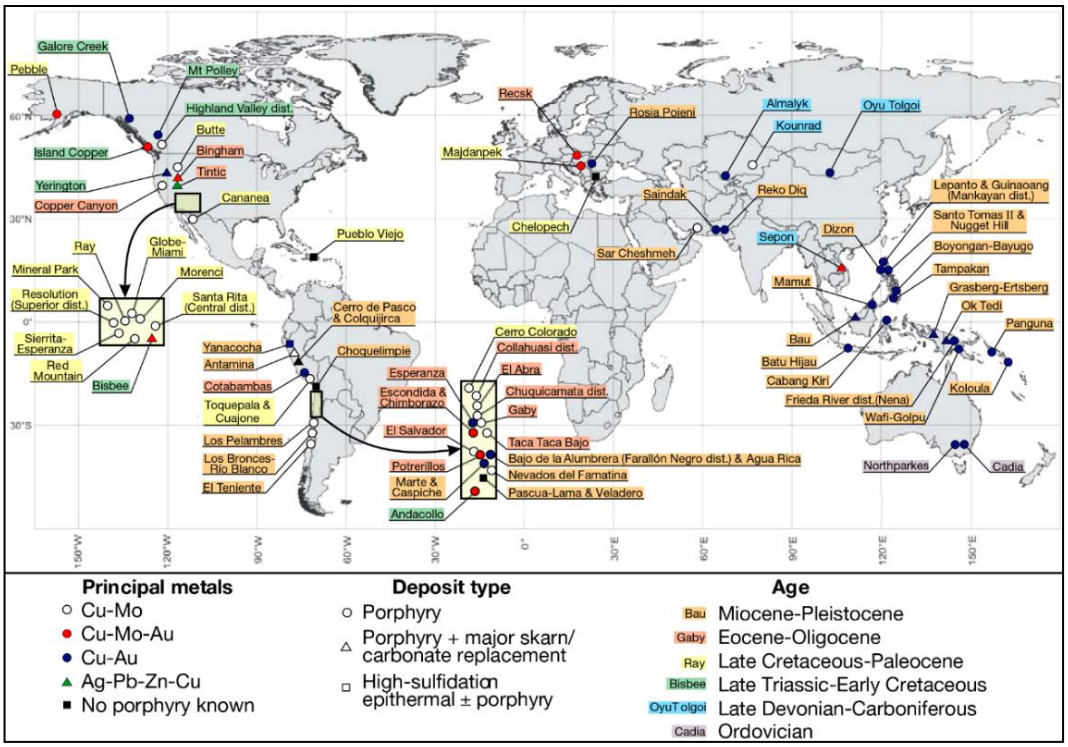

Figure 2-3: Worldwide locations of porphyry copper systems (Sillitoe 2010).

Some porphyry deposits have also been found in Archean fold belts (Cooke *et al.* 2005). Cooke *et al.* (2005) demonstrated the spatial co-occurrence of many of the world's largest porphyry deposits in Tertiary and Quaternary magmatic arcs near subduction zones, oceanic plateaus, and seamount chains and suggested that tectonic "triggers" might have played a significant role during mineralisation. By reviewing the characteristics of the 25 largest porphyry copper deposits, Cooke *et al.* (2005) also indicated that giant porphyry systems are confined to a few mineral regions and time-periods. Figure 2-4 shows the 25 largest porphyry deposits identified by age; the data are provided in Table 2-1.

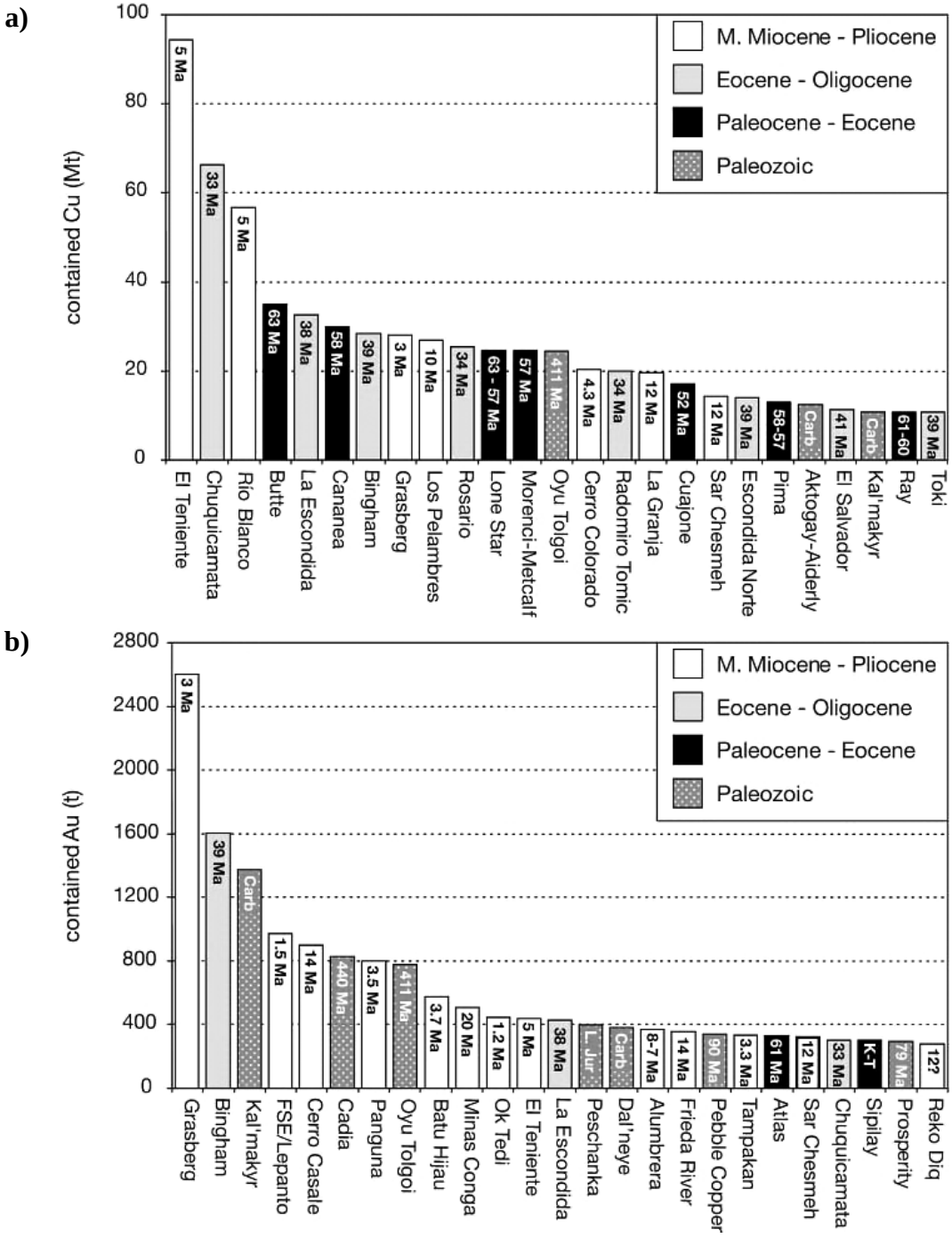

Figure 2-4: The 25 largest porphyry deposits identified by ages. (A) Giant copper deposits. (B) Giant gold deposits (Cooke et al. 2005).

Table 2-1: The 25 largest gold-rich porphyry copper deposits, ranked on contained gold (Cooke et al. 2005).

	Deposit	Province	Age (Ma)	Tonnage (Mt)	Au (g/t)	Au (t)	Cu (wt %)	Cu (Mt)	Mo (wt %)	Mo (Mt)
1	Grasberg	Irian Jaya	3	2,480	1.05	2,604	1.13	28.02		
2	Bingham	Utah	38.8	3,228	0.5	1,603	0.88	28.46	0.02	0.81
3	Kal'makyr	Uzbekistan	310-294	2,700	0.51	1,374	0.4	10.8		
4	Lepanto-Far South East	N. Luzon	1.5-1.2	685	1.42	973	0.8	5.48		
5	Cerro Casale	Chile	13.5	1,285	0.7	900	0.35	4.5		
6	Cadia	NSW	440	1,070	0.77	823	0.31	3.38		
7	Panguna	Bougainville	3.5	1,415	0.57	799	0.46	6.51		
8	Oyu Tolgoi	Mongolia	411	2,467	0.32	790	0.83	20.57		
9	Batu Hijau	Indonesia	3.7	1,644	0.35	572	0.44	7.23		
10	Minas Conga	Northern Peru	20	641	0.79	506	0.3	1.92		
11	Ok Tedi	PNG	1.2-1.1	700	0.64	446	0.64	4.48		
12	El Teniente	Central Chile	4.8	11,845	0.035	437	0.63	94.35	0.02	2.5
13	La Escondida	Northern Chile	38	2,262	0.19	430	1.15	32.49	0.021	0.48
14	Peschanka	Kamchatka	L. Jur.	940	0.42	395	0.51	4.79		
15	Dal'neye	Uzbekistan	310-294	545	0.69	376	0.59	3.21		
16	Bajo de la Alumbrera	Argentina	8-7	551	0.67	369	0.52	2.87		
17	Frieda River	PNG	14-11	1,103	0.32	354	0.61	6.73		
18	Pebble Copper	Alaska	90	1,000	0.34	340	0.3	3		
19	Tampakan	Philippines	3.3-2.2	1,400	0.24	336	0.55	7.7		
20	Atlas	Philippines	61	1,380	0.24	331	0.5	6.9		
21	Sar Cheshmeh	Iran	12.2	1,200	0.27	324	1.2	14.4	0.03	0.36
22	Chuquicamata	Northern Chile	33.6	12,066	0.04	301	0.55	66.37	0.024	1.81
23	Sipilay	Philippines	K-T	884	0.34	301	0.5	4.42	0.01	0.09
24	Prosperity	BC, Canada	79	631	0.46	290	0.25	1.58		
25	Reko Diq	Pakistan	Miocene?	855	0.33	282	0.65	5.56		

The precursor plutons, which are typically multiphased, equigranular intrusions, batholithic type, and dioritic to granitic compositions have a relationship with porphyry copper systems (Sillitoe 2010). They are spatially, temporally and most probably genetically related to porphyry copper and incumbent epithermal gold formation (Sillitoe 2010). The precursor plutons may act as host to a single deposit (Mt. Polley, British Columbia) or clusters of two or more discrete deposits (El Abra intrusive complex, northern Chile).

Porphyry copper deposits may be associated with comagmatic, calc-alkaline, or alkaline volcanic rocks. Tectonic triggers for the formation of porphyry ores are epithermal in nature, and plate subduction may consumed the evidence (Cooke *et al.* 2005). Figure 2-5 shows the geological settings associated with the porphyry ore deposits formation and their relationship with the host rocks.

The shape and orientation of the deposit reflect the nature of host intrusions. Vertical stocks consisted of cylindrical ore-bodies, narrow and elongated shaped ores are deposited in the laterally extended dykes (Evans 1993). Deep drilling in a few large porphyry copper deposits demonstrated that the mineralised intrusions have vertical extents of more than 2 km (Sillitoe 2010). Due to the differences in post-ore intrusions, host rock types, erosional processes, post-ore folding and faulting, the configurations and dimensions of the porphyry deposits vary widely (Sillitoe 2010).

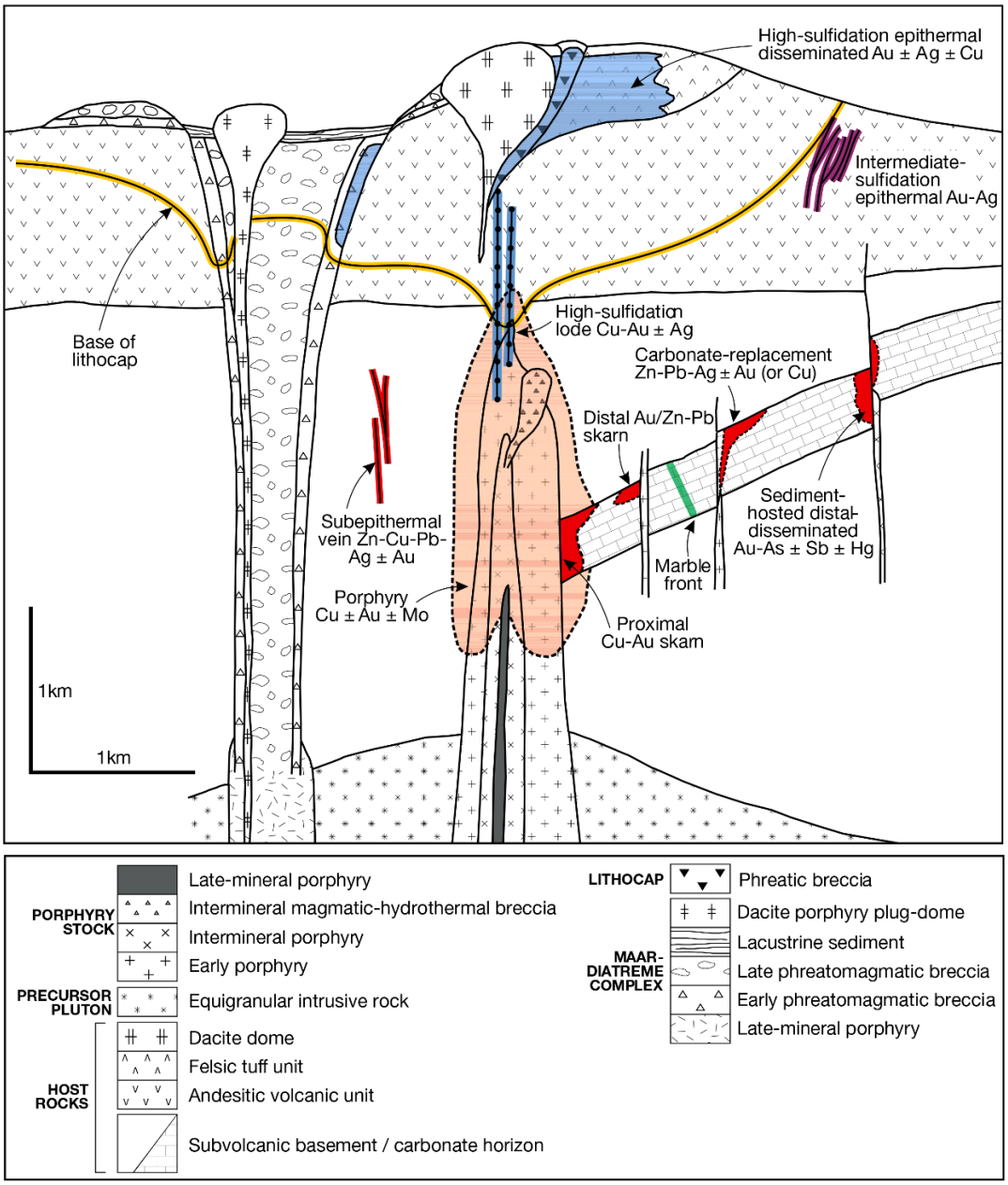

Figure 2-5: The geological relationship between different types of porphyry deposits and their host rocks as well as the temporal sequences (Sillitoe 2010).

2.3.2. Iron Oxide-Copper-Gold deposits

The discovery of giant Olympic Dam deposit in the Stuart Shelf region of South Australia in 1976 has stimulated renewed interest in Iron Oxide-Copper-Gold (IOCG) deposits of the Early to mid-Proterozoic age (Hitzman *et al.* 1992). The term Iron Oxide-Copper-Gold was suggested by Hitzman *et al.* (1992) and they referred to this class as a Proterozoic iron oxide (Cu-U-Au-REE) deposit. IOCG systems occur on all continents and range in age from the present to Late Archean (Williams *et al.* 2005). Hitzman *et al.* (1992) suggested that shallow-level hydrothermal processes probably related to deep-seated magmatism formed these deposits. Most of the IOCG deposits are associated with batholithic granitoids, occur in very extensive and commonly pervasive alkali metasomatic crustal settings (Williams *et al.* 2005). The IOCG deposits are enriched in a geochemically distinctive, diverse suite of minor elements, e.g., F, P, Co, Ni, As, Mo. Ag, Ba, LREE, and U (Williams *et al.* 2005). Figure 2-6 shows the worldwide distribution of the Proterozoic Iron-Oxide deposits.

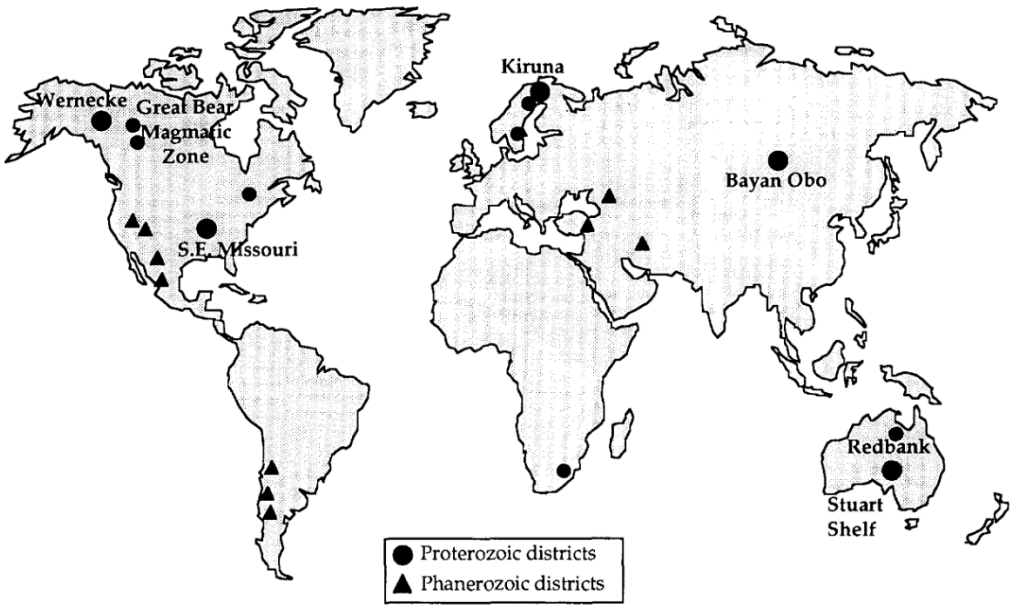

Figure 2-6: Worldwide distribution of the Proterozoic Iron-Oxide (Cu-U-REE-Au) deposits (Hitzman et al. 1992).

According to Williams *et al.* (2005), the IOCG deposit class includes the following key features: (i) presence of copper with or without gold as economic minerals; (ii) hydrothermal vein, breccia and/or replacement ore styles in some specific structural

sites; (iii) abundant magnetite and/or hematite with a few exceptions; (iv) iron-oxides with low titanium content compared to those in most igneous rocks; and (v) absence of spatial association with igneous intrusions.

The morphology of Iron Oxide ores (Cu-U-REE-Au) ranges from steep, pipe or dyke-like bodies, along faults or intrusive contacts or tabular to concordant shaped within stratified volcanic or sedimentary rocks (Hitzman *et al.* 1992). In addition to discordant or concordant shapes, numerous deposits exhibit irregular bulbous shapes or stockwork zones that are sometimes referred as ore breccias (Hitzman *et al.* 1992). The diversity of the alteration zoning, mineral domains and contributions of different fluid sources for many IOCG deposits worldwide are illustrated in Figure 2-7.

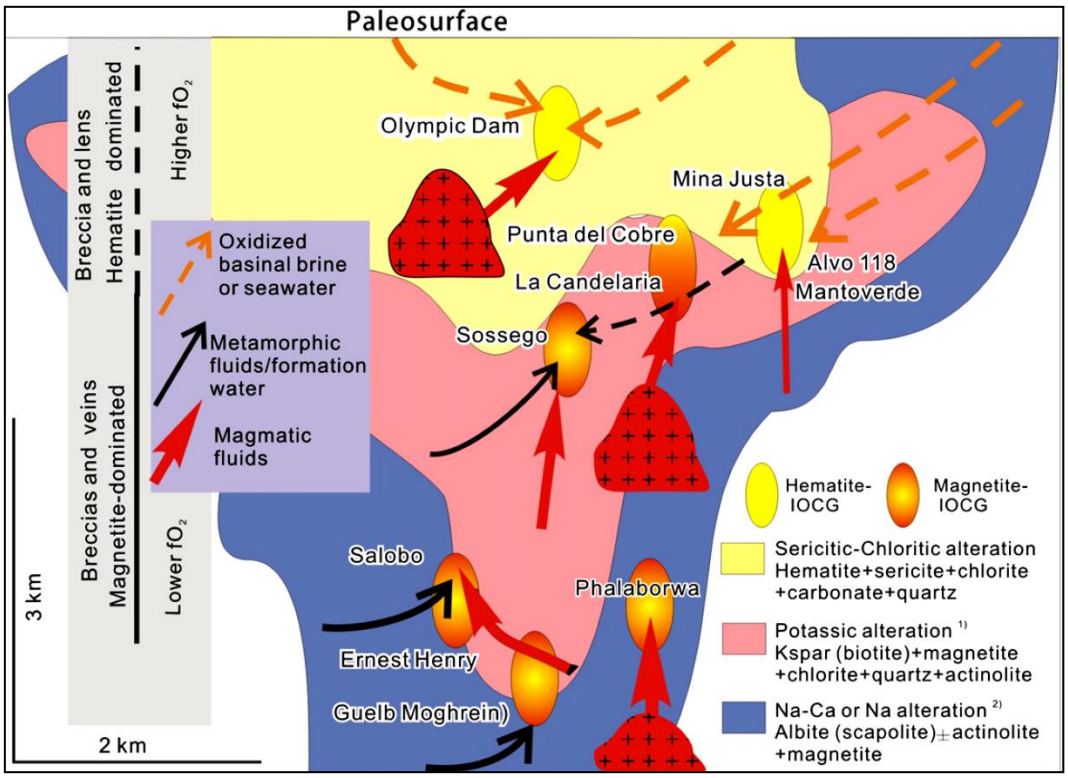

Figure 2-7: The diversity of Iron Oxide-Copper-Gold deposits settings. The thickness of the arrows indicates the relative contribution of various fluids (Chen 2013).

This thesis includes volumetric interpretation of the high-resolution 3D seismic data collected from Hillside, South Australia, the recent IOCG discovery on the east coast of the Yorke Peninsula.

2.3.3. Banded Iron Formations

Banded Iron Formations (BIFs) are the world's most valuable source of economic iron ore deposit (Cloud 1973). BIFs are a thinly layered rock, enriched in primary bedded charts with alternating iron-rich layers (Krapež *et al.* 2003). Giant deposits of Banded Iron Formations occur in Australia, South Africa, Brazil, and Russia with individual reserves of tens of billions of tonnes (Cloud 1973). These formations commonly occur in rocks associated with Precambrian sedimentary sequences and consists of clays, dolomites, mafic volcanic rocks, which indicates shelf depositional environment (Krapež *et al.* 2003). According to Krapež *et al.* (2003), the theories concerning the depositional conditions during the global accumulation of BIFs in Precambrian time are still debatable. Ewers and Morris (1981) and Morris (1993) studied the environmental factors associated with the iron precipitation. Cloud (1973) assumed that during the depositional period, the atmosphere contained little to no oxygen, and higher carbon-dioxide and the depositional environments were anoxic. The only oxidising environments were related to the photolytic dissociation or photosynthesising biota.

The sources of the BIFs are different; mainly volcanic in Archean and Phanerozoic deposits; accumulated through upwelling in stagnant waters (Cloud 1973). The late-Proterophytic deposits probably leached from adjacent low-lying lands to attain a state of general supersaturation in the water that had no silica-secreting microorganisms (Cloud 1973). The lack of free oxygen in hydrosphere and atmosphere compelled the iron to circulate wildly in solution in the ferrous state, that led to the formation of thin, persistent iron layers by combining with the oxygen generated by the microorganisms as shown in Figure 2-8 (a) (Cloud 1973). Figure 2-8 (b) demonstrates the abiotic mechanism in the anoxic ocean water where ultraviolet light caused the oxidation of Fe^{2+}. This model has recently been discounted by Konhauser *et al.* (2007). Figure 2-8 (c) shows the direct anoxygenic microbial oxidation model.

The chemical similarities and differences among the Archean and Proteophytic banded iron formations occurs due to turbulence and depth of deposition combined with the inconsistent availability of biologically generated oxygen (Cloud 1973). In Australia, the Precambrian BIFs in the Hamersley Basin are the largest sources of iron ore in the world (Pirajno and Bagas 2008).

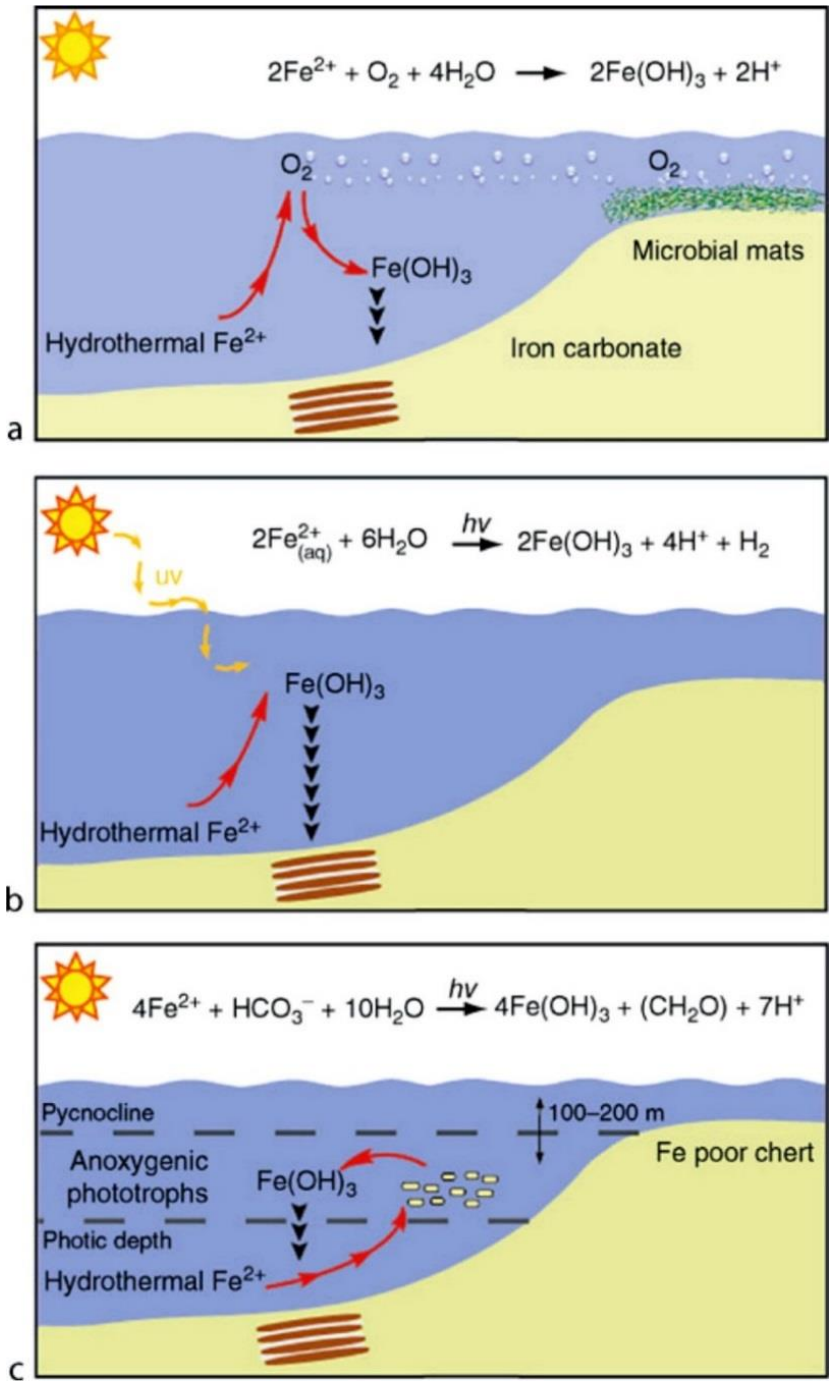

Figure 2-8: Models of Banded Iron Formations deposition. (a) The traditional model of BIF deposition by chemical reaction between hydrothermal dissolved Fe^{2+} and oxygen generated by microorganisms. (b) Photo-oxidation of abiotic Fe^{2+} by ultraviolet light in anoxic ocean water. (c) Fe^{2+} oxidation by anoxygenic microbial organisms (Posth et al. 2011).

2.3.4. Volcanogenic Massive Sulphide deposits

Volcanogenic Massive Sulphide (VMS) deposits are a significant source of copper, silver, gold, lead, zinc and a range of by-products including cadmium, tin, antimony and bismuth (Lydon 1984). There are about 800 known VMS deposits worldwide with reserves over 200,000 tonnes (Chen *et al.* 2015; Galley 1993; Piercey *et al.* 2010; Scott 2001; Zaccarini and Garuti 2008). VMS deposits are also known as volcanic-associated, volcanic-hosted and volcano-sedimentary-hosted massive sulphide deposits (Barrie and Hannington 1999; Dindi and Maneno 2016; Galley 1993; Rao and Naqvi 1997; Wang *et al.* 2010). The age of the VMS deposits range from about 3.5 Ga in the Pilbara region of Australia to the modern deposits at the East Pacific Rise (Lydon 1984). These deposits are mineral accumulations that form on or near the seafloor by the precipitation of sulphide minerals around hydrothermal vents where high-temperature, metal and sulphur-rich fluids mix with cold water (Jamieson *et al.* 2014). The exhalative hydrothermal activity in the oceans recognises that most sulphide deposits are precipitated by replacing the sedimentary and igneous rocks below the hydrothermal mound on the seafloor (Tornos 2006). There are more than 300 sites of high-temperature seafloor hydrothermal systems and associated mineral deposits have been found worldwide (Figure 2-9; Jamieson *et al.* 2014).

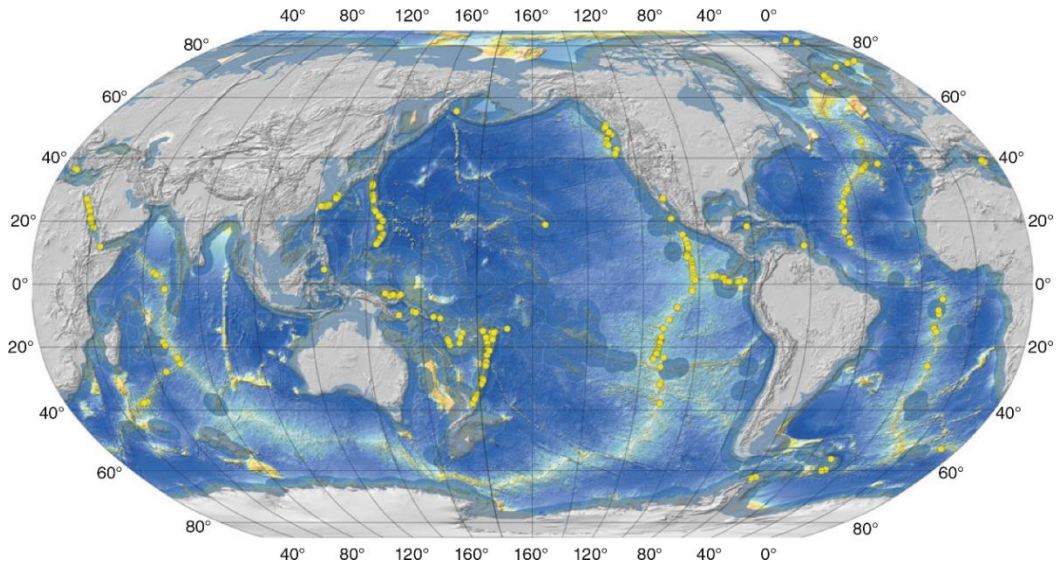

Figure 2-9: Worldwide distribution of seafloor hydrothermal systems and related mineral deposits (Jamieson et al. 2014).

Hydrothermal vents were first discovered on the East Pacific Rise spreading centre, which provided the very first direct evidence of VMS deposits on the seafloor (Jamieson *et al.* 2014). VMS deposits are classified according to base metal content, gold content and host rock lithology (Galley 1993). The deposits are divided into Cu-Zn, Zn-Cu and Zn-Pb-Cu groups according to the relative content of these three metals.

VMS deposits are syngenetic in nature and typically consist of a conformable massive sulphide lens and commonly underlie sulphide-silicate vein-type mineralised zone commonly known as Stringer or stockwork zone (Gibson *et al.* 2007). Altered volcanic and/or sedimentary rocks surround this zone. Figure 2-10 shows a cross-sectional view of a typical active volcanogenic massive sulphide mound on the seafloor.

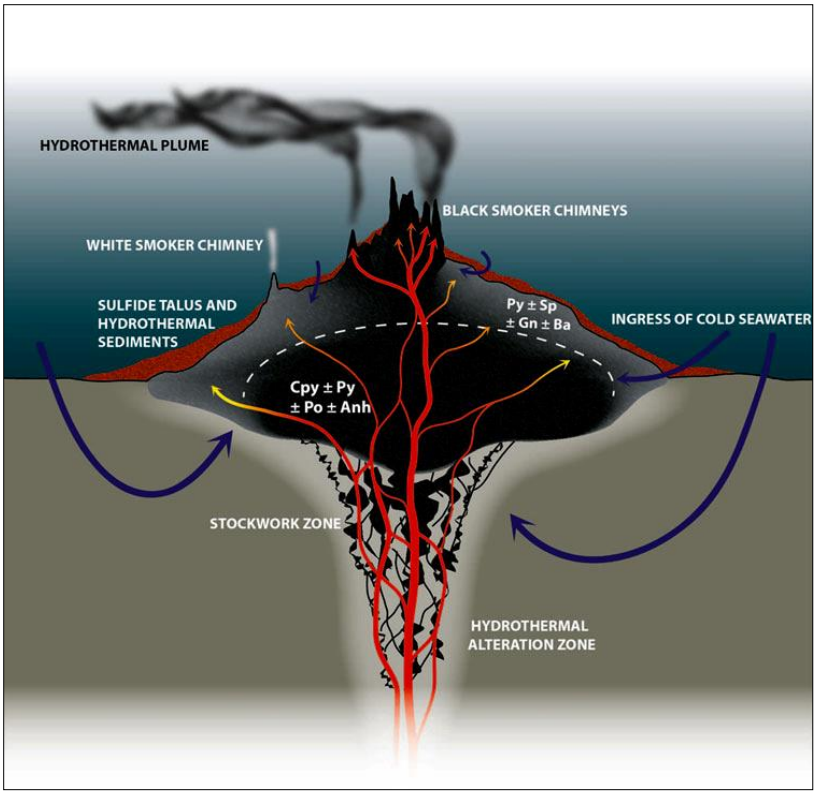

Figure 2-10: Cross-section through a typically active volcanogenic massive sulphide mound on the seafloor. Mixing of cold seawater with the ascending high-temperature hydrothermal fluids results in the precipitation of massive sulphide minerals and formation of chimneys and mounts on or below the seafloor. Py=pyrite, Cpy=chalcopyrite, Sp=sphalerite, Po=pyrrhotite, Gn=Galena, Anh=anhydrite and Ba=barite (Jamieson et al. 2014).

In Australia, the VMS deposits are concentrated in the Mount Read Volcanics in Tasmania and the Mount Windsor Volcanics in Queensland (Large 1992; Large *et al.* 2001). The Archean deposits host about 4 million Mt. of metal and the Silurian deposits host about 3.5 million Mt. of metal with some isolated deposits from the Devonian and Permian periods (Large 1992). There is a wide range of styles of VMS deposits e.g., mounds, sheets, pipes, stacked deposits, layered deposits, stockwork and disseminated deposits, distal reworked deposits, and cyclic layered deposits (DeMatties 1994; Doyle and Allen 2003; Large 1992). However, the consistency across the metal zonation, alteration mineralogy, alteration chemistry, sulphur isotopes, macrotextures, microtextures, and host volcanic relationship indicates that they all belong to one genetic group of deposit (Large 1992).

2.3.5. Orogenic gold deposits

Orogenic gold deposits have been the source of a quarter of world gold resources (Goldfarb *et al.* 2001; 2005; Pitcairn *et al.* 2006). These deposits have formed over a period of more than 3 Ga of earth's history during the Middle Archaean to late Precambrian and throughout the Phanerozoic aeon (Goldfarb *et al.* 1998; 2001; Groves *et al.* 1998). The spatial association of these deposits with deformed metamorphic terranes of all ages indicates a direct relationship between continental growth and orogenesis (Goldfarb *et al.* 2001; Groves *et al.* 1998). Gold mineralisation occurs in second or third order structures and is commonly brittle to ductile in nature (Groves 1993; Groves *et al.* 1998; Holden *et al.* 2008; McCuaig *et al.* 1993). The deposits commonly occur in the accretionary belts adjoining the continental magmatic arcs in the upper crust during accretion/subduction. According to Groves *et al.* (1998), as a subduction zone steps seaward, a series of gold deposits develop toward the trench part of the orogen. For example, Alaskan part of the North American margin is composed of accreted oceanic rock sequences (Churkin *et al.* 1980; Groves *et al.* 1998; Page *et al.* 1986).

Figure 2-11 illustrates the potential scenarios for the formation of orogenic lode gold deposits from orogenic-scale hydrothermal systems driven by the lithosphere-scale thermal anomaly by a series of sketches. Figure 2-11 (A) shows crustal thickening, increased geotherms and formation of magmatic arc due to subduction (Goldfarb *et al.*

2001). Orogenic lode gold deposits precipitate from associated fluids at most crustal depths. Upward convection of fluids deposits Hg-Sb-rich lodes within the top few kilometres of the thickened crust (Goldfarb *et al.* 2001). Figure 2-11 (B) demonstrates the thermal consequences of the plume subduction (impact). The process deposited the Late Archean orogenic gold deposits (Goldfarb *et al.* 2001). Figure 2-11 (C) portrays subduction rollback or seaward subduction. This mechanism acts as a trigger for gold deposition (Goldfarb *et al.* 2001). Jurassic Mother Lode gold belt in California, USA, is an example of rollback subduction (Goldfarb *et al.* 2001). Figure 2-11 (D) displays the subduction of an oceanic ridge. Figure 2-11 (E) exhibits upwelling of asthenosphere and melting at the base of the curst (Goldfarb *et al.* 2001). Erosion of mantle lithosphere takes place by convective removal, and finally, Figure 2-11 (F) presents delamination of mantle lithosphere for late Archean orogenic gold deposits (Goldfarb *et al.* 2001).

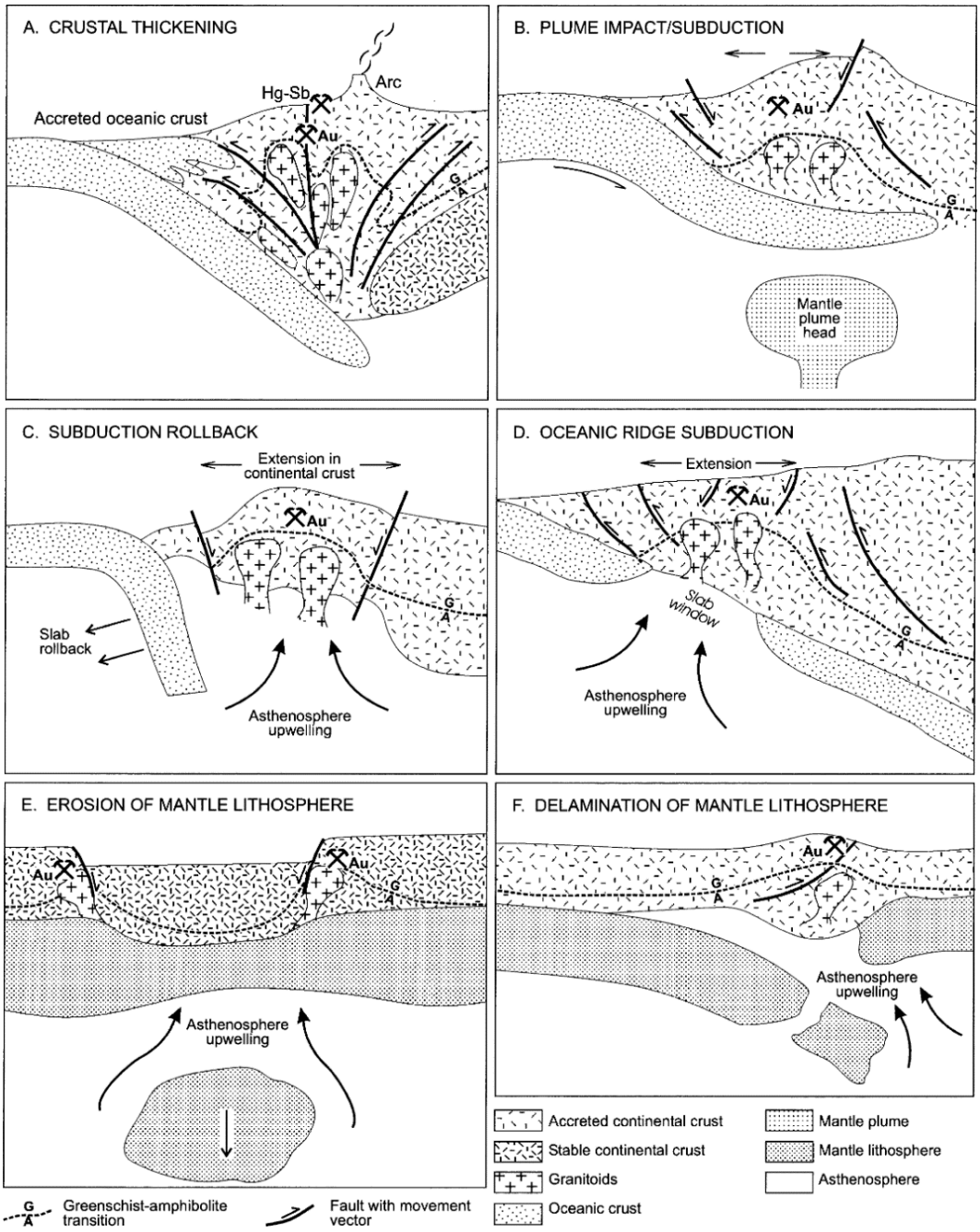

Figure 2-11: A series of simplified sketches showing the formation of orogenic lode-gold deposits (Goldfarb et al. 2001).

The Yilgarn Craton is the largest source of orogenic gold deposits in Australia (Eilu and Groves 2001; Urosevic *et al.* 2005). More than 80% of the orogenic gold deposits in Yilgarn Craton are located in second or third-order structures, near crustal to regional-scale deformation zones, in brittle, brittle-ductile and ductile deformation environments (Eilu and Groves 2001). The gold deposits in the Yilgarn Craton are structurally controlled because of predominantly ENE-WSW trending extension and

NE-SW trending tectonic compression (Blewett *et al.* 2010). The gold mineralisation occurred in all rock types over the range of metamorphic grades, e.g., Banded Iron Formations, sedimentary rocks, felsic igneous rocks, felsic-intermediate volcaniclastic rocks, granitoids, and mafic and ultramafic rocks (Witt and Vanderhor 1998). The ore-bodies are often associated with quartz veins, brittle faults, brittle to ductile shear zones and some strongly ductile shear zones but the geometry of the individual veins within a particular camp may vary depending upon the variation in stress fields (Eilu and Groves 2001; Witt and Vanderhor 1998).

2.3.6. Mississippi Valley-type deposits

Mississippi Valley-type (MVT) deposits contribute nearly 27% of the world's current Zn and Pb resources (Paradis *et al.* 2005). These deposits are composed primarily of sphalerite, galena, pyrite, marcasite, calcite and dolomite (Paradis *et al.* 2007; Zhou *et al.* 2013). Most MVT deposits are restricted to rocks younger than 2 billion years and occur primarily within Phanerozoic rocks (Leach *et al.* 2010). MVT deposits are epigenetic, stratabound, and carbonate-hosted bodies formed from regional fluid migration (Paradis *et al.* 2007). Most of the MVT deposits are located in carbonate platforms neighbouring the cratonic sedimentary basins and formed due to the migration of warm saline aqueous solutions similar to oilfield brines (Paradis *et al.* 2005). MVT deposits are also common in foreland thrust belts; however, they rarely occur in inner continental basins (Paradis *et al.* 2007). The deposits commonly form in dolostone as open-space fillings, collapsed breccias and often as a replacement of the carbonate host rock (Paradis *et al.* 2005). Figure 2-12 exhibits the worldwide distribution of Mississippi Valley-type (MVT) deposits.

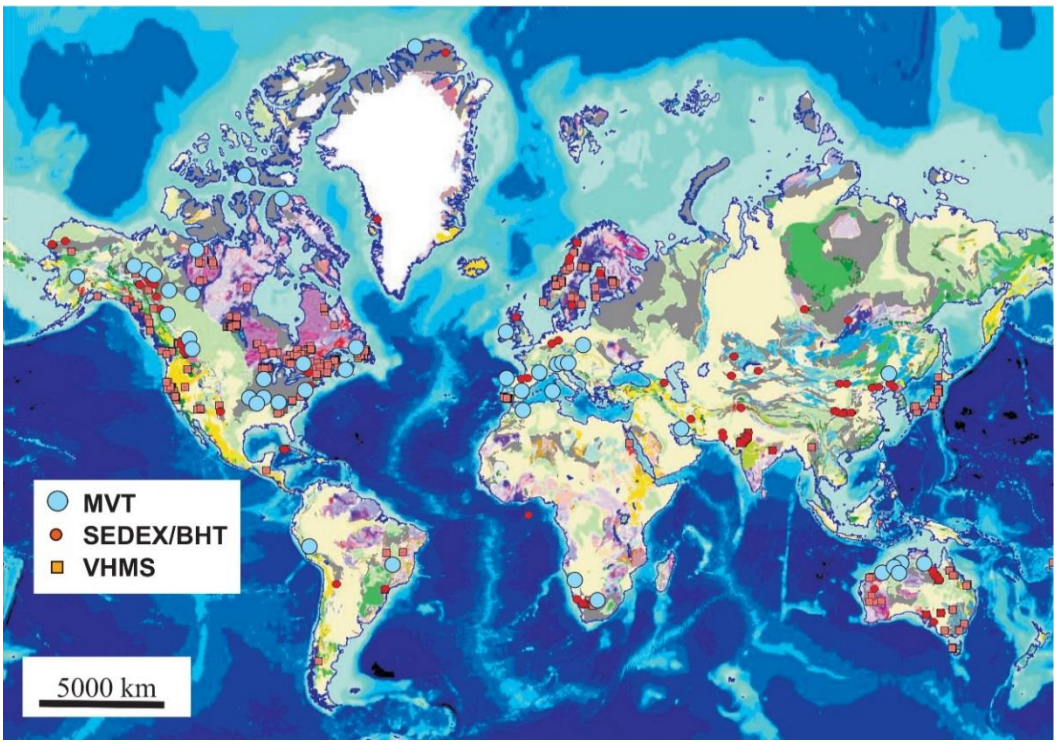

Figure 2-12: Worldwide distribution of Mississippi Valley-type (MVT) deposits. BHT=Broken Hill-type, MVT=Mississippi Valley-type, SEDEX=Sedimentary exhalative, and VHMS=Volcanic-hosted massive sulphides (Paradis et al. 2007).

One of the most popular models suggests that the ore-fluid migration is related to compressional tectonic setting; however, it is not universally applicable, and some of the MVT deposits formed under extensional tectonic settings (Paradis *et al.* 2005). The tectonic setting defines the ultimate fate of a sediment-hosted Pb-Zn deposit. The host-rock type, ore controls, temperature, and pressure of the depositional processes, as well as the survivability of the deposit during tectonic recycling, is determined based on the tectonic setting. Figure 2-13 demonstrates the foreland evolution during plate convergence. Figure 2-13 (a) exhibits the formation of foreland basin, extensional domain and forebulge. These features continually migrate across the foreland plate and the foreland basin remained unfilled due to the migration of depocentre (Bradley and Leach 2003). Figure 2-13 (b) demonstrates favourable hydrological conditions for MVT deposition (Leach *et al.* 2010).

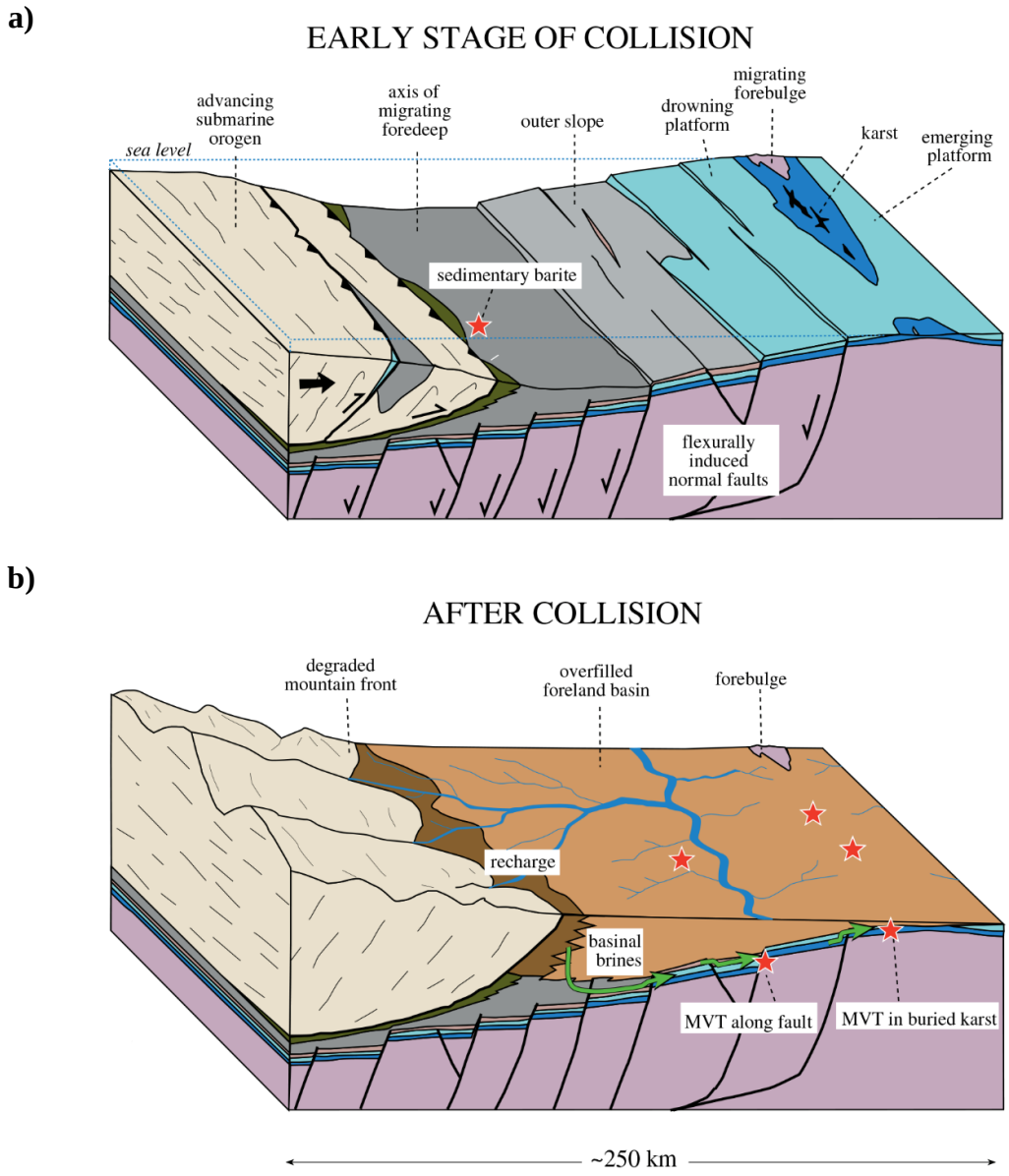

Figure 2-13: Illustration showing a favourable tectonic setting for Mississippi Valley-type (MVT) deposition. (a) early stage of collision and the formation of foreland basin, extensional domain, and forebulge. (b) favourable hydrological conditions for MVT deposition (Leach et al. 2010).

The MVT deposits are irregular in shape; as a result, it is difficult to evaluate the dimension of the ore-bodies. The deposits occur in clusters, commonly referred to as "districts" (Paradis *et al.* 2005). Individual deposits are usually less than 2 million tonnes in size and possess grades that rarely exceeds 10% (Pb + Zn) (Paradis *et al.* 2005).

2.3.7. Unconformity-type Uranium deposits

Geologically, uranium deposits vary widely in styles. The most significant mineralisation styles are unconformity-related Proterozoic deposits, mainly found in Canada and Australia (Lehmann 2008; Polito *et al.* 2005; Rajesh 2008). Uranium also occurs as a by-product of copper mining of IOCG deposits in hematite-granite breccias (Laznicka 2006; Lehmann 2008). Unconformity-related uranium ore deposits occur in extensional structures close to the unconformity between the thick oxidised cover and relatively reduced basement (Cui *et al.* 2012; McQueen 2005). Unconformity-type uranium deposits form at oxidation-reduction margins, where oxidised brines, or meteoric water encounters reducing lithogies or methane-bearing fluids (Komninou and Sverjensky 1996; Lehmann 2008; Raffensperger and Garven 1995). The primary process involves leaching of U^{6+} from uranium enriched rocks under oxidising conditions, and fixation in the U^{4+} state (Lehmann 2008; Zhou and Gu 2005). The formation of ore requires an abundance of oxidising warm water with km-thick sequences of red sandstone (Lehmann 2008). The reduction is achieved by the interaction of such water with reduced lithologies or with hydrocarbons (Lehmann 2008). The unconformity-type uranium deposits are usually structurally controlled and maintain the geometry of the faults and shear zones and are subparallel to the host units (Pirajno and Bagas 2008).

3. Seismic reflection exploration in hard rock environments

3.1. Introduction

Seismic exploration methods provide high-resolution images comparatively to other geophysical methods. The resolution of geophysical exploration methods such as gravity and electromagnetics are typically not effective at depths below 400 m (Gibson *et al.* 2007; Malehmir *et al.* 2012b; Manzi *et al.* 2012a; 2012b; 2015; Pretorius *et al.* 1994; Urosevic *et al.* 2012). The recent mining boom has encouraged mining companies to embrace various surface and downhole exploration techniques (Urosevic *et al.* 2012). Seismic data allow geophysicists to build geological models of the subsurface, and monitor production processes (Tertyshnikov 2014). Even though seismic methods have been used for petroleum exploration for decades with great success, it has failed to gain attention in the mineral exploration. To popularise seismic exploration methods in the mineral industry, certain issues, e.g., the low signal-to-noise ratio, lack of prominent marker horizons, scattering of seismic signals due to the heterogeneity of host rocks need to be resolved (L'Heureux *et al.* 2005). Seismic exploration in hard rock environments has a long history and many examples of successful applications (Gibson *et al.* 2007; Malehmir *et al.* 2012b; Manzi *et al.* 2012a; 2012b; 2015; Pretorius *et al.* 1994; Tertyshnikov 2014). Due to a diminishing supply of near-surface deposits, the mining industry is forced to explore deeper for economic mineral reserves (Malehmir *et al.* 2012b; Salisbury and Snyder 2007; Schodde 2011, 2012; Schodde and Guj 2012). As a result, seismic exploration methods have the potential to become an important tool for mineral exploration. The physics of seismic wave propagation within hard rock environments with emphasis placed on issues unique to the mineral industry is discussed in the following sections.

3.2. Seismic reflectivity of the hard rock media

The most important factor that affects the strength of seismic reflections at the lithological boundaries is the acoustic impedance contrast between the rock units (Greenwood 2013; Salisbury and Snyder 2007; Yilmaz 2001). Acoustic impedance, Z,

is defined as the product of density (ρ) and P-wave velocity (V_p) of the rock unit (Yilmaz 2001),

$$Z = \rho V_p \qquad \textbf{(3-1)}$$

The reflection coefficient, R, is defined as the ratio of reflected energy and incident energy (Yilmaz 2001). For a normal incidence of P-wave, R is given by,

$$R = \frac{\rho_2 V_{p2} - \rho_1 V_{p1}}{\rho_2 V_{p2} + \rho_1 V_{p1}} = \frac{Z_2 - Z_1}{Z_2 + Z_1} \qquad \textbf{(3-2)}$$

where Z_2, ρ_2, and V_{p2} are the impedance, density, and P-wave velocity of the lower medium, and Z_1, ρ_1, and V_{p1} are the corresponding parameters for the upper medium. Equation 3-2 is known as the Zoeppritz equation for P-waves for the case of normal incidence. S-wave impedance and reflectivity can also be calculated by replacing P-wave velocity with S-wave velocity for elastic media.

The minimum reflection coefficient required for a reflection event to be detected above background noise is 0.06 (Yilmaz 2001). This value results from an acoustic impedance contrast (Z_2-Z_1) of 2.5×10^6 m/s kg/m^3 in hard rock environment that is equivalent to the difference between mafic and felsic rocks (Salisbury *et al.* 1996).

Nafe and Drake (1957) used laboratory measurements and borehole data to determine the relationship between depth and porosity for shallow and deep marine sediments. They also used a simple density-porosity relationship to derive a depth-density relationship. Combining these results, they derived a velocity-density relationship (Wyss *et al.* 1993). During the 1960s, additional data were included to refine the velocity-density relationship (Ludwig *et al.* 1970). Barton (1986) applied the Nafe-Drake relationship to convert the velocity distribution of seismic models into corresponding density model. Salisbury *et al.* (1996) measured samples of pure Pyrite, Chalcopyrite, Sphalerite, and Pyrrhotite at 200 MPa to determine the theoretical boundaries of the velocity-density field for common ores. Salisbury *et al.* (2003) observed that the average velocities of common crystalline rocks increase with density along the Nafe-Drake curve. Increasing velocity and density with increasing metamorphic grade were also observed (Salisbury *et al.* 2003). Acoustic properties of

common igneous and metamorphic rocks at 200 MPa and room temperature are provided in Table 3-1. Salisbury *et al.* (2003) revised these data from Holbrook *et al.* (1992) by recalculating the velocities up to 200 MPa assuming a V_P vs. pressure gradient of +0.04 km/s/100 MPa, and a V_S vs. pressure gradient of approximately +0.02 km/s/100 MPa. Apart from anomalously low Poisson's ratio of Quartzite, most of the other rocks show little variation in acoustic properties. Consequently, offset-dependent reflectivity is rarely used for hard rock characterisation.

Table 3-1: Acoustic properties of common igneous and metamorphic rocks at 200 MPa pressure and at room temperature (Salisbury et al. 2003).

Rock type	Density (g/cm^3)	V_P (km/s)	V_S (km/s)	Poisson's ratio	Acoustic impedance *
Quartzite	2.57 ± 0.12	5.48 ± 0.57	3.55 ± 0.41	0.14 ± 0.07	14.1 ± 2.1
Granite	2.66 ± 0.05	6.03 ± 0.23	3.50 ± 0.23	0.24 ± 0.04	16.0 ± 0.9
Granodiorite	2.69 ± 0.07	6.04 ± 0.35	3.41 ± 0.21	0.27 ± 0.02	16.2 ± 1.4
Quartz-mica schist	2.79 ± 0.07	6.22 ± 0.11	3.55 ± 0.17	0.26 ± 0.04	17.4 ± 0.8
Felsic gneiss (amphibolite facies)	2.73 ± 0.07	6.14 ± 0.17	3.55 ± 0.16	0.25 ± 0.03	16.8 ± 0.9
Felsic granulite	2.70 ± 0.06	6.17 ± 0.11	3.49 ± 0.09	0.27 ± 0.02	16.7 ± 0.7
Metapelite	3.10 ± 0.11	7.09 ± 0.36	3.99 ± 0.21	.27 ± 0.01	22.0 ± 1.9
Intermediate granulite	2.79 ± 0.11	6.31 ± 0.20	3.53 ± 0.14	0.27 ± 0.03	17.6 ± 1.3
Metagabbro (greenschist facies)	2.91 ± 0.09	6.55 ± 0.30	3.69 ± 0.11	0.27 ± 0.01	19.1 ± 1.5
Gabbro	2.94 ± 0.09	6.91 ± 0.22	3.72 ± 0.18	0.29 ± 0.02	20.3 ± 1.3
Mafic granulite	3.03 ± 0.17	6.78 ± 0.27	3.56 ± 0.22	0.31 ± 0.02	20.5 ± 2.0
Anorthosite	2.80 ± 0.10	6.73 ± 0.31	3.61 ± 0.20	0.30 ± 0.02	18.8 ± 1.5
Amphibolite	3.05 ± 0.10	6.99 ± 0.24	3.75 ± 0.21	0.30 ± 0.02	21.3 ± 1.4
Pyroxenite	3.27 ± 0.04	7.63 ± 0.15	4.19 ± 0.27	0.28 ± 0.04	25.0 ± 0.8
Peridotite/dunite	3.28 ± 0.04	7.94 ± 0.23	4.33 ± 0.18	0.29 ± 0.02	26.0 ± 1.1
Eclogite	3.43 ± 0.09	7.86 ± 0.28	4.34 ± 0.16	0.28 ± 0.02	27.0 ± 1.7
Serpentinite	2.59 ± 0.09	5.46 ± 0.55	2.69 ± 0.44	0.34 ± 0.03	14.1 ± 1.9

*$\times 10^5$ g/cm^2 s (Based on V_P and Density)

Figure 3-1 demonstrates the relationship between P-wave velocity and density of common hard rocks at 200 MPa confining pressure and at room temperature. According to the Figure, serpentinite, kimberlite, metasedimentary rocks have the lowest velocities and densities, followed by felsic igneous and metamorphic rocks, intermediate metamorphics, and then greenschist, amphibolite, and granulite facies mafic rocks, and finally, pyroxenite, peridotites, and eclogites (Salisbury *et al.* 2003). Since an acoustic impedance contrast of 2.5×10^5 m/s kg/m^3 is required to produce a discernible P-wave reflection, therefore, granites will not produce strong reflections against granodiorite (Salisbury *et al.* 2003). Most mafic rocks will produce strong reflections against felsic rocks, and fresh ultramafic rocks reflect against any lithology (Salisbury *et al.* 2003).

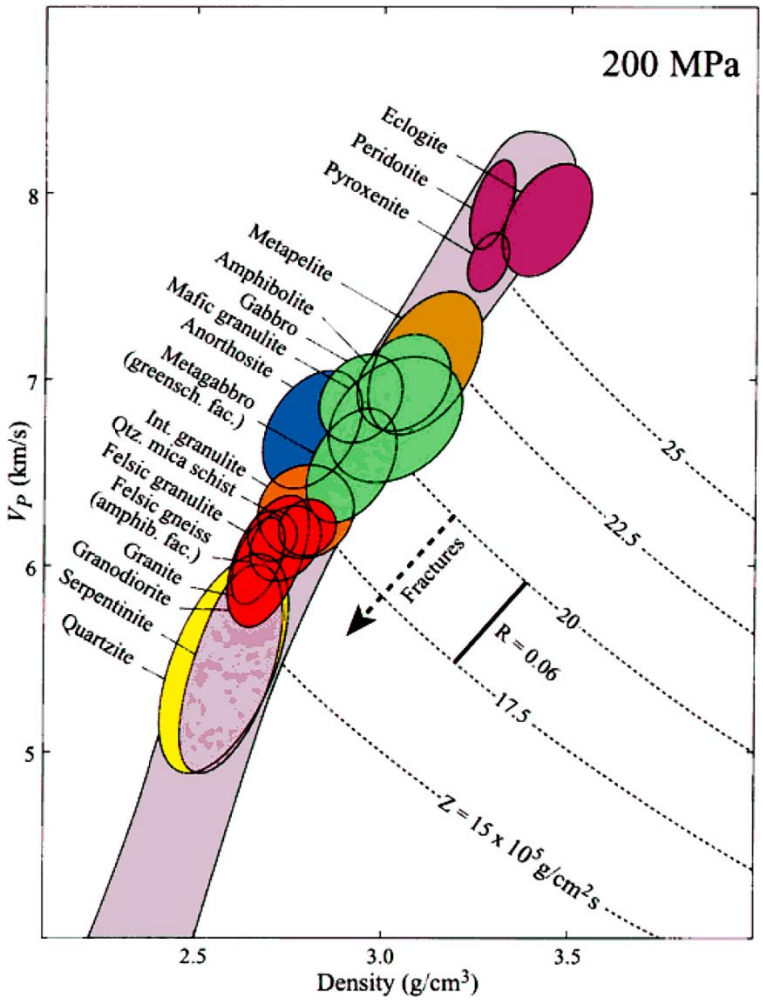

Figure 3-1: P-wave velocity vs. density at 200 MPa confining pressure for common hard rocks. The constant acoustic impedance for felsic and mafic rocks are shown as dotted lines. The minimum reflection coefficient R=0.06 required to produce strong reflection is superimposed for reference (Salisbury et al. 2003).

Figure 3-2 shows the relationship between S-wave velocity and density for common hard rocks at room temperature and 200 MPa confining pressure. Salisbury *et al.* (2003) demonstrated that the relationship between V_S and density follows a similar trend of V_P vs. density when the velocity is low. However, V_S is much slower compared to V_P ($V_P \sim V_S \sqrt{3}$), therefore, with increasing V_P and V_S, the V_S vs. density trend departs from the V_P vs. density trend. In hard rock environment, reflection coefficient generally depends on the ratio of velocities due to little changes in density between the rocks. Reflection coefficient R_c is the ratio of velocities; therefore, the values will be rational for a given temperature-pressure condition (Salisbury *et al.* 2003). However, in case of massive ores, reflection coefficient depends on the density compared to the velocity contrast.

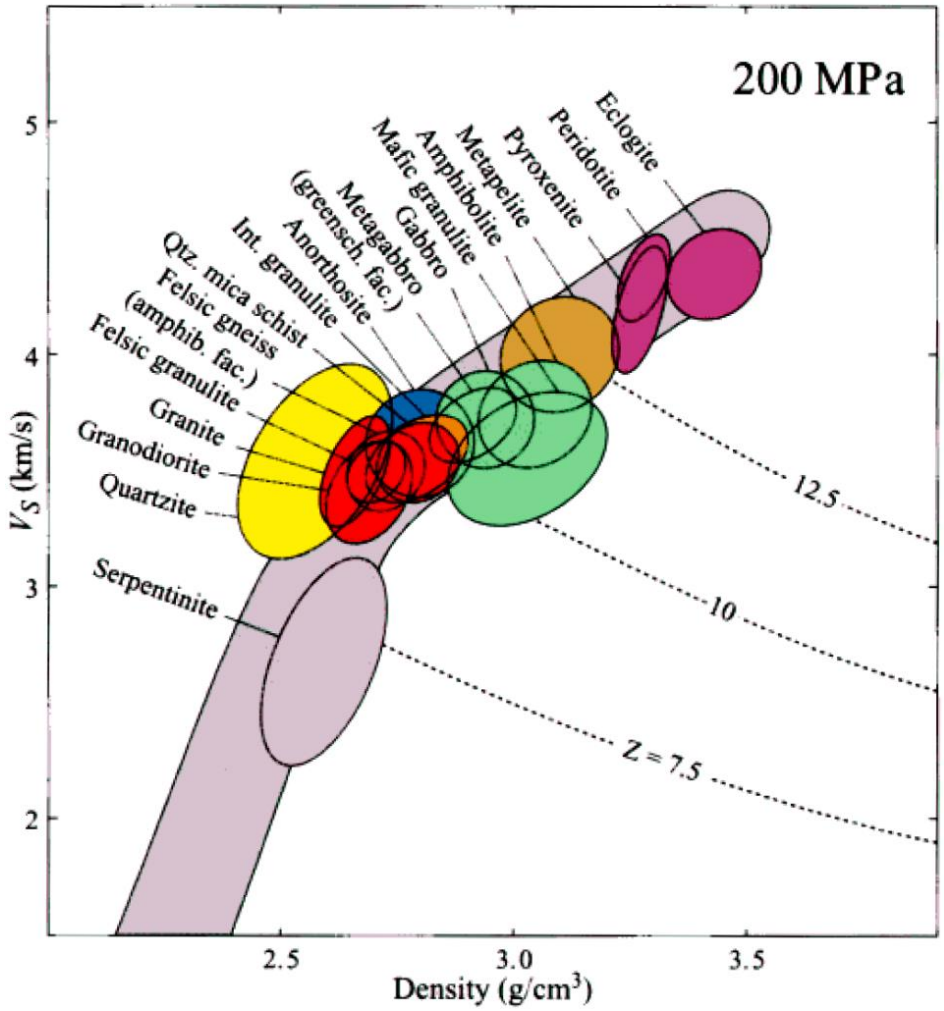

Figure 3-2: Relationship between S-wave velocity and density at 200 MPa confining pressure and at room temperature for common hard rocks. Lines of constant acoustic impedance are shown as dotted lines for reference (Salisbury et al. 2003).

Physical property analysis of the core samples from the Hillside case study provided P- and S-wave velocity, density and magnetic susceptibility. The P-wave velocity and density plots suggest that the rocks have overlapping physical properties that may produce relatively small acoustic impedance contrast at the lithological boundaries. The details of the analysis are discussed in the next chapter.

3.3. Seismic resolution

Seismic exploration methods were developed based on the propagation of acoustic waves through geological formations. Different geological formations have different elastic properties. Seismic energy propagating through a mafic or ultramafic rock generates strong P-wave reflections at formation boundaries where the acoustic impedance contrast is 2.5×10^6 m/s kg/m^3 or more (Salisbury *et al.* 2003). The acoustic waves generated from a source propagate in 3D space, increasing in size over time. In seismic data, an object can be seen if it is larger than either the vertical or horizontal resolution limit. The horizontal and vertical resolution play a significant role in ore-body delineation using seismic methods.

Vertical resolution depends on the wavelength and the thickness of the layer. Vertical resolution relates to the thickness of a layer to allow discernible reflections from the top and bottom boundaries, so that, a bed with finite thickness and a single reflecting surface can be distinguished (Sheriff 1993). In a noise-free condition, the minimum thickness t_{min} is commonly estimated as the ¼ of the dominant wavelength (Widess 1973).

$$t_{min} = \frac{V}{4f} \qquad \textbf{(3-3)}$$

where V is the velocity, and f is the dominant frequency of the wavelet. However, a layer can still be detected down to $^1/_{32}$ λ but it is typically ¼ λ (Widess 1973). A layer with the thickness less than the first zero-crossing interval of the wavelet cannot be resolved (Kallweit and Wood 1982). In sedimentary environments, seismic wave velocities in the subsurface range between 2000 m/s and 5000 m/s and increase with depth (Yilmaz 2001). The dominant frequency of the seismic signal ranges between 50 and 20 Hz and decrease with depth (Yilmaz 2001). Hence, typical seismic wavelengths

range from 40 m to 250 m and generally increase with depth (Yilmaz 2001). Taking into account the realistic velocity and frequency ranges, a shallow feature with a 2000 m/s velocity and 50 Hz dominant frequency can be detected if it is thicker than 10 m (Yilmaz 2001). Likewise, a deep feature with a seismic velocity as high as 5000 m/s and dominant frequency as low as 20 Hz has to be at least 62 m thick for it to be detectable.

The horizontal resolution is the ability to distinguish two horizontally separated objects on the seismic data (Sheriff 1993). According to Huygen's Principle, a seismic source generates a spherical wavefront conforming to the envelope of spherical wavelets originating from every point on the wavefront at the prior instant (Sheriff 1993). In Figure 3-3, the wavefront AA' can be visualised as a band of point diffractors. S is the seismic source on the Earth's surface. From the subsurface point O, the energy will reach the receiver at the surface at time $t_0 = 2Z_0/v$ (Yilmaz 2001). Whereas, the energy from the subsurface point A or A' will reach the receiver at time $t_1 = 2(Z_0 + \lambda/4)/v$. Therefore, the energy from any point within the reflecting disc with diameter AA' will sometimes arrive between t_0 and t_1. The reflected energy arriving between the time t_0 and t_1 equals to half the dominant period and generates a constructive interference (Yilmaz 2001). The reflecting disc with radius AA' is called a half-wavelength Fresnel zone or the first Fresnel zone (Hilterman 1982; Sheriff 1993; Yilmaz 2001). The reflection from any point within this zone will be indistinguishable on the seismogram recorded at the Earth's surface. The radius of the Fresnel zone can be approximated as,

$$r = \sqrt{\frac{Z_0 \lambda}{2}} \qquad \textbf{(3-4)}$$

where Z_0 is the depth, λ is the wavelength (Yilmaz 2001). Concerning the dominant frequency, the radius of the Fresnel zone can be equated as

$$r = \frac{v}{2}\sqrt{\frac{t_0}{f}} \qquad \textbf{(3-5)}$$

Where t_0 is the two-way travel time, and v is the seismic velocity (Yilmaz 2001).

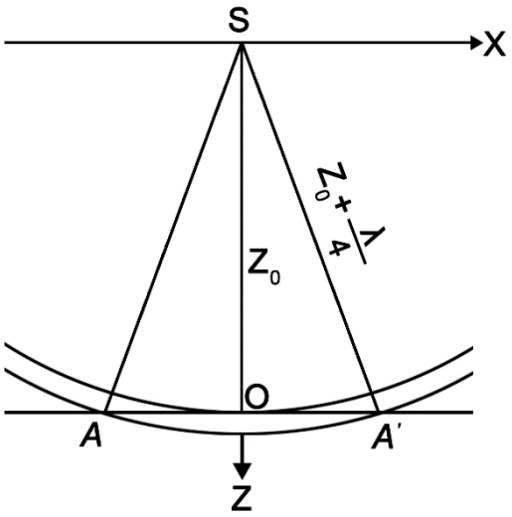

Figure 3-3: Definition of the Fresnel zone AA' (Yilmaz 2001).

Horizontal resolution limit based on the Fresnel zone applies to unmigrated seismic data. Migration manages to collapse the Fresnel zone to approximately the dominant wavelength as shown in Equation 3-4 (Yilmaz 2001). Migration repositions the data events to their appropriate locations. That is, it tends to move the return signals to illuminate an interface point being encountered by a seismic wave rather than where it has been recorded (Tertyshnikov 2014). Amplitude information and peak-to-peak time measurements can assist in identifying pinchouts that may otherwise be unresolvable (Yilmaz 1987). The fidelity of the analysis, i.e., the confidence of detecting subsurface structures depends on the signal-to-noise ratio (Yilmaz 1987).

Whether or not the seismic reflection method can image an ore-body relies on several factors, i.e., size, shape, dip, and the acquisition parameters (Salisbury *et al.* 1996). No single relationship regulates the seismic resolving power (Salisbury *et al.* 1996). Seismic resolution depends on the diameter *d*, thickness *t*, depth *z*, the formation velocity *v* of the deposit and the dominant frequency *f* of the seismic survey (Salisbury *et al.* 1996). For example, let us assume a scenario in hard rock environment where the formation P-velocity V_p is 6000 m/s, two-way-traveltime *t* is 300 ms and the dominant frequency *f* of the survey is 50 Hz. In such environment, the radius of the Fresnel zone will be 232 m and in a noise-free environment, the minimum thickness t_{min} will be 30 m. Hence, the horizontal and vertical resolution of the above scenario will be 464 m and 30 m respectively.

Concerning physical properties, common sulphide ores should behave as a strong seismic reflector (Salisbury *et al.* 1996). The density and the acoustic impedance of sulphide deposits are higher than felsic and mafic host rocks. Therefore, seismic methods should be capable to image massive sulphide deposits presuming that the size and dip constraints required to generate strong reflections are fulfilled. Recent studies have demonstrated that seismic methods can successfully delineate massive sulphide deposits (Calvert and Li 1999; Malehmir *et al.* 2009; Malehmir and Bellefleur 2009; Milkereit *et al.* 1996; 2000a; Salisbury *et al.* 1996; Urosevic *et al.* 2012; White *et al.* 2012). In addition to massive sulphides, seismic methods have been successfully exploited on an industry scale to delineate gold-bearing horizons in Kaapvaal Craton (Malehmir *et al.* 2014; Manzi *et al.* 2012a; 2012b; 2015; Pretorius *et al.* 1994) and magmatic PGE deposits in the Bushveld igneous complex (Düweke *et al.* 2002). Seismic methods have been tested in Australia, Europe, Canada and South Africa with promising results for the exploration of gold, nickel, zinc, copper and uranium deposits (Malehmir *et al.* 2012b).

3.4. Seismic interpretation

The purpose of seismic interpretation is to convert the geophysical image of the subsurface into geological image or model of the subsurface (Gadallah and Fisher 2005). Recent advancement in computer technology, such as the increased processing power, faster data transfer rate, and improved computer 3D graphics rendering engine integrated with 3D volume visualisation techniques have enabled the interpreters to manipulate and view seismic data in 3D, in real time (Hossain *et al.* 2015a).

Acceptable interpretation of seismic data is one of the most important elements of a successful exploration programme (Chopra and Marfurt 2007; Herron and Latimer 2011). Seismic interpretation depends critically on the quality of the seismic data (Herron and Latimer 2011). The primary elements of the seismic data quality are detection (signal-to-noise ratio), resolution (temporal and spatial) and image fidelity (focusing and positioning) (Herron and Latimer 2011). Seismic interpretation is subjective and depends on the perspective and powers of observation of the interpreter (Herron and Latimer 2011). Seismic interpretation utilises the routine use of multi-scale seismic attributes in conjunction with well logs, petrophysics and rock physics to make

quantitative predictions about the lithology and fluid content (Thompson *et al.* 2011). Post-acquisition forward modelling facilitates volumetric interpretation of the processed seismic data. This is of particular interest when targeting small, high-grade mineral bodies (Urosevic *et al.* 2012). Post–acquisition synthetic seismic records assist confident correlation of the observed reflections and the geologic interfaces and verify that the seismic response of the geological model is consistent with the field seismic data (Anderson and Cardimona 1995). In the cases studied in this research, forward modelling was not employed due to the lack of "ground-truth" models of overly complex geological settings, lack of prominent marker horizons, lack of good quality borehole sonic and density data. Moreover, the interpretation was performed on depth converted seismic datasets and borehole tops were employed to correlate the seismic response with the corresponding lithologies.

3.5. 2D and 3D seismic interpretation strategies

By the mid-1990s, 3D seismic technology became affordable and hundreds of 3D seismic surveys were being conducted every year (Chopra and Marfurt 2005). 3D interpretation workflows were being improved, however, 3D seismic interpretation was still being performed using the conventional method by slicing the seismic cube into vertical inlines and crosslines (Chopra and Marfurt 2005). In general, conventional interpretation methods produce maps while volume visualisation methods produce 3D perspectives (Bland and Stewart 1993; Kidd 1999). In 3D seismic data processing, traces are collected into common-cell gathers (bin) to create a common-cell stack (Yilmaz 1987). A CMP gather coincides with a common-cell gather from swath shooting. Typical cell sizes are 25 m × 25 m for land surveys and 12.5 m × 12.5 m for marine surveys (Yilmaz 1987). The interpretation based on 2D imaging is considerably different from the interpretation based on 3D imaging. The conventional interpretation approach involves slicing a seismic volume in the X–Y or Y–Z planes to create inline and crossline sections (Bland and Stewart 1993; Yilmaz 1987). Slicing a seismic volume into horizontal planes creates time or depth slices. The individual inline and crossline slices can be interpreted using conventional 2D techniques, but the data coherency along the axis perpendicular to the slice plane cannot be seen (Wolfe and Liu 1988).

The traditional approach to demonstrate a 3D seismic data utilised wireframe drawing techniques (Bland and Stewart 1993). A conventional cube-view of the 3D seismic data provides more points of reference, however, the opaque cube sides prohibit an interpreter from seeing the interior of the data volume (Bland and Stewart 1993). Volume rendering techniques overcome this issue by representing the data volume using voxels (Bland and Stewart 1993). The volume rendering based on 3D visualisation technique was originally developed for medical imaging using three-dimensional pixel elements called voxels (Marsh *et al.* 2000). Voxel technology is now being used widely in the petroleum industry in the form of advanced 3D seismic interpretation software (Marsh *et al.* 2000; Roberts 1998). In voxel-based volume visualisation method, the data samples are converted into 3D pixels equal to the bin size and sample spacing (Kidd 1999). A voxel incorporates a colour value in red, green and blue, and an opacity value that allows the degree of transparency that can be controlled (Kidd 1999). Hence, a seismic trace is represented by a column of voxels (Kidd 1999).

3.6. Pitfalls in interpretation of hard rock seismic data

In 1973, Paul M. Tucker and Howard J. Yorston published a monograph entitled *Pitfalls in Seismic Interpretation,* one of the most useful books available to seismic interpreters. In that monograph, Tucker and Yorston (1973) classified the pitfalls in seismic interpretation into three categories:

1) Pitfalls related to velocity
2) Pitfalls related to the geometry of the reflectors
3) Pitfalls related to the recording, processing and playback of the seismic data

Most of the pitfalls described by Tucker and Yorston (1973) can be cured with modern acquisition and data processing methods. Lines and Newrick (2004) revised the pitfalls in seismic interpretation into the following categories:

1) Interpretation of time sections as depth sections, hence failing to recognised velocity effects
2) Interpretation of 3D effects on a 2D section

3) Failure to recognise that some seismic arrivals are not related to the desired geologic structures but may be caused by "noise".

Pitfalls associated with velocity occur when seismic data are presented in traveltime (Lines and Newrick 2004; Tucker and Yorston 1973). The phenomena commonly observed in seismic data due to velocity related pitfalls include downdip thinning of reflection intervals, thinning of reflection intervals on the downside of a vertical fault, high amplitude beneath high amplitude and low amplitude beneath high amplitude due to superimposed structures (Tucker and Yorston 1973). These pitfalls are velocity induced, and can be recognised by velocity analysis. Depth migration eliminates velocity-associated pitfalls. However, accurate depth migration requires a very precise and detailed knowledge of velocity (Lines and Newrick 2004; Tucker and Yorston 1973). Inaccurate usage of velocity can become a pitfall itself.

Pitfalls associated with geometry depend on the shape and steepness of the structures. Geometry-associated pitfalls include shallow reversal due to steep-dip structures, abrupt termination of reflections at the intrusive boundary, anticlines and synclines, and diffraction-like events (Tucker and Yorston 1973). Most of these issues can be solved by migrating the data (Tucker and Yorston 1973).

The most serious pitfall is computer-derived (Tucker and Yorston 1973). When projected on a 2D map view, the 3D aspect of the information gets lost. Hence, the volume visualisation techniques should be used concurrently during conventional mapping and digitising of the prospect-specific target. The digital interpretation is performed independently and the results are integrated with the semi-transparent volumes (Kidd 1999). Volume visualisation method reveals a great deal of information in a short period. As a result, during the initial stages of volume visualisation, there is a probability of reaching premature conclusions. Interpreters should familiarise themselves with the visualisation characteristics and parameters to see what was encountered by visualising as many drilled prospects as possible to avoid this problem (Kidd 1999).

Application of conventional interpretation techniques and workflows to volume visualisation can lead to substandard visualisations (Kidd 1999). A detailed understanding of visualisation functionality and their expected outputs must be

contemplated during all stages of visualisation (Kidd 1999). The most common pitfalls of volume visualisation are the misinterpretation of faults or horizons due to visual alignment, false truncations of events at the data boundaries and overuse/underuse of the opacity (Kidd 1999).

Seismic interpretation balances between geology, geophysics and computer science (Brown 2005). Constant liaison between the geologist, the interpreter and the processing expert during the recording, processing and interpretation phase can mitigate these pitfalls. Brown (2005) proposed the following recommendations to avoid common interpretation pitfalls and get more geology out of the 3D seismic data: i) use all the data, ii) understand the data and its defects, iii) select colour scheme with care, iv) question data phase and polarity, v) use horizontal sections (time/depth slices), vi) understand the seismic attributes that you use, and vii) use techniques that maximise signal-to-noise ratio.

Most economic mineral deposits occur in hard rock environments. The biggest challenge of employing seismic methods for mineral exploration in hard rock environments is the low signal-to-noise ratio. The impedance contrasts and reflection coefficients between most common igneous and metamorphic rocks are smaller than the contrasts between the sedimentary rocks (Salisbury and Snyder 2007). As a result, it is more difficult to image structures in hard rock environments. This issue can be resolved to some extent by using explosives in shallow boreholes, by using cemented or clamped geophones to ensure better source coupling, by careful testing of different sources before the survey and by maximising the data fold (Eaton *et al.* 2003; Salisbury and Snyder 2007).

Acoustic velocities in igneous and metamorphic rocks are higher than sedimentary rocks (Salisbury *et al.* 2003). Since the wavelength varies with velocity for any given frequency, therefore, higher frequencies are required to image often complex and subvertical structures (Salisbury and Snyder 2007). Ore deposits are small (<1 km) compared to the sedimentary reflectors, as a results, they often appear as diffractions rather than reflections (Salisbury and Snyder 2007). Conventional processing tends to treat these small targets as noise, therefore, prestack migration techniques should be used to process the hard rock seismic data. It is often advisable to conduct laboratory measurements of the velocities and densities of the host rocks and country rocks to

determine whether the survey is worth conducting due to low signal-to-noise ratio (Salisbury and Snyder 2007).

3.7. Seismic attributes

Seismic attributes provide robust support during seismic interpretation (Chopra and Marfurt 2007). Interpretation of faults and channels, depositional environment recognition, and unravelling the history of structural deformation can be attained from a seismic volume by employing attributes (Chopra and Marfurt 2007; Herron and Latimer 2011). According to the Oxford Dictionary, an attribute is "*a quality ascribed to any person or thing*" (Taner 2001). Seismic Attributes are the subset of seismic data, attained by direct measurements or by logical or experience based reasoning (Taner 2001). Currently, more than two hundred seismic attributes are in use. Their great variety makes it challenging to decide which attribute to choose for interpretation (Brown 1996). Many duplicate seismic attributes are obscure, unreliable, unstable, and purely mathematical in nature (Barnes 2007). Barnes (2007) proposed some common-sense principles to distinguish useful seismic attributes: i) seismic attributes should be unique; ii) they should have clear and useful meanings; iii) attributes that differ only in resolution are the same attribute; and iv) seismic attributes should not vary greatly in response to small data changes.

Seismic attributes achieved a new dimension with the introduction of 3D volume visualisation techniques (Subrahmanyam and Rao 2008). Seismic attributes can be broadly classified into two categories: physical attributes and geometrical attributes (Chopra and Marfurt 2005; Subrahmanyam and Rao 2008; Taner 2001). Physical attributes are directly related to the wave propagation and physical parameters of the subsurface lithology. Amplitude, phase and frequency are the main physical attributes (Chopra and Marfurt 2005). Geometrical attributes enhance the geometrical characteristics of seismic data, e.g., dip, azimuth and continuity (Chopra and Marfurt 2005). Brown (1996) proposed function of time, amplitude, frequency and attenuation as the main attributes that are subdivided into poststack and prestack attributes. (Liner *et al.* 2004) classified seismic attributes into two major categories: general and specific. Based on their classification, general attributes (reflector amplitude, reflector dip and azimuth, frequency, illumination, edge detection, Amplitude Versus Offset (AVO) and

spectral decomposition) measure the geometric, kinematic, dynamic or statistical features from the seismic data. On the contrary, specific attributes that are correlated to the geological features in a specific geological setting are not applicable to a different geological setting (Chopra and Marfurt 2005; Liner *et al.* 2004). Chopra and Marfurt (2005) amended the classification of Liner *et al.* (2004) by adding a third category and named it composite attributes. These composite attributes are sums, products or other mathematical combinations of general attributes.

3.8. 3D seismic visualisation techniques

In 3D volume visualisation method, the seismic reflectivity of the subsurface media is evaluated by utilising transparency to the data (Kidd 1999). Direct integration of structural, stratigraphic, and amplitude data helps to reveal and evaluate regional and prospect-specific details before the digital interpretation (Kidd 1999).

Multiple-volume visualisation is a new technology where multiple seismic volumes are blended into a new seismic volume (Marsh *et al.* 2000). Volume blending is an intuitive and interactive visualisation technique that allows an interpreter to compare visually and evaluate multiple seismic cubes simultaneously and synchronously, using RGB/CMY blend and mask workflows (Schlumberger 2015). Analysing the attribute or volumes effectively and efficiently is a critical component of any seismic processing, interpretation, and modelling phase of a project. Multiple volume visualisation techniques can be successfully applied to: i) visualise poststack time migration, prestack time migration and prestack depth migration results to verify the effects of seismic processing approach, ii) multi-attributes visualisation to scrutinise their interrelationships and iii) time-lapsed seismic data visualisation to evaluate changes in reservoir size/shape over time (Marsh *et al.* 2000).

To implement volumetric interpretation, the seismic data can be scaled to 8-bit and the voxel values are represented by a histogram (Kidd 1999). The first step of volumetric interpretation involves the preparation of three 2D slices of the data volume along the three primary axes (Bland and Stewart 1993). Next step is to prepare the 2D slices by setting the survey parameters, colour scale, opacity level so that the data represent settings similar to those in conventional interpretation (Kidd 1999). Setting the survey parameters and data scaling must be done carefully to avoid poor scaling and/or

excessive clipping that may underutilise full dynamic range of the data (Bland and Stewart 1993; Kidd 1999). Then, scanning is performed on the slices for both regional and prospect-specific overviews (Kidd 1999). Once the objective is identified, the data is cropped using a time/depth window or a box probe for the application of opacity filter (Kidd 1999). This step is crucial as it removes irrelevant data above and below the targeted volume. Time/depth windowed visualisation is very effective for evaluating low-dipping geological features (Kidd 1999). Prospect-specific identification is performed based on the physical connectivity of the voxels within a user-defined amplitude range (Bland and Stewart 1993; Kidd 1999). The result can be further evaluated for internal variations of the amplitude or to generate a surface (Kidd 1999). This approach is useful for evaluating stratigraphic features, faults blocks mapping, and creating regional surfaces. This approach can be much improved by specifying the zone of interests using two horizons or by creating a bulk-shifted interval by using a single horizon for evaluation of structured depositional units (Kidd 1999).

Structural visualisation is performed to quickly identify subtle and complex fault patterns. In the conventional method, fault interpretation is performed manually. The interpreter decides which fault to interpret and how each of them is connected (Kidd 1999). Hence, the quality and thoroughness depends upon the interpreter. The objective of the structural visualisation is to reveal all the faults in the seismic data (Kidd 1999). Seismic signature of a fault can be delineated by applying transparency to the seismic data (Kidd 1999). In a seismic volume, faults are generally characterised by abrupt amplitude terminations with associated offset (Kidd 1999). The overall lateral amplitudes of a seismic horizon decreases at the faults (Bland and Stewart 1993; Kidd 1999; Marsh *et al.* 2000). By lowering the opacity of the decreased amplitude to transparent, the faults will appear as a physical gap within the horizon (Kidd 1999).

4. Case study: Hillside copper–gold mine, South Australia

4.1. Introduction

The Exploration Geophysics Department of Curtin University conducted an experimental 3D high-resolution seismic reflection survey at Rex Minerals' Copper-Gold mining project at Hillside between the 22 November and 13 December 2012. The mine site is located on the east coast of Yorke Peninsula, ~15 km south of the port city Ardrossan, South Australia. The survey was a part of the DET CRC research project 3.1 "*3D Seismic Exploration for Hard Rock Environments*". The seismic survey covers an area of 0.44 km^2 (1375m×320m). The main objective of this survey was to investigate the response of seismic reflection method over an excessively complex Iron Oxide-Copper-Gold (IOCG) deposit. The 3D seismic survey at Hillside was the first 3D seismic survey undertaken over an IOCG deposit.

Rex Minerals Ltd discovered the copper-gold mineralisation at the Hillside Copper Project in 2008. Geologists believed that IOCG style of mineralisation could occur beneath a thin (up to 30 m) cover rock on the Yorke Peninsula. The presence of the historical Hillside Copper Mine in the area also played an influential role to initiate an exploration programme to search for magnetic and gravity anomalies. Following the discovery of the deposit, the company funded a drilling programme down to 600 m to estimate the reserve.

The mineral resource at the Hillside project is one of Australia's largest open pit copper deposit. The deposit consists of 337 Mt at 0.6% Cu and 0.14 g/t Au, equating to approximately 2.0 Mt of copper and 1.4 Moz of gold (Rex Minerals Ltd 2015).

According to May 2015 report released to Australian Securities Exchange (ASX), the Hillside ore reserve stands at 82 Mt at 0.62% Cu and 0.16% g/t Au, which is about 0.51 Mt of copper and 0.43 Moz of gold. The proved ore reserve of 42 Mt corresponds to 51% of the total ore reserve with the remaining 49% in the probable category (Rex Minerals Ltd 2015). The measured, indicated and inferred mineral resource summary

of the Hillside Cu-Au Mining Project is provided in Table 4-1. Table 4-2 provides the ore reserve at Hillside as of May 2015.

Table 4-1: Measured, indicated and inferred mineral resources summary of Hillside Cu-Au Mining Project - May 2015 (Rex Minerals Ltd 2015).

Zone	Resource Category	Tonnes (Mt)	Cu (%)	Au (g/t)	Contained Cu (t)	Contained Au (oz)
Oxide Copper	Measured	16	0.54	0.23	86,400	118,315
	Indicated	4	0.51	0.13	20,400	16,718
	Inferred	0.2	0.70	0.20	1,400	1,286
Secondary Sulphide	Measured	9	0.61	0.20	54,900	57,871
	Indicated	3	0.55	0.12	16,500	11,574
	Inferred	0.1	0.60	0.10	600	322
Primary Sulphide	Measured	47	0.54	0.16	253,800	241,774
	Indicated	144	0.59	0.13	849,600	601,862
	Inferred	114	0.60	0.10	684,000	366,519
Total		**337**	**0.60**	**0.14**	**1,967,600**	**1,416,240**

* Measured and indicated resources are rounded to two significant figures and inferred resources are rounded to one significant figures.

Table 4-2: Ore reserve at Hillside - May 2015 (Rex Minerals Ltd 2015).

Category	Tonnes (Mt)	Copper (%)	Gold (g/t)	Contained Cu (t)	Contained Au (oz)
Proved	42	0.55	0.19	228,049	250,454
Probable	40	0.70	0.14	281,213	181,051
Total	**82**	**0.62**	**0.16**	**509,262**	**431,504**

In their report, Rex Minerals Ltd removed iron ore from the probable category due to the prevailing market conditions. They may reconsider the option of iron ore-processing in the future if the market conditions improve.

Seismic data acquisition for the case study described in this chapter was conducted in conjunction with other researchers from the DEC CRC project 3.1 at Curtin University. My sole contribution to this case study involves physical property data analysis and seismic volumetric interpretation. Most of the works included in this case study were included in the DET CRC annual meeting presentations, conference papers (Hossain *et al.* 2013; 2014b; 2015b) and a manuscript in preparation.

4.2. Geological setting

The Hillside Cu-Au deposit is located on the east coast of the Yorke Peninsula, at the southern extremity of the Gawler Craton Olympic Cu-Au Province, approximately 15 km south of the port city Ardrossan, 72 km north-west of Adelaide, and 48 km southwest of Port Wakefield in South Australia.

The Hillside and other similar IOCG-style deposits of the Moonta-Wallaroo district, and the Olympic Dam, Prominent Hill, and Carrapateena Cu-Au deposits are hosted within Palaeo-to-Mesoproterozoic rocks of the Olympic IOCG Province (Figure 4-1). The deposit is underlain by the Mesoarchaean to Palaeoproterozoic basement and partly overlain by the thick Mesoproterozoic Gawler Range Volcanics (Conor *et al.* 2010; Goleby *et al.* 2005). The basement is most likely composed of gneissic granitoid of Donnington suite (~1850 Ma), which were uplifted and exposed by faulting (Conor *et al.* 2010; Raymond 2003).

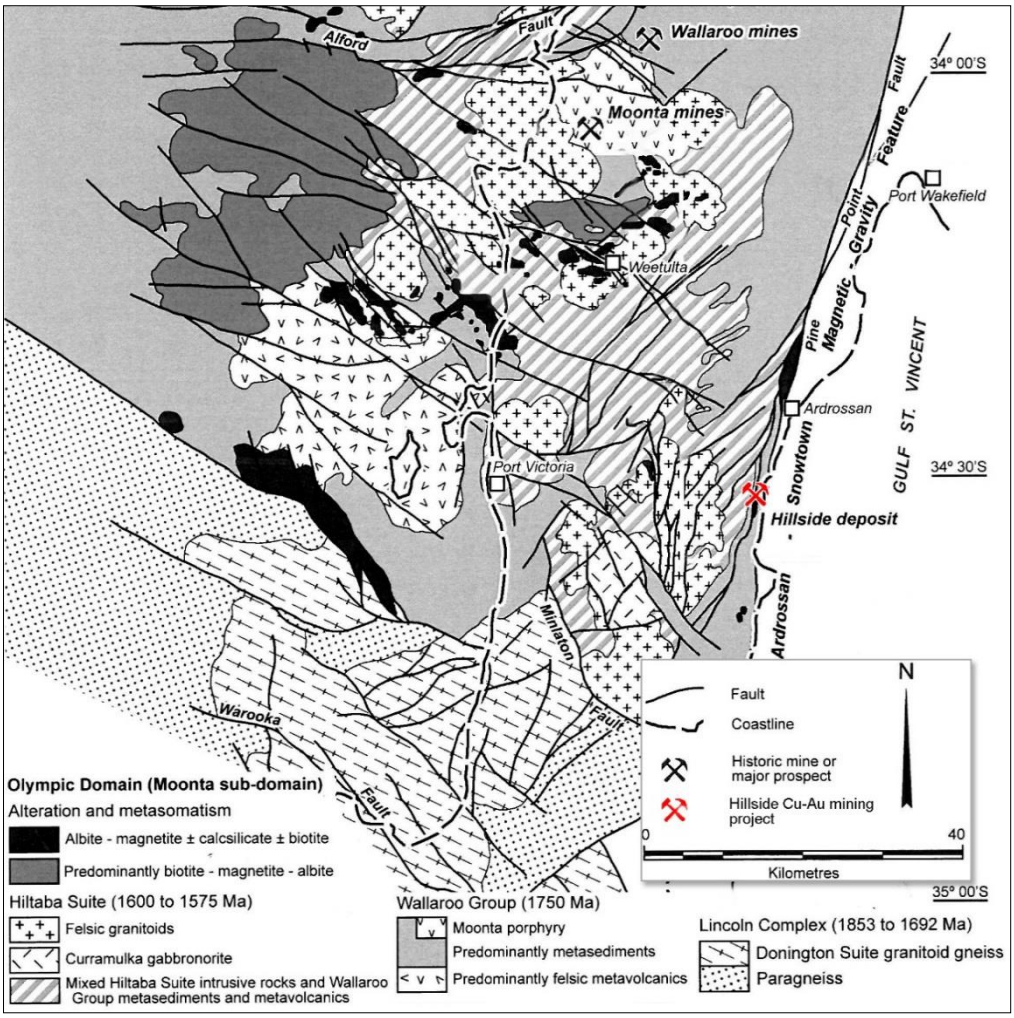

Figure 4-1: The regional geology of northern Yorke Peninsula shows the location of the Hillside deposit (red) on the east coast (modified after Conor et al. 2010, with the permission of PGC Publishing).

The Hillside IOCG deposit was discovered by Rex Minerals Ltd. in 2008 when they were exploring for discrete magnetic and gravity anomalies (Figure 4-2) spatially associated with the Pine Point Fault (Conor *et al.* 2010). The evolution of the IOCG deposits have been widely debated (Skirrow *et al.* 2013; Williams *et al.* 2005). Hayward and Skirrow (2010) proposed that earlier subduction-related processes (~1850 Ma) steered metasomatism of the upper mantle in a distal retro-arc environmental setting. Skirrow *et al.* (2013) suggested that mantle plume drove melts or melts driven by the removal of lithospheric mantle resulted in extensive crustal melting and produced high-temperature A- and I-type magmas associated with K-rich mafic melts (between ~1595 Ma and ~1575 Ma). Hiltaba Suite and Gawler Range Volcanics in the Gawler

Craton represents felsic melts that are temporally and spatially linked to the IOCG deposits in the Olympic IOCG Province (Skirrow *et al.* 2013).

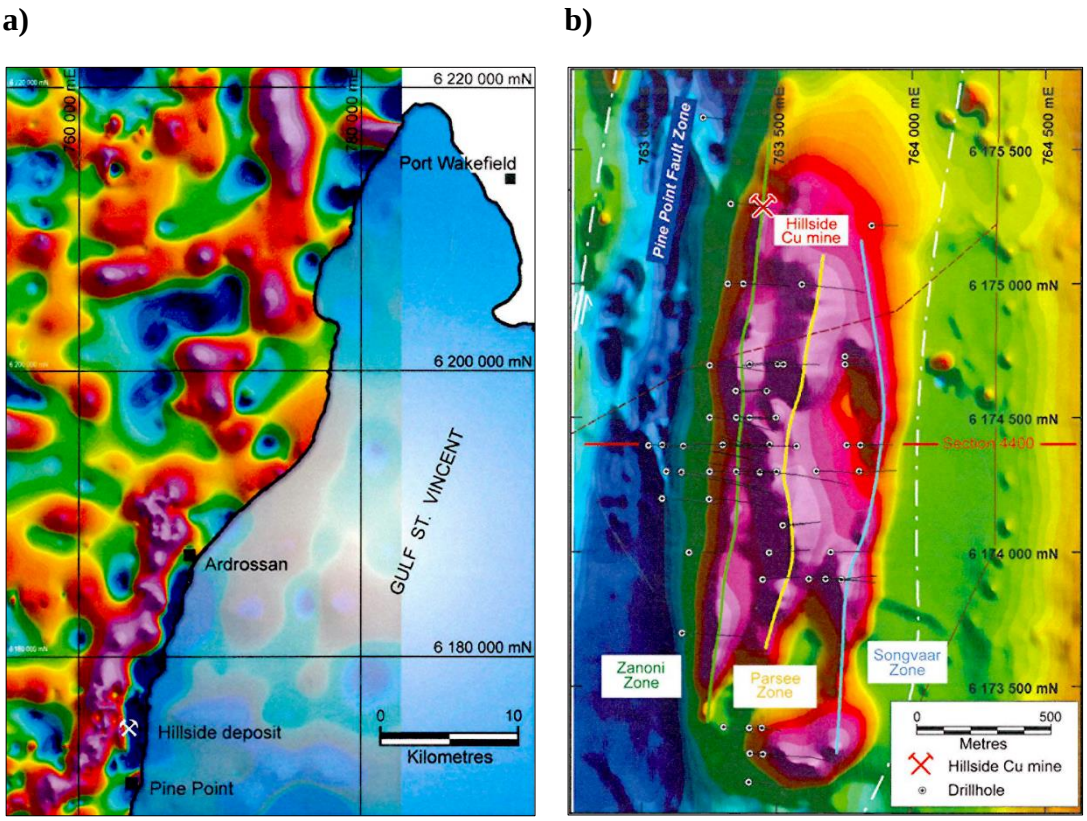

Figure 4-2: (a) Gravity anomaly map of the eastern Yorke Peninsula exhibits the location of Hillside deposit (Conor et al. 2010). (b) Residual magnetic anomaly map of the Hillside Cu-Au mining project area (Conor et al. 2010). The location of boreholes and interpreted mineralised zones are shown on the map.

The Hillside mineralisation is covered by a sequence of Tertiary calcareous sediments up to 30 m in thickness (Conor *et al.* 2010). The structural style of the Hillside mineralisation is similar to the Moonta-Wallaroo mines, and the IOCG-style deposits from the Curnamona Province with discrete mineralisation hosted in laterally and vertically continuous structures (Conor *et al.* 2010). The Cu-Au mineralisation in Hillside area is hosted adjacent to gabbro and felsic intrusives within metasediments and meta-mafic rocks (Conor *et al.* 2010). A large amount of mineralisation is concentrated in numerous, north-south trending, subvertical bodies associated with prograde and retrograde skarn assemblages and brecciated structures dipping toward the west (Conor *et al.* 2010). The primary copper mineralisation at Hillside is rich in chalcopyrite with a small amount of bornite and chalcocite, and gold mineralisation is

hosted in chalcopyrite (Conor *et al.* 2010). Post-mineralisation faulting, particularly north-south trending, vertical to subvertical faults are also evident in the area (Conor *et al.* 2010).

4.3. Physical property data analysis

A couple of trips to the Rex Minerals' core repository at Hillside mine site were organised on 29 July - 2 August 2013 and 4 November - 8 November 2013 to measure the physical properties (P- and S-wave velocity, density, and magnetic susceptibility) of the supplied core samples. Ultrasonic pulse transmission tests have been utilised and specific gravity measurements were carried out to investigate the physical properties of the core samples supplied by Rex Minerals Ltd. A comprehensive database with density measurements of the core samples were also acquired from Rex Minerals Ltd. The picture of a standard core tray (1 m length) is provided in Figure 4-3.

Figure 4-3: Core samples from the HDD-044 borehole (Tray length is 1 m and core diameter is approximately 45 mm).

In total, 505 core samples were analysed, and 471 of the samples produces P- and S-wave velocity data. However, only 289 measurements from five boreholes with confirmed lithological classification were utilised in this analysis.

Ultrasonic pulse transmission tests were conducted on dry, solid, 10-20 cm long core samples at atmospheric pressure using an ultrasonic pulse receiver (5077PR, Olympus

Ltd) with 1.0 MHz P-wave and S-wave transducers. The arrival times of the P-wave and S-wave were analysed on a 2 GHz digital oscilloscope (Tektronix DPO 2024, Olympus Ltd). Besides, the length of each core sample, their dry weight and weight in water were also measured to calculate density using Archimedes' principles. The measured parameters were used to calculate physical properties such as, P-wave velocity (*Vp*), S-wave velocity (*Vs*), *Vp/Vs* ratio, acoustic impedance and shear impedance. Malehmir *et al.* (2013) discussed that crystalline rocks have very low porosity due to deformation and metamorphism, which make them less pressure and frequency dependent. Therefore, the above mentioned physical properties could be considered as representative of *in situ* properties (Yavuz *et al.* 2015).

The core samples were chosen from four different classes, i.e., gabbro, granite, metasediments and mineralised host rocks. 10-20 cm long core samples were cut by using a core-cutting machine located at the core firm. The samples were chosen in a way so that they represent every dominant lithological unit in the borehole. Gabbro and granite, both demonstrate a range of grain sizes. Gabbro samples were typically coarse grained; intensive alteration to chlorite were also observed. Granitic samples contained mafic minerals within them. Intensely deformed granite-pegmatite were also observed in some cores. The mineralised rocks were mostly fine-grained, although variation in colour and texture was observed. Some sample contained garnet, pyroxene and epidote-group minerals.

The density value in the gabbro samples ranges from 2600 kg/m^3 to 3870 kg/m^3 with an average of 2910 kg/m^3. The density of granite samples ranges from 2610 kg/m^3 to 3840 kg/m^3 with a mean value of 2720 kg/m^3. The density of the metasediment samples varies from 2600 kg/m^3 to 3200 kg/m^3 with a mean value of 2780 kg/m^3, and in the mineralised host rock range from 2630 kg/m^3 to 4810 kg/m^3 with an average density of 3020 kg/m^3.

The P-wave velocity of the gabbro samples ranges from 4457 m/s to 7327 m/s with an average velocity of 5960 m/s. In granite samples, the P-wave velocity ranges from 5969 m/s to 7767 m/s with a mean value of 6397 m/s. The metasediment samples show that P-wave velocity ranges from 4639 m/s to 7347 m/s with an average of 6049 m/s and the mineralised samples range from 5558 m/s to 7358 m/s with an average of 6309 m/s. The physical properties are plotted in Figure 4-4.

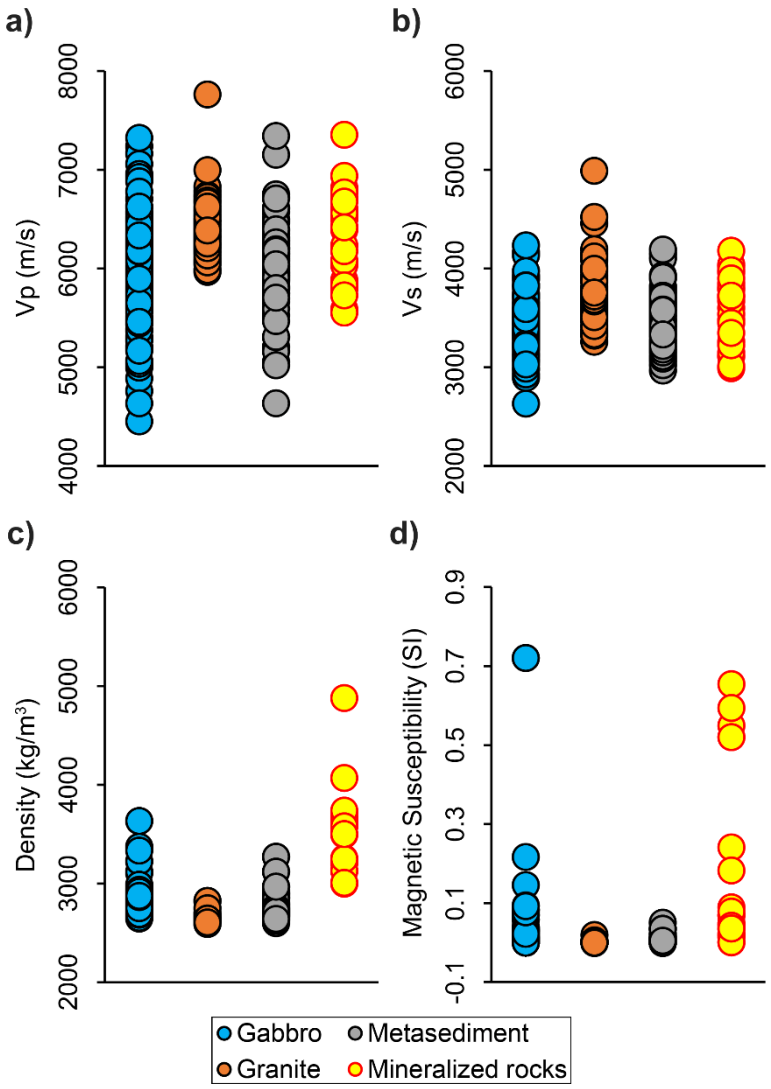

Figure 4-4: (a) P-wave velocity, (b) S-wave velocity, (c) density and (d) magnetic susceptibility distributions of the measured core samples.

Salisbury *et al.* (2003) suggested that an acoustic impedance contrast of 2.5×10^6 m/s kg/m^3 is required to produce discernible P-wave reflection by the seismic reflection method. However, most of the measurements in Figure 4-5 are below this limit suggesting that the rock units will not produce strong P-wave reflections at the boundaries. The reason could be exacerbated due to the presence of fractures in the rocks.

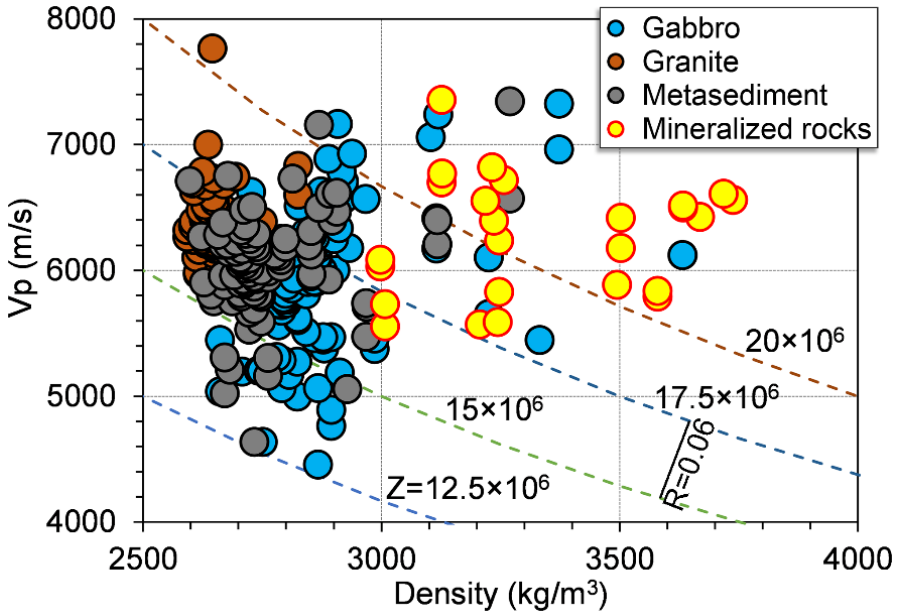

Figure 4-5: P-wave velocity vs. density measured from the core samples suggesting clustering of main lithological units. Dashed lines represent lines of constant impedance in m/s kg/m^3. The minimum reflection coefficient R=0.06 required to produce strong reflection (Salisbury et al. 2003) is superimposed for reference.

The velocity and density data collected from the core samples were plotted on the Nafe-Drake's velocity-density field to check the consistency of the physical properties with the mineral composition of the rock types. Figure 4-6 shows the distribution of the samples in the velocity-density field. Gabbro shows a gradual increase in P-wave velocity with increasing density. Most gabbroic rocks are characterised by tabular to blocky plagioclase crystals. Seismic velocities tend to increase with increasing pyroxene content and decrease with increasing plagioclase or chlorite content.

The mineralogical composition of the mineralised rock samples include varying quantities of magnetite, garnet, pyroxenes, plagioclase feldspar, apatite, pyrite, bornite and chalcocite (Conor *et al.* 2010; Ismail *et al.* 2014). The mineralised rock samples are scattered all over the velocity-density field also supports that the samples differ greatly in mineral composition.

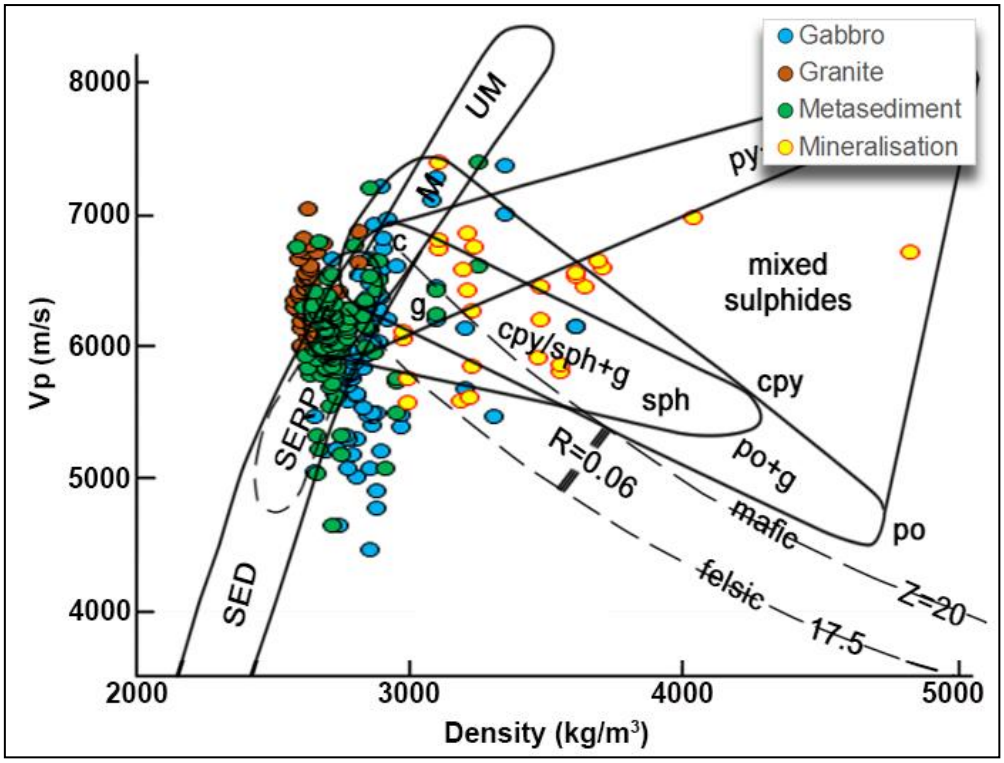

Figure 4-6: P-wave velocity (Vp)-density fields for sulphide ores and silicate host rocks adopted from Salisbury et al. (1996) were used to categorise samples from Hillside. Ores: py=pyrite, cpy=chalcopyrite, sph=sphalerite, po=pyrrhotite. Silicate rocks along Nafe-Drake curve: F=felsic, M=mafic, UM=ultramafic, SED=sediments, SERP=serpentinite, c=carbonate, g=gangue. The lines of constant acoustic impedance (Z) for felsic and mafic rocks are illustrated as dashed lines.

The empirical cumulative distribution function of the analysed samples is provided in Figure 4-7. The distribution suggests that ~90% of the gabbro, granite, and metasediment samples have density value ranging from 2600 kg/m^3 to 3000 kg/m^3. Mineralised rock samples are significantly different in terms of velocity and density from granite and metasediments but not from gabbro.

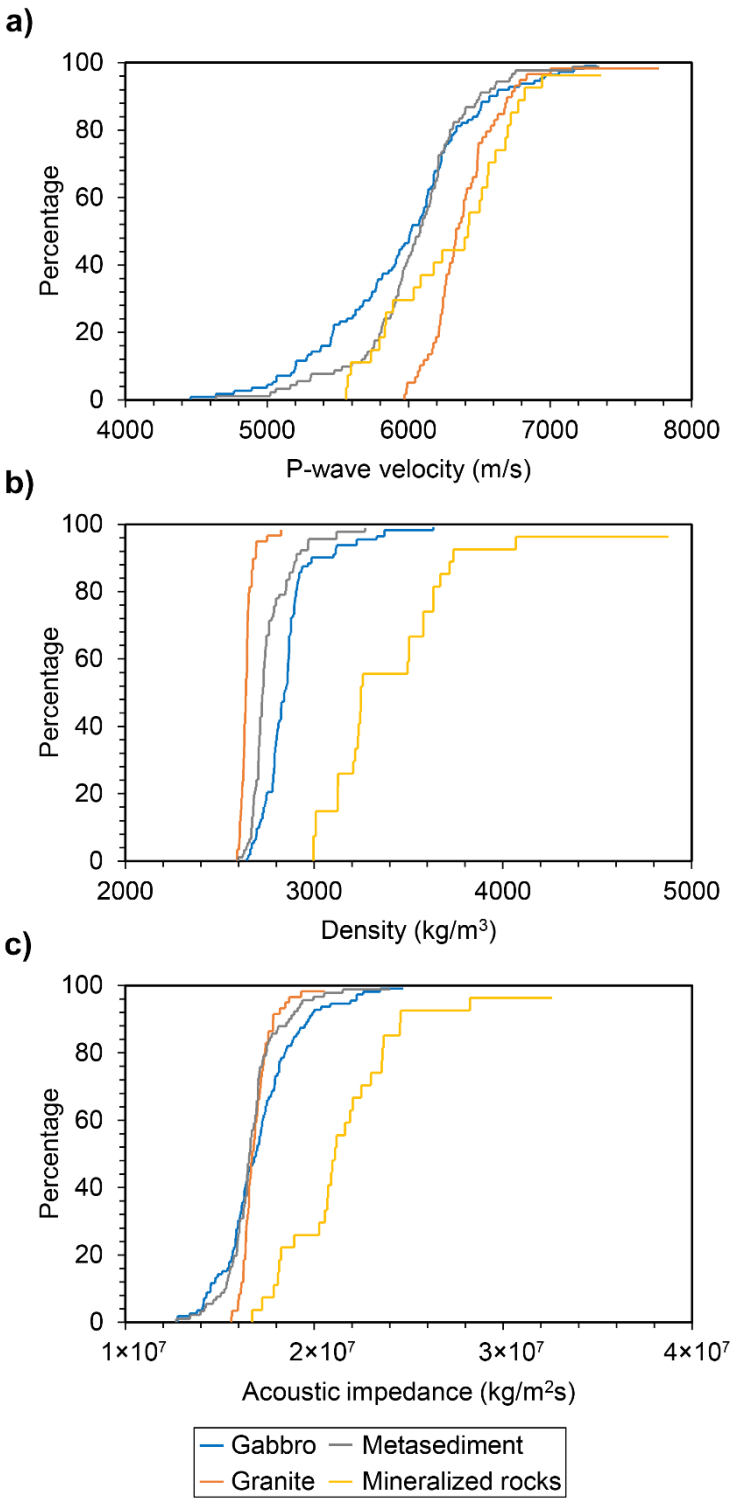

Figure 4-7: The empirical distribution function (empirical CDF) calculated from the (a) P-wave velocity, (b) density, and (c) acoustic impedance of the analysed core samples.

A database containing density values of core samples was supplied by Rex Minerals Ltd to use during the seismic interpretation phase. A density voxet (3-dimensional regular grid) equal to the area of the seismic cube was extracted from the supplied database. The density value of this extracted voxet ranges from 2500 kg/m^3 to 3710 kg/m^3 with mean value of 2760 kg/m^3 (Figure 4-8).

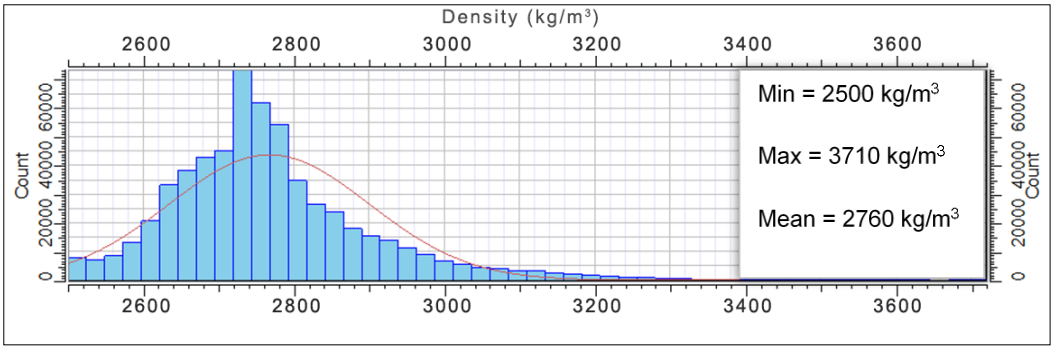

Figure 4-8: The density distribution of the measured core samples extracted from the supplied database.

Figure 4-9 (a) shows the density cube extracted from the supplied database. The density distribution in this cube ranges from 3000 kg/m^3 to 3719 kg/m^3. The density data were filtered according to the density range of mineralised rock units measured during the physical property data analysis. The filtered zones correspond to the high magnetic anomaly zones on the residual magnetic anomaly map in Figure 4-9 (b).

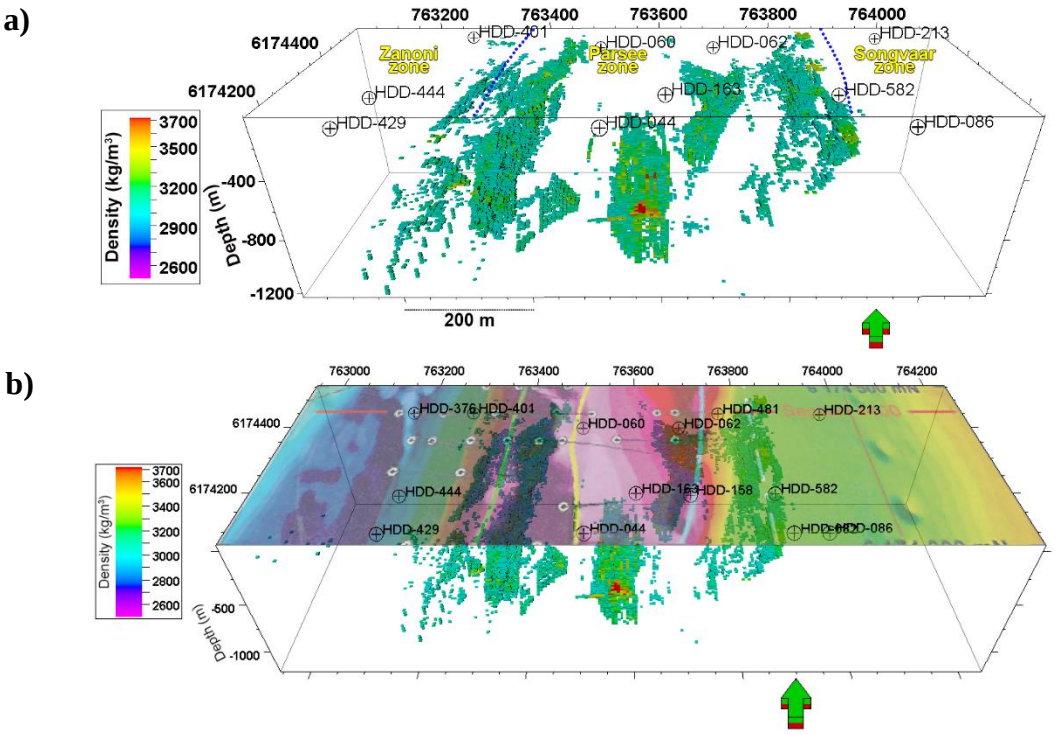

Figure 4-9: (a) The density cube extracted from the supplied database. The density data were filtered according to the range for mineralised rocks from the petrophysical data analysis (>3000 kg/m^3). (b) The filtered distribution corresponds to the high-magnetic anomaly zones on the residual magnetic anomaly map of Hillside in Figure 4-2 (b).

4.4. Seismic data acquisition and processing

Seismic reflection method is the most powerful geophysical technique that can provide high-resolution images at greater depth compared to other geophysical techniques. The performance of this method varies as a function of ground condition, and geological complexity of the survey area. In the case of IOCG deposits, this method is challenged by a very complex subsurface geology, which is characterised by subvertical to vertical mineralisations that are difficult to image from the surface. To investigate the potential of the 3D seismic method for exploration of such deposits; a high-density seismic survey was designed and executed. This survey also intends to demonstrate that even high-density 3D seismic surveys can be cost effective if undertaken by a small seismic crew with an alternative source. The location of the seismic survey over the Hillside IOCG deposit is shown in Figure 4-10.

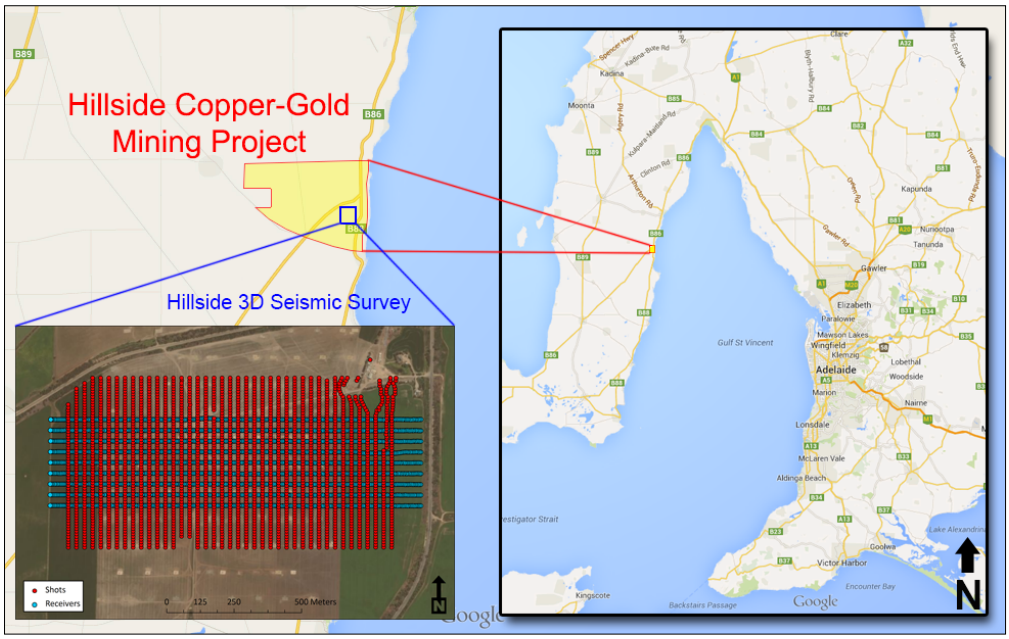

Figure 4-10: The location of the Hillside 3D seismic survey. Red and blue dots in the inset represent shot points and receiver locations respectively.

For the data acquisition, an EX-6 distributed seismic system with 844 live channels per patch and SM24 10 Hz (vertical) geophones were used. Each EX-6 acquisition unit can acquire six channels. Seismic cables through which Ethernet communication is established connected the units. Several 12 V batteries delivered power to the units that were topped up through the solar panels to increase the effective shooting time by minimising the necessity to pick up batteries for recharging (Figure 4-11).

Figure 4-11: The solar panels were used to top up the batteries to increase effective shooting time.

A 375 kg concrete breaker acting as a free-fall weight mounted on a skid-steer loader was used as a seismic source (Figure 4-12). A Wireless Optical Triggering Box was used to trigger the system for synchronising the shot and recording. The recording length was 2 seconds; the sample rate was 2 ms (220 Hz limit). The data acquisition parameters are provided in Table 4-3.

The 3D seismic survey was conducted using five overlapping receiver patches. Each patch consisted of nine receiver lines with 96 receivers each, and eight shot lines with 64 shots per line. Patch overlap was 50% along receiver lines. Receiver line spacing was 30 m and shot line spacing was 40 m. Data was re-binned from nominal 2.5 m × 5 m to 5 m × 5 m to double the fold and increase the signal-to-noise ratio. The actual in-field achieved CMP fold map is shown in Figure 4-13. Figure 4-14 demonstrates a raw 3D shot gather from Hillside seismic data.

Figure 4-12: 375 kg free-fall weight drop was carried by a skid-steer to navigate to each shot point by a spotter.

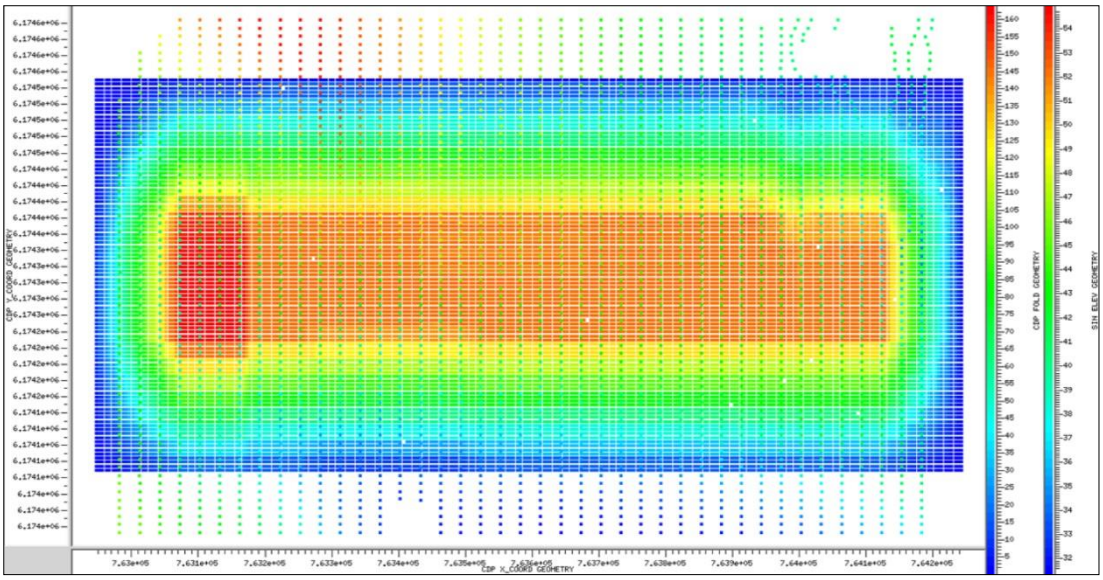

Figure 4-13: Actual CMP folds as achieved after 2575 shots.

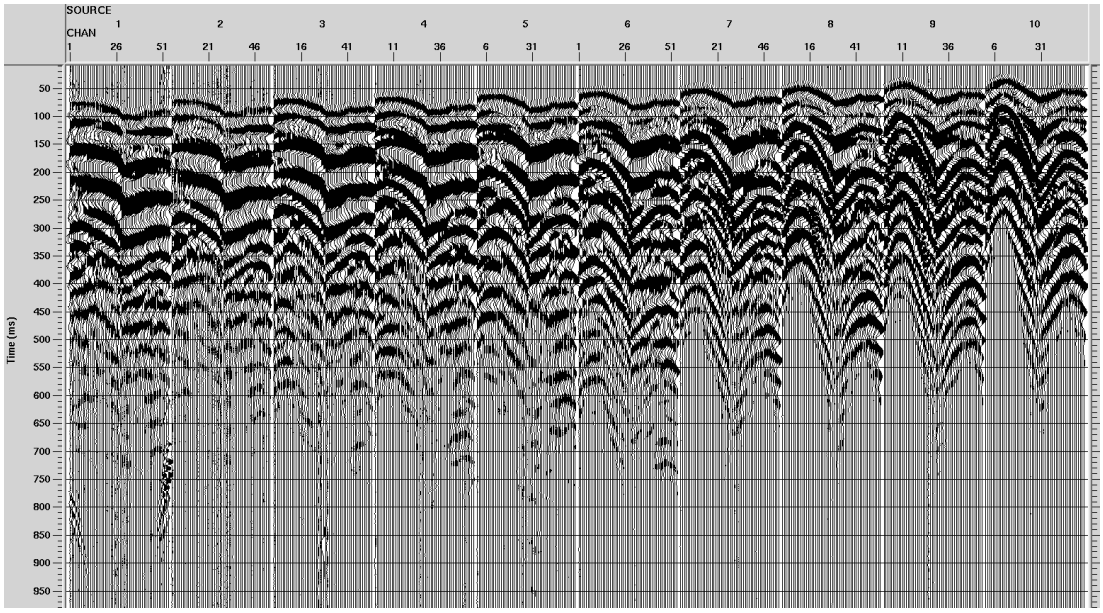

Figure 4-14: A raw 3D shot gather from Hillside seismic data

Table 4-3: Data acquisition parameters for Hillside 3D seismic survey.

Parameter	
Survey Type	3D orthogonal
Recording system	EX-6 distributed seismic system
No. of patch	5 (50% overlap)
No. of active channels	844
Total survey length	1375 m
Total survey width	320 m
Source	375 kg concrete breaker mounted on a skid-steer loader
Geophone frequency	SM24 10 Hz (vertical)
Source interval	10 m
No. of shots	2575
Receiver interval	5 m
Nominal fold	74
No. of shot lines	40 (8 lines per patch)
Shot line spacing	40 m
No. of receiver lines	9
Receiver line spacing	30 m
No. of active receiver lines per patch	8
Sampling rate	2 ms
Recording length	2 s

The seismic data processing was done at the Department of Exploration Geophysics of Curtin University. Very complex near-surface geological issues were resolved by using refraction statics on the dataset. The 375 kg free-fall weight drop used as a seismic source caused difficulties in imaging complex structures due to low resolution in the raw data. Much of the high frequencies were attenuated by the near-surface geology resulting in poor images of subvertical structures that acts as the actual pathways for the mineralisation. Source de-signature and spectral whitening were applied in the prestack domain to increase the spatial resolution without amplifying the noise. The 3D

prestack Kirchhoff time migration (PSTM) algorithm was used to image subvertical structures. A relatively simple velocity model was employed for time-to-depth conversion considering very small size of the survey area (Figure 4-15). The velocity data used in the velocity model is similar to the velocity values measured from the core samples, despite the velocity values from borehole HDD-064 shows some discrepancies at shallow depths. However, the differences become marginal with increasing depth. The flat datum is 51 m above the Australian Height Datum (AHD). The list of processes applied to the seismic data is shown in Table 4-4.

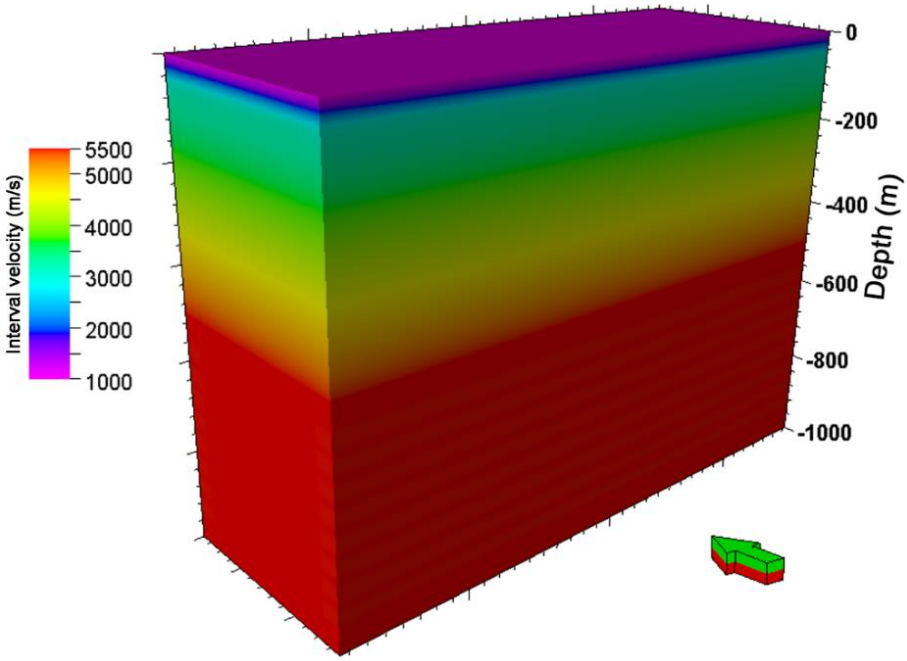

Figure 4-15: The velocity model employed in time-to-depth conversion of the Hillside 3D seismic dataset.

Table 4-4: Processing steps applied on the Hillside 3D seismic data

Processes	**Parameters**
Data reformat	From SEG-D to SeisSpace internal format
Geometry application	Source, receiver, offsets etc., assigned to each trace
Trace header math	Trace headers and data attributes assigned using fixed equation mode
Header statics	Bulk shift static applied and added to previous statics
Time frequency domain noise rejection	Time range: 0-1000, sampling window: 40, frequency of interest: 5-140 Hz, threshold multiplier: 3
Spiking/predictive deconvolution	Minimum phase spiking using an operator length of 60 and operator white noise level 0.1
Bandpass filter	Ormsby bandpass filter, zero phase, filter frequency values: 10-25-140-240
Automatic gain control	Mean AGC scalar, operator length 25
Surface wave noise attenuation	Velocity 170, frequency range 5-180 Hz, blend width 5 Hz, panel size 500, panel edge 50 and pane mix 30
Elevation statics	NMO static datum 51
Normal moveout correction	Direction of NMO application: forward, stretch mute percentage 30, NMO velocity functions: 1:0-700, 40-800, 60-1100, 90-1500,110-1600,200-2200
Spectral shaping	Mode: whiten, frequency amplitude pairs: 10-0,30-100,150-100,250-0
Bandpass filter	Ormsby bandpass filter, zero phase, filter frequency values: 10-60-100-250
Residual statics	Max. power autostatics

Processes	Parameters
Ensemble dip moveout in T-X domain	CDP interval 0.5, maximum offset of data: 94.0034, typical RMS velocity at early times 1100,
Prestack Kirchhoff 3D time migration	
Velocity manipulation	Stacking (RMS) velocity adjusted to the final datum, maximum velocity change: 5%
Stack 3D	In-line range: 1-260, x-line range: 1-97
Bandpass filter	Ormsby bandpass filter: 10-60-140-250
Time/depth conversion	Using interval velocity from the database

4.5. Seismic volumetric interpretation

3D seismic datasets, in comparison with the 2D seismic surveys, allow considerably better seismic-stratigraphic resolution because of improved acquisition and processing methods. Seismic interpretation requires an understanding of the subsurface formations and their effect on seismic wave propagation.

The Hillside 3D seismic cube covers a volume of 1295 × 480 × 1274 m^3. The signal amplitudes of the cube range from -0.538 to 0.577. The final processing yielded a PSTM cube with 5 m × 5 m grid. The vertical sampling interval is 1 m. The statistics for the Hillside 3D seismic dataset is provided in Table 4-5.

Table 4-5: Statistics for the Hillside 3D seismic dataset

Description	Value
Original CRS:	Map Grid of Australia Zone 53 (GDA 94)
Origin X:	762946
Origin Y:	6174072
End first inline X:	764241
End first inline Y:	6174072
End first crossline X:	762946
End first crossline Y:	6174552
Number of inlines:	97
Number of crosslines:	260
Inline length:	1295
Inline interval:	5
Crossline length:	480
Crossline interval:	5
Inline rotation from the north:	90
Number of samples per trace:	1275
Sample interval:	1

4.5.1. Seismic attribute analysis

Seismic attribute analysis utilised a 3D PSTM seismic data converted to depth (Figure 4-16). Time-to-depth conversion at the final stage of data processing utilised interval velocities. Seismic volume attributes were computed using the attribute libraries in Schlumberger Petrel, Paradigm GOCAD, OpendTect and GeoTeric software packages.

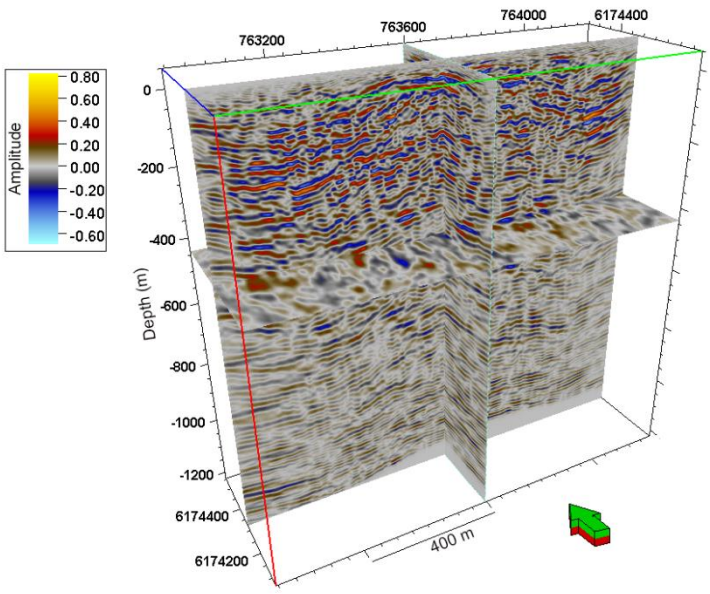

Figure 4-16: Amplitude display of the depth-converted PSTM volume from Hillside 3D seismic survey.

Advancement in algorithm development enabled us to calculate reflector dip and azimuth without explicitly picking seismic horizons (Chopra and Marfurt 2007). Dip and Azimuth attributes can play a crucial role in seismic interpretation. These attributes can be used to define a local reflector surface upon which the data can be filtered to extract their continuous component (Chopra and Marfurt 2007). However, due to the velocity distortions, reflector dip and azimuth from a poststack time-migrated seismic cube correlates loosely to the actual dip and azimuth. Dip and Azimuth attributes have been calculated from the Hillside PSTM volume.

Dip attribute has been calculated for Hillside seismic data (Figure 4-17). This attribute estimates local dip from the seismic data (Schlumberger 2014). The principal component of the dip attribute is estimated from principal component analysis of gradient covariant matrix (Randen *et al.* 2000). Both dip and azimuths are poststack attributes that calculates a best-fitting plane in 3D space for each trace with its neighbouring traces (Chopra and Marfurt 2007). For dip, the output is the dip magnitude of that best-fitting plane and for azimuth, it is the direction of the maximum slope of that best-fitting plane (Chopra and Marfurt 2007). The survey area is characterised by north-south trending subvertical to vertical faults as evidenced by sharp lateral changes in dip magnitude at shallow depth.

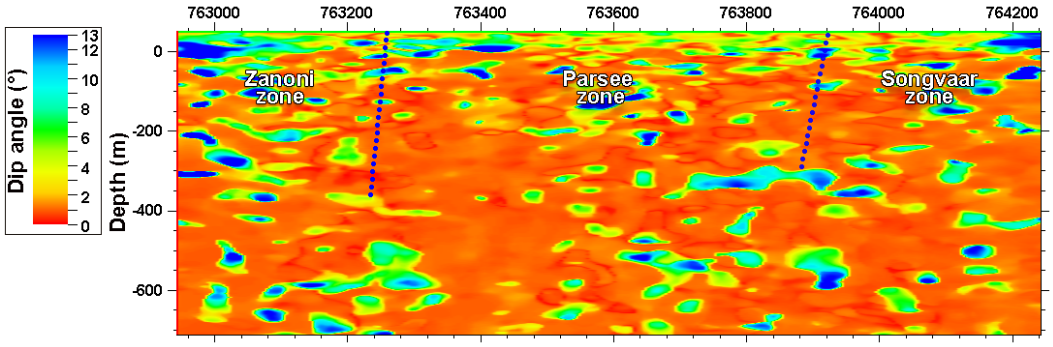

Figure 4-17: The dip attribute computed along inline N6174262 (V.E. 0.5 X).

Figure 4-18 depicts the azimuth computed using the sigma value (window) of 3 in X, Y, Z direction. The value of sigma specifies the window radius when calculating the chaotic nature of the signal. The Parsee mineralisation zone between E763200 and E763600 where residual magnetic anomaly response is high [Figure 4-2(B)], shows that the azimuth of the structures point toward the west. The area between the Pine Point Fault and Zanoni Fault (between the western boundary of the cube and E763200) shows that the dominant dip direction is toward the north. The azimuth of the signals between E763600 and E764000 shows variable directions. Sharp changes in azimuth along a line may indicate a lithological boundary or fault. The results from the dip and the azimuth attributes establish the fact that the survey area is characterised by numerous north-south trending subvertical to vertical structures.

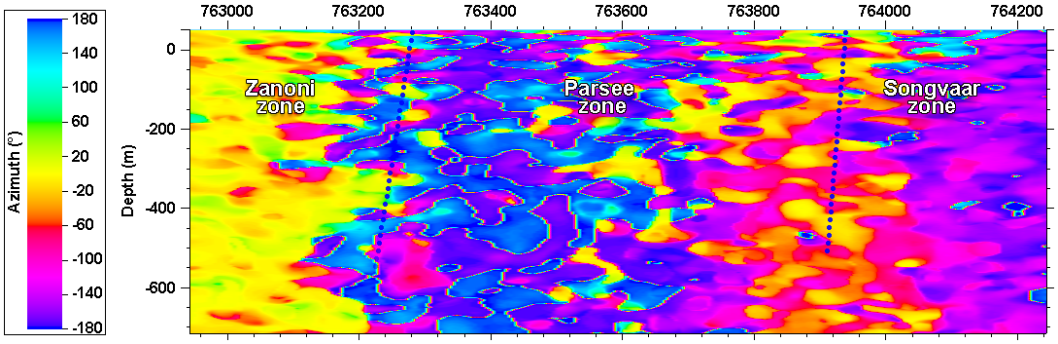

Figure 4-18: Azimuth attribute calculated along inline N6174262 (V.E. 0.5 X). The sigma value (window) 3 was chosen in X, Y, and Z direction for principal component of the azimuth attribute computation.

Variance attribute was computed from a structurally smoothed seismic cube (Figure 4-19). Dip correction was applied to add the directional parameters to the attribute. The dip-guided algorithm computes variance along a dipping plane with a corresponding

measure of the dip estimate confidence. The plane confidence threshold of 0.7 was selected. Areas, where the computed confidence is above the selected confidence threshold, used dip-guiding. Standard horizontal variance algorithm is used in areas where the confidence is below the threshold limit.

The red and yellow colour in Figure 4-19 represents areas with high variance, i.e., the breaks in the horizontal continuity of the signal. The presence of faults usually causes these discontinuities in the data. From the variance data, it is evidenced that the area is characterised by numerous north-south trending subvertical to vertical faults.

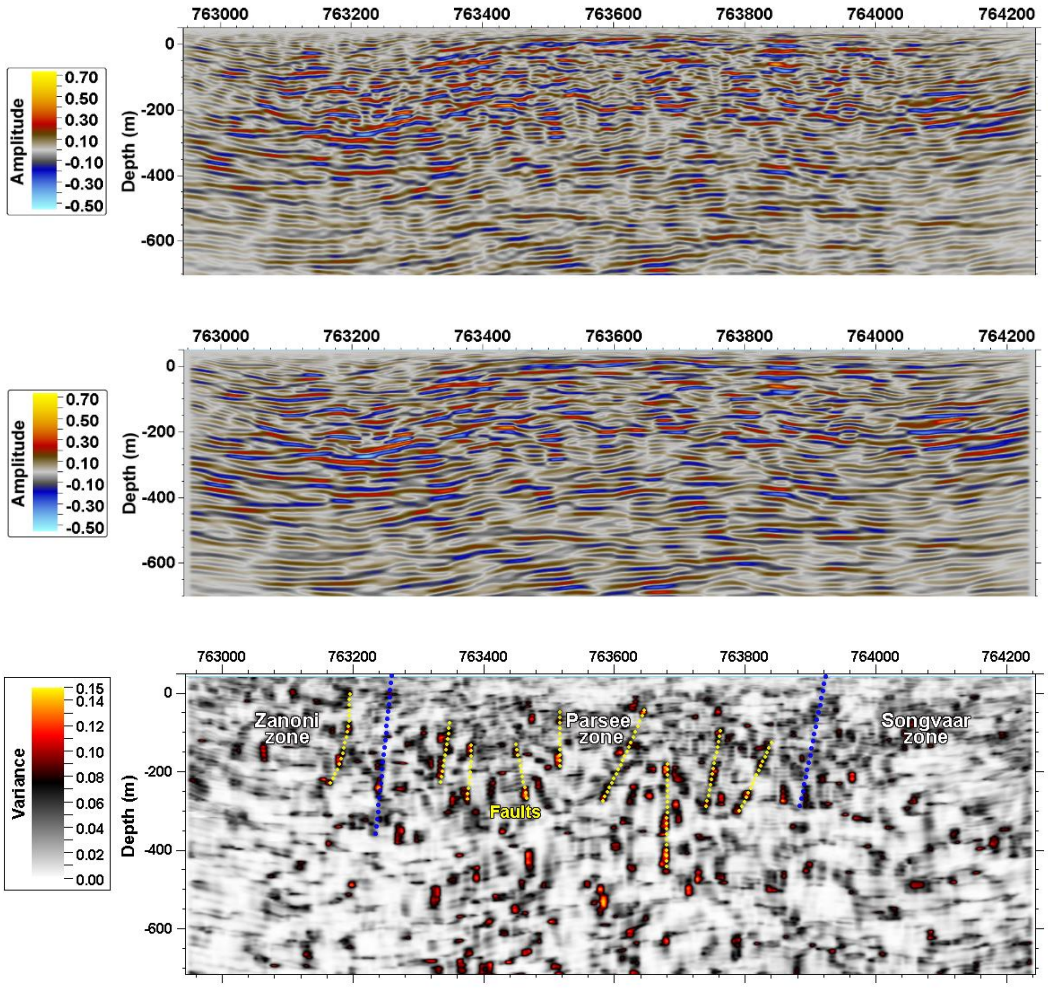

Figure 4-19 : (a) Amplitude display along inline 6174262 from the Hillside seismic volume, (b) structurally smoothed volume used as the input for variance attribute calculation, and (c) variance attribute display along inline 6174262 N. A smoothing operator of 10 samples was selected to reduce the noise. A plane confidence threshold of 0.7 was used for dip correction.

Fracture density attribute highlights the areas of high-density fractures, thereby improves visualisation of potential fracture anomalies. The algorithm computes the ratio of number of traces classified as being fractures to the total number of traces in a given radius along a horizontal plane. A discontinuity volume, i.e., maximum curvature was used as an input volume and an anomaly threshold of 0.04 was used to identify the areas with high-density fractures within a radius of 100 m. Figure 4-20 shows the high-density fractures computed along inline 6174262 N (a) and on two horizontal slices at -100 m AHD (b) and -200 m AHD (c). It is evidenced from the figures that the area is characterised by abundance of fractures.

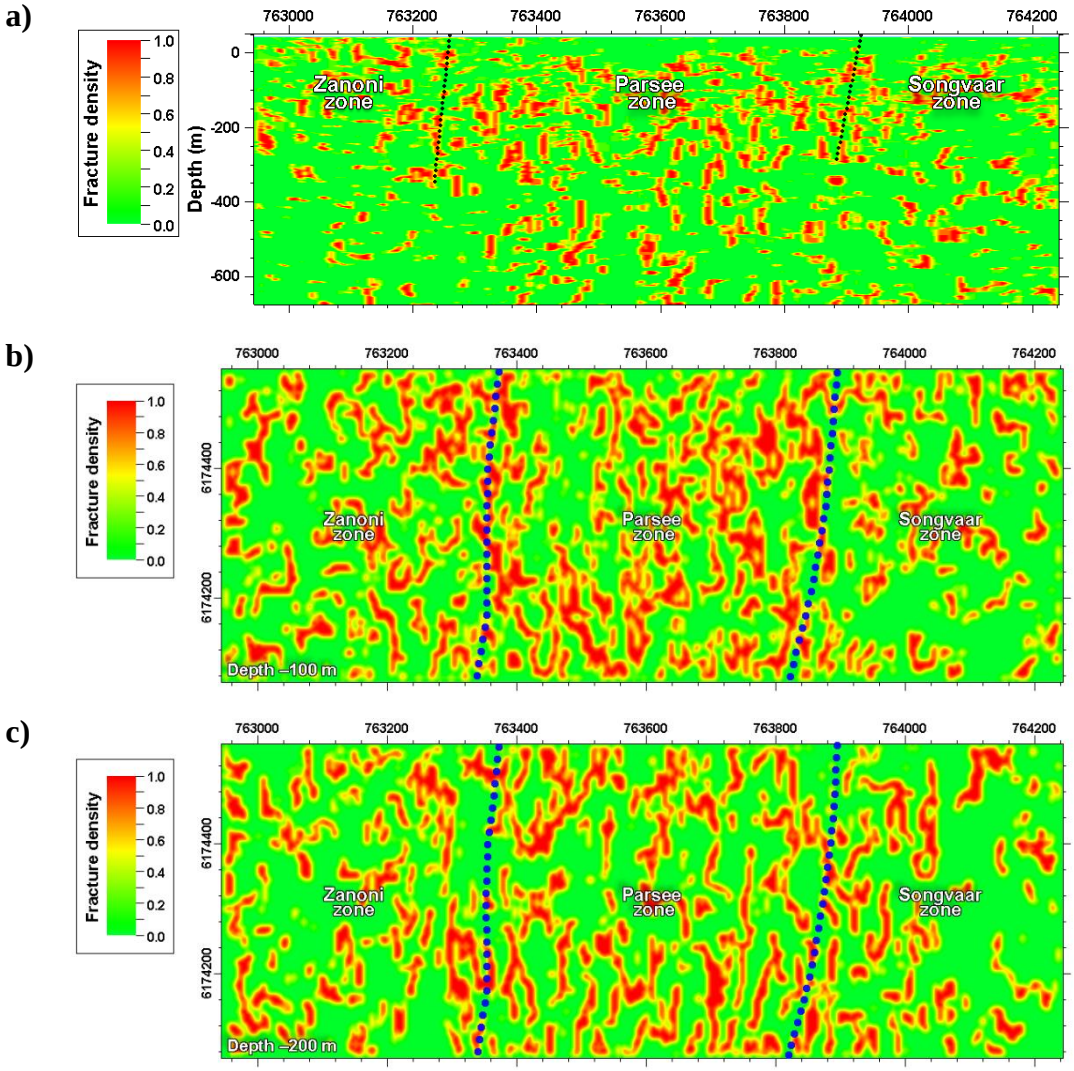

Figure 4-20: (a) Fracture density calculated from a maximum curvature volume using a radius of 100 m. Red colour indicates areas with high density fractures along inline 6174262 N (V.E. 0.5 X), horizontal slices at (b) 100 m below the Australian Height Datum, and (c) 200 m below the Australian Height Datum.

4.5.2. Fault detection

Fault imaging was done using the FaultApp workflow of GeoTeric software and Schlumberger Petrel's Ant-tracking workflow. GeoTeric's fault imaging workflow identifies and extracts discontinuities in the data that represent faults. The steps involved in the fault detection to extract potential faults are demonstrated in Figure 4-21. The workflow provides a detailed representation of the discontinuities in the data. Fault enhancement improves the continuity of the faults and reduces the background clutter. Fault-detection stage extracts the faults as single voxel thick lineations in volume form.

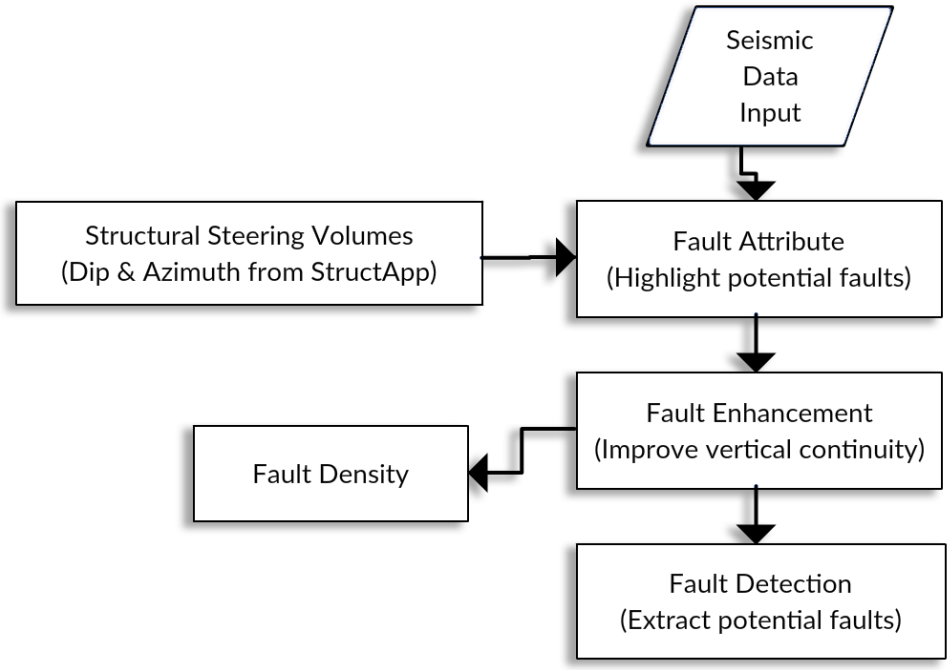

Figure 4-21: A flowchart exhibits the steps of FaultApp workflow (Courtesy: GeoTeric user's manual 2015).

Fault detection was also performed by utilising Schlumberger Petrel's ant-tracking workflow on an edge-detected seismic cube. Ant-tracking uses coherent signal tracking algorithm to find optimal connectivity for fault features from an edge-detected volume (Hossain et al. 2014; Schlumberger 2014). The steps involved in the ant-tracking workflow are presented in Figure 4-22.

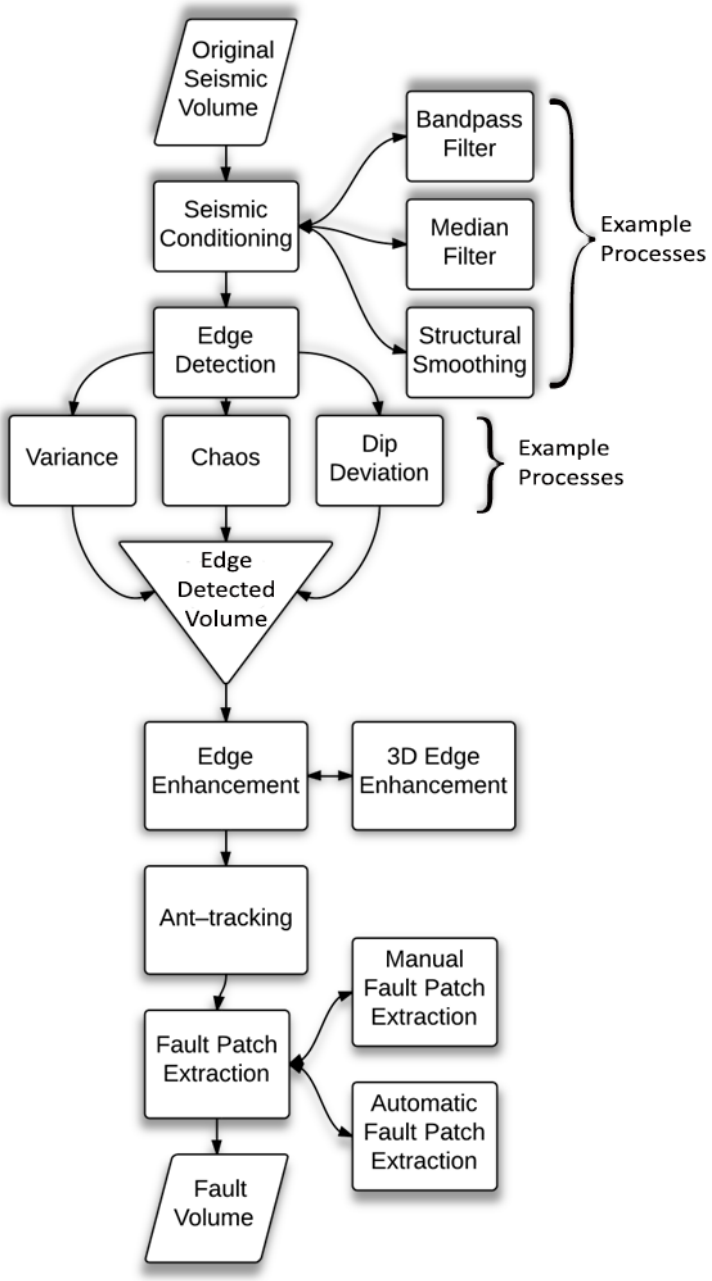

Figure 4-22: A flowchart demonstrates the steps of Schlumberger Petrel's ant-tracking workflow (modified after Schlumberger 2014)

The ant-tracking process involves four steps: i) data conditioning, ii) edge detection, iii) edge enhancement, and iv) ant-tracking. The original seismic volume is prepared for edge detection by applying bandpass filter, and structural smoothing on the original seismic volume. The next step involves utilising edge detection attributes, e.g., variance. Edge detection operation identifies the discrete edges, thereby enhancing confidence in the modelled fault network. It can be used either to rapidly highlight a

fault network or potential low throw structures not discernible in seismic sections. Edge enhancement was performed on an edge-detected volume. Edge enhancement improves edge detection through comparing and summing the values of the surrounding pixels along a plane on the edge-detected seismic cube. The mean of the values is displayed on the output cube. The resulting cube enhances the larger features while the smaller features such as noise are smoothed away. Then the enhanced cube was used for ant-tracking. Figure 4-23 shows a horizontal slice of the ant-tracking result placed over an inline section of the Hillside seismic volume.

A horizontal slice at 220 m below Australian Height Datum (AHD) demonstrates a comparative performance of the FaultApp workflow of GeoTeric [Figure 4-24 (a)] and Schlumberger Petrel's ant-tracking workflow [Figure 4-24 (b)]. It is evident that the performance of Schlumberger Petrel's ant-tracking workflow is significantly better than GeoTeric's FaultApp workflow.

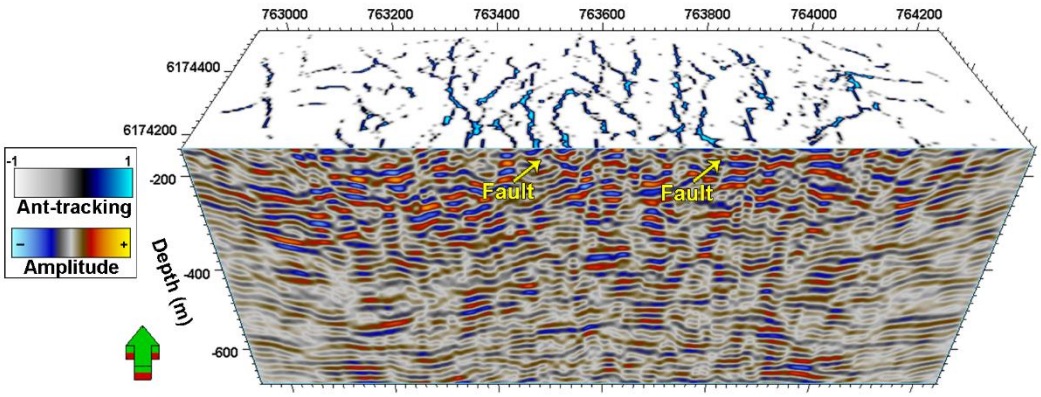

Figure 4-23: A horizontal slice of the ant-tracked volume placed on an inline section of the amplitude volume shows the comparison of the faults detected from the seismic data.

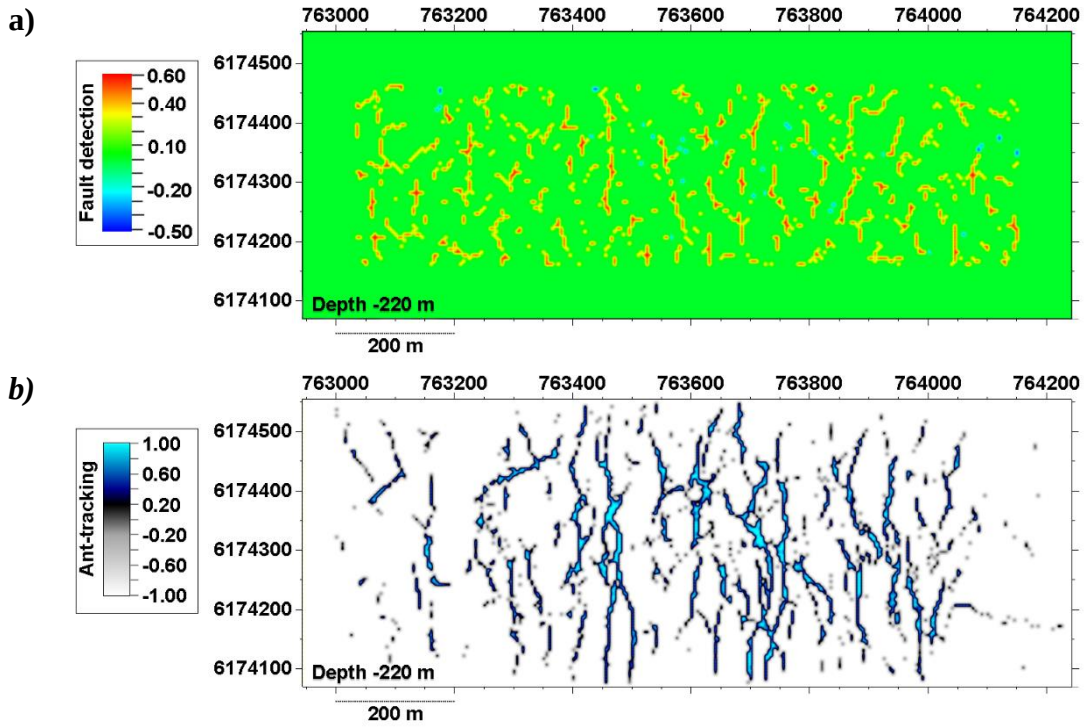

Figure 4-24: Horizontal slice at 220 m below the datum shows the faults detected using (a) FaultApp workflow, and (b) ant–tracking workflow.

A multi-attribute depth slice at 175 m below AHD from the ant-tracking volume is plotted against a geological cross-section along N6174200 to compare the correlation between the faults extracted from the seismic volume and the geological cross-section (Figure 4-25). The geologists of Rex Minerals Ltd constructed the geological cross-section from the borehole information. The figure demonstrates a very good agreement between the ant-tracking result and the geological boundaries drawn from borehole information.

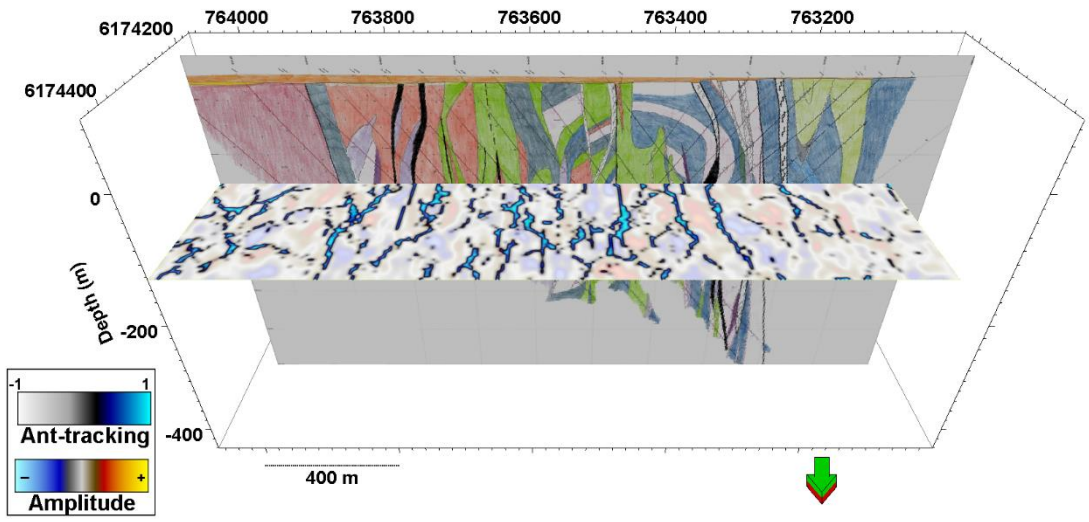

Figure 4-25: Multi-attribute horizontal slice at 175 m below the datum shows the faults extracted from the Hillside 3D seismic volume (view from north). A geological cross-section supplied by Rex Minerals Ltd placed as the vertical section along 6174200 N to display the correlation between the geological interpretation and ant-tracking. The geologists of Rex Minerals Ltd constructed the cross-section from the borehole information. The top regolith is shown as orange colour, granite as red, gabbro as blue, metasediment as green and the shear zones as black.

Figure 4-26 (a) and (b) demonstrate a fault network for the top 200 m extracted from the ant-tracked volume and placed against a geological cross-section along 6174200 N to show the performance of the ant-tracking result and geological interpretation. The fault network extracted from the ant-tracked volume shows an excellent correlation with the geological boundaries.

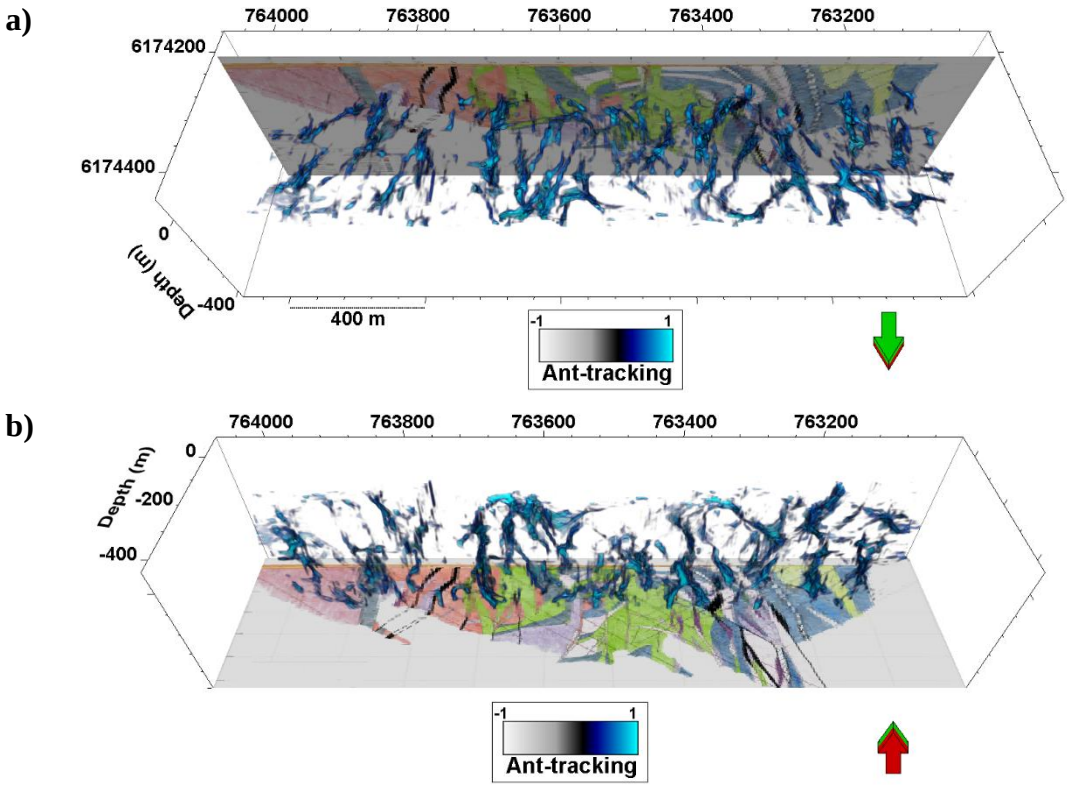

Figure 4-26: Fault network extracted for the top 200 m from the ant-tracked volume is placed against a geological cross-section along 6174200 N. (a) Viewing towards south from above and (b) viewing towards south from below.

To extract the fault network a box probe was created from the ant-tracked volume and transparency threshold of 0.5 was applied to the box probe to filter the low values. Figure 4-27 shows the fault network extracted for the top 500 m from the ant-tracked volume.

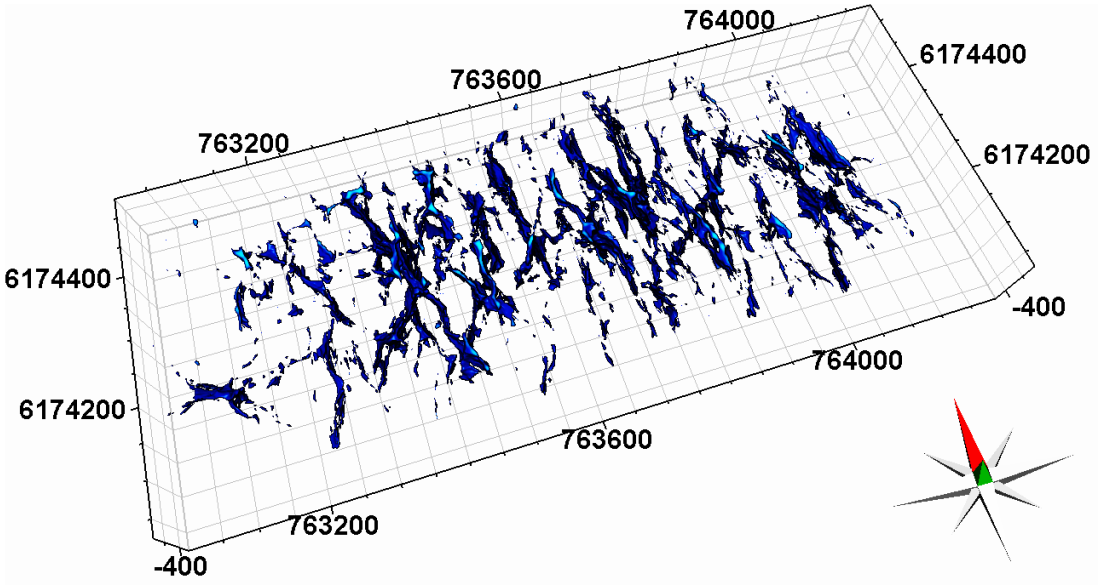

Figure 4-27: Fault volume extracted for the top 500 m from the ant-tracked volume by applying a transparency threshold of 0.5 to the data (Hossain et al. 2015b).

4.6. Summary

The 3D high-resolution seismic reflection survey of Rex Minerals' Cu-Au mining project at Hillside is the very first 3D seismic reflection survey undertaken over an IOCG deposit in the world. The goal of this experimental research project was to study the seismic response over a complex geological environment. The seismic source was a 375 kg concrete breaker acting as a free-fall weight mounted on a skid-steer loader. The survey was conducted using five overlapping patches with a patch overlap of 50% along receiver lines. The data were re-binned from 2.5 m × 5 m to 5 m × 5 m to double the fold and increase signal-to-noise ratio. The data processing was completed at the Department of Exploration Geophysics of Curtin University. The near-surface regolith layer attenuated much of higher frequencies, which resulted in poor imaging of subvertical structures. The 3D Kirchhoff prestack time migration algorithm was applied to migrate the data and a relatively simple velocity model was used to convert the cube from time-domain to depth-domain.

The physical properties suggest that most of the gabbro, granite and metasediment samples have similar density and P-wave velocity values; however, the P-velocity and density of the mineralised rock samples are significantly different from granite and gabbro, but not from metasediments. The analysis implied that the acoustic impedance

contrast between the rocks in Hillside is not strong enough to produce effective P-wave reflections at the stratigraphic boundaries. The above analysis infers that massive mineralised bodies bigger than the minimum horizontal and vertical resolution would have produced discernible reflections to be directly detected by seismic reflection method.

Both structural and stratigraphic attributes were implemented to interpret the data. The stratigraphic attributes was unable to add additional values to the analysis due to low signal-to-noise ratio, lack of prominent marker beds, abundance of fractures and sensitivity of the attributes to the noise in the input data. However, the main objective of the data interpretation was to extract the subvertical to vertical faults that acted as the pathways for the mineralisation. Structural attributes that emphasise discontinuities in the data were able to produce good results. Edge detection attribute, e.g., variance and fracture density were able to identify the discontinuities in the seismic data.

Fault detection was done using FaultApp workflow and ant-tracking workflow on the edge-detected seismic volume. Ant-tracking workflow provided significantly better output compared to FaultApp workflow. The ant-tracking result demonstrated a very good agreement when compared with a geological cross-section. A fault volume for the top 500 m was extracted from the Hillside 3D seismic dataset. These results are to be used in future drilling campaign and subsequent mine development programme.

5. Case study: Kevitsa nickel–copper–platinum group elements mine, northern Finland

5.1. Introduction

Kevitsa is a large, low-grade, disseminated, Sulphide Ni-Cu-PGE deposit located within layered sedimentary and volcanic rocks of the Central Lapland Greenstone Belt in northern Finland (Koivisto *et al.* 2012; Malehmir *et al.* 2012a; 2014). The estimated ore reserves of the Kevitsa intrusion are about 240 million tonnes (using a nickel cut-off grade of 0.1%), with low-grade metal concentrations of Ni 0.3 wt.% and Cu 0.41 wt.% (Koivisto *et al.* 2012). The Geological Survey of Finland discovered the deposit in 1987. They also carried out diamond drilling on 563 holes for a total length of 48,474 m and 278 holes summing 32,845 m to delineate the deposit (First Quantum Minerals Ltd 2013). First Quantum Minerals Ltd owns the Kevitsa mine through a 100% owned subsidiary, Scandinavian Minerals Ltd. Construction at Kevitsa has been completed, and the facility has reached commercial production on August 2012. The final pit depth will be 550-600 m and the expected mine-life is 29 years (First Quantum Minerals Ltd 2013).

The Kevitsa Ni-Cu-PGE mine is situated about 142 km north-northeast of the capital of Finnish Lapland, Rovaniemi. Kevitsa is an open-pit mine. Ores are processed traditionally. Copper and Nickel is recovered separately in two different concentrates, Ni-Cu-PGE-Au concentrate (~12% Ni grading) and Cu-Au-PGE concentrate (~28% Cu grading) (First Quantum Minerals Ltd 2015). The mineral production in Kevitsa is expected to be about 17,000-19,000 tonnes of Cu, 9,000-10,000 of Ni, 12,000-13,000 tonnes of Au and 22,000-24,000 ounces of Pl and Pd (First Quantum Minerals Ltd 2015).

In the first quarter of 2014, Ni production increased by 20% and Cu production rose by 25% compared to the first quarter of 2013 due to increased recoveries and higher grades (First Quantum Minerals Ltd 2015). Table 5-1 provides the total output from the Kevitsa mine in 2013.

Table 5-1: Total production in 2013 from the Ni-Cu-PGE mine in Kevitsa (First Quantum Minerals Ltd 2015).

Production	Amount
Mining	
Total Ore mined	21,604,000
Processing	
Ore milled	6,314,000
Ni ore grade	0.2 %
Ni recovery	63 %
Ni production	8,963 tonnes
Cu ore grade	0.3 %
Cu recovery	83 %
Cu production	14,775 tonnes
Au production	11,723 ounces
Pl production	30,403 ounces
Pd production	24,639 ounces

The mineral resources in Kevitsa was estimated by professional experts from FAusIMM of CSA Global Pty Ltd and geologists of the Kevitsa Mining Oy (First Quantum Minerals Ltd 2015). Table 5-2 provides the estimated mineral resources in the Kevitsa mine.

Table 5-2: The estimated mineral resources in the Kevitsa mine – 31 December 2013 (First Quantum Minerals Ltd 2015).

	Tonnes	%			g/tonne		
Ni Cut-off Grade of 0.1%	**(Mt)**	**Ni**	**Ni(S)**	**Cu**	**Au**	**Pd**	**Pt**
Measured	86.2	0.29	0.26	0.40	0.12	0.17	0.23
Indicated	151.2	0.32	0.29	0.42	0.11	0.34	0.19
Total Measured & Indicated	237.4	0.30	0.28	0.41	0.12	0.27	0.21
Total Inferred	34.8	0.29	0.27	0.36	0.09	0.10	0.14

Table 5-3 exhibits the mineral reserves estimated from the mineral resources in the Kevitsa mine.

Table 5-3: The estimated mineral reserves in Kevitsa – 31 December 2013 (First Quantum Minerals Ltd 2015).

	Tonnes	%			g/tonne		
Ni Cut-off Grade of 0.13%	**(Mt)**	**Ni**	**Ni(S)**	**Cu**	**Au**	**Pd**	**Pt**
Proven	81.0	0.29	0.26	0.40	0.13	0.17	0.23
Probable	76.0	0.33	0.30	0.42	0.12	0.18	0.25
Total Proven & Probable	157.0	0.31	0.28	0.41	0.12	0.18	0.24

HiSies Pty Ltd and the Uppsala University of Sweden conducted the 3D Seismic data acquisition in Kevitsa. My sole contribution to this case study involves seismic volumetric interpretation and physical property modelling.

Most of the works included in this chapter were included in the DET CRC annual meeting presentations, conference papers (Hossain *et al.* 2014a; 2015a) and a manuscript in preparation.

5.2. Geological setting

The Kevitsa ultramafic, layered intrusion is located within the Central Lapland Greenstone Belt (CLGB) in the northeastern part of the Fennoscandian Shield (Mutanen and Huhma 2001). The CLGB is characterized by Paleoproterozoic supracrustal rocks of volcano-sedimentary stratigraphic groups (Koivisto *et al.* 2012; Rasanen *et al.* 2001). The Kevitsa intrusion is part of the Kevitsa-Satovaara igneous complex. The intrusions have been inferred to represent a single intrusion separated by the Satovaara fault zone (Lindqvist 2014; Mutanen 1997). The Kevitsa intrusion is located within a basin delimited by 2.4 Ga old Koitelainen layered intrusion in the north and Satovaara intrusion in the east (Mutanen and Huhma 2001). The rocks of CLBC were deformed during the Svecofennian orogeny ~1.9 Ga ago (Hanski and Huhma 2005). The geologic map of Kevitsa Ni-Cu-PGE deposit is provided in Figure 5-1.

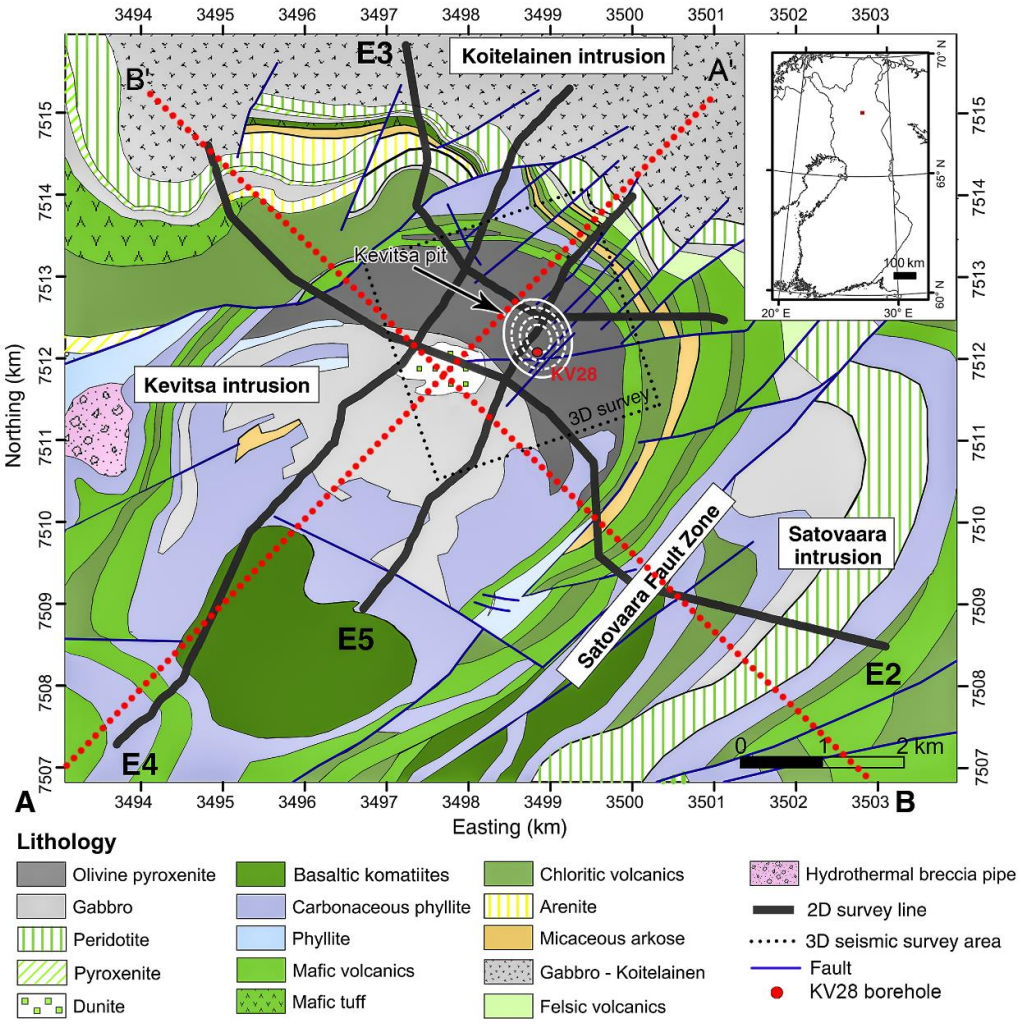

Figure 5-1: The Geologic map of the Kevitsa Ni-Cu-PGE deposit, showing the location of the 3D seismic survey (boxed area). White lines show the location of the open-pit mine and its extension. Thick black lines represent the Kevitsa 2D seismic survey lines E2, E3, E4, and E5. The location of the drill hole KV28 is shown as a red dot (Malehmir et al. 2014). Red dashed lines (AA' and BB') show approximate locations of the geological cross-section shown in Figure 5-2.

The Kevitsa intrusive complex is characterised by an oval-shaped surface expression and northeast-southwest trending long axis and dips south-southwest (Koivisto *et al.* 2012; Törmänen and Iljina 2007). Disseminated Ni and Cu-sulphide ore deposits are located within the ultramafic Kevitsansarvi area in northern part of the intrusion (Lindqvist 2014). The intrusion is hosted by the Savukoski group which comprises phyllites, black schists, tuffites, Fe-tholeiites, and ultramafic (komatiitic and pcritic) metavolcanic rocks (Räsänen *et al.* 1996). The ore deposits are located within olivine

pyroxenite, websterite and their altered derivatives (Koivisto *et al.* 2012; Lindqvist 2014). The southern part of the Kevitsa intrusive complex is characterised by gabbroic rocks (Koivisto *et al.* 2012). Figure 5-2 shows a couple of simplified geological cross-sections along SW-NE and SE-NW directions.

The basal contact of Kevitsa intrusion to the host rocks dips approximately 50° to 60° towards south in the northern part of the complex (Koivisto *et al.* 2012; Malehmir *et al.* 2014; Törmänen and Iljina 2007). The igneous layers parallel to the basal contact in the lower part of the intrusion also dip towards south (Törmänen and Iljina 2007). In the upper part of the intrusion, the igneous layers dips at an angle of 20° to 30° (Törmänen and Iljina 2007). The metasediment beds show a variety of orientations toward north, south and east, and dip at 10° to 30° (Koivisto *et al.* 2012). The gabbro and granophyre zones are almost horizontal in the upper part of the ultramafic zone (Törmänen and Iljina 2007).

The Contact metamorphism caused by the intrusion altered the rocks to hornfels near the contacts of the Kevitsa intrusion (Koivisto *et al.* 2012). The metamorphism has reached up to amphibolite facies stage on a regional scale and affected especially the host rocks and the upper parts of the intrusion (Koivisto *et al.* 2012). Clear evidence of faulting and folding is present in the metasedimentary layers, and felsic and mafic volcanic rocks (Malehmir *et al.* 2012a).

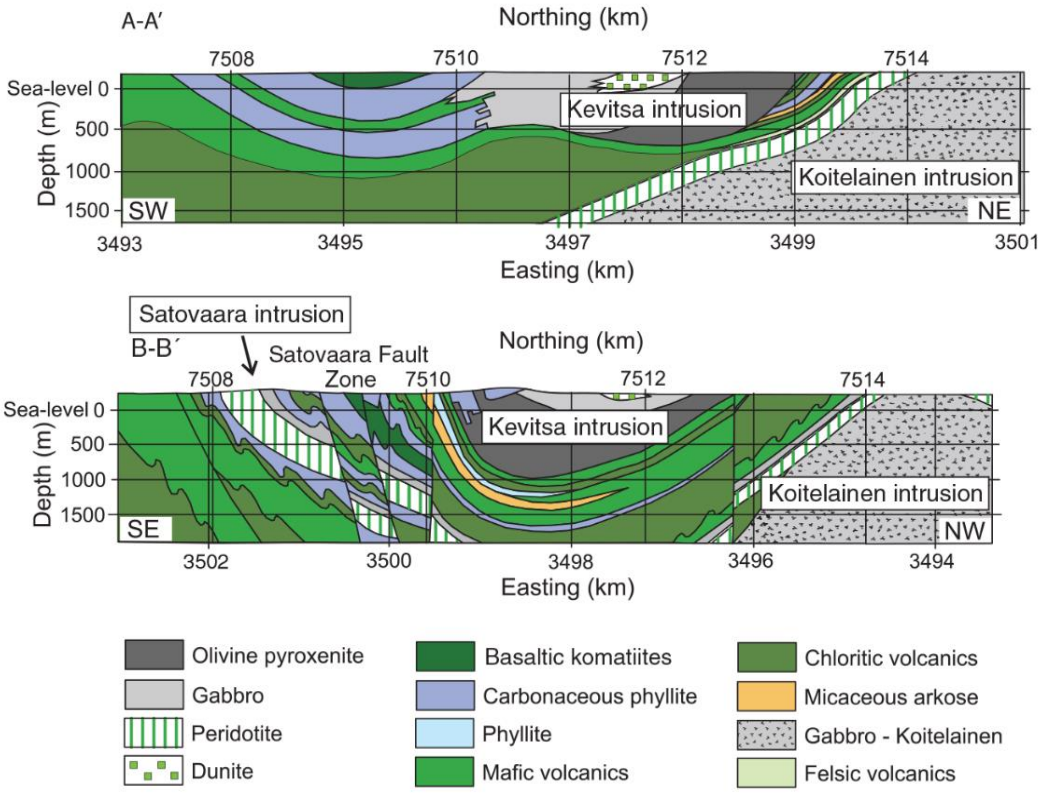

Figure 5-2: Schematic geological cross-sections along southwest-northeast (AA') and southeast-northwest (BB') demonstrate the shape of the Kevitsa intrusion and fault systems (Koivisto et al. 2012).

Authentic age data for metasediments and metavolcanics in the area are unavailable; however, an approximate age of 2.6 Ga was determined by crosscutting Kevitsa intrusion (Mutanen and Huhma 2001). Age data from the nearby Rantavaara area suggests that Phyllites in the area are older than 2.15 Ga (Rasanen *et al.* 2001), and the gabbro of Koitelainen intrusion have been dated to be 2.4 Ga old (Mutanen and Huhma 2001).

The typical faults of the Kevitsa area strike southwest-northeast (Lindqvist 2014). The orientation of these structures is interpreted to be a consequence of tectonic stress along northwest-southeast direction (Lindqvist 2014).

Lindqvist (2014) studied regional scale brittle structures around the Kevitsa intrusion to correlate them with the local-scale structures. He interpreted the regional lineaments as narrow linear zones from the regional aeromagnetic map (Figure 5-3) and the regional hillshade maps (Figure 5-4). The narrow linear zones represent relief in

the data as magnetic high adjacent to magnetic low on the aeromagnetic map, and topographic high and low combined with steep slopes and linear forms on the hillshade map.

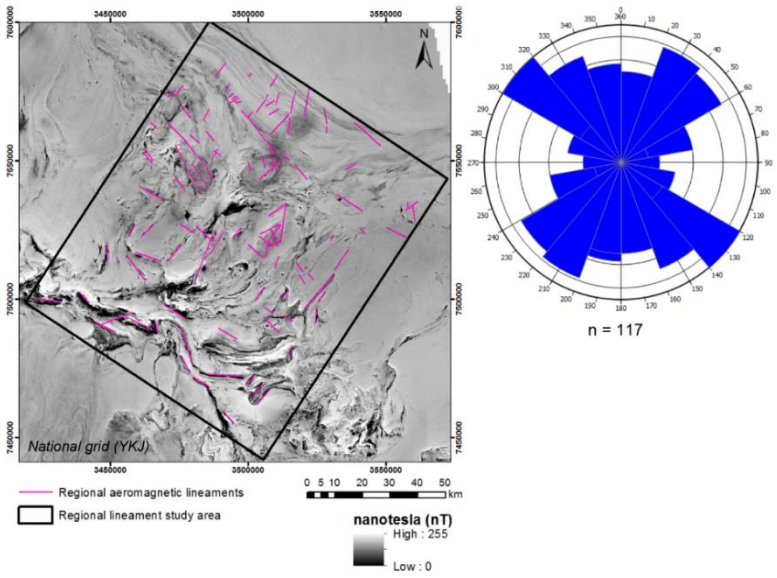

Figure 5-3: Regional lineaments interpreted from total magnetic field data. Rose diagram shows the major orientations, NW-SE and SW-NE (Lindqvist 2014).

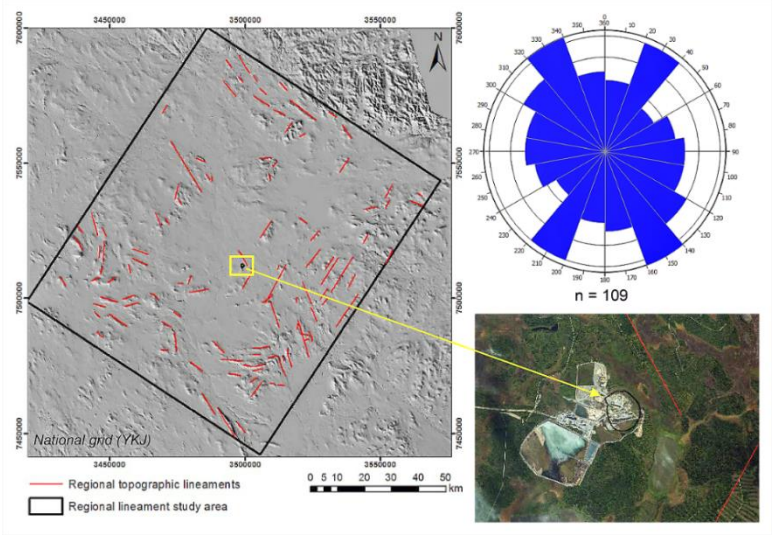

Figure 5-4: Regional lineaments interpreted from topographic hillshade map. Rose diagram shows two major orientations NNW-SSE and SSW-NNE. Aerial photograph shows the location of the Kevitsa open-pit (Lindqvist 2014).

The mineralised area of the Kevitsa intrusion exhibits internal layering resulting from the changes in chemical composition due to successive pulses of magma (Malehmir *et al.* 2012a). The olivine-pyroxenite zone within the main intrusion hosts mineralisation, which contains up to 5% sulphide, dominantly as granular masses interstitial to the silicate mineral crystals (Malehmir *et al.* 2012a). Olivine and orthopyroxene with finely disseminated sulphides forms the dominant portion of the silicate mineralogy (Malehmir *et al.* 2012a). The sulphides are composed of pyrrhotite, pentlandite, chalcopyrite, and various less important platinum group minerals (Malehmir *et al.* 2012a).

The dykes within the Kevitsa intrusions can be roughly classified as gabbro, diorite-felsite, and diabase (Törmänen and Iljina 2007). The earliest phase is represented by porphyric gabbroic veins with sharp contacts (Törmänen and Iljina 2007). The diorite-felsite veins show a paragenetic and compositional continuum with some composite veins of felsite occurring in the middle of diorite veins (Törmänen and Iljina 2007). Variable amounts of plagioclase, hornblend, and quartz comprise these rocks, and U-Pb zircon gives a comagnetic age of 2.05 ± 5 Ga (Mutanen and Huhma 2001; Törmänen and Iljina 2007).

5.3. Seismic data acquisition and processing

In December 2007, four 2D reflection seismic profiles between 6 and 11 km long were acquired in the Kevitsa area as part of the High-Resolution Reflection Seismic for Ore Exploration (HIRE) project of the Geological Survey of Finland and its mining company partners (Figure 5-1; Koivisto *et al.* 2012; Malehmir *et al.* 2012a). The objectives of these seismic acquisition surveys were to delineate the overall extent of the Kevitsa ore-bearing zone, study the seismic response of the deposit, and to search for new ore deposits (Malehmir *et al.* 2014). The successful outcome of the 2D seismic profiles encouraged conducting a 3D seismic reflection survey in 2010 (Koivisto *et al.* 2012; Malehmir *et al.* 2014). The 3D seismic data acquisition survey provided valuable information about the subvertical structures near the ore deposit (Malehmir *et al.* 2014).

The 3D seismic survey at Kevitsa was conducted over a period of 2 months between February and April 2010 covering an area of ~9 km^2. The survey area was divided into nine orthogonal patches with 50% overlap (Malehmir *et al.* 2012a). Two recording

systems were utilised jointly to collect the data. HiSeis Pty Ltd operated a Seistronix system and Uppsala University operated a Sercel 408 system (Malehmir *et al.* 2012a). 1000 active channels recorded the data from about 3000 source points. Mechanical hammer (Vibsist) and explosives were utilised as the energy source (Malehmir *et al.* 2012a). The shot point spacing was 45 m, shot line spacing was 80 m, receiver spacing was 15 m, and receiver line spacing was 70 m. Figure 5-5 illustrates the 3D fold map achieved after 3300 shots. During the data acquisition survey, the near-surface conditions changed from frozen ground to thick layer of snow. Geophones were placed on the frozen ground or compacted snow to achieve excellent coupling. For the Vibsist mechanical hammer, each shot consisted three sweep stacks to increase the signal-to-noise ratio (Malehmir *et al.* 2012a). The sampling interval was 1 ms and 2 ms for the Sercel 408 system and Seistronix system respectively. The data acquired through Seistronix were resampled to 1 ms sampling interval and merged with the Sercel data (Malehmir *et al.* 2012a). The seismic data acquisition parameters are provided in Table 5-4.

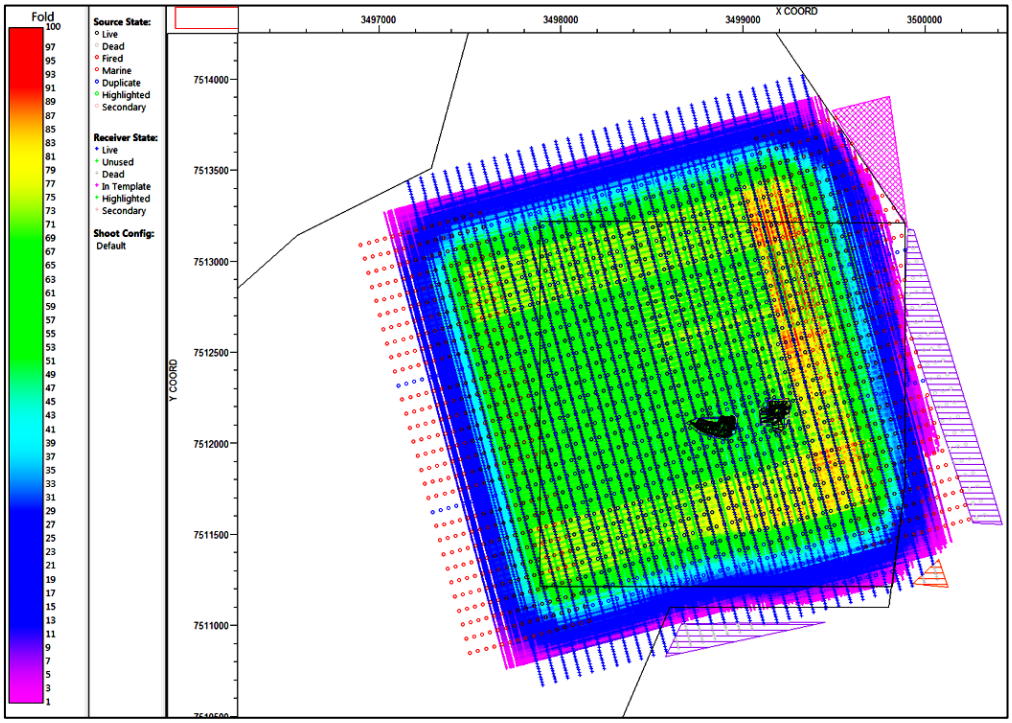

Figure 5-5: Actual CMP fold map achieved after 3300 shots. Higher fold (red) is due to extra source and receiver lines (Courtesy: HiSeis Pty Ltd). The areas in black were inaccessible during data acquisition.

HiSeis Pty Ltd, the main data acquisition contractor, also performed the data processing. The first attempt of the data processing was done through several steps in 2010. Firstly, Vibsist data were processed using shift and stack method. Repetitive hammer blows were rejected to avoid harmonics appearing in the stacked shot record. Poor base-plate signal from one of the two Vibsist vehicles required designature and amplitude balance before shift and stack could be accomplished. Decoded vibsist shot records and explosive data were then phase matched (Dzunic, 2014, personal communication). Noisy and low-quality shots were rejected during the decoding phase (Malehmir *et al.* 2012a). The data processing included the application of surface consistent static corrections, followed by dynamic corrections (Dzunic, 2014, personal communication). Accurate refraction statics were applied to eliminate variable time delays through the regolith. Figure 5-6 illustrates estimated regolith thickness in the survey area. This estimated thickness is typically greater than the actual thickness of the regolith; however, portrays the local variation of regolith topography (Ziramov *et al.* 2015).

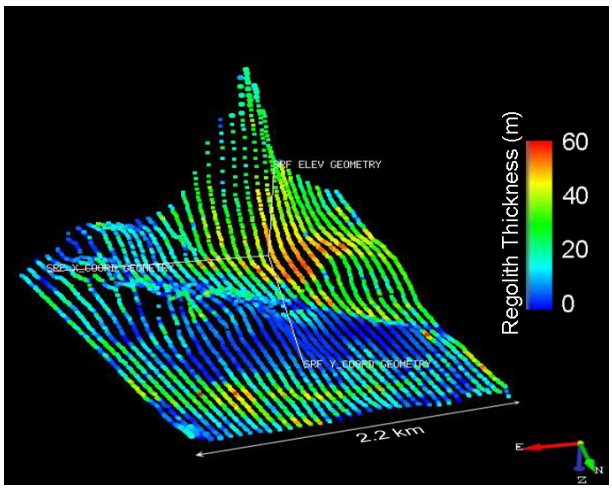

Figure 5-6: Estimated regolith thickness at the survey area (Ziramov et al. 2015)

In the 2010 processing, AGC was used for amplitude recovery and noise normalisation (Ziramov *et al.* 2015). The imaging phase included 3D DMO correction followed by poststack migration (Ziramov *et al.* 2015). After the DMO correction, the CDP gathers were used to obtain the velocity field used for migration. However, the migration result was not optimal due to the inaccurate velocity estimates because of the geological complexity of the hard rock environment (Ziramov *et al.* 2015). Since the conventional DMO correction followed by poststack migration was not able to handle the lateral

velocity variations, therefore, in 2014, prestack time-migration (PSTM) approach was taken to tackle the complex velocity field (Ziramov *et al.* 2015).

Table 5-4: Reflection seismic data acquisition parameters for Kevitsa 3D conducted in 2010 (Courtesy: HiSeis Pty Ltd; Malehmir et al. 2014).

Parameter	
Survey type	3D orthogonal
Source	VIBSIST and dynamite
Recording system	SERCEL408 and Seistronix
Dynamite (charge) size	0.5 kg
Dynamite (charge) depth	3 m
Total survey area	~ 9 km^2
No. of active channels	864
Maximum offsets	1700 m
Nominal fold	60
Source interval	45 m
Receiver interval	15 m
No. of shots	~ 3300
No. of shot lines	34
Shot line spacing	80 m
No. of receiver lines	35
Receiver line spacing	70 m
Geophone frequency	10 Hz
No. of active receiver lines per patch	9 lines × 96 active channels
Sampling rate	1 ms and 2 ms

In 2014, the 3D dataset was reprocessed with preserved relative amplitudes to improve imaging at shallow depths by refining the static solutions and velocity model used for the imaging (Ziramov *et al.* 2015). The basic processing steps followed in 2014 processing are shown in Figure 5-7. The amplitude consistent processing included trace editing, spherical divergence correction, the application of surface consistent amplitude recovery and deconvolution (Ziramov *et al.* 2015). 3D Kirchhoff prestack time-migration (PSTM) was used to migrate the data volume. The static correction was further refined due to lower fold coverage at shallow depths. The objective of PSTM

was to derive a velocity model appropriate for the geological setting and the migration algorithm in use. The data processing was finalised by using sonic logs to convert the seismic volume from two-way travel time to depth. The result of the final reprocessed data is compared with the 2010 processing in Figure 5-8.

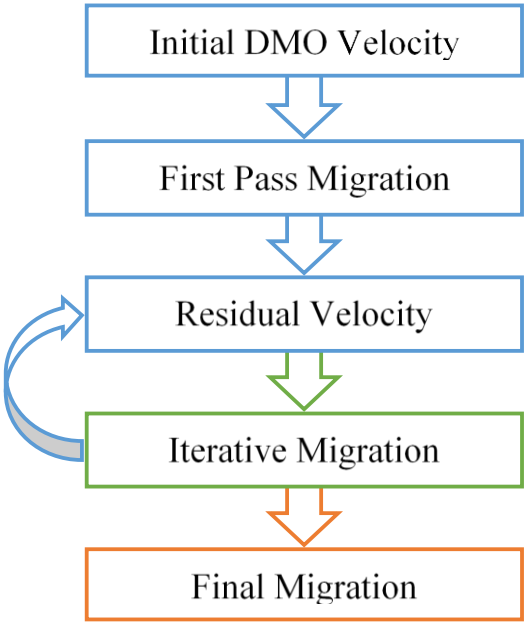

Figure 5-7: Basic steps used in the 3D PSTM in 2014 (Ziramov et al. 2015).

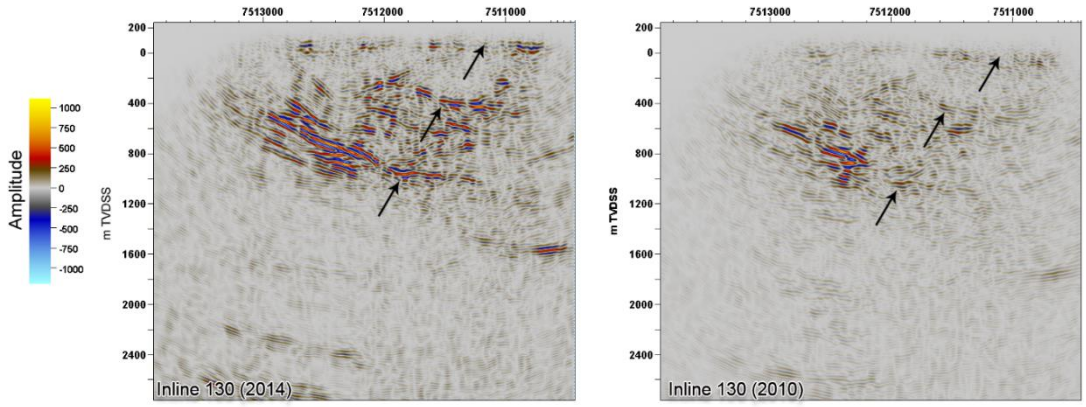

Figure 5-8: Amplitude display of the Kevitsa seismic data along inline 130 to compare between 2014 and 2010 processing methods. Black arrows point to the areas with improved signal to noise ratio.

5.4. Seismic volumetric interpretation

The Kevitsa 3D seismic cube covers a volume of 3368×3907×1194 m^3. The signal amplitude of the data ranges from -1021 to 1029. The final processing yielded a prestack time-migrated volume with 10 m×10 m grid. The vertical sampling interval was 6 m. The survey details of the Kevitsa 3D seismic dataset is provided in Table 5-5.

Table 5-5: Survey details of the Kevitsa 3D seismic volume

Description	Value
Original CRS:	KKJ (Finnish National Coordinate System)
Origin X:	3497714
Origin Y:	7510670
End first inline X:	3496850
End first inline Y:	7513897
End first crossline X:	3500206
End first crossline Y:	7511337
Number of inlines:	259
Number of crosslines:	335
Inline length:	3341
Inline interval:	10
Crossline length:	2580
Crossline interval:	10
Inline rotation from the north:	-15
Number of samples per trace:	199
Number of cells total:	17266235
Inline interval:	10
Crossline interval:	10
Sample interval:	6

5.4.1. Seismic horizon extraction

Seismic horizons were interpreted from the Kevitsa seismic volume by employing a few different seismic attributes. Both manual and automatic 2D and 3D seeded tracking were utilised during the horizon interpretation. A continuity attribute was calculated from the Kevitsa seismic data to enhance continuity of the signals. Continuity attribute smooths the seismic data to increase the continuity of the seismic reflectors.

The major stratigraphic boundaries between the metasediments and metavolcanics, olivine pyroxenite and gabbro dominated areas were interpreted using 50 to 75% seed confidence. Densely populated seed points were used to maintain a high surface stability index. A few boreholes (KV28, KV78, KV80 and KV171) were used to identify the corresponding reflections at the lithological boundaries. The boundary between the overlying Kevitsa intrusive complex (olivine pyroxenite and mafic peridotite) and the underlying metasedimentary/metavolcanics have been characterised from the KV28 borehole and the borehole tops were used as reference points to extract the base of Kevitsa.

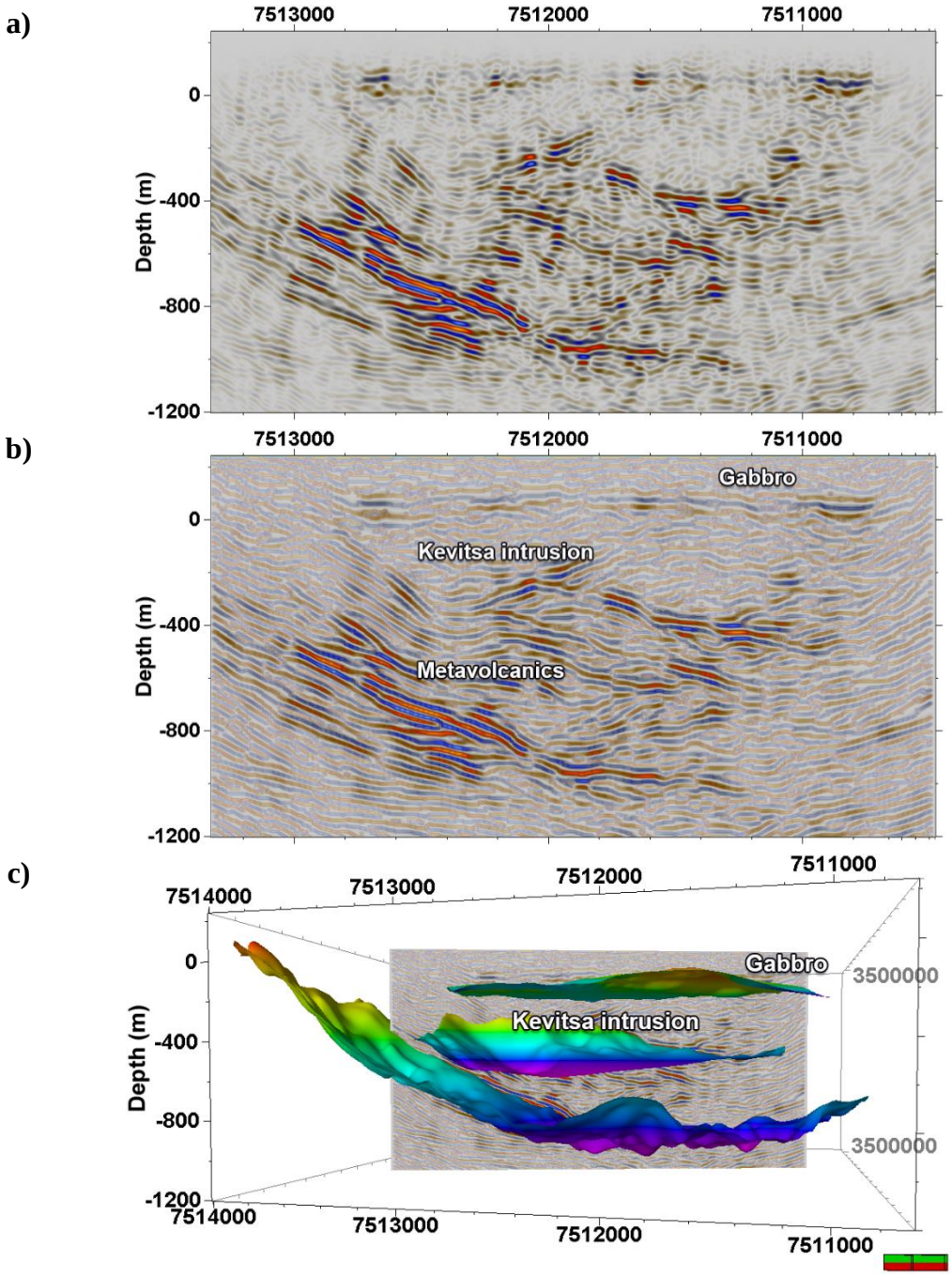

Figure 5-9: (a) Amplitude display of the Kevitsa seismic data, (b) Continuity attribute projected over the amplitude data to enhance lateral continuity of the reflection events, and (c) horizons picked from the Kevitsa seismic data.

5.4.2. Seismic attribute analysis

Seismic attribute analysis of the Kevitsa seismic volume utilised a prestack time-migrated 3D seismic cube in depth-domain (processed in 2014). Seismic volume attributes were computed by using the attribute libraries in Schlumberger Petrel, Paradigm GOCAD and OpendTect.

The upper part of the Kevitsa seismic cube is devoid of any reflections. The shallowest reflections were observed at 156 m TVDSS (~84 m below the surface). Reflections start to appear after 120 m TVDSS (~120 m below the surface). Lack of reflections at the shallower part of the cube was explained by Koivisto *et al.* (2015). According to Koivisto *et al.* (2015), most of the near-offset traces have an offset of 50 m to 100 m because of the shot line spacing of 80 m and receiver line spacing of 70 m. As a result, the reflectors within the shallower part (~top 100 m) did not produce any image. Moreover, the near-surface structures were undersampled due to lower fold number at the shallower part of the data (Koivisto *et al.* 2015). The padded portion in the northern part of the cube was removed and a cropped volume with 259 inlines × 277 x-lines was used in the interpretation (Figure 5-10). The depth range of the cropped cube is 240 m to -1764 m TVDSS. Figure 5-11 shows the cropped seismic cube employed in seismic attribute analysis.

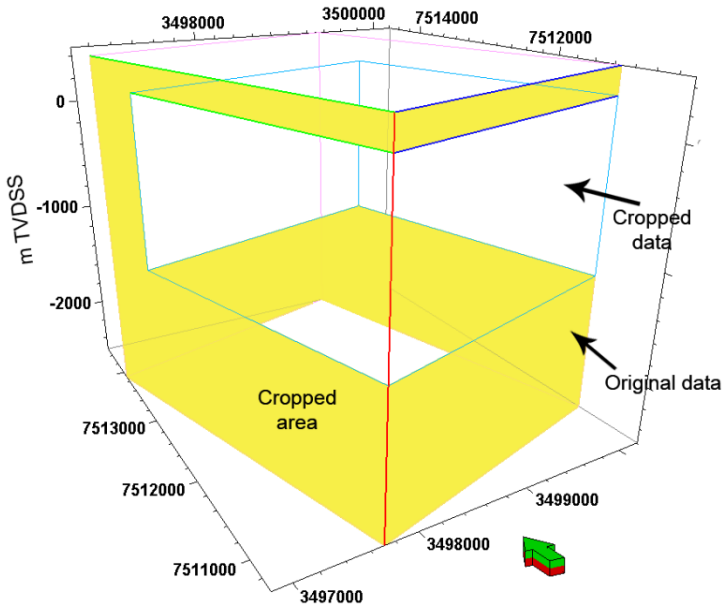

Figure 5-10: The PSTM cube was cropped to remove the padded areas with low signal-to-noise ratio.

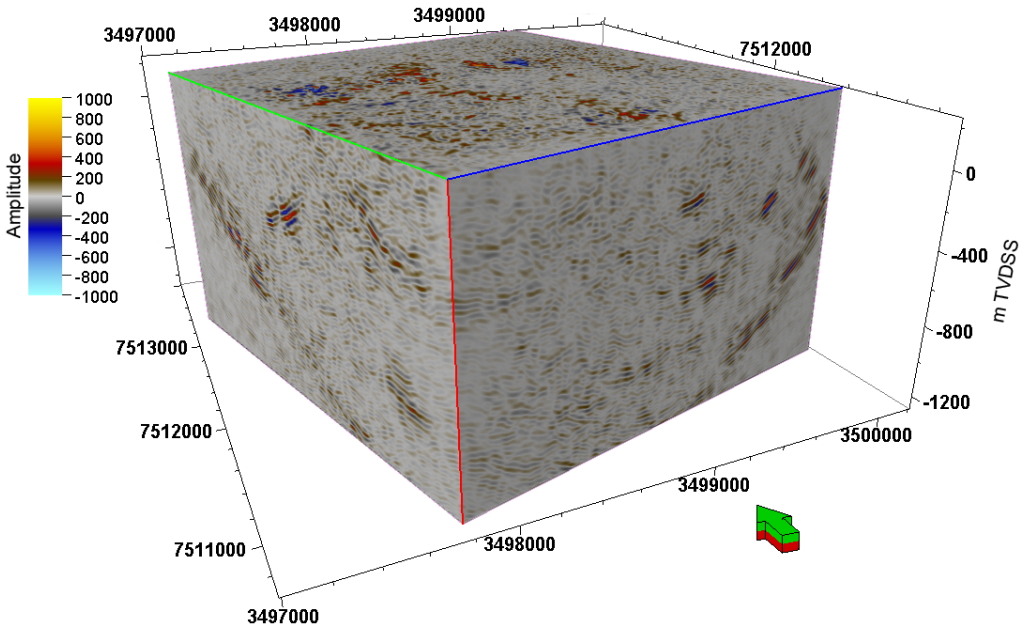

Figure 5-11: The cropped seismic cube employed in attribute analysis.

Seismic attribute analysis employed volume attributes and workflows such as dip illumination, local structural dip, local structural azimuth, 3D edge enhancements, RMS amplitude, variance, and ant-tracking workflow. The main objective of this analysis was to delineate subvertical faults from the seismic data. The seismic horizons extracted from the seismic dataset were utilised during the physical property modelling.

3D edge enhancement performs edge enhancement within a seismic volume. This attribute has proven abilities to detect edges for any surface, faults and discontinuities. The filter is applied in planes in a 3D environment, and then the plane is implemented in a rotation to filter in all directions and angles as shown in Figure 5-12 (Schlumberger 2014). The algorithm compares and sums the values of the surrounding pixels along a plane on the edge-detected cube and displays the mean value (Schlumberger 2014). This process is repeated for every pixel in all directions and angles for the planes (Schlumberger 2014). As a result, larger features are enhanced, while smaller features and noise are smoothed away (Schlumberger 2014).

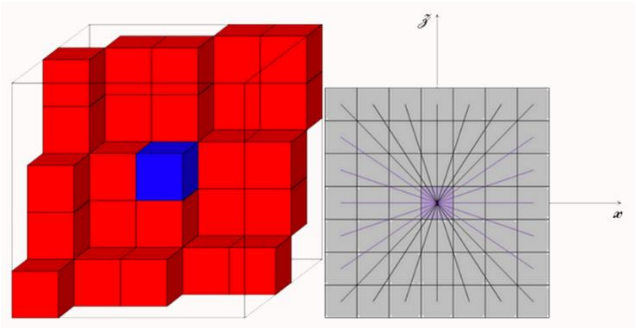

Figure 5-12: The working principal of 3D edge enhancement for a single pixel (Schlumberger 2014).

3D edge enhancement attribute was calculated from the Kevitsa seismic data. 3D edge enhancement is a volume attribute filter that performs edge enhancement within seismic data. The filter is applied in planes in 3D environment. The plane is then applied in rotations in all directions and angles to filter the seismic volume and the output is an edge-enhanced volume. Figure 5-13 shows the edge enhancement attribute on a vertical section along ENE-WSW direction. The attribute was able to enhance the major stratigraphic units from the Kevitsa seismic data.

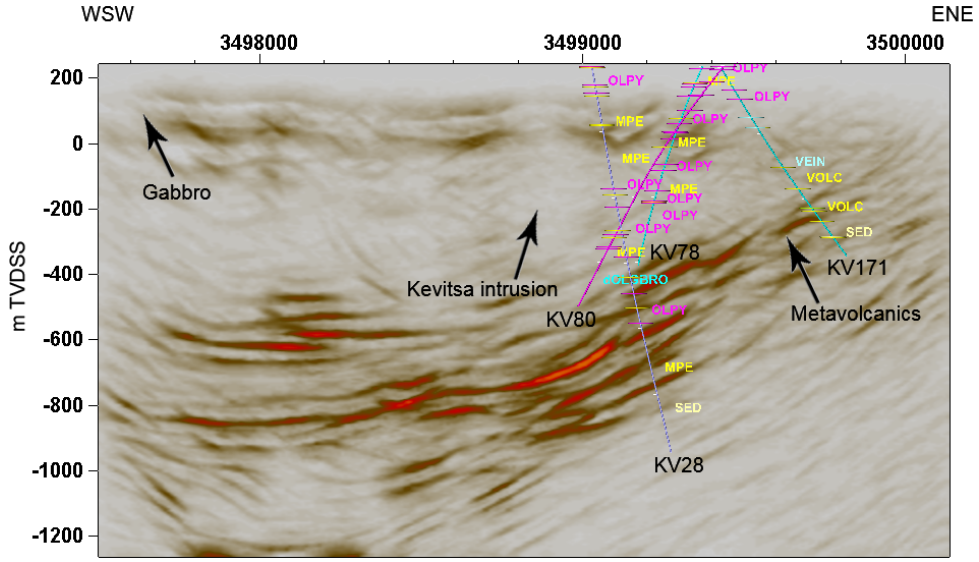

Figure 5-13: A 3D edged enhancement attribute on a vertical section along ENE-WSW direction shows the major stratigraphic boundaries in Kevitsa.

Dip illumination attribute is a good structural geology indicator (Schlumberger 2014). This attribute estimates dip to reveal various structural geology including discontinuities, and noisy areas (Schlumberger 2014). Dip illumination was applied on the Kevitsa seismic data and result is demonstrated in Figure 5-14. The attribute was

able to reveal the major stratigraphy of the area. Previous studies indicated that the layers in the metasediment and metavolcanics, olivine pyroxenite and gabbro dominated areas are dipping at a different angle and different directions (Koivisto *et al.* 2012). Scattered patterns also indicate the noisy nature of the data. The result shows an excellent correlation with the bedrock geology map provided in Figure 5-1.

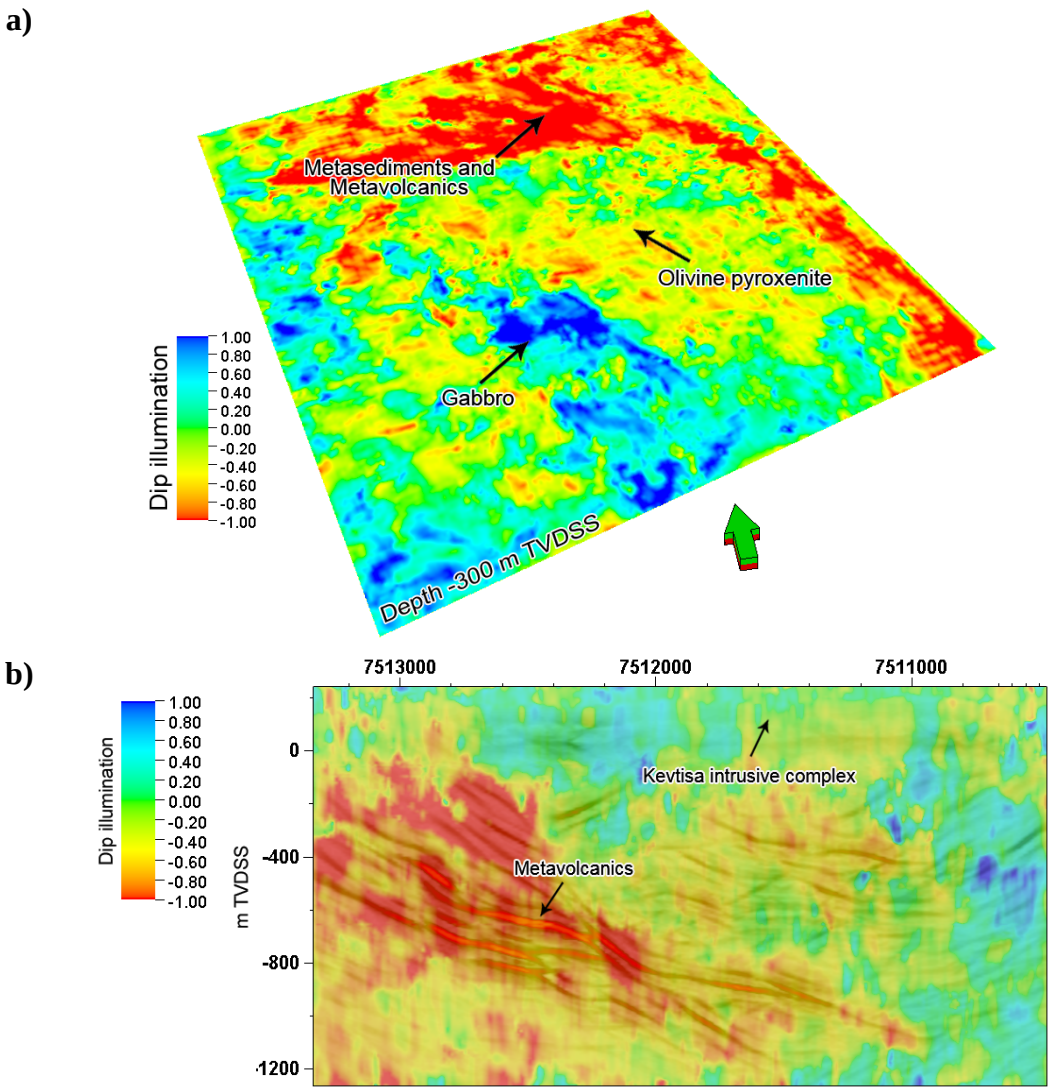

Figure 5-14: (a) Dip illumination attribute displayed on a horizontal slice reveals major stratigraphy of the area. The result displays an excellent agreement with the bedrock geology of the area shown in Figure 5-1. (b) Dip illumination projected over 3D edge enhancement along inline 151 illustrates the major stratigraphic boundaries.

Local structural dip attribute estimates local dip from the seismic data (Schlumberger 2014). Local structural dip has been computed for principal components from the

Kevitsa seismic data. The principal component of the dip attribute is estimated from principal component analysis of gradient covariant matrix (Randen *et al.* 2000). It is a poststack attribute that computes a best-fitting plane in 3D for each trace with its neighbouring traces and the output is the dip magnitude of that best-fitting plane (Chopra and Marfurt 2007). Figure 5-15 demonstrates the principle component of the local structural dip attribute on two depth slices at -200 m TVDSS and -300 m TVDSS. The dip magnitude ranges from 0° to 90°. The areas dominated by metasediments and metavolcanics dips at an angle of 50° to 60°. However, sharp changes in dip magnitude were observed in the northeastern corner of the survey area (Figure 5-15). The olivine pyroxenite and gabbro dominated areas dip at an average angle of 30° to 40°. Sharp variation in dip magnitude was also observed in these areas.

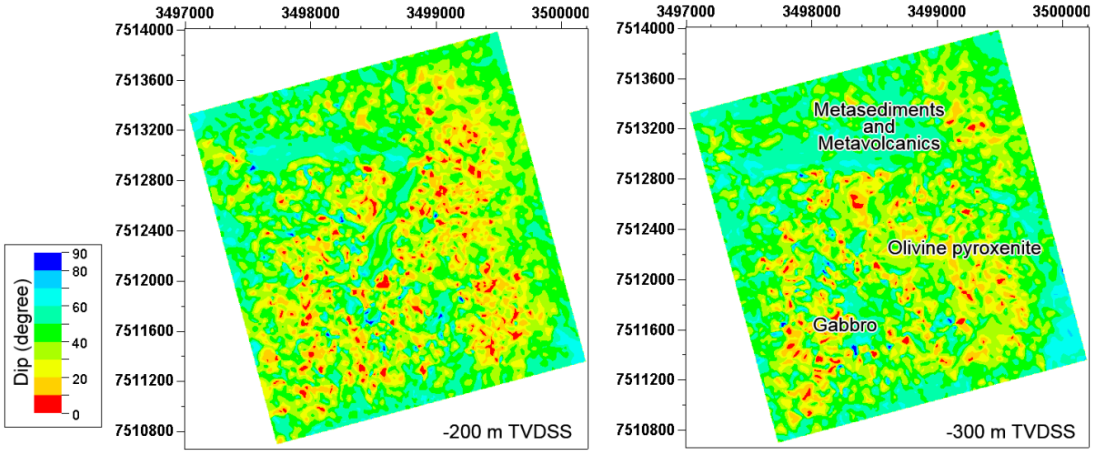

Figure 5-15: The principal component of the local structural dip attribute computed from the Kevitsa seismic data. Horizontal slices at (a) 200 m below the datum, and (b) 300 m below the datum demonstrate the variation in dip magnitude at different depths.

Local structural azimuth calculates a best-fitting plane in 3D space for each trace with its neighbouring traces and the output is the direction of the maximum slope of that best-fitting plane (Chopra and Marfurt 2007). Figure 5-16 depicts the principal component of the local structural azimuth calculated from the Kevitsa seismic volume. The result shows significant variations in azimuth in the gabbro, olivine pyroxenite and metasediments and metavolcanics part of the area.

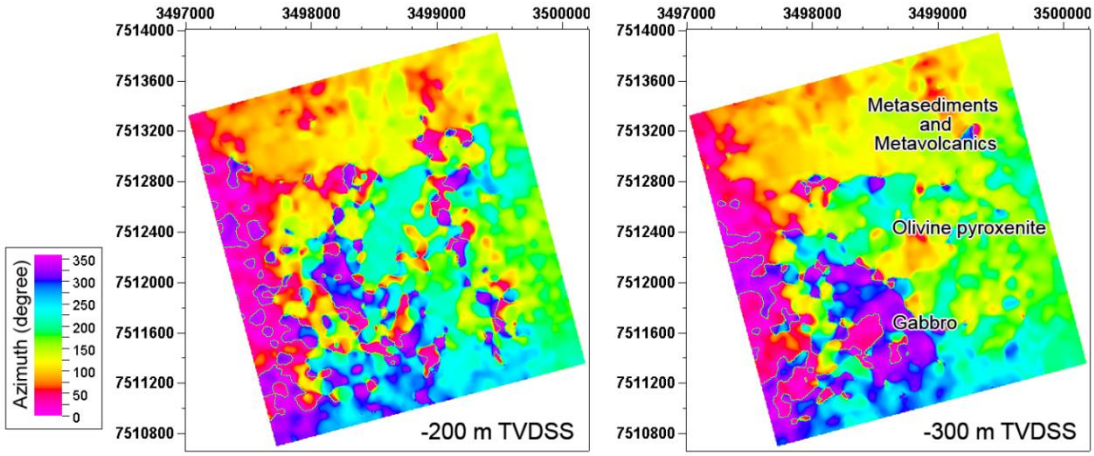

Figure 5-16: The principal component of the local structural azimuth volume calculated from the Kevitsa seismic data. Horizontal slices at (a) 200 m below the datum, and (b) 300 m below the datum demonstrate the changes in azimuth at different depths.

RMS amplitude computes Root Mean Squares on instantaneous trace samples over a specified window (Schlumberger 2014). The higher amplitude spots on an RMS amplitude map indicate geological features. RMS amplitude was computed for -200 m TVDSS and -300 m TVDSS (Figure 5-17). RMS amplitude did not provide acceptable output of the geological features at the shallower parts of the dataset due to low signal-to-noise ratio. The structures were more noticeable toward the deeper part of the cube.

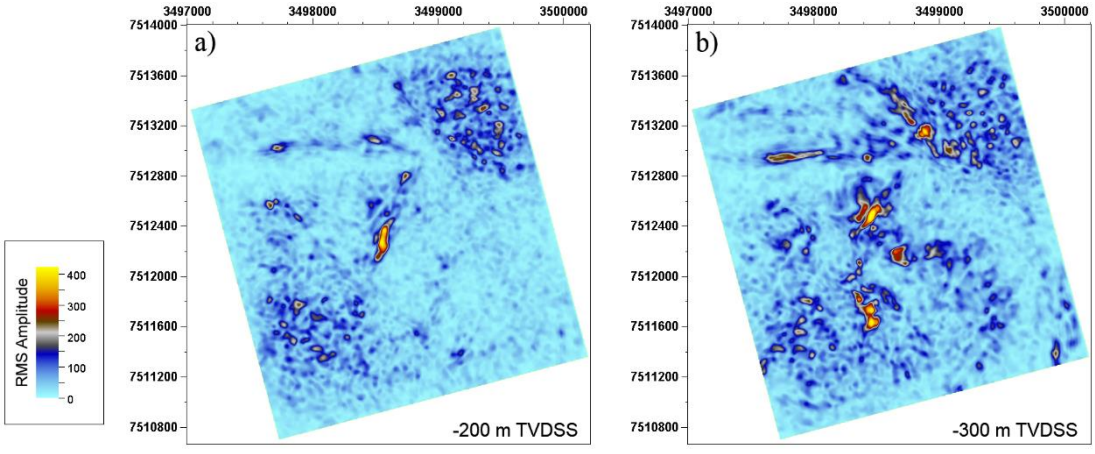

Figure 5-17: RMS amplitude map at (a) 200 m below the datum and (b) 300 m below the datum computed from the Kevitsa seismic volume.

Variance (edge method) estimates local variance in the signal (Schlumberger 2014). It is the state-of-the-art attribute for edge detection. Variance attribute was computed

using an operator size of 1.5 for inline and crossline range. A standard smoothing operator of 20 was used. The smoothing operator is a triangular weighting filter to perform smoothing to enhance continuity of the seismic signals. The window size 20 was chosen to filter the random noise from the data without affecting the signal. Dip correction was applied to add directional parameters to the attribute. The dip-guided algorithm computes variance along a dipping plane with the corresponding measure of the dip estimate confidence. The default value (0.75) of plane confidence threshold was selected. Areas, where the computed confidence is above the selected confidence threshold, used dip-guiding. Standard horizontal variance algorithm is used in areas where the confidence is below the threshold limit (Schlumberger 2014). Figure 5-18 demonstrates the computed variance volume, an inline and a crossline section. The areas with high variance values (red to yellow) indicate potential fault events.

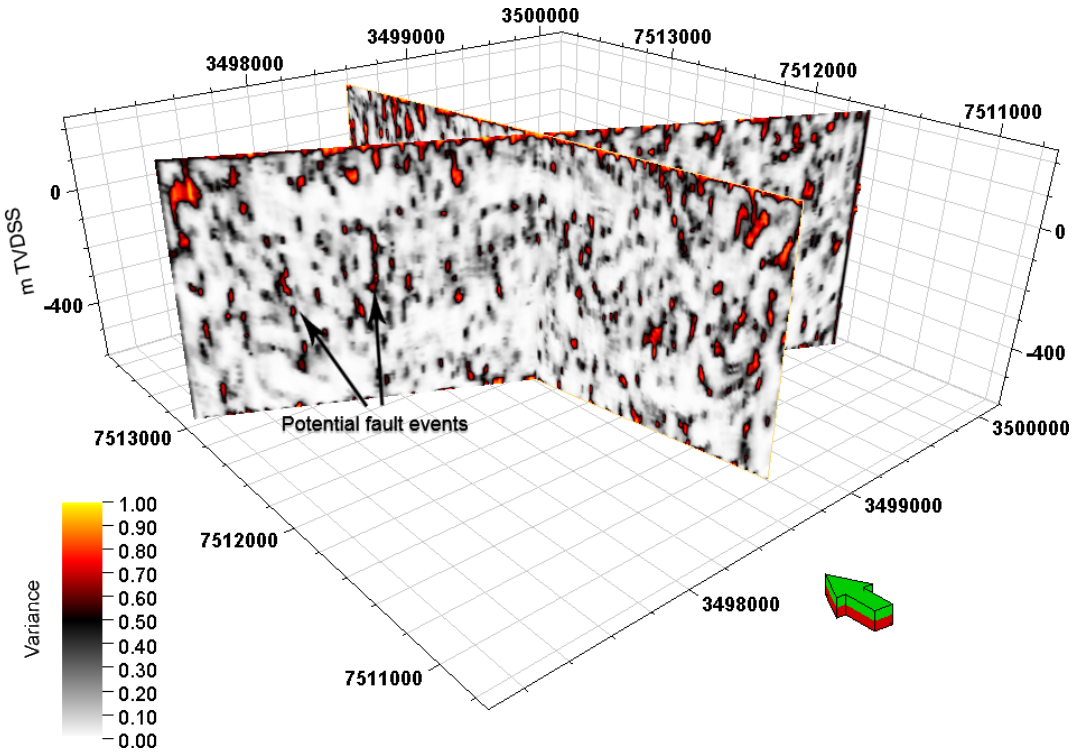

Figure 5-18: Variance attribute (edge method) was computed from the Kevitsa seismic data using a smoothing operator of 20 to reduce the noise in vertical direction. The default plane confidence threshold of 0.75 was used for dip correction.

5.4.3. Fault detection

Fault detection was performed on an edge-detected volume using Schlumberger Petrel's Ant-tracking workflow. The flowchart demonstrating the steps involved in ant-tracking is provided in the previous chapter in Figure 4-22.

In the first step of seismic conditioning, the seismic volume was prepared for edge detection by applying median filter and structural smoothing. The next step involves utilising edge detection attributes, e.g., variance. Edge enhancement was performed on an edge-detected volume and the enhanced cube was used for ant-tracking.

The ant-tracked volume significantly improves the fault attributes by suppressing noise and remains for non-faulting events. Figure 5-19 exhibits an ant-tracked volume, where the blue features represent faults events. Figure 5-20 demonstrates a 3D representation of the fault events detected from the Kevitsa seismic cube for the top 600 m. However, due to the absence of reflections at the top 120 m, ant-tracking did not perform optimally for the upper part of the data (Figure 5-21).

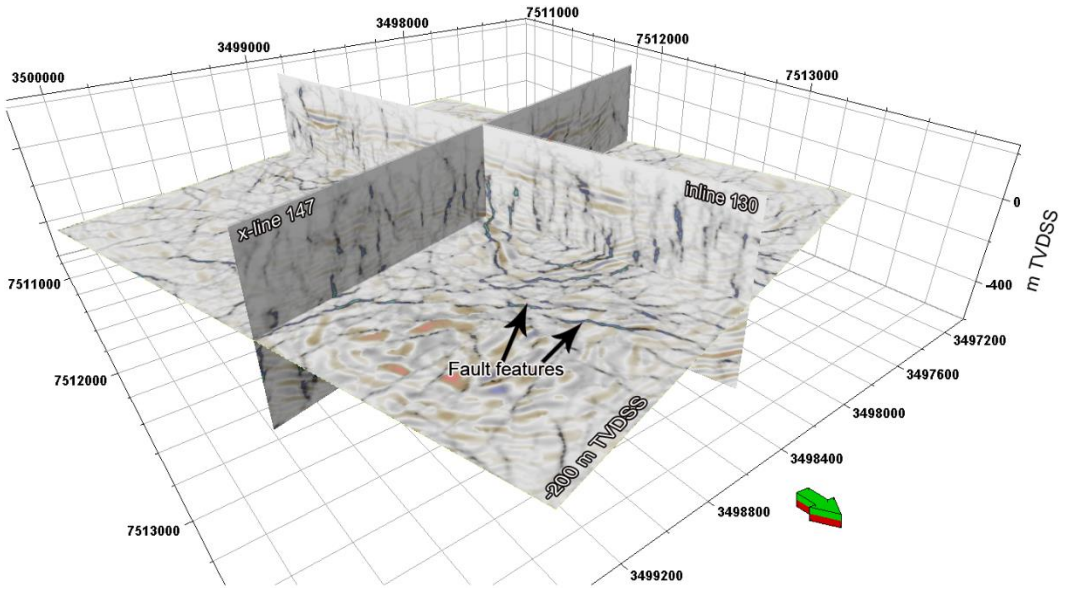

Figure 5-19: Fault events detected from the Kevitsa seismic volume using Schlumberger Petrel's Ant-tracking workflow (Hossain et al. 2015a).

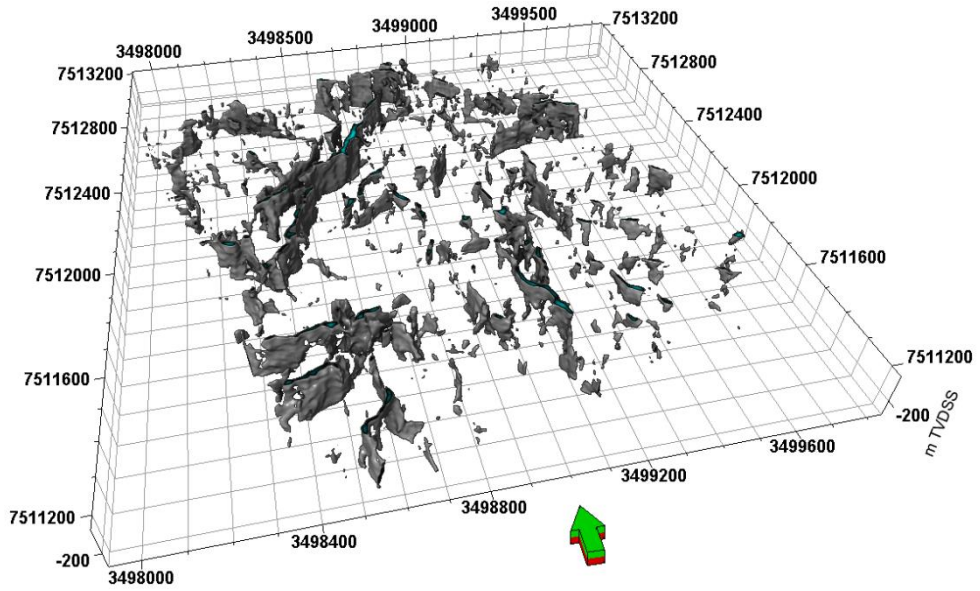

Figure 5-20: A 3D representation of the fault events extracted from the ant-tracked volume.

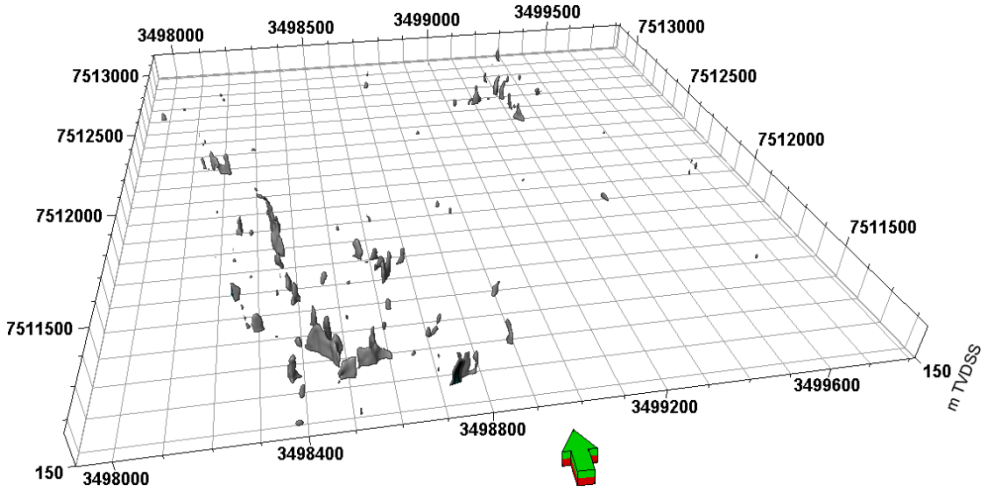

Figure 5-21: Ant-tracking exhibited poor performance at the upper part of the data due to low signal to noise ratio.

5.4.4. Physical property modelling

The horizons extracted from the Kevitsa seismic volume were gridded as a surface and utilised to build a property model. Geophysical properties from the borehole logs, e.g., P-wave velocity and density were upscaled to the model. The modelling also employed Cu (wt.%) and Ni (wt.%) from boreholes. Property modelling was performed by Schlumberger Petrel's Structural Modelling module.

A structural grid was constructed using Schlumberger Petrel's corner point gridding method. The boundary definitions from the cropped Kevitsa seismic cube were utilised as the model boundary. Figure 5-22 portrays a block model of the Kevitsa structural grid. The details for the Kevitsa structural grid are provided in Table 5-6.

The upscaled values were used in the property modelling to simulate continuous data throughout the model grid. Sequential Gaussian Simulation (stochastic) algorithm was chosen as the modelling algorithm for data interpolation. Sequential Gaussian Simulation (SGS) produces a realisation of the property, which honours borehole data, input distributions, variogram and trends to create local variations (Schlumberger 2014). Since, it is a stochastic simulation; the result depends on a random seed number. Gaussian variogram was computed for each property to be used in the simulation.

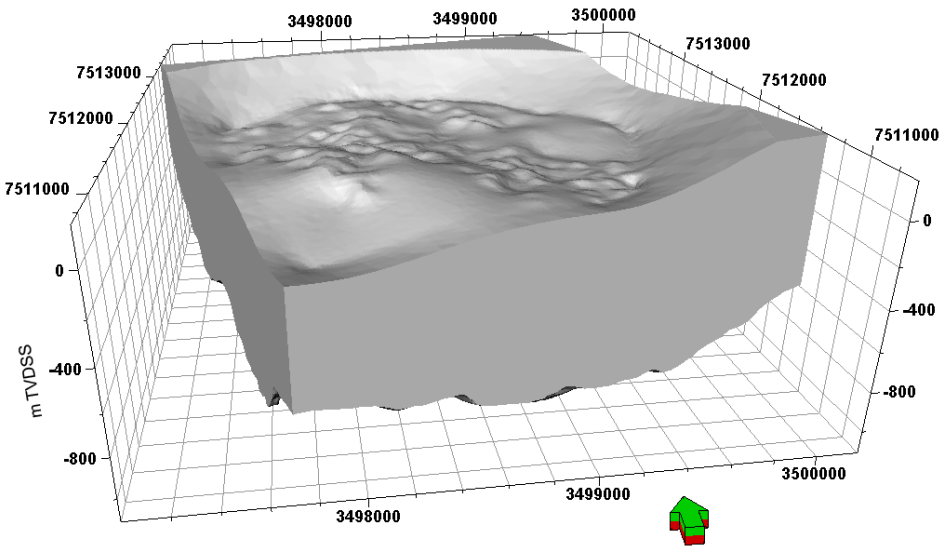

Figure 5-22: 3D block model of the Kevitsa structural grid employed in the physical property modelling.

Table 5-6: Details for the Kevitsa structural grid

Axis	Min	Max
X	3497002.65	3500196.48
Y	7510676.22	7513997.38
Depth range (m)	-1110.93	172.2

Description	Value
Grid cells (I × J × K)	257 x 275 x 100
Grid nodes	258 x 276 x 101
Total number of grid cells	7067500
Total number of grid nodes	7192008
Number of geological horizons	10464000
Number of geological layers	101
Total number of 2D cells	70675
Total number of 2D nodes	71208
Total number of defined 2D nodes	71208
Average X increment	10
Average Y increment	10
Rotation angle	14.99

5.4.4.1. P-wave velocity

P-wave velocity from 13 borehole logs was upscaled to the grid resolution (Figure 5-23). A Gaussian variogram was computed from the boreholes and used during property modelling. SGS algorithm was used to interpolate the P-velocity data throughout the grid. Output data range of the model was set to 4827 m/s to 8151 m/s with a mean velocity of 6893 m/s and standard deviation of 555.173.

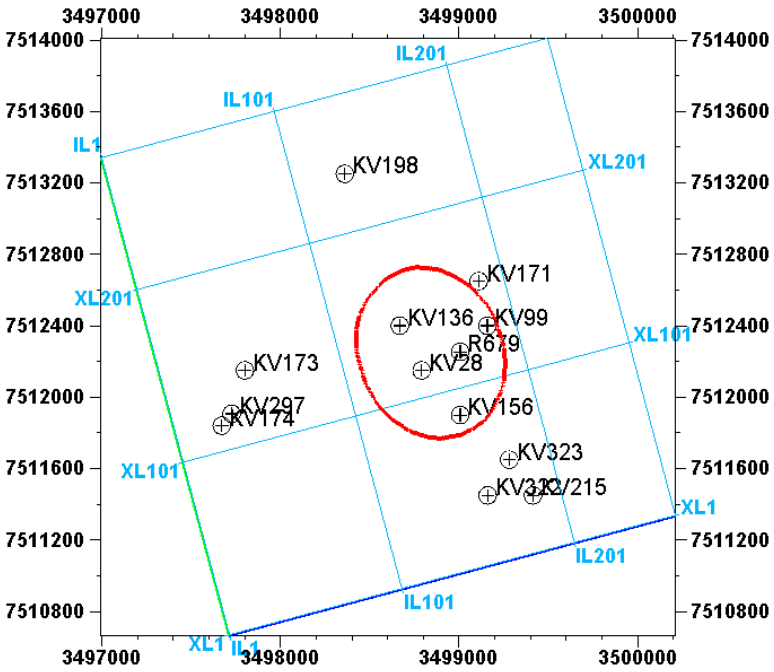

Figure 5-23: 13 boreholes with Vp (m/s) were upscaled to the grid for property modelling. Red ellipse indicates the boundary of the Kevitsa pit.

Figure 5-24 exhibits the P-wave velocity model constructed from borehole logs after 25 simulations. Two vertical cross-sections along NNW-SSE (a-a′) and SSE-NNW (b-b′) and a horizontal section were extracted from the model to examine the P-velocity distribution within the Kevitsa pit area (Figure 5-25). The cross-sections are presented in Figure 5-26.

The figures denote that the metasediments and metavolcanics in the north and eastern part of the survey area are characterised by lower P-wave velocity (5500 m/s to 6500 m/s). The velocity is relatively higher in the areas where olivine pyroxenite (6400 m/s to 7400 m/s) and gabbro (> 6800 m/s) are the dominant rock types.

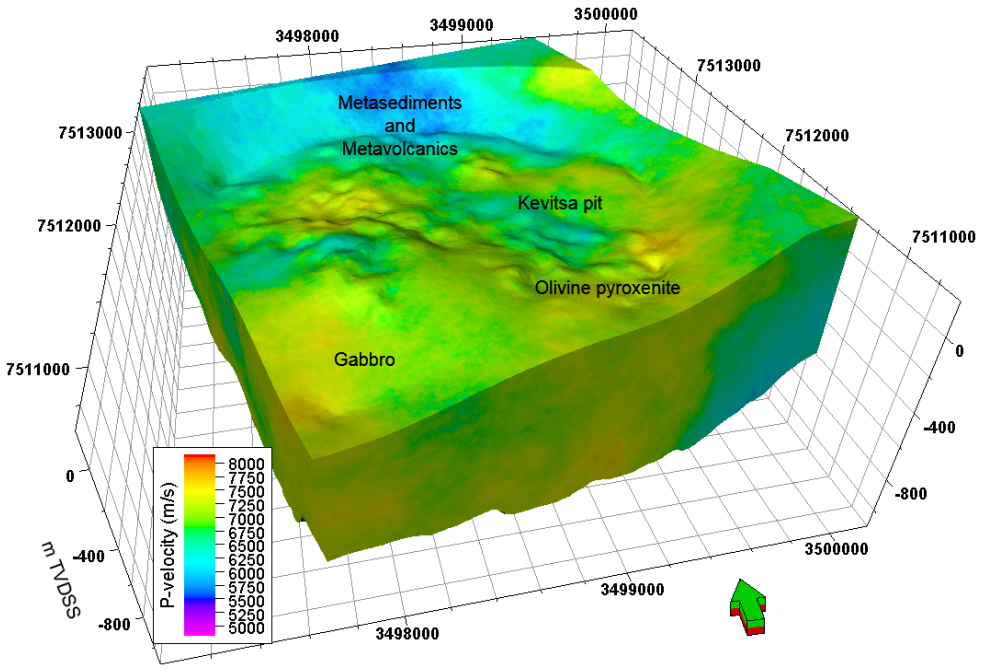

Figure 5-24: P-wave velocity (m/s) model from 13 borehole logs after 25 simulations. Continuous data were generated using Sequential Gaussian Simulation (stochastic) and a Gaussian variogram calculated from the boreholes.

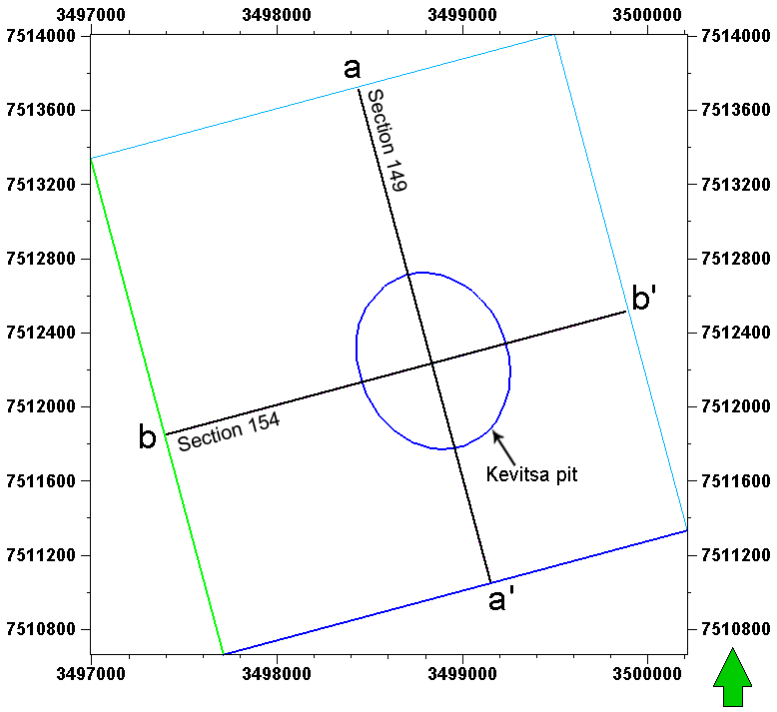

Figure 5-25: Location of the P-velocity cross-sections along NNW-SSE (a-a') and SSW-NNE (b-b') directions. Blue ellipse marks the boundary of the Kevitsa pit.

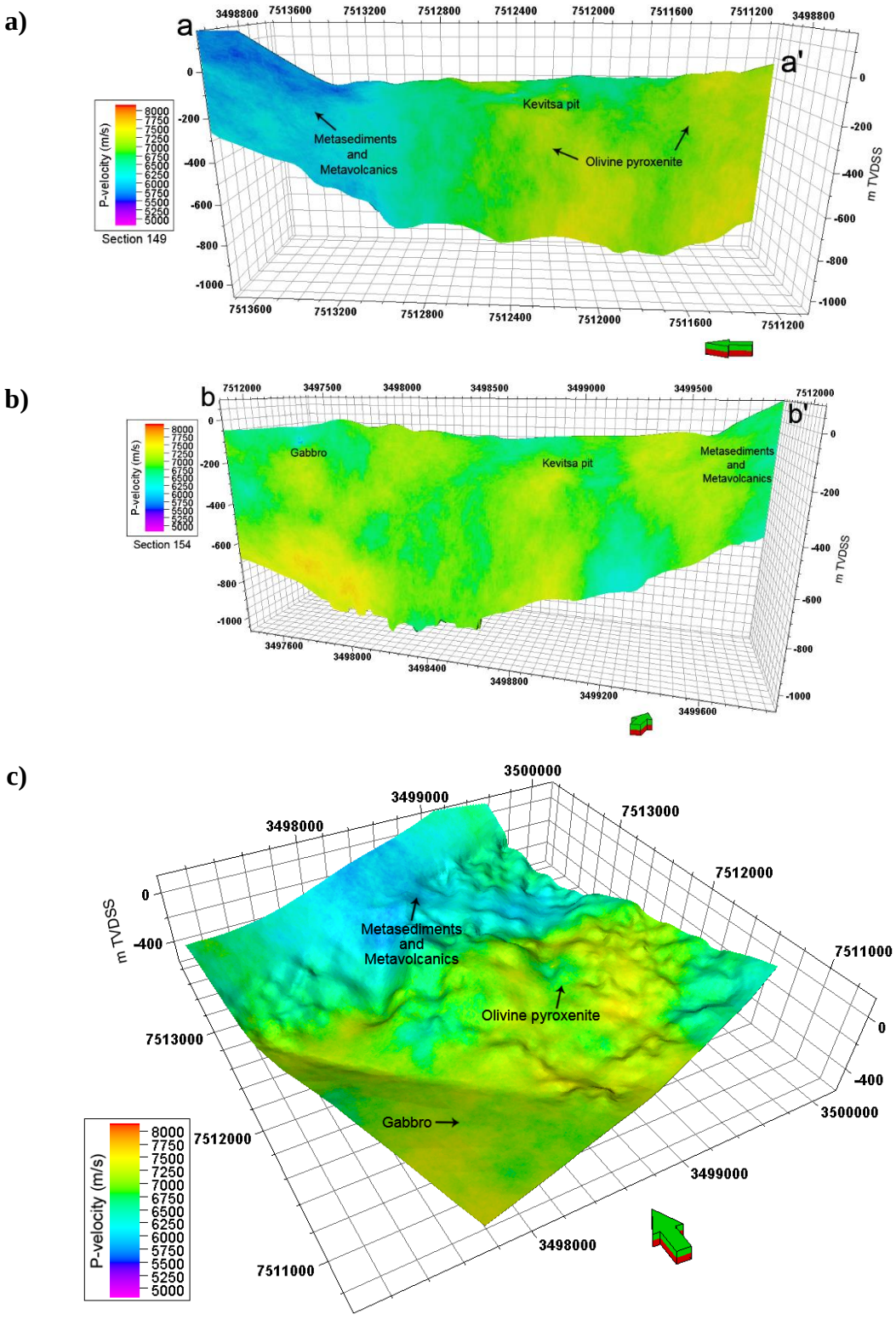

Figure 5-26: Cross-section of the upscaled P-velocity model (a) along NNW-SSE (a-a') direction, (b) along SSW-NNE (b-b') direction, and (c) a horizontal slice show P-wave velocity (m/s) distribution in Kevitsa. The areas where metasediments and metavolcanic rocks are dominant, demonstrate lower P-velocity. Gabbro-rich areas shows higher P-velocity distribution.

5.4.4.2. Density

A density model was constructed using density logs from 74 boreholes using the similar procedure as P-velocity modelling (Figure 5-27). A Gaussian variogram was calculated utilising the boreholes and SGS (stochastic) algorithm was chosen to simulate continuous data.

Figure 5-28 shows the density model of the Kevitsa area. The northern and northeastern part of the model where metasediments and metavolcanic rocks are dominant, exhibits density between 2800 kg/m^3 and 3000 kg/m^3. The central and southcentral part of the model where olivine pyroxenite rocks are dominant, shows highest density distribution in the area (3200 -3400 kg/m^3). Gabbro-rich areas exhibit a density range between 3000 kg/m^3 and 3200 kg/m^3.

Two vertical and a horizontal cross-section was extracted from the model at the same location as Figure 5-25. The cross-sections of the model in NNW-SSE (a-a′), SSW-NNE (b-b′) and horizontal directions are displayed in Figure 5-29 . The horizontal cross-section exhibits that the rocks with the highest density are located within olivine pyroxenite-rich areas in the Kevitsa pit area.

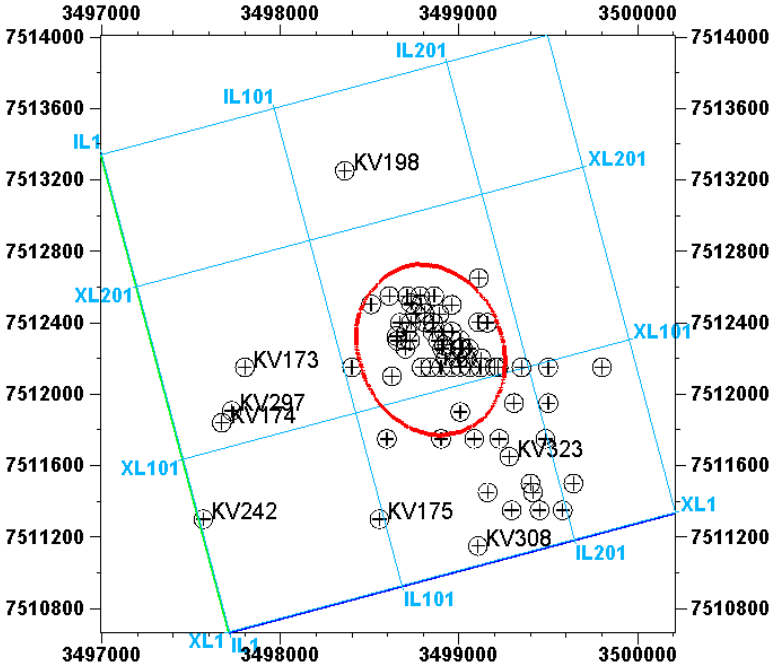

Figure 5-27: 74 boreholes with density (kg/m^3) were upscaled to the grid for property modelling. Red ellipse marks the boundary of the Kevitsa pit.

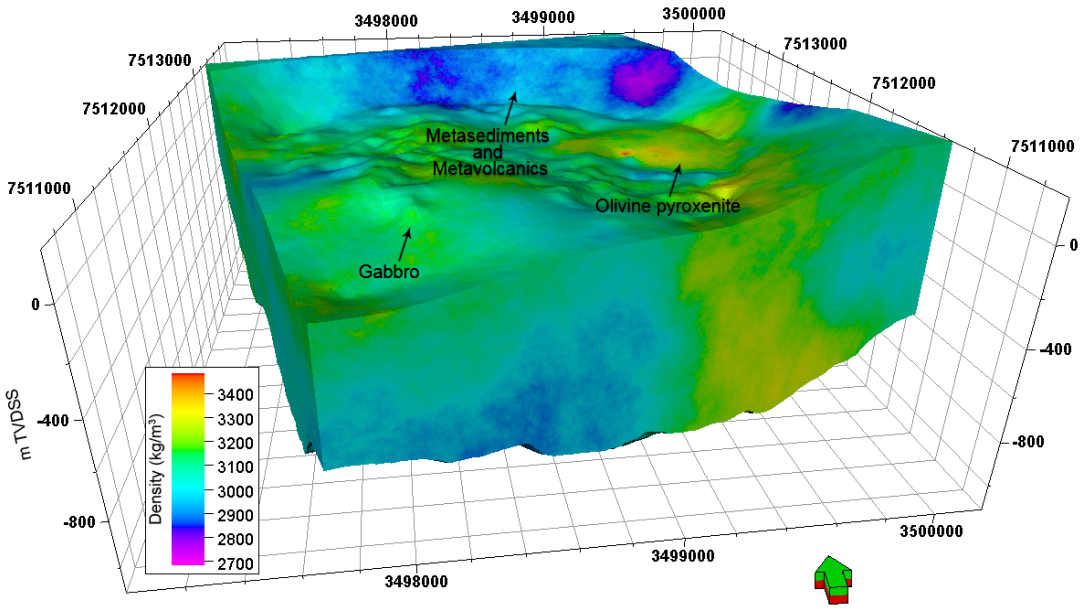

Figure 5-28: Density (kg/m3) model after 25 simulations from 74 borehole logs upscaled to the grid. Continuous data were generated using Sequential Gaussian Simulation (stochastic) algorithm and a Gaussian variogram calculated from boreholes.

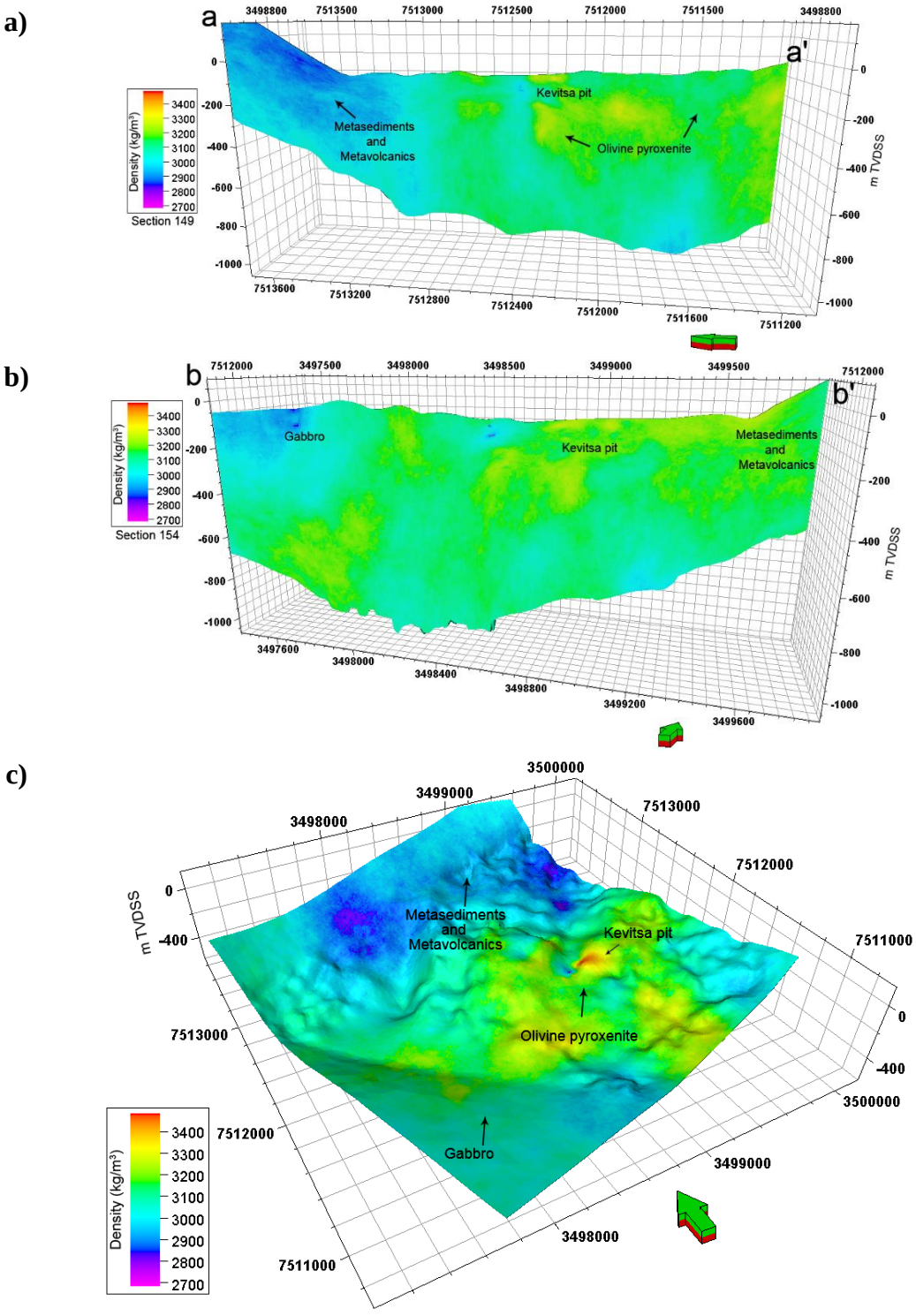

Figure 5-29: Cross-section of the upscaled density model (a) along NNW-SSE (a-a') direction), (b) along SSW-NNE (b-b') direction, and (c) a horizontal slice show density (kg/m^3) distribution in Kevitsa. The areas where metasediments and metavolcanic rocks are dominant, demonstrate lower density values. Olivine pyroxenite-rich areas within Kevitsa pit show highest density distribution in the area.

5.4.4.3. Copper and Nickel

242 boreholes containing Cu (wt.%) and Ni (wt.%) logs were also utilised in the modelling. A Gaussian variogram was calculated from the boreholes and used during property modelling. SGS (stochastic) algorithm was chosen to generate continuous data. Figure 5-30 shows the location of the 242 boreholes upscaled to the grid resolution for modelling.

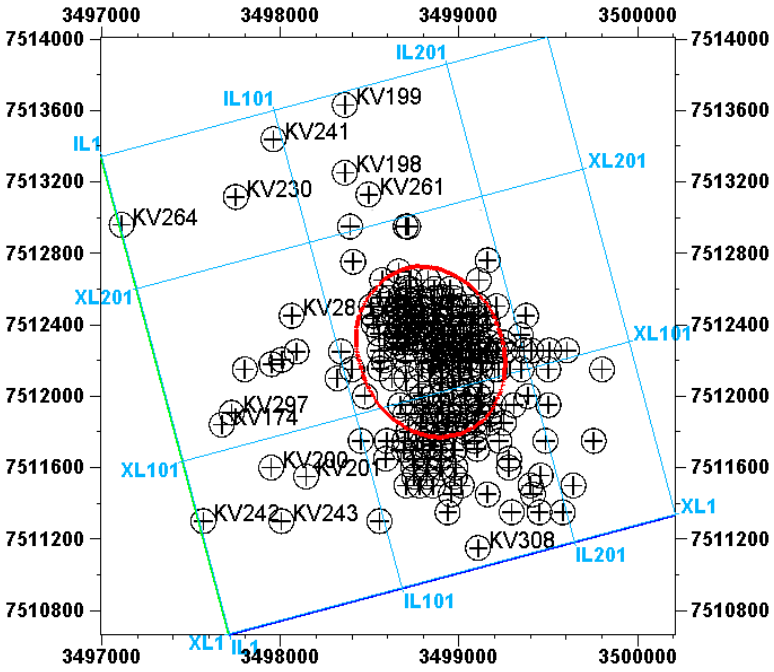

Figure 5-30: 242 boreholes with Cu (wt.%) and Ni (wt.%) logs were upscaled to the grid for property modelling. Red ellipse marks the boundary of the Kevitsa pit.

Figure 5-31 shows the Cu (wt.%) model of the Kevitsa area. Two vertical and a horizontal cross-section were extracted at the same location as Figure 5-25.

Figure 5-32 displays the location of the cross-sections from the Cu and Ni model in NNW-SSE (a-a′), SSW-NNE (b-b′) and horizontal directions. The cross-sections displayed in Figure 5-32 demonstrate that Cu–grade (0.41 wt.%) concentration is mostly located within the Kevitsa pit area.

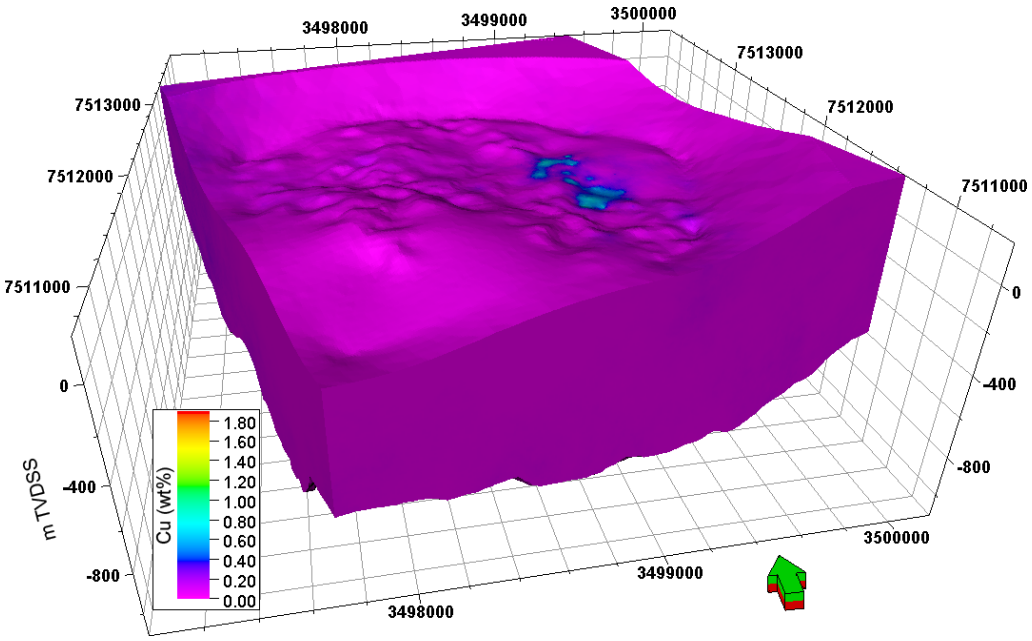

Figure 5-31: Cu (wt.%) model of the Kevitsa area created from 242 borehole logs.

Figure 5-33 (a and b) show the estimated minable Cu ore-reserves. The figures demonstrate a filtered volume of the Cu model using a cut-off grade of 0.41 wt.%. Figure 5-33 (a) shows that the minable Cu-grade is located within the Kevitsa pit area. Figure 5-33 (b) shows the distribution of the Cu-grade in 3D volume.

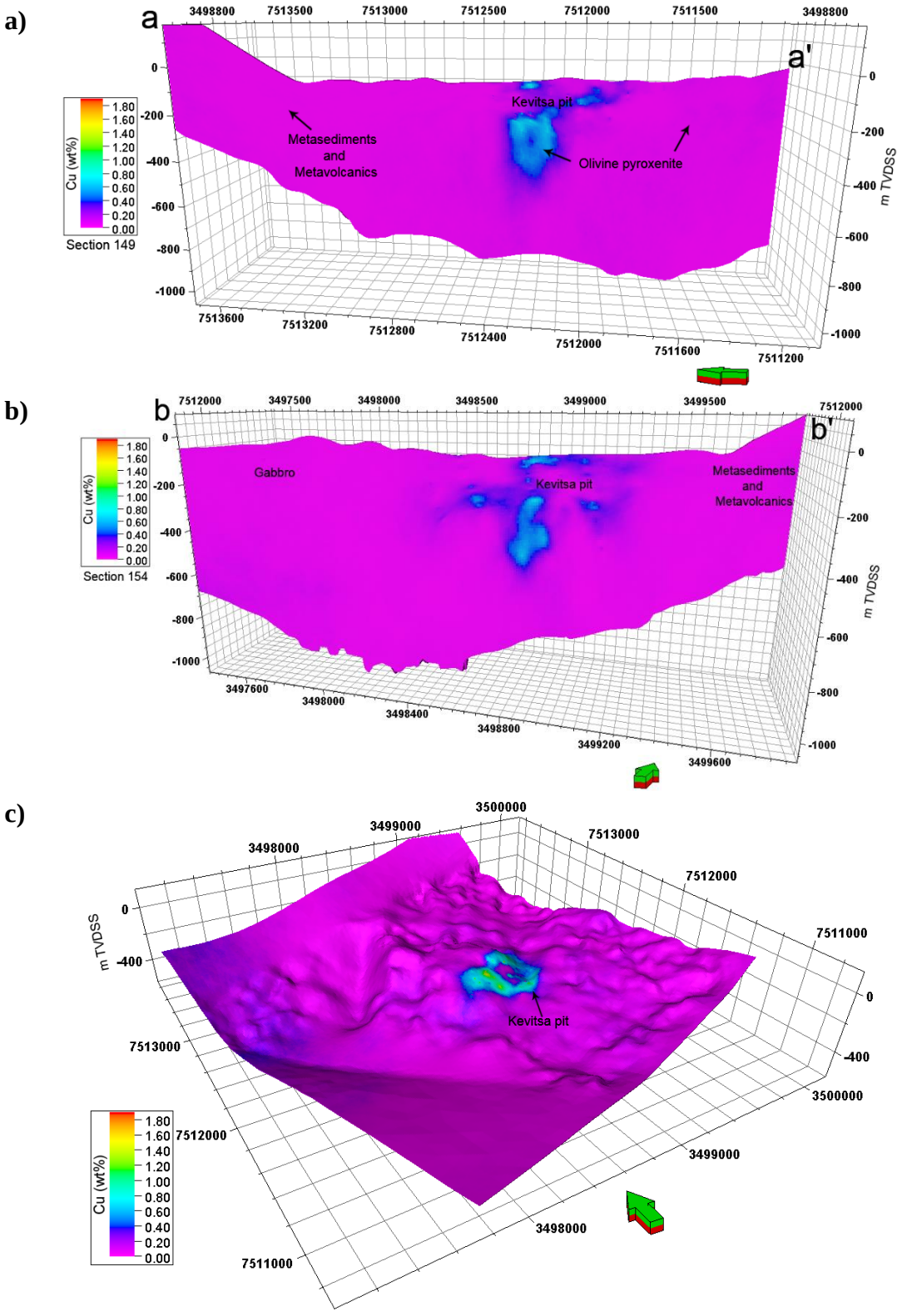

Figure 5-32: Cross-section of the upscaled Cu model (a) along NNW-SSE (a-a') direction), (b) along SSW-NNE (b-b') direction, and (c) a horizontal slice show that minable Cu-grade (0.41 wt.%) is located within the Kevitsa pit area.

a)

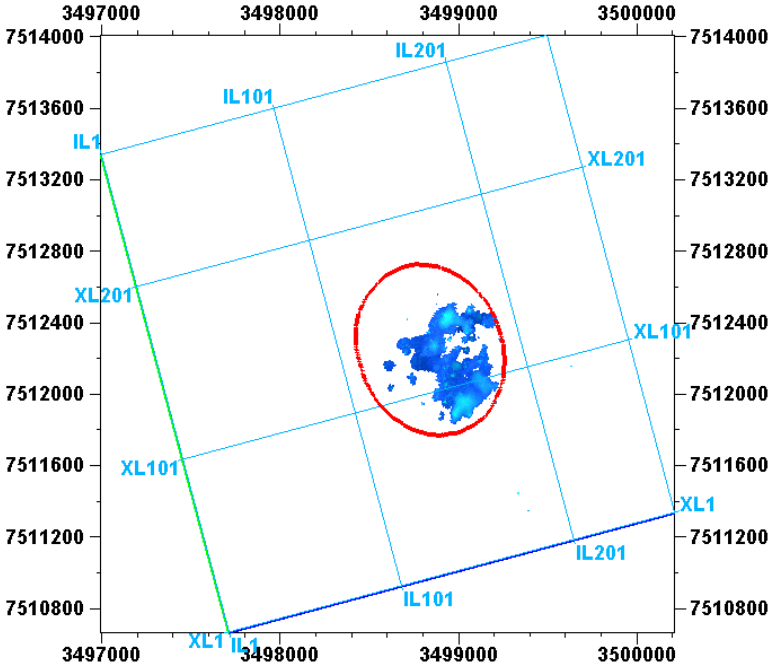

b)

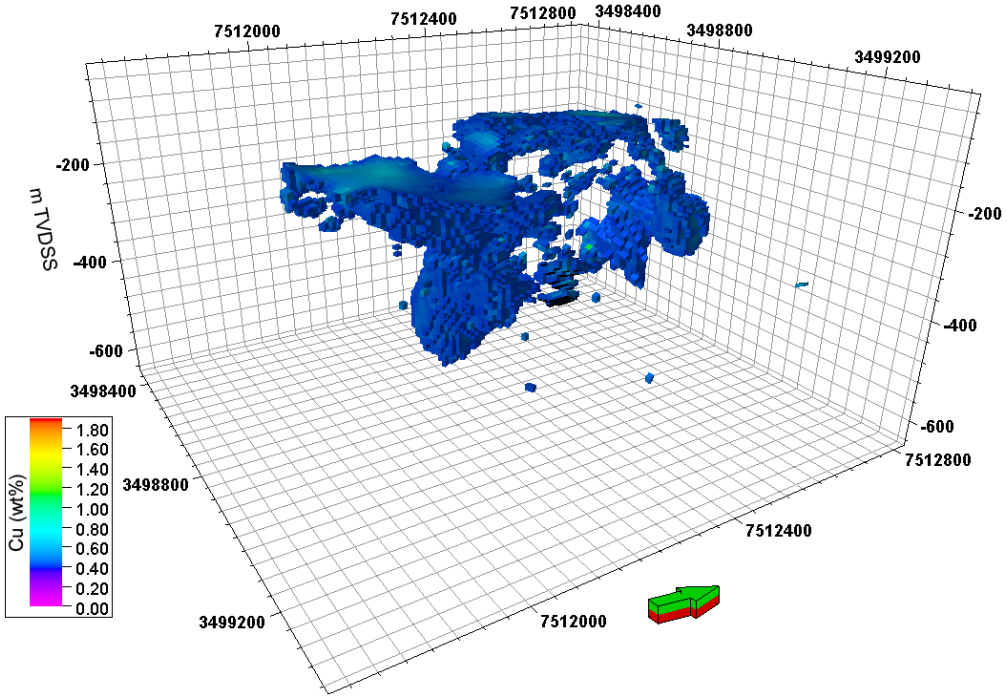

Figure 5-33: (a) Plan view of the estimated minable Cu-grade using 0.41 wt.% cut-off limit. Red ellipse marks the boundary of the Kevitsa pit. (b) Minable Cu-grade volume using 0.41 wt.% cut-off limit.

Figure 5-34 exhibits the Ni (wt.%) model simulated from the borehole data. The cross-sections along a-a′, b-b′ and horizontal directions are portrayed in Figure 5-35.

The cross-sections in Figure 5-35 (a, b and c) show that minable-grade nickel concentration is also higher in the Kevitsa pit area. Low-grade nickel concentration (0.1 wt.%) was also observed in a few boreholes in the southwestern part of the survey area that contributed to the distribution of low-grade nickel in the southwestern part of the model.

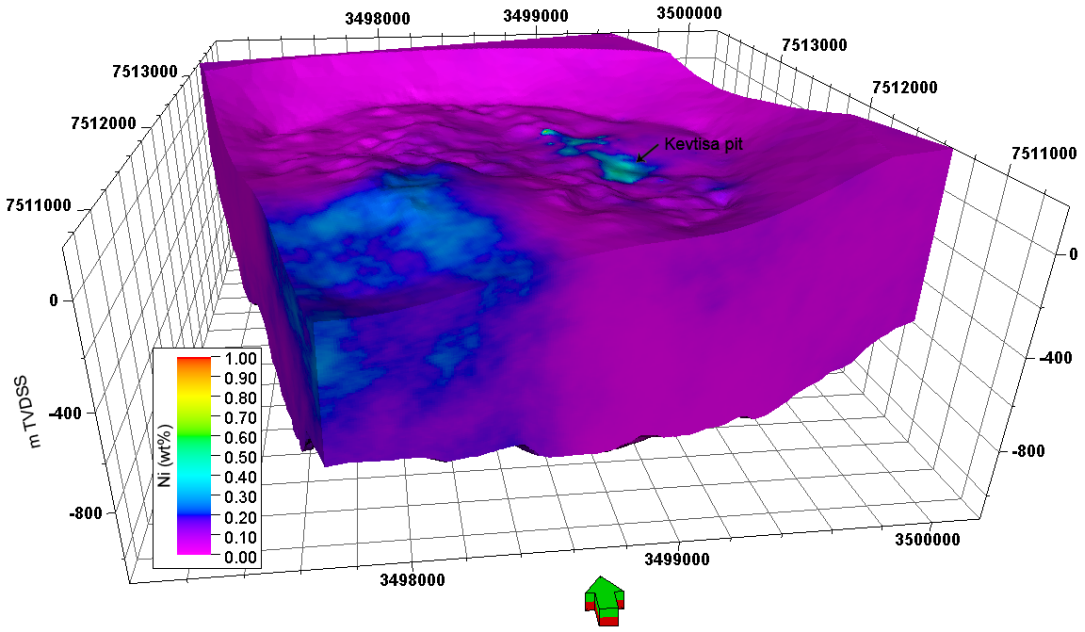

Figure 5-34: Ni (wt.%) model of the Kevitsa area simulated from the borehole data.

Figure 5-36 (a and b) demonstrate the estimated minable Ni-ore reserves. The figures exhibit a filtered volume of the Ni model using a cut-off grade of 0.3 wt.%. Figure 5-36 (a) shows that the minable Ni-ore reserve is located within the Kevitsa pit area. Figure 5-36 (b) depicts the distribution of the Ni-grade in 3D volume.

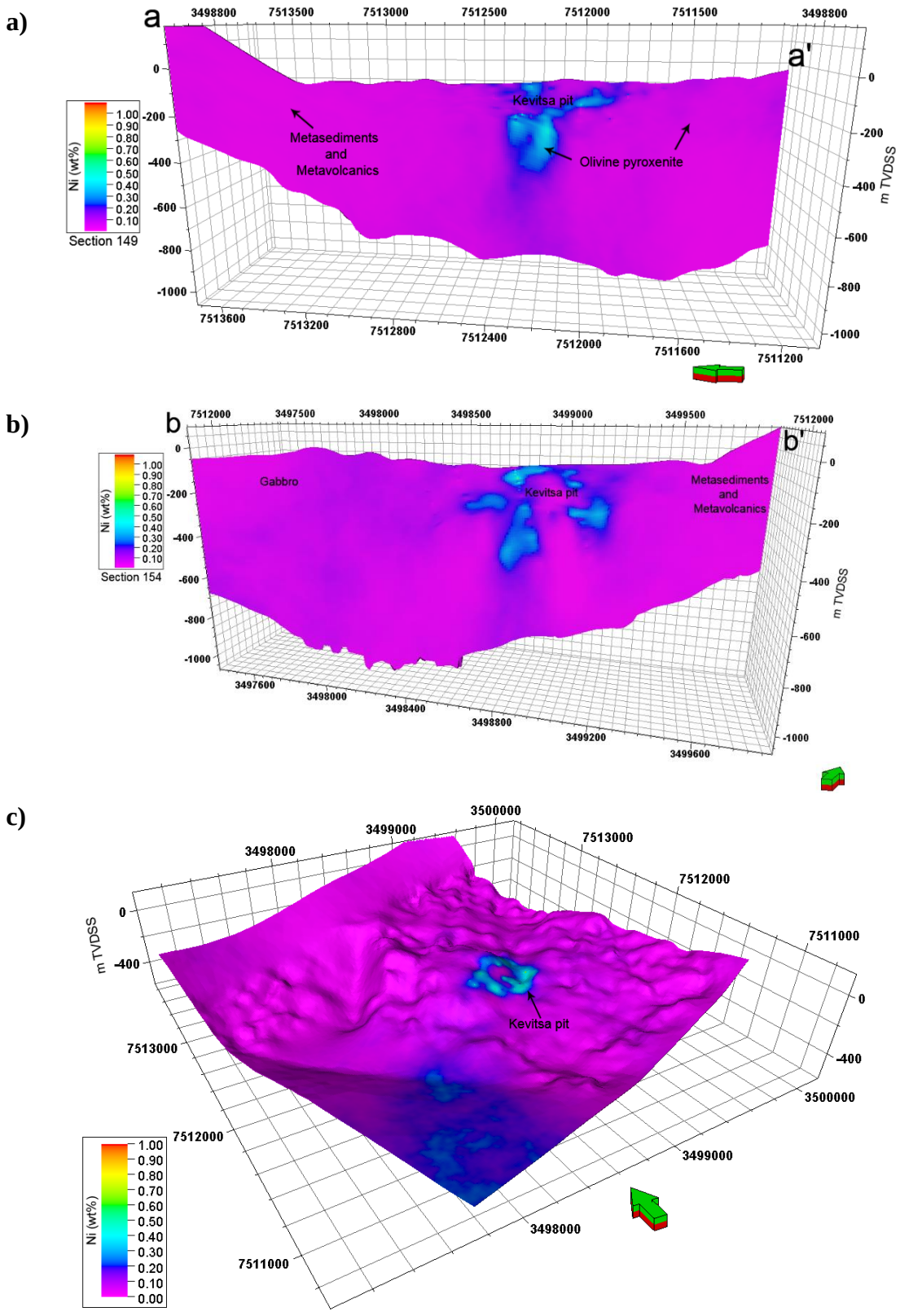

Figure 5-35: Cross-section of the upscaled Ni model (a) along NNW-SSE (a-a') direction, (b) along SSW-NNE (b-b') direction, and (c) a horizontal slice show that minable Ni-grade (0.3 wt.%) is located within the Kevitsa pit area.

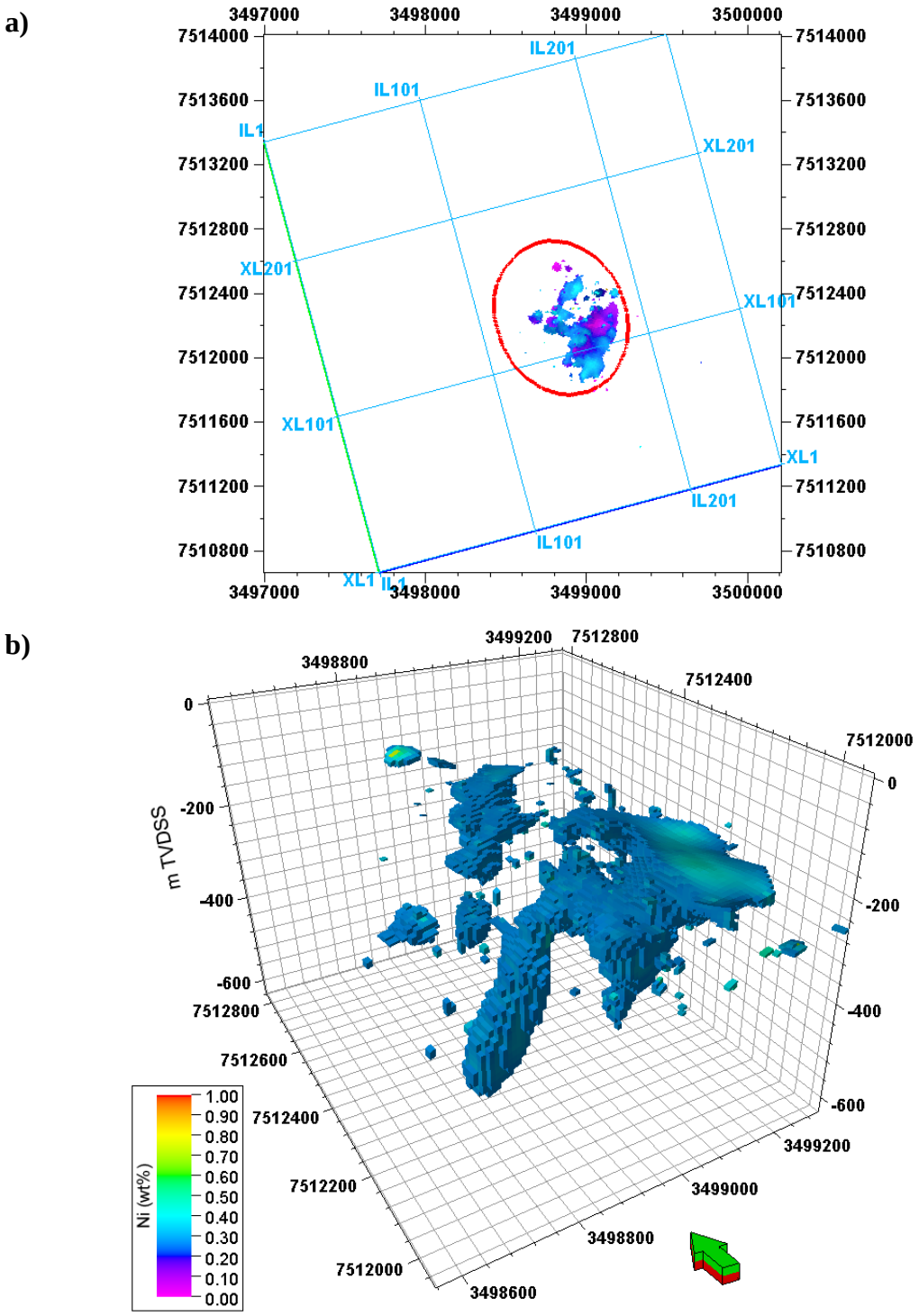

Figure 5-36: (a) Plan view of the estimated minable Ni-grade using 0.3 wt.% cut-off limit. Red ellipse marks the boundary of the Kevitsa pit. (b) Minable Ni-grade volume using 0.3 wt.% cut-off limit.

At the final stage of modelling, the structural grid was upscaled with the exact seismic amplitudes. The objective was to correlate the seismic response with Cu and Ni-bearing areas. Figure 5-37 shows the exact seismic amplitude model of Kevitsa.

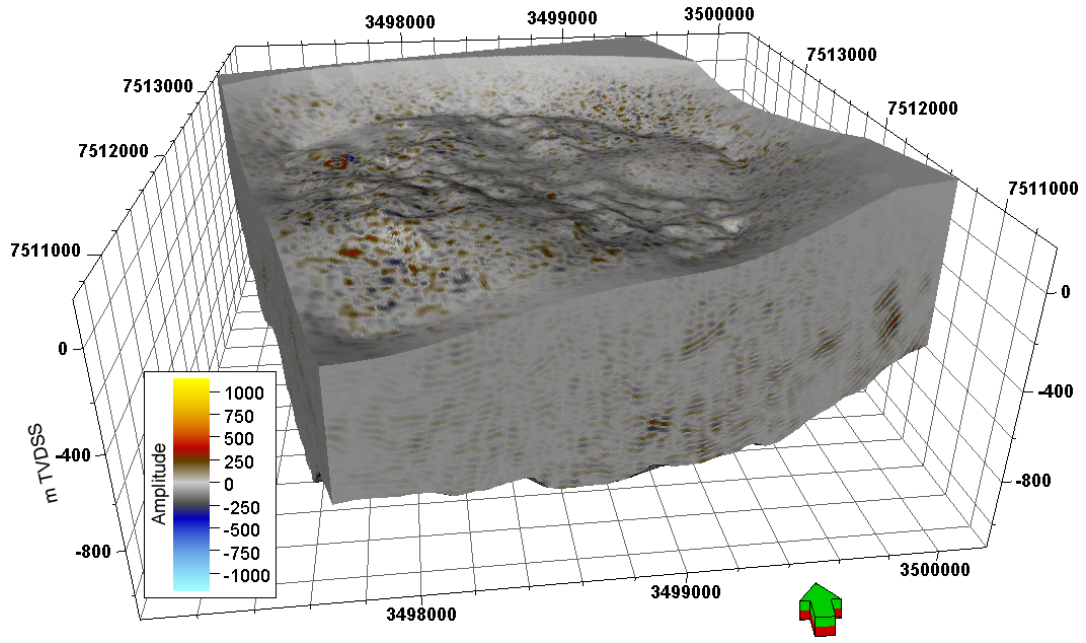

Figure 5-37: Exact seismic amplitudes from the Kevitsa seismic volume was upscaled to grid resolution.

Figure 5-38 (a, b and c) demonstrates the cross-sections of the resampled seismic grid along a-a′, b-b′ and horizontal directions. The figures demonstrate that continuous reflections are present at the boundaries of the major stratigraphic units; however, the signal-to-noise ratio is low within each stratigraphic unit.

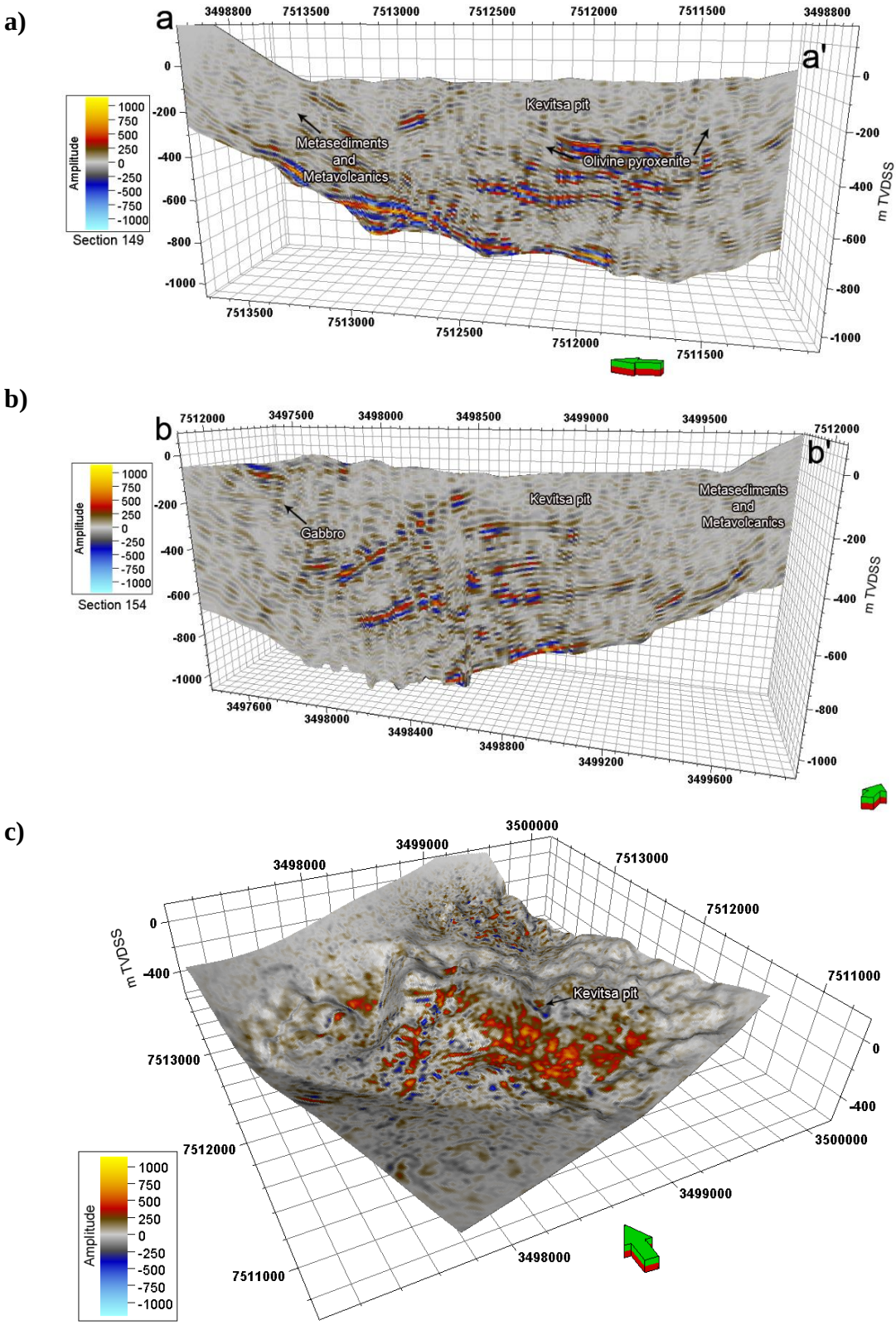

Figure 5-38: Cross-section of the upscaled seismic model (a) along NNW-SSE (a-a') direction, (b)along SSW-NNE (b-b') direction, and (c) a horizontal slice show the distribution of upscaled exact amplitude.

Figure 5-39 depicts the Cu-grade (0.41 wt.%) distribution. All values below 0.41 wt.% were removed from the model. The distribution was plotted against the seismic volume to correlate the seismic response of the copper-bearing layers.

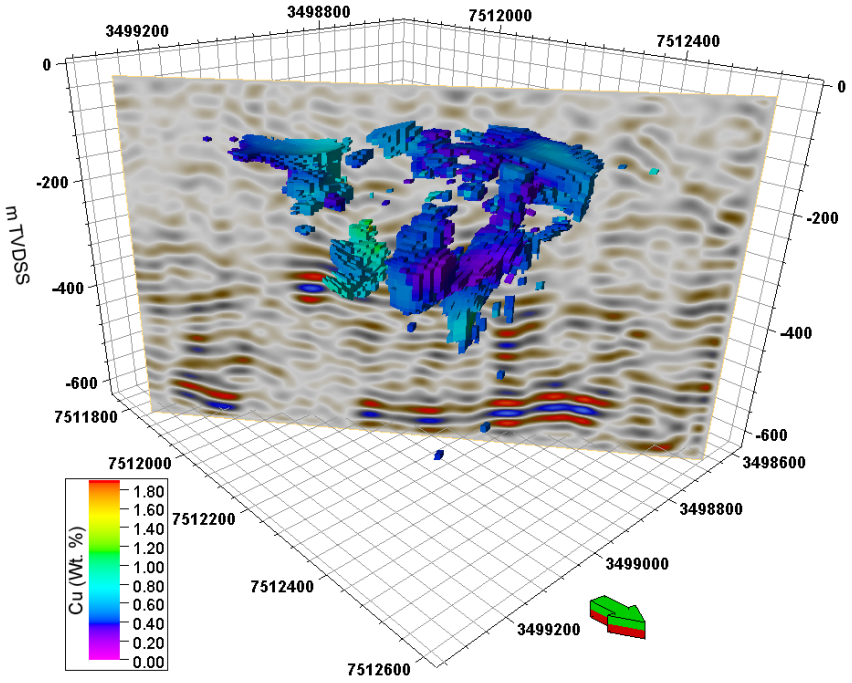

Figure 5-39: Minable Cu-grade (0.41 wt.%) volume was projected over the Kevitsa seismic data to identify the correlation between seismic data and Cu-ore.

Nickel model was also filtered using the nickel cut-off grade of 0.3 wt.%. All values below 0.3 were removed from the model. The filtered distribution was plotted over the Kevitsa seismic volume to check the seismic response of the nickel-bearing layers (Figure 5-40).

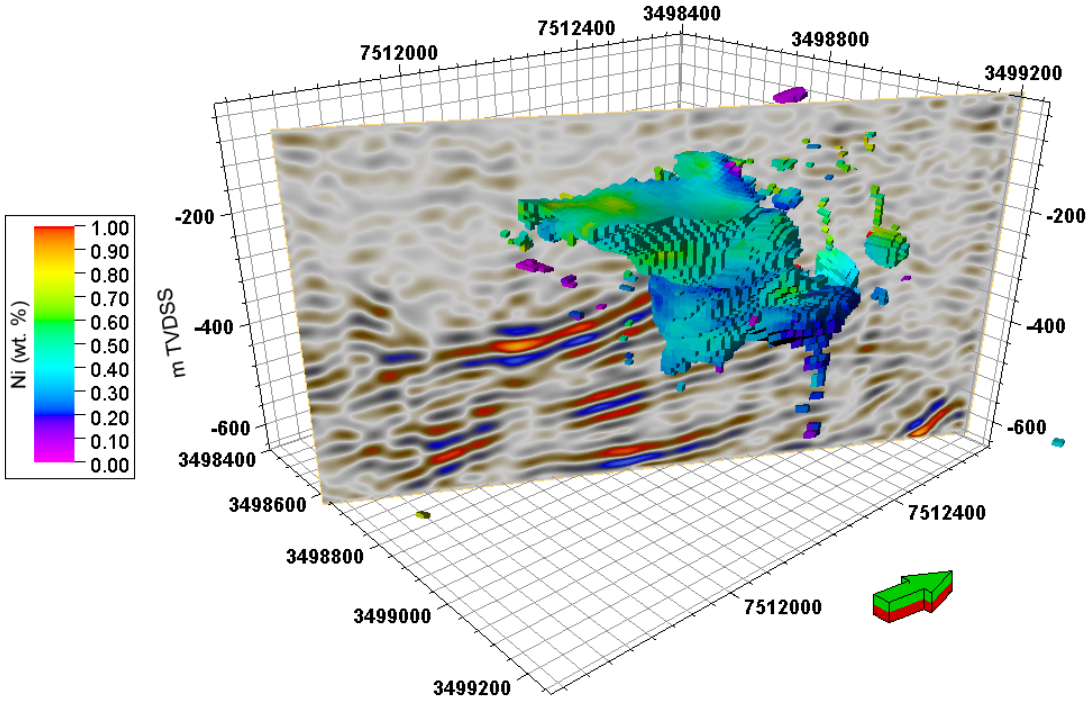

Figure 5-40: Minable Ni-grade (0.3 wt.%) volume was projected over the Kevitsa seismic data to identify the correlation between seismic data and Ni-ore.

Strong and continuous seismic responses were observed within both filtered volumes. However, no continuous seismic response was witnessed at the boundaries of the filtered distributions.

5.5. Summary

The 3D seismic survey at Kevtisa Ni-Cu-PGE mine was conducted to delineate the subvertical structures within the Kevitsa open-pit area. HiSeis Pty Ltd and the Uppsala University of Sweden jointly operated the seismic acquisition programme. Both explosives and Vibsist were used as the energy source. Two recording systems (Seistronix system was operated by HiSeis Pty Ltd and Sercel 408 system was operated by Uppsala University) were used to record the data. The survey was conducted using nine overlapping patches with 50% overlap in receiver directions. The sampling interval was 1 ms and 2 ms for the Sercel 408 system and Seistronix system respectively. The data acquired through Seistronix were resampled to 1 ms sampling interval and merged with Sercel data. The first data processing was done by HiSies Pty Ltd in 2010. The data was reprocessed in 2014 at the Department of Exploration

Geophysics of Curtin University by utilising 3D Kirchhoff prestack time-migration algorithm.

The volumetric interpretation approach was taken implementing seismic attribute analysis to interpret the subvertical faults. Most stratigraphic attributes did not add any additional value to the analysis due to low signal-to-noise ratio in the data. However, dip illumination, 3D edge enhancement and azimuth were able to extract the major stratigraphic horizons. Fault detection was performed using Schlumberger Petrel's ant-tracking workflow. Fault extraction did not perform optimally at the top 120 m due to low signal-to-noise ratio and low data fold at shallow depths. A fault volume for top 600 m was extracted.

Property modelling was performed by utilising borehole logs and the horizons extracted from the seismic volume. A structural grid was constructed and physical properties, e.g., density, P-wave velocity were upscaled to the grid. Cu (wt.%) and Ni (wt.%) from 242 boreholes were also utilised in the modelling. No direct correlation was observed between the ore-grade and seismic.

6. Case study: Cracow gold mine, Queensland

6.1. Introduction

This case study is based on a consultancy work done for HiSeis Pty Ltd, leading to a report entitled, *"The application of edge enhancement attributes to detect and characterise high order structures for the direct interest of gold exploration in Cracow, Queensland"*. In 2014, HiSies conducted a 3D seismic survey at Evolution Mining Ltd owned Cracow gold mine in Queensland, Australia. The gold field is located on the southeastern margin of the Bowen Basin in Queensland (Dong and Zhou 1996). Although, the gold discovery took place in 1875; however, payable gold was not found in the Cracow area until 1931 (Creenaune *et al.* 2003). From 1932 to 1992, about 850,000 ounces of gold was produced from the mine (Creenaune *et al.* 2003). In 2002, underground mine development programme was approved by joint venture participants (Evolution Mining 2015b). Mine development commenced in December 2003 and gold production started in November 2004 (Evolution Mining 2015a). In June 2011, Catalpa Resources and Conquest Mining merged and announced to buy the Cracow gold mine from the Newcrest Mining. In November 2011, Evolution Mining Limited was founded via the merger of Catalpa Resources and Conquest Mining (Evolution Mining 2015a).

The Camboon Andesite comprising dominantly of andesitic to dacitic welded tuff with minor andesitic and basaltic flows, volcanic breccias and agglomerate hosts the gold deposit in the Cracow gold mine (Dong and Zhou 1996). The mineralisation is confined within subvertical faults (>70°) and low sulphidation epithermal veins (Evolution Mining 2015a; Micklethwaite 2009). Micklethwaite (2009) studied the breccia textures and suggested that the fault rock formed through repeated events, encompassing significant components of dilation during fracture, wall-rock fragmentation and mineral precipitation.

The estimated resources at the Cracow mine as of 31 December 2014 is 3.22 Mt at 6.82 g/t gold for 707 koz gold (Evolution Mining 2015a). The estimated ore reserves as of 31 December 2014 is 1.16 Mt at 6.67 g/t gold for 248 koz gold (Evolution Mining 2015a). The ore is free milling and is treated on-site by conventional crush-grind-CIP processing to produce gold-silver-dorè (Evolution Mining 2015a). For the financial

year 15, a total of 142,699 tonnes of ore was processed at an average grade of 7.03 g/t gold at a recovery rate of 93% (Evolution Mining 2015a). Table 6-1 demonstrates the production statistics between October 2015 and December 2015 from the Cracow gold mine.

Table 6-1: December 2015 quarter production from the Cracow mining project (Evolution Mining 2016).

Production	**Amount**
Total ore processed	121,000 tonnes
Grade processed	6.12 g/t
Recovery	93.2 %
Gold produced	22,120 oz
Silver produced	14,274 oz

Most of the works included in this chapter were submitted as a report to HiSeis Pty Ltd and in a manuscript in preparation. The objective of this case study is to show the usability of edge enhancement attributes and fault detection workflows to detect subvertical fault network from the seismic data collected over a complex geological setting for the direct interest of gold exploration.

6.2. Geological Setting

The Cracow gold field is located in Queensland, Australia, approximately 500 km northwest of Brisbane by road (Evolution Mining 2015a, Figure 6-1). The gold field is situated within the upper Palaeozoic Camboon Volcanic Arc on the southeastern margin of the Bowen Basin (Dong and Zhou 1996). The gold deposits are hosted in the Camboon Andesite and is bordered by Torsdale bed on the east and Back Creek Group in the west (Dong and Zhou 1996). Outliers of the Precipice Sandstone covers the higher hills in the area (Dong and Zhou 1996).

Whitaker *et al.* (1974) compiled the stratigraphic units in the area on the Mundubbera 1:250,000 sheet. Felsic crystal-lithic welded tuffs dominates the Torsdale beds (Dong and Zhou 1996). In the Cracow area, the Camboon Volcanics are composed of andesite–trachyandesite volcanics, with minor volcaniclastic and fine-grained

epiclastic units (Dong and Zhou 1996; Jones *et al.* 1996; Micklethwaite 2009). It unconformably overlies the Torsdale Beds and dips towards the south-west at 15° to 20° (Dong and Zhou 1996; Jones *et al.* 1996; Micklethwaite 2009). Faunal evidence in the Moonta sheet area suggests that the Camboon Andesite was deposited during Lower Permian time (Dong and Zhou 1996). Holcombe *et al.* (1997) suggested that the Camboon Volcanics in the western margin of the New England orogeny was a part of the active collision margin between Cambrian and Carboniferous period. $^{40}Ar/^{39}Ar$ age dating demonstrates that part of the Camboon Andesite has yielded an age of 281 Ma and 294 Ma in the Cracow area (Dong and Zhou 1996; Runnegar 1979). The sequence is intruded by basalt and rhyodacite-dacite dykes and some diorite bodies that are believed to be synchronous with the epithermal fault-vein system in Cracow (Micklethwaite 2009). The Back Creek Group consists mainly of fossiliferous limestone, marine mudstone, lithic sandstone and argillite is exposed to the west of Cracow and forms the southeastern part of the Bowen Basin (Dong and Zhou 1996). It disconformably overlies the Camboon Andesite and dips toward the west at 15° to 30° angle. The faunal evidence suggests an age of Early Permian to Early Upper Permian. The Precipice Sandstone of Early Jurassic age unconformably overlies the Camboon Andesite and Back Creek Group caps the higher hills in the district.

Figure 6-1: Location map of Cracow (Courtesy: Google)

The Camboon Andesite in Cracow district is intruded by numerous rhyolite dykes having porphyritic texture and flow banding at the contact (Dong and Zhou 1996; Micklethwaite 2009). The relationship between the rhyolites and the mineralisation indicates that rhyolites were actively being emplaced during epithermal activity and gold mineralisation and some of the dykes utilised faults as the lodes (Dong and Zhou 1996). The U-Pb zircon dating from the rhyolite dyke at Cracow gave an age of 291.1 ± 5.3 Ma that indicates the age of mineralisation (Dong and Zhou 1996; Micklethwaite 2009). The gold deposits are hosted by subvertical low sulphidation epithermal fissure quartz veins within the Camboon Andesite (Dong and Zhou 1996). High-grade gold mineralisation occurs within the Royal Shoot, Crown Shoot, Sovereign Shoot, Klondyke North, and Kilkenny Shoot deposits developed at the intersection of major structures (Evolution Mining 2014). Figure 6-2 shows the geology of the Cracow area and the location of different ore shoots, veins, dykes and alterations.

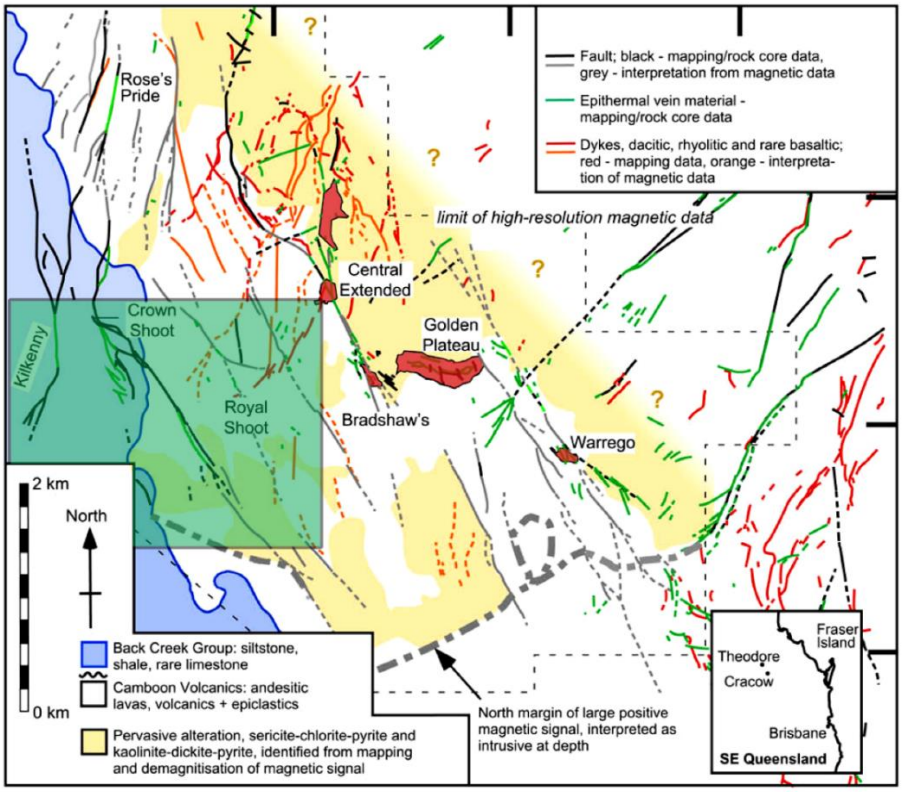

Figure 6-2: Geology of the Cracow gold field area showing the faults, veins, dykes and alterations. Polygons with red colour fill show pit outlines. Green colour-filled polygon shows the location of the 3D seismic survey. Inset map shows the location of Cracow in southeast Queensland (modified after Micklethwaite 2009).

6.3. Seismic data acquisition

In July and August 2013, a 2D seismic reflection profile was acquired at Cracow to assist the epithermal deposits exploration for gold (Turner 2014). The survey was able to identify subvertical structures consists of andesitic lava, tuffs and fragments (Turner 2014). Drilling confirmed that these structures are coincident with the veins that contain gold (Turner 2014). Based on the success of the 2D seismic survey, HiSeis Pty Ltd conducted a 3D seismic acquisition survey at Cracow in 2014. Table 6-2 records the acquisition parameters used for the 3D seismic survey. The data acquisition was completed using six overlapping patches. Figure 6-3 displays the prestack time-migrated (PSTM) seismic data acquired at Cracow in 2014.

Table 6-2: 3D Seismic data acquisition parameters for Cracow (Courtesy: HiSeis Pty Ltd)

Parameter	
Receiver interval	15 m
Receiver line spacing	75 m
Source interval	30 m
Source line spacing	90 m
Receiver flag format	[L][L][STN][STN][STN]
Total receivers line per patch	10
Total receiver points per patch-line	108
Total source lines per patch	9
Total source points per patch-line	50
Source points per patch	450

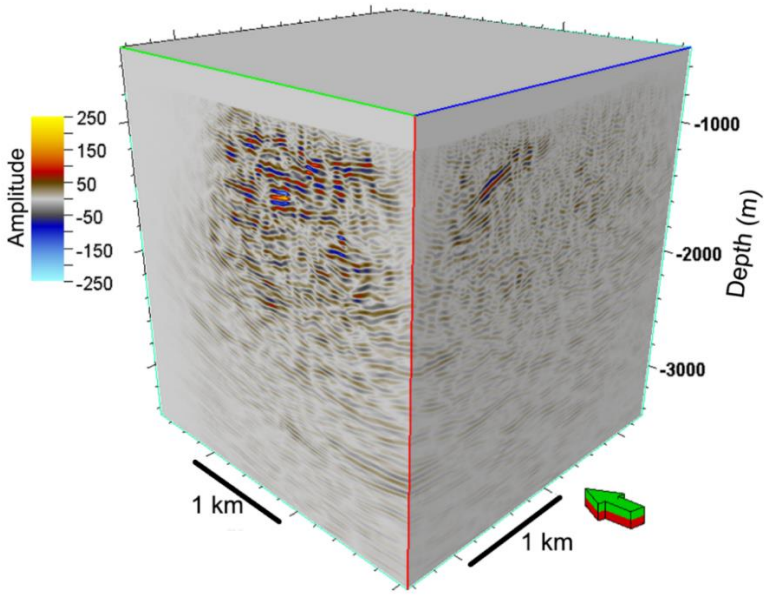

Figure 6-3: The prestack time-migrated seismic data acquired at Cracow in 2014 by HiSeis Pty Ltd.

The main goal of the seismic survey was to delineate the subvertical to vertical epithermal fault-vein network that host gold mineralisation. Table 6-3 represents the statistics for the Cracow seismic dataset collected from Cracow.

Table 6-3: Statistics for the Cracow 3D prestack time-migrated seismic volume.

Description	Value
Original CRS:	Map Grid of Australia Zone 56 (GDA 94)
Origin X:	223562
Origin Y:	7198942
End first inline X:	223562
End first inline Y:	7201747
End first crossline X:	226367
End first crossline Y:	7198942
Number of inlines:	188
Number of crosslines:	188
Inline length:	2805
Inline interval:	15
Crossline length:	2805
Crossline interval:	15
Inline rotation from north:	0
Seismic type:	3D
Number of samples per trace:	1501
Number of cells total:	53051344
Inline interval:	15
Crossline interval:	15
Sample interval:	2

In addition to seismic data, Newcrest Mining Ltd collected geological, geochemical and geophysical data from surface exploration and drilling of the Royal Shoot in the search for additional high-grade epithermal gold mineralisation (Creenaune and Braund 2001). Ground magnetics conducted over the Klondyke structure shows a strong correlation between the quartz vein structure and a north-west trending linear magnetic low (Creenaune and Braund 2001).

6.4. Seismic volumetric interpretation

The prestack time-migrated seismic data supplied by HiSeis Pty Ltd were preconditioned by applying amplitude cropping and filters. The source amplitude range on the original seismic data was ~-1673 to ~1561 which was clipped using a range of ~-250 to ~250 to visually improve the data quality. About 0.2% of the data were lost both from the lower and upper source amplitude range. The remove bias filter was applied to the data to remove deconvolution bias from the seismic data. Structural smoothing filter was applied to the filtered volume to increase the lateral continuity of the seismic reflections. In structural smoothing, local structures are determined from principle component dip and azimuth computations, and Gaussian smoothing is then applied parallel to the orientation of the structures (Schlumberger 2014). Table 6-4 catalogues the steps used to condition the seismic data for edge detection.

Table 6-4: Conditioning steps used to prepare the data for edge detection

Process	Description
Amplitude Cropping	▪ Original amplitude: -1673 to 1561 ▪ New amplitude: -250 to 250
Remove bias	▪ Remove deconvolution bias
Structural Smoothing	▪ Dip-guided with edge enhancement ▪ Filter size: 0.5, 0.5, 0.5
Seismic volume cropping	▪ Original volume: 188, 188, 3000 ▪ Cropped volume: 188, 158, 2000

Cracow seismic dataset suffers from acquisition footprints due to the low data fold at shallow depths. Moreover, a significant change in elevation from east to west also contributed to the generation of acquisition footprints in the low-lying areas. The seismic dataset was cropped to remove the padded area (crossline 159-188) in the northern part of the cube where reflection is absent. The top of the volume was cropped from 470 m to 250 m to remove the empty area and acquisition footprints. The cropped

dataset was realised and used for further analysis. Figure 6-4 demonstrates the cropped seismic dataset preconditioned for the seismic attribute analysis and fault detection.

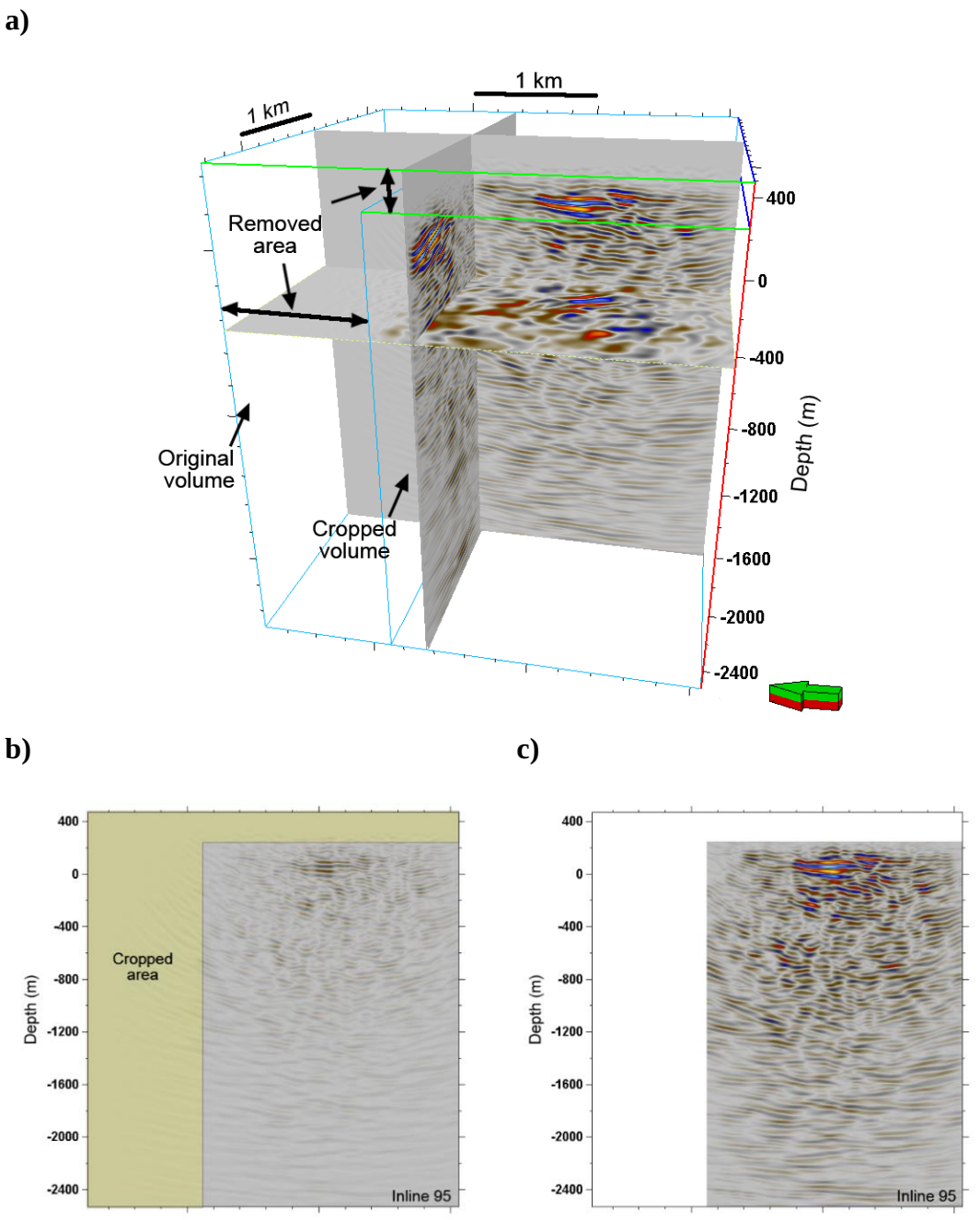

Figure 6-4: (a) The cropped and preconditioned prestack time-migrated seismic volume employed in seismic attribute analysis and fault detection. (b) The seismic cube before cropping and conditioning, and (c) the seismic cube after cropping and conditioning.

6.4.1. Seismic attribute analysis

Seismic attribute analysis of the Cracow seismic data utilised the depth-converted PSTM dataset acquired from HiSeis Pty Ltd. Seismic attribute analysis was performed by employing OpendTect and Schlumberger Petrel's volume attribute libraries.

The upper part of the supplied dataset is devoid of any signal (Figure 6-4). The shallowest reflections were observed around 250 m above the Australian Height Datum; therefore, the cube was cropped to remove the empty area at the top. The areas between inline 159 to inline 188 in the northern part of the dataset were also removed due to the absence of discernible signals (Figure 6-4).

Instantaneous phase is an excellent indicator of continuities, faults, pinch-outs, bed interfaces, sequence boundaries and on-lap patterns (Schlumberger 2014). This attribute provides an amplitude independent display that is useful for revealing the continuity of the reflectors. It is commonly used to find the continuity of the weak events and to distinguish small faults and dipping events. Figure 6-5 (a) demonstrates the instantaneous phase calculated along crossline 95. The discontinuous nature of the reflectors implies an abundance of subvertical faults. This attribute is often used with the Cosine of phase attribute. The Cosine of phase or cosine of the Instantaneous phase is also known as paraphrase (Manzi *et al.* 2013). Figure 6-5 (b) portrays the Cosine of phase attribute along crossline 95. Cosine of phase attribute also provides an evidence that subvertical faults are in abundance in the study area.

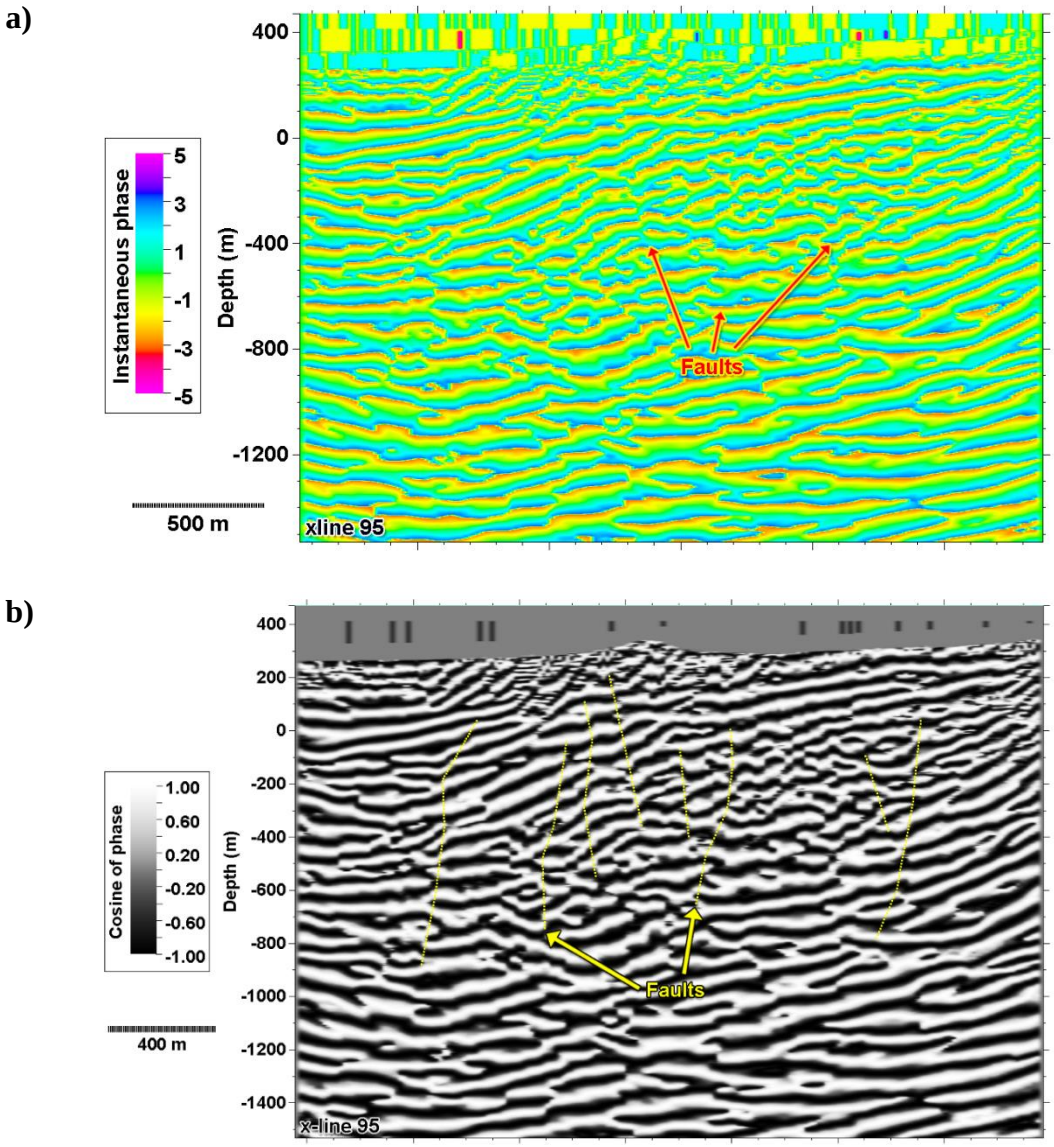

Figure 6-5: (a) Instantaneous phase attribute exposes the subvertical faults along crossline 95, (b) cosine of phase attribute along crossline 95 also supports the fact that the study area is characterised by an abundance of subvertical faults.

Semblance is a coherency attribute that emphasises faults and noisy zones in a seismic volume. It is the energy of the sum of the traces divided by the sum of each trace's energy (Neidell and Taner 1971). Zones of high semblance values are zones of high coherency. Low semblance values in Figure 6-6 exhibit zones of low coherency where the data is discontinuous or noisy. These discontinuous zones correlate with the areas where cosine of phase attribute indicates the presence of faults or veins.

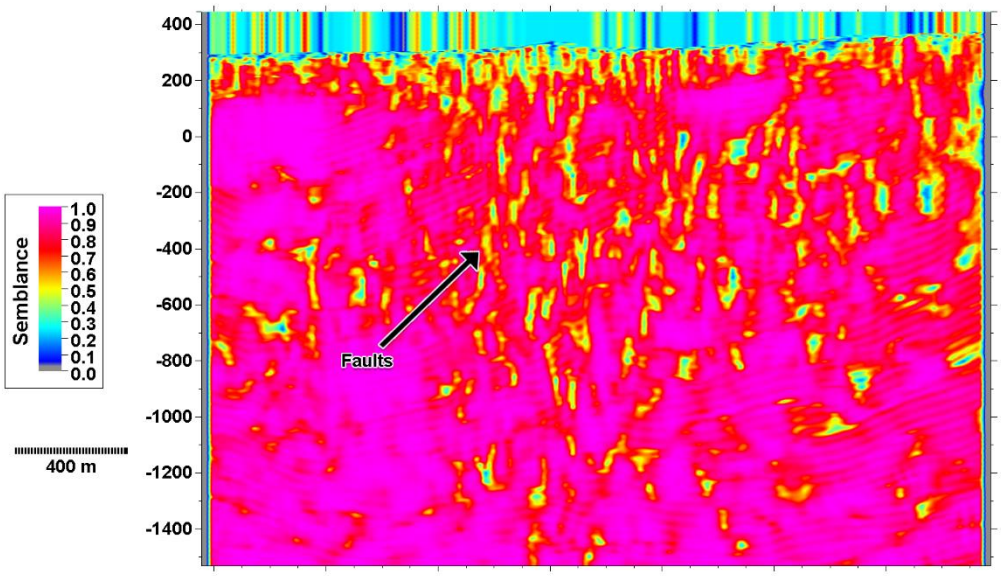

Figure 6-6: Semblance attribute demonstrates zones of low coherency.

The traditional approach of volumetric dip calculation is done through instantaneous dip estimation based on cross-correlation of gradient-based eigenvalue decomposition (Schlumberger 2014). These methods apply a smoothing filter for a spatially continuous display that reduces lateral and vertical resolution. Consistent dip, on the other hand, uses an iterative global optimisation method to calculate the dip that honours consistency constraints. Figure 6-7 shows the volumetric consistent dip estimation along inline and crossline directions for the Cracow seismic dataset.

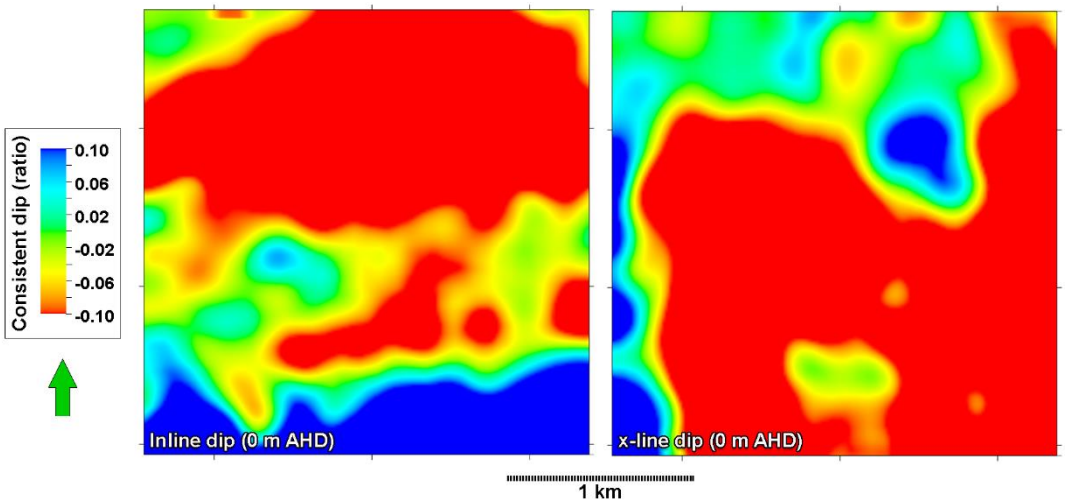

Figure 6-7: Consistent dip attribute along a horizontal slice at 0 m Australian Height Datum showing (a) inline dip and (b) crossline dip.

In the presence of discontinuities due to faults/channel cuts or due to poor signal-to-noise ratio, a robust method should not try to estimate the dip; instead, the method should output a by-product (residual dip or dip quality attribute) which highlights the area of uncertainty in the dip estimation (Schlumberger 2014). Residual dip can be used as an input for mapping faults or fracture volumes. Figure 6-8 displays dip estimation errors highlighting the areas with faults or low signal-to-noise ratio.

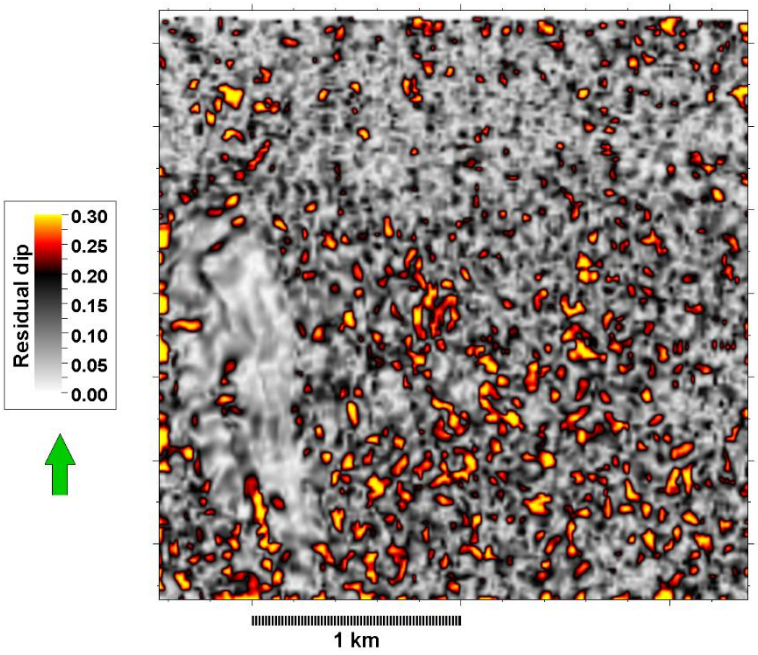

Figure 6-8: Residual dip on a horizontal slice at 0 m Australian Height Datum highlights the areas of uncertainty in the dip estimation where the data is discontinuous due to the presence of faults or low signal-to-noise ratio.

Similarity is a form of coherency that returns trace-to trace similarity properties. Similarity attribute is calculated by finding the direction of best match between two or more trace segments. Best similarity between adjacent traces are then calculated by using the direction of best match between the trace segments. Figure 6-9 (a) shows minimum similarity attribute along the crossline 95 has highlighted the areas with potential faults. Figure 6-9 (b) demonstrate the areas with maximum similarity along crossline 95.

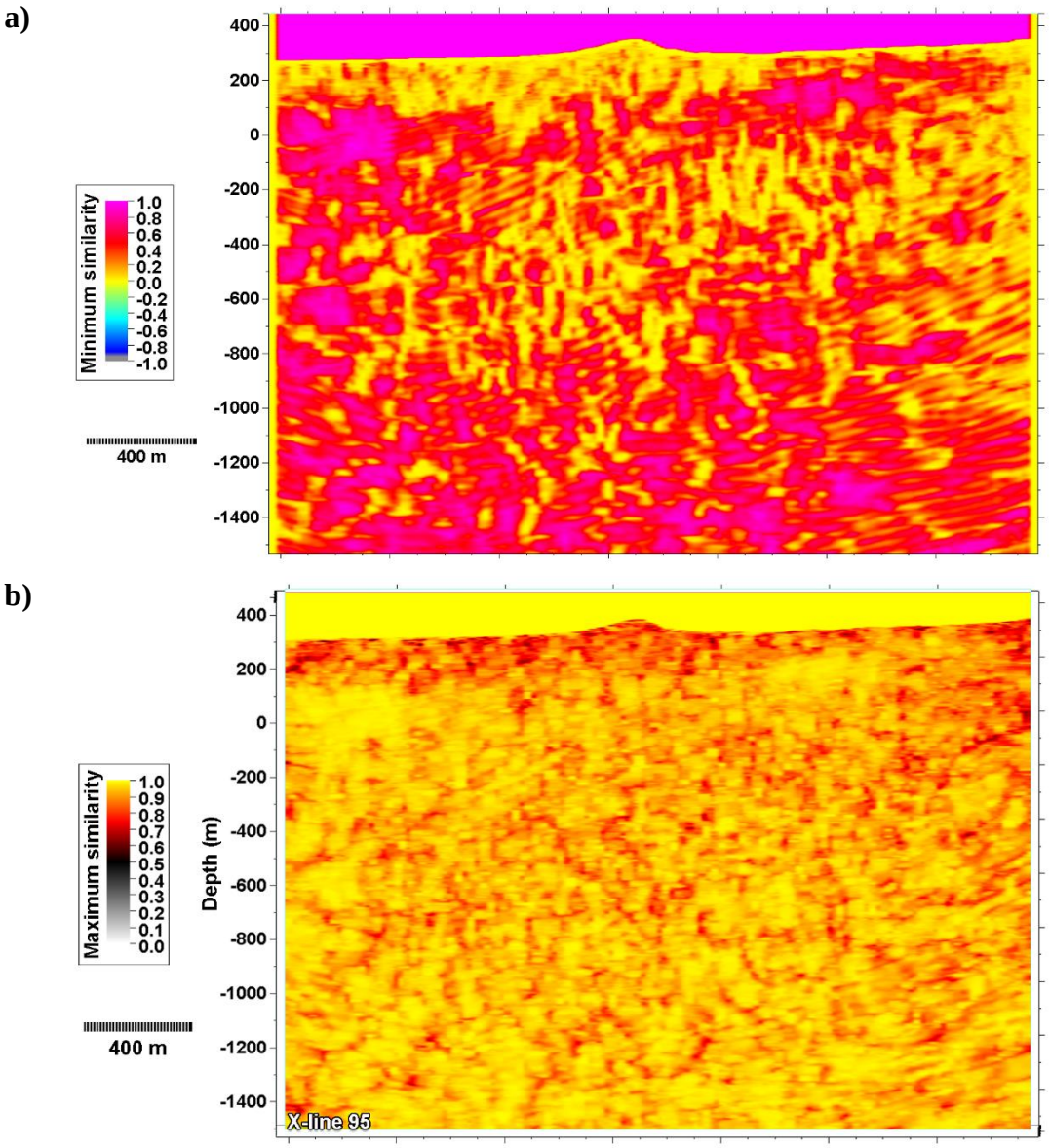

Figure 6-9: (a) Minimum similarity attribute on a vertical section along crossline 95 highlights areas with potential faults. (b) Maximum similarity attribute along the same crossline shows the areas with consistent signals.

Laplacian edge is a convolve attribute used to preserve and enhance edges. The filter size determines the sharpness of the edges. Figure 6-10 demonstrate the application of Laplacian edge enhancement filter on the Cracow seismic data to preserve edges and highlight areas with potential faults.

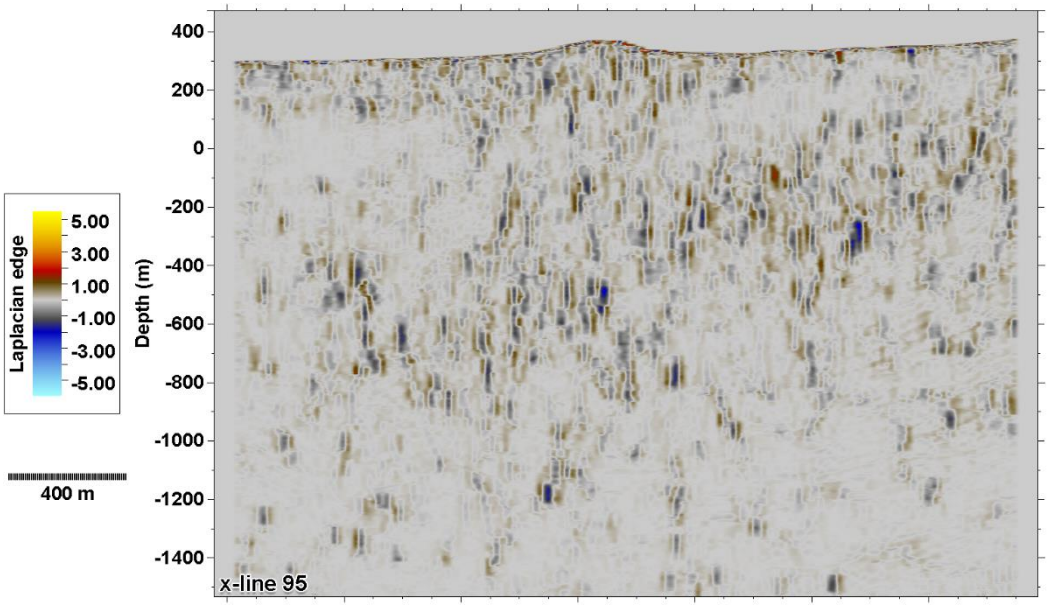

Figure 6-10: Laplacian edge enhancement filter preserves edges, thereby, highlights the areas with potential faults.

6.4.2. Fault detection

Schlumberger Petrel's ant-tracking workflow has been utilised on the edge-enhanced seismic volume to delineated subvertical faults. The steps involved in the fault detection workflow to extract potential discontinuities are demonstrated in the fourth chapter in Figure 4-22. Ant-tracking was performed using the aggressive-ant mode with an initial ant boundary of 5. This parameter controls how closely the initial ant agents can be placed within the volume. The distance is measured in terms of voxels and is the primary control for the number of agents generated. The larger this value, the fewer the number of agents will be produced. A lower value of ant track deviation 2 was used to allow the ants to search for voxels on either side of the tracking direction. A value of ant step size 3 was chosen. This value allows ants to search further for more connections. A value of stop criteria 10 was used to limit the ant advancement to search beyond current location when an edge has not been detected. Figure 6-11 (a) demonstrates a 3D representation of the fault network extracted from the ant-tracked dataset. Red coloured dots show the location of the faults detected in the borehole. The ant-tracking result shows a very good agreement with the faults detected in the boreholes. Figure 6-11 (b) shows a plan view of the ant-tracked faults from the Cracow seismic data.

a)

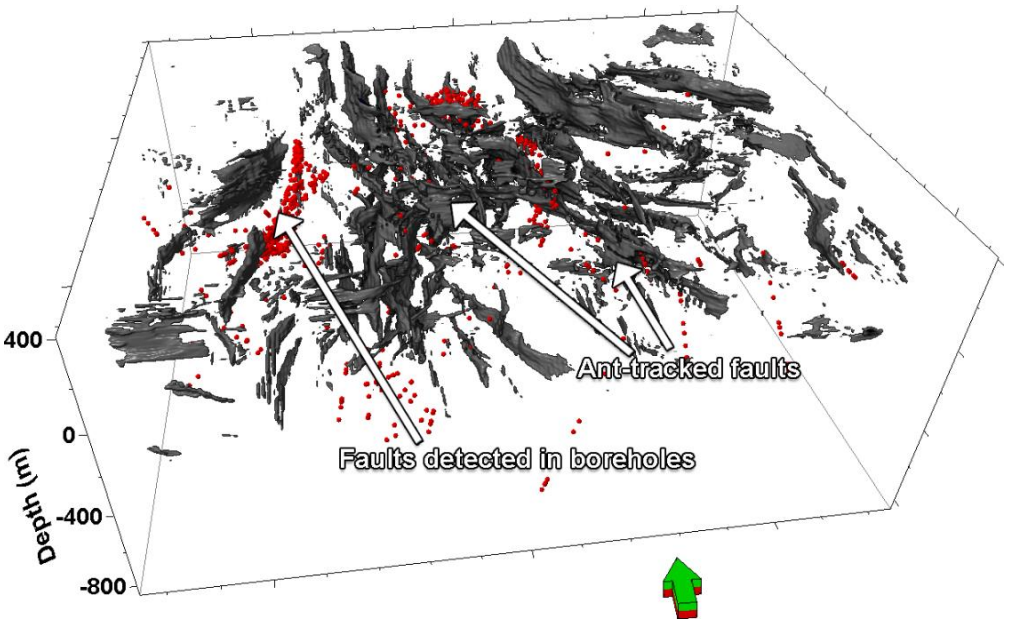

b)

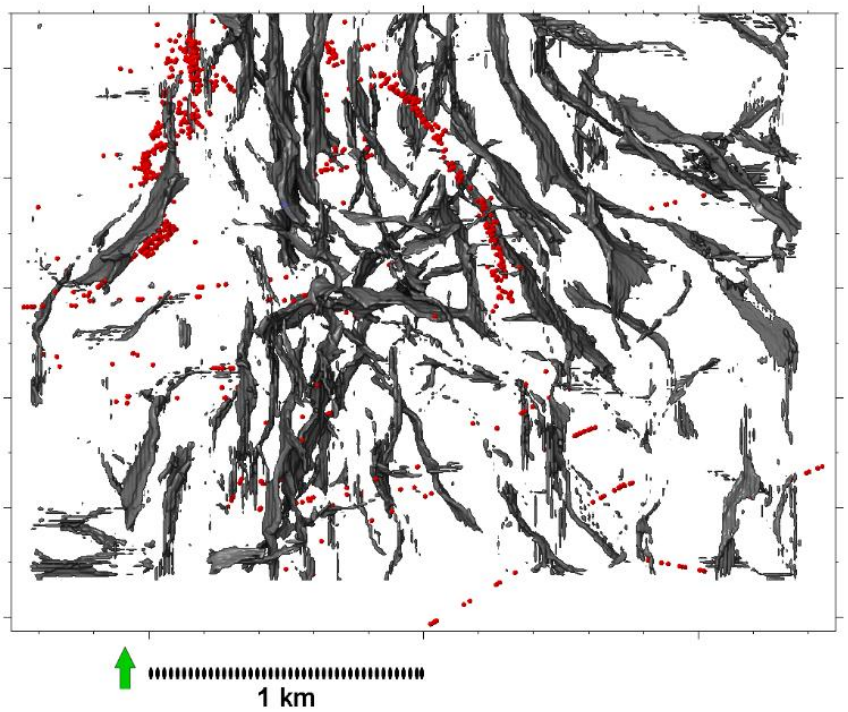

Figure 6-11: (a) Faults detected from the Cracow seismic volume using Schlumberger Petrel's ant-tracking workflow. The grey events indicate discontinuities detected from the seismic data. Red dots are the faults detected in the borehole during drilling. Ant-tracking result shows an excellent agreement with the faults detected during drilling. (b) A plan view of the ant-tracked faults from the Cracow seismic data.

Micklethwaite (2009) provided a comprehensive structural description of the epithermal fault network in the Cracow gold field area by studying geometry, dimensions, macroscopic deformation mechanisms and displacement characteristics. The study employed surface mapping, drill-core logging, underground exposures and geophysics datasets supplied by Newcrest Mining to constrain the fault systems and associated dykes network. Figure 6-12 represents a comparison between the ant-tracking results and Micklethwait's interpretation of the fault network and associated dykes. The location information for the faults, dykes and epithermal quartz veins provided in Micklethwaite (2009) were converted from the Australian Map Grid AMG 84 Zone 56 to the Map Grid Australia 94 Zone 56 before comparison.

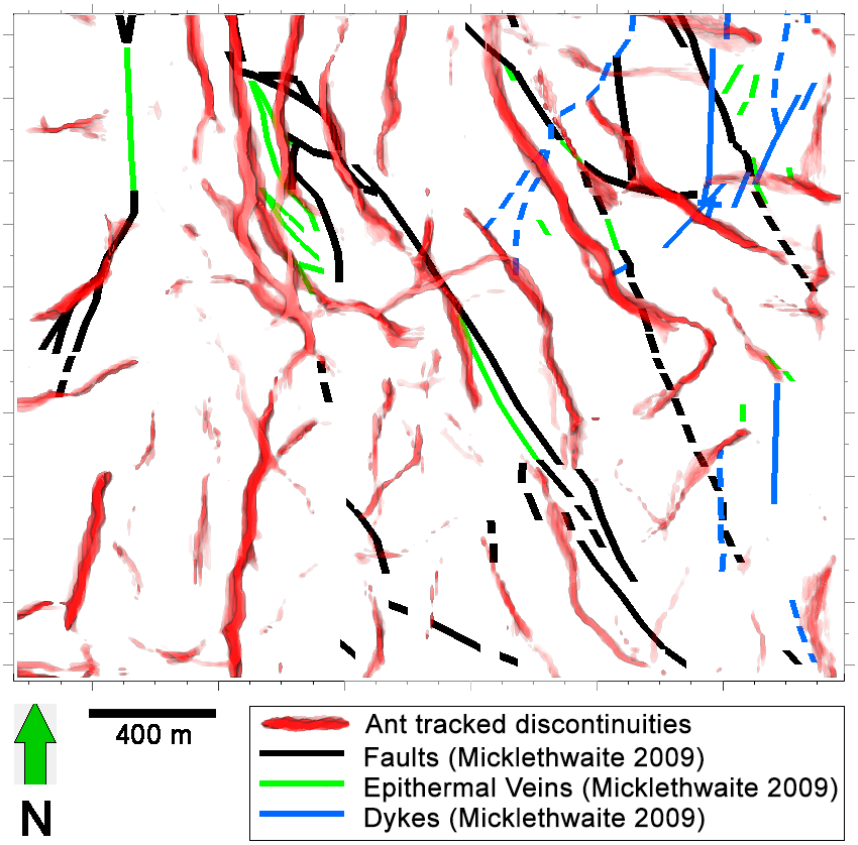

Figure 6-12: Comparison of ant-tracking result with the interpretation of (Micklethwaite 2009).

Ant-tracking results were also compared with the quartz-vein map provided in Evolution Mining's June 2014 Quarterly Report (Evolution Mining 2014). Figure 6-13 exhibits the comparison between the faults and veins extracted from the ant-tracked seismic data and the vein lode map provided by Evolution Mining. However, the

information was used without any conversion since no information about the mapping projection was found.

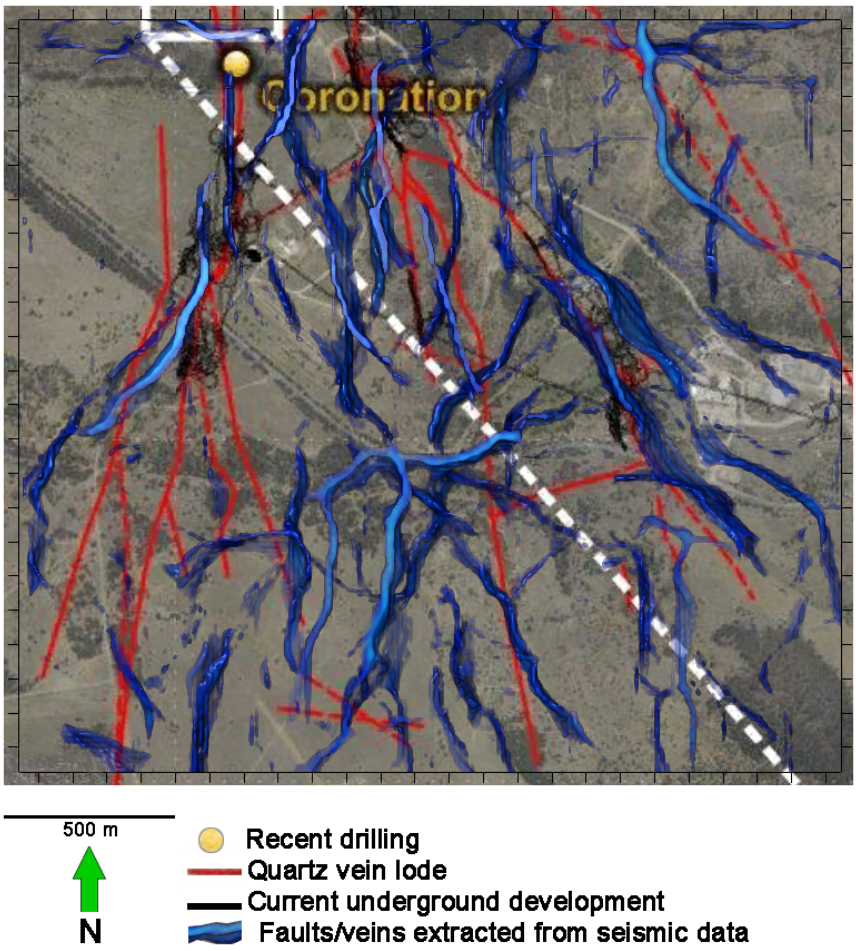

Figure 6-13: Comparison of ant-tracking results with the quartz vein lode map provided in (Evolution Mining 2014).

6.4.3. Property modelling

A 3D grid was constructed using a cell size of 20 m×20 m ×10 m. HiSeis Pty Ltd supplied the lithological logs collected from the boreholes in the Cracow mining area. Fault and the horizon borehole tops from 457 boreholes were employed to create zone log for each borehole. Thirteen major lithologic types that consist of more than 95% of the total lithology were upscaled to the grid. The zone logs were upscaled using the Property modelling module in Schlumberger Petrel. Figure 6-14 displays the zone logs upscaled to the grid resolution.

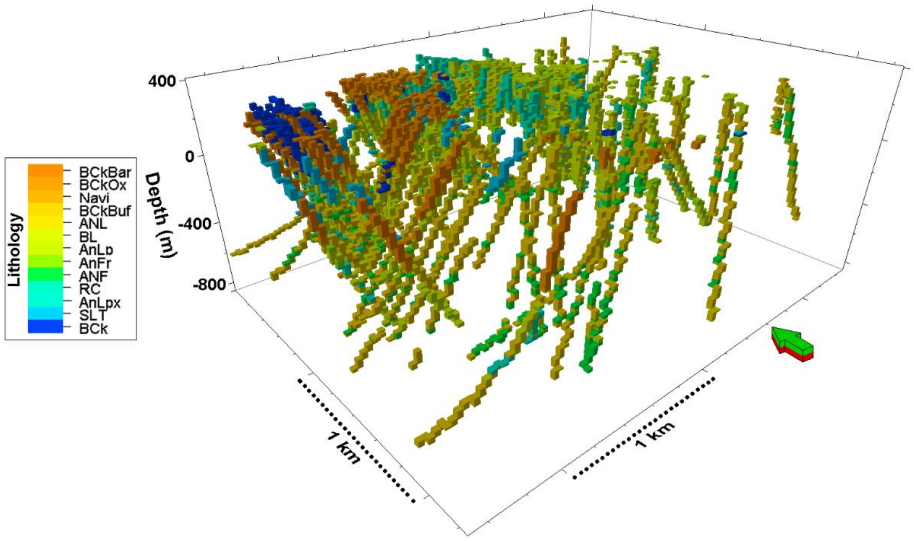

Figure 6-14: Zone logs created from 457 boreholes were upscaled to the grid to create a facies model.

A facies model was constructed by using the upscaled lithological data. To minimise the effect of horizontal interpolation, a Gaussian variogram was calculated from the upscaled property using the data analysis toolbox in Schlumberger Petrel. Facies modelling employed Sequential Gaussian Simulation (SGS) algorithm to interpolate the upscaled property. Figure 6-15 exhibits the constructed facies model of the study area.

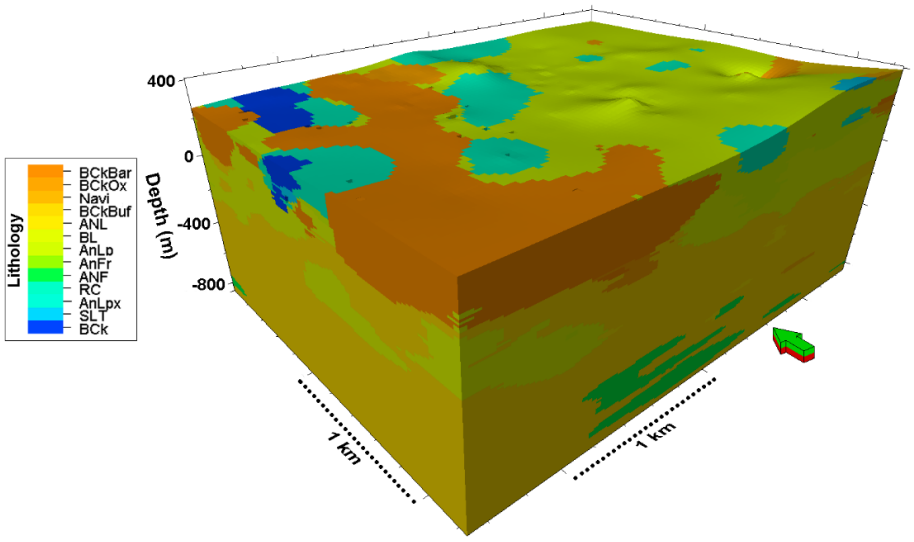

Figure 6-15: Facies model of Cracow was constructed by interpolating the upscaled zone logs from 457 boreholes using a Gaussian variogram calculated from the upscaled property.

Figure 6-16 shows a projection of the faults tracked from the edge-detected seismic data over the facies model. The lithological boundaries on the facies model are showing a moderate correlation with the projected fault network.

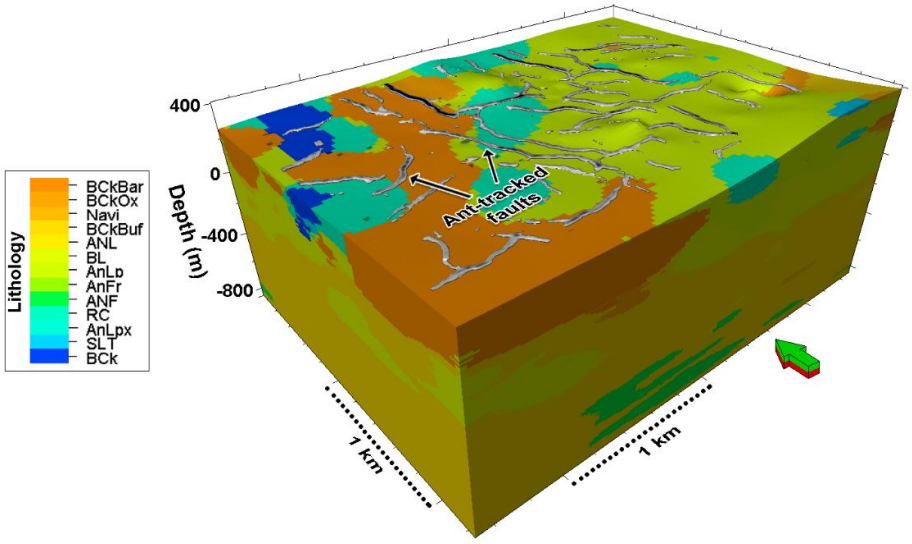

Figure 6-16: Projection of the fault network extracted from the edge-detected seismic data over the facies model. The discontinuities demonstrate a moderate correlation with the lithological boundaries of the facies model.

The faults extracted by ant-tracking workflow were projected on the facies model at various depth levels. Faults detected in the boreholes were also projected to check the consistency of the ant-tracking output. Figure 6-17 demonstrates a horizontal slice of the facies model at 200 m AHD. Discontinuities extracted from the seismic data shows a good match with the lithological boundaries. Faults encountered in the borehole were also projected on the horizontal section to check the accuracy of the ant-tracked discontinuities. Fault borehole tops projected on the horizontal slice were within 25 m.

Similar procedures were also undertaken at 0 m AHD, -140 m AHD and -300 m AHD to check the precision of the ant-tracking output. Figure 6-18 shows a horizontal slice of the facies model at 0 m AHD with the associated discontinuities extracted from the seismic data and faults encountered in the boreholes within 25 m of the horizontal slice. Figure 6-19 and Figure 6-20 exhibit the performance of ant-tracking at -140 m AHD and -300 m AHD respectively.

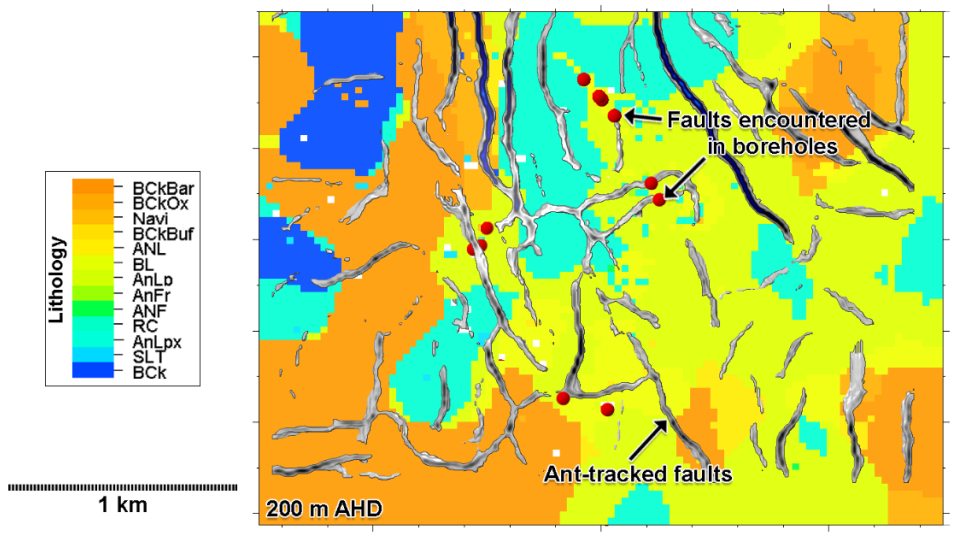

Figure 6-17: Comparison of ant-tracking, facies model and faults encountered in the borehole on a horizontal slice at 200 m above the Australian Height Datum.

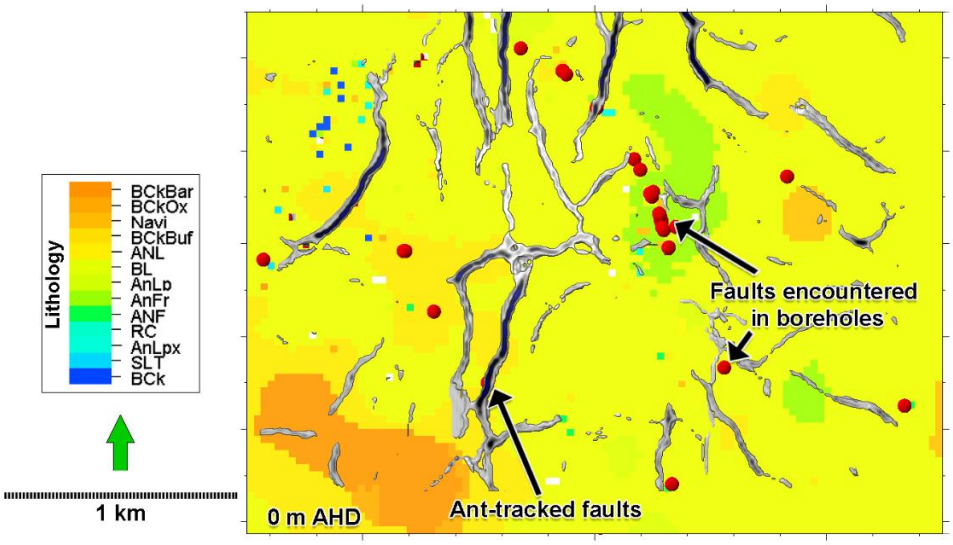

Figure 6-18: Comparison of ant-tracking, facies model and faults encountered in the borehole on a horizontal slice at the Australian Height Datum.

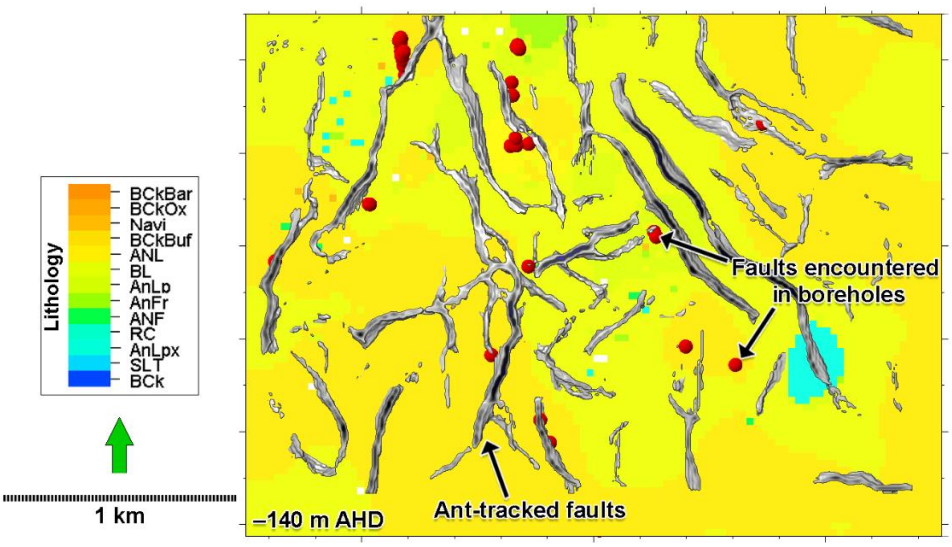

Figure 6-19: Comparison of ant-tracking, facies model and faults encountered in the borehole on a horizontal slice at 140 m below the Australian Height Datum.

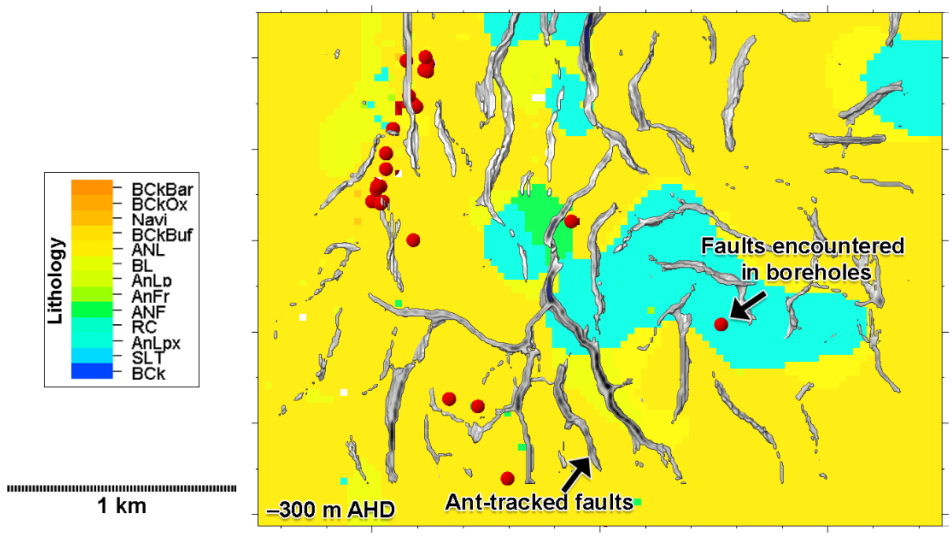

Figure 6-20: Comparison of ant-tracking, facies model and faults encountered in the borehole on a horizontal slice at 300 m below the Australian Height Datum.

Ant-tracking workflow performed poorly at depths beyond -500 m AHD due to the fact that signal-to-noise ratio deteriorate with increasing depth. However, the extracted discontinuities showed some correlation with the facies model and faults observed in the boreholes.

6.5. Summary

The 3D seismic reflection survey at Cracow gold mine was conducted to delineate the fault network where high-grade gold mineralisation occurs. HiSeis Pty Ltd operated the seismic acquisition programme. The seismic data was processed at HiSies Pty Ltd by utilising 3D Kirchhoff prestack time-migration algorithm.

Acquisition footprints were observed in the ant-tracked volume parallel to the source and receiver lines at shallow depths. Cracow seismic dataset suffers from acquisition footprints due to the low data fold at shallow depths. Moreover, a significant change in elevation from east to west also contributed to the generation of acquisition footprints in the low-lying areas. The empty part of the dataset to the top was cropped from 470 m to 250 m above the Australian Height Datum to reduce the effect of acquisition footprints during ant-tracking and to remove the areas that are devoid of seismic reflections.

The volumetric interpretation approach implemented seismic attribute analysis to interpret the subvertical to vertical faults and epithermal veins. It has been observed that cropping the source amplitude makes no visual difference; however, cropping the amplitude (~0.2% data were shredded from the lower and upper amplitude range) improved edge detection and edge enhancement outputs.

Faults extracted from the seismic volume using ant-tracking workflow showed very good correlation with the facies model simulated from borehole lithology. The discontinuities showed good agreement with the facies boundaries up to 750 m depth. At depths beyond 750 m, ant-tracking workflow performed poorly; however, discontinuities extracted from the seismic data showed correlation with the facies boundaries and fault borehole tops.

7. Discussion and conclusions

Discovery of new mineral deposits requires a thorough knowledge of rock formation processes, subvertical to vertical faults and fractures that may act as the fluid pathway for mineralisation and complex subsurface geological conditions. High-resolution seismics can delineate deep and complex structures with better accuracy compared to the conventional geophysical methods in mineral exploration. Despite being successful in sedimentary environments, seismic methods are facing some challenges in hard rock environments:

- The velocity contrast between the overburden regolith layer and the bedrock causes attenuation of seismic signals by distorting, scattering, and absorbing seismic energy.
- The absence of continuous reflectors and very complex subsurface geology in hard rock environments makes it hard to obtain information to construct a velocity model.
- Seismic data collected over hard rock environments suffers from low signal-to-noise ratio due to the small range of elastic properties of the hard rock media.
- Hard rock environments are characterised by the abundance of fracture zones, fissures, subvertical to vertical faults, and alterations. These geological complexities make hard rock seismic imaging a challenge.
- Commercial interpretation software packages are developed to work in sedimentary environments. Direct application of some attributes and workflows on hard rock seismic data does not produce an acceptable outcome.

The challenges faced during the volumetric interpretation of 3D hard rock seismic datasets and the approaches taken to overcome them are discussed in the following section.

7.1. Discussion

Seismic volumetric interpretation has several advantages over the conventional interpretation methods. In conventional interpretation, a seismic volume is sliced into 2D planes for interpretation whereas in volumetric interpretation a seismic volume is interpreted by employing different levels of transparency to the data. This provides an interpreter with the 3D insight into the geology. Multiple volume attributes are displayed together by applying different levels of transparency to each volume. Furthermore, multiple volume visualisations and volume blending visualisation techniques provide an interpreter advantages to integrate structural, stratigraphic and amplitude data to reveal and evaluate regional and prospect-specific details. However, detailed understanding of visualisation functionality and their expected outputs must be contemplated during the interpretation processes.

7.1.1. Case study: Hillside copper-gold mine, South Australia

Interpretation of the 3D seismic data collected from Hillside Cu-Au mining project in Yorke Peninsula of South Australia was a challenging task. Attenuation of seismic energy due to the presence of regolith overburden, very complex subsurface geological setting, numerous subvertical mineralisation pathways along faults and fractures made the seismic acquisition survey a daunting task. The seismic acquisition was conducted by using a high-density design. Seismic data acquisition was accomplished using a 375 kg concreted breaker acting as a free-fall weight mounted on a skid-steer loader as the seismic source. The survey was conducted using five overlapping receiver patch with 50% overlap along receiver lines. The shot point spacing was 10 m, shot line spacing was 40 m, receiver spacing was 5 m, and receiver line spacing was 30 m.

In total, 505 core samples from five boreholes were analysed to measure P-wave velocity, density and magnetic susceptibility. However, only 289 measurements with confirmed lithology were used in this study. P-wave velocity data was measured from dry, solid, 10-20 cm long core samples using ultrasonic pulse transmitter, receiver and a 2 GHz digital oscilloscope. The density of the cores was measured using Archimedes' principle. Physical property data analysis surmises that the acoustic impedance contrast

between the rocks in Hillside is not strong enough to produce effective P-wave reflections at the stratigraphic boundaries.

The seismic data processing employed refraction statics to resolve near-surface geological issues due to the presence of a regolith overburden. The regolith layer attenuated much of higher frequencies, which resulted in poor imaging of subvertical structures that may have acted as the mineralisation pathways. The data was re-binned to double the fold and increase the signal-to-noise ratio. Source de-signature and spectral whitening were applied in the prestack domain to increase the spatial resolution without amplifying the noise. 3D prestack Kirchhoff time-migration algorithm was used to image subvertical structures. The velocity model employed in time-to-depth conversion was constructed using the velocities picked from the seismic data. The velocity data measured from the core samples was similar to the velocity data picked from seismic. However, velocity measured from the core samples from borehole HDD-064 showed some discrepancies at shallow depths with the velocity picked from the seismic data.

Interpretation of 3D seismic data from Hillside Cu-Au mine in South Australia involved seismic attribute analysis. Information from the physical property data analysis was evaluated during the seismic interpretation. Seismic attributes were implemented to interpret the data. The stratigraphic attributes did not perform well due to low signal-to-noise ratio, lack of continuous seismic reflectors, attenuation of seismic signals in the regolith overburden, and low-fold data at shallow depths. However, structural attributes such as variance and fracture density provided good results. Complex workflows, e.g., Ant-tracking, GeoTeric FaultApp, produced results in agreement with the geological interpretation. Fault detection using ant-tracking provided excellent outputs. The faults demonstrated a very good agreement with the geological cross-section provided by Rex Minerals Ltd. A fault volume for the top 500 m was extracted from the ant-tracked data. These results are to be used in future drilling campaign and subsequent mine development programme.

7.1.2. Case study: Kevitsa nickel-copper-platinum group elements mine, Finland

Kevitsa is a large, low-grade, disseminated Sulphide Ni-Cu-PGE deposit located within layered sedimentary and volcanic rocks of the Central Lapland Greenstone Belt in northern Finland. The Central Lapland Greenstone Belt is characterised by Paleoproterozoic supracrustal rocks of volcano-sedimentary stratigraphic groups. The 3D seismic data acquisition survey in Kevitsa was conducted over a period of two months covering an area of nine square kilometres. The survey was divided into nine orthogonal patches with 50% overlap. HiSeis Pty Ltd and Uppsala University jointly operated two recording systems (Seistronix and Sercel 408) to collect the data. Explosives and a mechanical hammer (Vibsist) were exploited as the seismic source. The shot point spacing was 45 m, shot line spacing was 80 m, receiver spacing was 15 m, and receiver line spacing was 70 m. The data acquired through Seistronix were resampled to 1 ms sampling interval and merged with Sercel data.

In 2010, the first attempt of the data processing was done through several steps. Vibsist data were processed using shift and stack method. Repetitive hammer blows were rejected to avoid harmonics in the stacked shot record. Source de-signature and amplitude balance were performed before shift and stack could be accomplished. The processing flow also included surface consistent static corrections followed by dynamic corrections. The imaging phase included 3D dip moveout correction followed by poststack migration. In 2014, the 3D dataset was reprocessed with preserved relative amplitudes to improve imaging at shallow depths by refining the static solution and the velocity model. The amplitude consistent processing included trace editing, spherical divergence correction, surface consistent amplitude recovery and deconvolution. 3D Kirchhoff prestack time-migration was used to migrate the seismic data. The data processing was finalised by using sonic logs to convert the data from time-domain to depth-domain.

The interpretation of Kevitsa seismic data was performed implementing seismic attribute analysis. Seismic attributes such as 3D edge enhancement, dip illumination were able to trace the major stratigraphic boundaries. Local structural azimuth and local structural dip provided the general trend of the data. However, the stratigraphic

attributes were unable to add any additional value to the interpretation due to lack of continuous reflections, low signal-to-noise ratio and low data fold at the shallower part of the data. Most of the near-offset traces have an offset of 50 m to 100 m in the shallower part of the data because of the shot line spacing of 80 m and receiver line spacing of 100 m. As a result, the near-surface structures were undersampled due to lower fold number at shallow depths. Fault detection by employing ant-tracking workflow provided a moderate result. However, the absence of reflections at the top 200 m contributed to substandard output for the shallower part of the data.

Physical property modelling was performed by upscaling P-wave velocity, Density, Cu (wt.%) and Ni (wt.%) logs from the Kevitsa boreholes to the structural grid to simulate petrophysical models. The Kevitsa structural grid was constructed by using the horizons and faults interpreted from the seismic data. No direct relationship between Cu and Ni-grade and seismic was observed.

7.1.3. Case study: Cracow gold mine, Queensland

The Cracow gold mine is situated within the upper Palaeozoic Camboon volcanic arc on the southeastern margin of the Bowen basin in Queensland. HiSeis Pty Ltd conducted a 3D seismic data acquisition programme to delineate and characterise subvertical faults and epithermal quartz veins along which gold mineralisation is confined. The seismic data acquisition was completed using six overlapping patches with 15 m receiver interval and 30 m source interval. The source line spacing was 90 and the receiver line spacing was 75 m.

The seismic data interpretation employed a depth converted 3D Kirchhoff prestack time-migrated volume supplied by HiSeis Pty Ltd. The seismic volume was preconditioned by amplitude filtering, removing deconvolution bias and dip-guided structural smoothing. The seismic dataset suffers from acquisition footprints due to low data fold at shallow depths. Moreover, a significant change in elevation from east to west also contributed to the generation of acquisition footprints in low-lying areas. The top part and the northern part of the seismic volume was cropped to remove the low data fold area and the padded area in the north. Seismic attribute analysis by utilising instantaneous phase, cosine of phase, semblance, consistent dip, similarity, Laplacian edge enhancement was able to detect and enhance discontinuities imaged by the seismic

data. However, the stratigraphic attributes did not work optimally at shallow depths due to low data fold, absence of prominent marker beds and poor signal-to-noise ratio. Fault detection employing ant-tracking workflow provided an excellent output.

Borehole lithological logs supplied by HiSies Pty Ltd were utilised in facies modelling. Thirteen major lithological types representing 95% of the data were upscaled to the structural grid to perform facies modelling. The modelled facies boundaries shows moderate correlation with the discontinuities delineated by ant-tracking workflow. The faults delineated using ant-tracking workflow demonstrates an exquisite relationship with the drilling data. The result obtained from the seismic data interpretation can contribute significantly in future drilling programmes and brownfield exploration in the area.

7.2. Conclusions

The biggest challenge of employing seismic reflection method for mineral exploration in hard rock environments is the low signal-to-noise ratio. The impedance contrasts and reflection coefficients between the most common igneous and metamorphic rocks are smaller than the required level to produce discernible reflections. Hence, it is more difficult to image structures in hard rock environments. The traditional seismic interpretation approach does not work optimally on the seismic data collected over hard rock environments. Lack of prominent marker horizons in hard rock environments makes the traditional interpretation approach insurmountable.

This thesis addressed three case studies from different geological settings. The traditional attribute analysis on the seismic data provided mixed results. Although, some structural attributes identified subvertical to vertical structures but most stratigraphic attributes failed to provide satisfactory results; implying that currently existing interpretation approaches are not adequate for hard rock seismic data interpretation.

The application of 3D edge detection and enhancement attributes and fault-detection workflows was able to provide moderate to excellent results. Fault detection using ant-tracking workflow was performed for the first time on hard rock seismic datasets. All three case studies provided good results.

This research shows that the application of volumetric interpretation techniques greatly helps in delineating subvertical to vertical structures that hosts mineral deposits. Direct integration of structural, stratigraphic and physical property data with seismic amplitudes helps to reveal prospect-specific details.

Undoubtedly, seismic reflection method is the most powerful tool for deep mineral exploration that provides reliable images of complex subsurface structures. Adaptation of cutting-edge volume-based interpretation approaches and development of new ones is an essential component for the evolution of hard rock seismic exploration.

In this research the method of volumetric seismic interpretation, widely used in oil industry, has been successfully transferred and adapted to mineral exploration objectives. The techniques and approaches applied to vastly different geological settings unquestionably demonstrate the value of the application of seismic volumetric interpretation for characterisation of mineral deposits.

Bibliography

Alapieti, T. 2005. "Early Palaeoproterozoic (2.5–2.4 Ga) Tornio–Näränkävaara Layered Intrusion Belt and Related Chrome and Platinum-Group Element Mineralization, Northern Finland." *Field trip guidebook: Early palaeoproterozoic (2.5-2.4) Tornio-Näränkävaara layered intrusion belt and related chrome and platinum-group element mineralization, Northern Finland. Ed. by TT Alapieti & AJ Kärki. Geological survey of Finland. Guide nro 51a. Espoo*: 5-11.

Anderson, N., and S. Cardimona. 1995. "Forward Seismic Modeling: The Key to Understanding Reflection Seismic and Ground Penetrating Radar (GPR) Techniques." Department of Geology and Geophysics, University of Missouri-Rolla, Rolla, MO.

Barnes, A. 2007. "Redundant and Useless Seismic Attributes." *Geophysics* 72 (3): P33–P38. doi: 10.1190/1.2716717.

Barrie, C., and M. Hannington. 1999. "Classification of Volcanic-Associated Massive Sulfide Deposits Based on Host-Rock Composition." *Reviews in Economic Geology* 8: 1-11.

Barton, P. 1986. "The Relationship between Seismic Velocity and Density in the Continental Crust - a Useful Constraint?" *Geophysical Journal of the Royal Astronomical Society* 87: 195–208.

Beard, A., H. Downes, E. Hegner, and S. Sablukov. 2000. "Geochemistry and Mineralogy of Kimberlites from the Arkhangelsk Region, Nw Russia: Evidence for Transitional Kimberlite Magma Types." *Lithos* 51 (1): 47-73.

Bell, F., and L. Donnelly. 2006. *Mining and Its Impact on the Environment*. London: Taylor and Francis.

Bellefleur, G., C. Müller, D. Snyder, and L. Matthews. 2004. "Downhole Seismic Imaging of a Massive Sulphide Orebody with Mode-Converted Waves, Halfmile Lake, New Brunswick, Canada." *Geophysics* 69: 318–329.

Blain, C. 2000. "Fifty-Year Trends in Minerals Discovery—Commodity and Ore-Type Targets." *Exploration and Mining Geology* 9 (1): 1-11.

Bland, H., and R. Stewart. 1993. "3-D Seismic Visualization." *Consortium for Research in Elastic Wave Exploration Seismology Research Report* 5 http://www.crewes.org/ForOurSponsors/ResearchReports/1993/1993-23a.pdf.

Blewett, R., K. Czarnota, and P. Henson. 2010. "Structural-Event Framework for the Eastern Yilgarn Craton, Western Australia, and Its Implications for Orogenic Gold." *Precambrian Research* 183 (2): 203–229.

Bowie, S., A. Kvalheim, and H. Haslam. 1978. *Mineral Deposits of Europe: Northwest Europe*. Vol. 1: Institution of mining and metallurgy.

Bradley, D., and D. Leach. 2003. "Tectonic Controls of Mississippi Valley-Type Lead–Zinc Mineralization in Orogenic Forelands." *Mineralium Deposita* 38 (6): 652-667.

Brown, A. 1996. "Seismic Attributes and Their Classification." *Leading Edge* 10: 1090.

Brown, A. 2005. "Pitfalls in 3D Seismic Interpretation: Keynote Presentation at the 11th Annual 3-D Seismic Symposium, Denver." *The leading edge* 24 (7): 716-717.

Calvert, A., and Y. Li. 1999. "Seismic Reflection Imaging over a Massive Sulfide Deposit at the Matagami Mining Camp, Quebec." *Geophysics* 64 (1): 24-32.

Campbell, G., and J. Crotty. 1990. "3-D Seismic Mapping for Mine Planning Purposes at the South Deep Prospect" *Proceedings of the International Deep Mining Conference: SAIMM Symposium Series SIO, 2*,

Campbell, G. 1994. "Geophysical Contributions to Mine-Development Planning: A Risk Reduction Approach" *15th CMMI Congress: The Southern African Institute of Mining and Metallurgy Symposium Series*,

Chen, H. 2013. "External Sulphur in Iocg Mineralization: Implications on Definition and Classification of the Iocg Clan." In *Ore Geology Review*.

Chen, H., P. Ni, R.-C. Wang, G.-G. Wang, K.-D. Zhao, J.-Y. Ding, C. Zhao, Y.-T. Cai, and Y.-F. Xu. 2015. "A Combined Fluid Inclusion and S–Pb Isotope Study of the Neoproterozoic Pingshui Volcanogenic Massive Sulfide Cu–Zn Deposit, Southeast China." *Ore Geology Reviews* 66: 388-402.

Chopra, S., and K. Marfurt. 2005. "Seismic Attributes—a Historical Perspective." *Geophysics* 70 (5): 3SO-28SO.

Chopra, S., and K. Marfurt. 2007. *Seismic Attributes for Prospect Identification and Reservoir Characterization*, *Geophysical Developments Series*: Society of Exploration Geophysicists and European Association of Geoscientists and Engineers.

Churkin, M., C. Carter, and J.H. Trexler. 1980. "Collision-Deformed Paleozoic Continental Margin of Alaska—Foundation for Microplate Accretion." *Geological Society of America Bulletin* 91 (11): 648-654.

Clark, D. 2014. "Magnetic Effects of Hydrothermal Alteration in Porphyry Copper and Iron-Oxide Copper–Gold Systems: A Review." *Tectonophysics* 624–625: 46-65. doi: http://dx.doi.org/10.1016/j.tecto.2013.12.011.

Cloud, P. 1973. "Paleoecological Significance of the Banded Iron-Formation." *Economic Geology* 68 (7): 1135-1143.

Conor, C., O. Raymond, T. Baker, G. Teale, P. Say, and G. Lowe. 2010. "Alteration and Mineralisation in the Moonta-Wallaroo Copper-Gold Mining Field Region, Olympic Domain, South Australia." In *2010 Hydrothermal Iron Oxide Copper-Gold and Related Deposits: A Global Perspective*, ed. T.M. Porter, 147–170. Adelaide: PGC Publishing, Adelaide.

Cooke, D., P. Hollings, and J. Walshe. 2005. "Giant Porphyry Deposits: Characteristics, Distribution, and Tectonic Controls." *Economic Geology* 100 (5): 801–818.

Cosma, C., P. Heikkinen, J. Keskinen, and N. Enescu. 2001. "Vsp in Crystalline Rocks – Form Downhole Velocity Profiling to 3-D Fracture Mapping." *International Journal of Rock Mechanics and Mining Sciences* 38 (6): 843–850.

Creenaune, P., and K. Braund. 2001. "The Klondyke Gold Discovery, Cracow Queensland – Exploration Strategies Leading to Discovery." In *SMEDG - AIG Symposium 2001*, *Sydney, Australia*. http://www.smedg.org.au/Sym01PC.htm.

Creenaune, P., K. Braund, and R. McLeod. 2003. "The Cracow Gold Project, Cracow, Queensland, a Discovery Case History" *NewGenGold 2003*, *Glenside, S. Aust.*: Louthean Media Pty Ltd.

Cui, T., J. Yang, and I.M. Samson. 2012. "Tectonic Deformation and Fluid Flow: Implications for the Formation of Unconformity-Related Uranium Deposits." *Economic Geology* 107 (1): 147-163.

DeMatties, T. 1994. "Early Proterozoic Volcanogenic Massive Sulfide Deposits in Wisconsin; an Overview." *Economic Geology* 89 (5): 1122-1151.

Dindi, E., and J. Maneno. 2016. "Geological and Geophysical Characteristics of Massive Sulphide Deposits: A Case Study of the Lirhanda Massive Sulphide Deposit of Western Kenya." *Journal of African Earth Sciences* 120: 89-101.

Dong, G., and T. Zhou. 1996. "Zoning in the Carboniferous-Lower Permian Cracow Epithermal Vein System, Central Queensland, Australia." *International Journal of Geology, Mineralogy and Geochemistry of Mineral Deposits* 31 (3): 210–224. doi: 10.1007/BF00204028.

Doyle, M., and R. Allen. 2003. "Subsea-Floor Replacement in Volcanic-Hosted Massive Sulfide Deposits." *Ore Geology Reviews* 23 (3): 183-222.

Düweke, W., J. Trickett, K. Tootal, and M. Slabbert. 2002. "Three-Dimensional Reflection Seismics as a Tool to Optimize Mine Design, Planning and Development in the Bushveld Igneous Complex." In *64th Auunal International Conference and Exhibition, EAGE, Extended Abstracts*, D-20.

Eaton, D., B. Milkereit, and M. Salisbury. 2003. "Seismic Methods for Deep Mineral Exploration: Mature Technologies Adapted to New Targets." *The Leading Edge* 22 (6): 580-585.

Eerola, T. 2013. "A Model for Stakeholder Engagement in Mineral Exploration in Finland" *Proceedings, 6th International Conference on Sustainable Development of Mining Industry, Milos, Greece*,

Eilu, P., and D. Groves. 2001. "Primary Alteration and Geochemical Dispersion Haloes of Archaean Orogenic Gold Deposits in the Yilgarn Craton: The Pre-Weathering Scenario." *Geochemistry: Exploration, Environment, Analysis* 1 (3): 183–200.

Eilu, P., P. Sorjonen-Ward, P. Nurmi, and T. Niiranen. 2003. "A Review of Gold Mineralization Styles in Finland." *Economic Geology* 98 (7): 1329-1353.

Eilu, P. 2015. "Chapter 5.1 - Overview on Gold Deposits in Finland." In *Mineral Deposits of Finland*, ed. W.D.M.L. O'Brien, 377-410. Elsevier.

Evans, A. 1993. *Ore Geology and Industrial Minerals : An Introduction*. 3rd ed. Oxford: Blackwell Scientific Publications.

Evolution Mining. 2014. "June 2014 Quarterly Report." http://www.evolutionmining.com.au/wp-content/uploads/2015/04/1099.pdf.

Evolution Mining. 2015a. Cracow Fact Sheet. Accessed 09/02/2016, http://www.evolutionmining.com.au/wp-content/uploads/2015/12/Cracow-Fact-Sheet_Dec-2015_web.pdf.

Evolution Mining. 2015b. Cracow. Accessed 09/02/2016, http://www.evolutionmining.com.au/cracow/.

Ewers, W., and R. Morris. 1981. "Studies of the Dales Gorge Member of the Brockman Iron Formation, Western Australia." *Economic Geology* 76 (7): 1929–1953.

Fiorentini, M., S. Barnes, C. Lesher, G. Heggie, R. Keays, and O. Burnham. 2010. "Platinum Group Element Geochemistry of Mineralized and Nonmineralized Komatiites and Basalts." *Economic Geology* 105 (4): 795-823.

First Quantum Minerals Ltd. 2013. *Annual Report*. http://www.first-quantum.com/files/doc_downloads/2013_FQM%20Annual%20Report.pdf.

First Quantum Minerals Ltd. 2015. Production Stats. First Quantum Minerals Ltd. Accessed 19-11-2015, http://www.first-quantum.com/Our-Business/operating-mines/Kevitsa/default.aspx.

Gadallah, M., and R. Fisher. 2005. *Applied Seismology: A Comprehensive Guide to Seismic Theory and Application*: PennWell Books.

Galley, A. 1993. "Characteristics of Semi-Conformable Alteration Zones Associated with Volcanogenic Massive Sulphide Districts." *Journal of Geochemical Exploration* 48 (2): 175–200.

Geological Survey of Finland. 2014. Copper in Finland. Geological Survey of Finland. 14/11/2014 Accessed 15/08/2015, http://en.gtk.fi/informationservices/commodities/copper.html.

Gervilla, F., and K. Kojonen. 2002. "The Platinum-Group Minerals in the Upper Section of the Keivitsansarvi Ni–Cu–PGE Deposit, Northern Finland." *The Canadian Mineralogist* 40 (2): 377–394.

Gibson, H., R. Allen, G. Riverin, and T. Lane. 2007. "The Vms Model: Advances and Application to Exploration Targeting." In *Proceedings of Exploration 07: Fifth Decennial International Conference on Mineral Exploration*, ed. B. Milkereit, 713–730. Toronto, Canada.

Goldfarb, R., G. Phillips, and W. Nokleberg. 1998. "Tectonic Setting of Synorogenic Gold Deposits of the Pacific Rim." *Ore Geology Reviews* 13 (1–5): 185-218. doi: http://dx.doi.org/10.1016/S0169-1368(97)00018-8.

Goldfarb, R., D. Groves, and S. Gardoll. 2001. "Orogenic Gold and Geologic Time: A Global Synthesis." *Ore geology reviews* 18 (1): 1–75.

Goldfarb, R., T. Baker, B. Dube, D. Groves, C. Hart, and P. Gosselin. 2005. "Distribution, Character, and Genesis of Gold Deposits in Metamorphic Terranes." *Economic Geology 100th anniversary volume* 40.

Goleby, B., D. Johnstone, L. Jones, B. Drummond, and T. Barton. 2005. "Choosing the Lines." In *The 2003 Gawler Craton Seismic Survey: Notes from the Seismic Workshop Held at Gawler Craton State of Play 2004*, eds P. Lyons and B.R. Goleby, 11–16. Geoscience Australia, Government of South Australia.

Greenhalgh, S., I. Masonz, and C. Sinadinovski. 2000. "In-Mine Seismic Delineation of Mineralization and Rock Structure." *Geophysics* 65 (6): 1908–1919.

Greenwood, A. 2013. "Application of Vertical Seismic Profiling for the Characterisation of Hard Rock." Exploration Geophysics, Curtin University, Perth, WA. http://link.library.curtin.edu.au/p?cur_digitool_dc192268.

Groves, D. 1993. "The Crustal Continuum Model for Late-Archaean Lode-Gold Deposits of the Yilgarn Block, Western Australia." *Mineralium deposita* 28 (6): 366-374.

Groves, D., R. Goldfarb, M. Gebre-Mariam, S. Hagemann, and F. Robert. 1998. "Orogenic Gold Deposits: A Proposed Classification in the Context of Their Crustal Distribution and Relationship to Other Gold Deposit Types." *Ore Geology Reviews* 13 (1–5): 7–27. doi: http://dx.doi.org/10.1016/S0169-1368(97)00012-7.

Halkoaho, T., T. Alapieti, and J. Lahtinen. 1990. "The Sompujärvi PGE Reef in the Penikat Layered Intrusion, Northern Finland." *Mineralogy and Petrology* 42 (1–4): 39–55.

Hanski, E., and H. Huhma. 2005. "Chapter 4: Central Lapland Greenstone Belt." In *Developments in Precambrian Geology*, eds M. Lehtinen, P.A. Nurmi and O.T. Rämö, 139–193. Elsevier.

Hayward, N., and R. Skirrow. 2010. "Geodynamic Setting and Controls on Iron Oxide Cu-Au (±U) Ore in the Gawler Craton, South Australia." *Hydrothermal iron oxide copper-gold and related deposits: A global perspective* 3: 105-131.

Herron, D., and R. Latimer, eds. 2011. *First Steps in Seismic Interpretation*. Tulsa, Oklahoma: Society of Exploration Geophysicists.

Hilterman, F. 1982. "Interpretative Lessons from Three-Dimensional Modeling." *Geophysics* 47 (5): 784-808.

Hitzman, M., N. Oreskes, and M. Einaudi. 1992. "Geological Characteristics and Tectonic Setting of Proterozoic Iron Oxide (Cu–U–Au–Ree) Deposits." *Precambrian Research* 58 (1): 241–287. doi: 10.1016/0301–9268(92)90121–4.

Holbrook, W., W. Mooney, and N. Christensen. 1992. "The Seismic Velocity Structure of the Deep Continental Crust." In *Continental Lower Crust*, 1–43. Elsevier Amsterdam.

Holcombe, R., C. Stephens, C. Fielding, D. Gust, T. Little, R. Sliwa, J. McPhie, and A. Ewart. 1997. "Tectonic Evolution of the Northern New England Fold Belt: Carboniferous to Early Permian Transition from Active Accretion to Extension." In *Tectonics and Metallogenesis of the New England Orogen*, 52-65. Special Publication of the Geological Society of Australia.

Holden, E.-J., M. Dentith, and P. Kovesi. 2008. "Towards the Automated Analysis of Regional Aeromagnetic Data to Identify Regions Prospective for Gold Deposits." *Computers & Geosciences* 34 (11): 1505-1513.

Hossain, M., M. Urosevic, and A. Kepic. 2013. "Volumetric Interpretation of 3D Hard Rock Seismic Data." *ASEG Extended Abstracts* 2013 (1): 1-3. doi: 10.1071/ASEG2013ab088

Hossain, M., M. Urosevic, and A. Kepic. 2014a. "Volumetric Interpretation of 3D Seismic Data from the Hillside Iocg Deposit in South Australia." In *76th EAGE Conference and Exhibition–Hard Rock Seismic Imaging Workshops*, *Amsterdam, The Netherlands,* 16–19 June 2014. WS5–P05. EAGE.

Hossain, M., M. Urosevic, and A. Kepic. 2014b. "Volumetric Interpretation of 3D Seismic Data from the Hillside Iocg Deposit in South Australia" *76th EAGE Conference and Exhibition-Workshops*, doi: 10.3997/2214–4609.20140516

Hossain, M., M. Urosevic, and C. Wijns. 2015a. "Seismic Volumetric Interpretation of a Disseminated Copper System in Kevitsa, Northern Finland." In *24th International Geophysical Conference and Exhibition*, 1–4. ASEG–PESA 2015.

Hossain, M., M. Urosevic, and A. Kepic. 2015b. "Interpretation of 3D High-Resolution Seismic Data Collected over an Iocg Deposit in South Australia." *ASEG Extended Abstracts* 2015 (1): 1-5. doi: 10.1071/ASEG2015ab210.

Hughes, F. 1990. *Geology of the Mineral Deposits of Australia and Papua New Guinea*. Edited by F.E. Hughes. 2 vols. Parkville, VIC: Australasian Institute of Mining and Metallurgy.

Ismail, R., C. Ciobanu, N. Cook, G. Teale, D. Giles, A. Mumm, and B. Wade. 2014. "Rare Earths and Other Trace Elements in Minerals from Skarn Assemblages, Hillside Iron Oxide–Copper–Gold Deposit, Yorke Peninsula, South Australia." *Lithos* 184–187: 456-477. doi: http://dx.doi.org/10.1016/j.lithos.2013.07.023.

Jamieson, J., M. Hannington, S. Petersen, and M. Tivey. 2014. "Volcanogenic Massive Sulfides." In *Encyclopedia of Marine Geosciences*, eds J. Harff, M. Meschede, S. Petersen and J. Thiede. Dordrecht: Springer Netherlands.

Jones, J., C. Stephens, and A. Ewart. 1996. "Constraints on the Early Permian and Late Carboniferous of the Northern New England Fold Belt from the Camboon Volcanics and the Torsdale Beds" *Geological Society of Australia Abstracts*,

Juhlin, C., and M. Stephens. 2006. "Gently Dipping Fracture Zones in Paleoproterozoic Metagranite, Sweden; Evidence from Reflection Seismic and Cored Borehole Data and Implications for the Disposal of Nuclear Waste." *Journal of Geophysical Research* 111, B09302. doi: 10.1029/2005JB003887.

Kallweit, R., and L. Wood. 1982. "The Limits of Resolution of Zero-Phase Wavelets." *Geophysics* 47 (7): 1035-1046.

Kellaway, B. 2013. *Updated Review of the Mineral Potential of the Piilola Group of Licences, Eastern Finland*. Cardiff, UK. http://kareliangold.com/wp-content/uploads/2013/02/MENFin_2013_FINAL_20130221.pdf.

Kennedy, C., and G. Kennedy. 1976. "The Equilibrium Boundary between Graphite and Diamond." *Journal of Geophysical Research* 81 (14): 2467-2470.

Kidd, G. 1999. "Fundamentals of 3D Seismic Volume Visualization." In *1999 Offshore Technology Conference Paper 11054*, *Houston, Texas,* 3–6 May 1999. 823–836.

Koivisto, E., A. Malehmir, P. Heikkinen, S. Heinonen, and I. Kukkonen. 2012. "2D Reflection Seismic Investigations at the Kevitsa Ni-Cu-PGE Deposit, Northern Finland." *Geophysics* 77 (5): WC149-WC162. doi: 10.1190/geo2011-0496.1.

Koivisto, E., A. Malehmir, N. Hellqvist, T. Voipio, and C. Wijns. 2015. "Building a 3D Model of Lithological Contacts and near-Mine Structures in the Kevitsa Mining and Exploration Site, Northern Finland: Constraints from 2D and 3D Reflection Seismic Data." *Geophysical Prospecting* 63: 754-773. doi: 10.1111/1365-2478.12252.

Komninou, A., and D. Sverjensky. 1996. "Geochemical Modeling of the Formation of an Unconformity-Type Uranium Deposit." *Economic Geology* 91 (3): 590-606.

Konhauser, K., L. Amskold, S. Lalonde, N. Posth, A. Kappler, and A. Anbar. 2007. "Decoupling Photochemical Fe(Ii) Oxidation from Shallow-Water Bif Deposition." *Earth and Planetary Science Letters* 258 (1-2): 87-100. doi: 10.1605/01.301-0001774029.2007.

Krapež, B., M. Barley, and A. Pickard. 2003. "Hydrothermal and Resedimented Origins of the Precursor Sediments to Banded Iron Formation: Sedimentological Evidence from the Early Palaeoproterozoic Brockman Supersequence of Western Australia." *Sedimentology* 50 (5): 979-1011. doi: 10.1046/j.1365-3091.2003.00594.x.

Kukkonen, I., and P. Peltonen. 1999. "Xenolith-Controlled Geotherm for the Central Fennoscandian Shield: Implications for Lithosphere–Asthenosphere Relations." *Tectonophysics* 304 (4): 301-315.

Kukkonen, I., P. Heikkinen, S. Heinonen, and J. Laitinen. 2011. "Reflection Seismics in Exploration for Mineral Deposits: Initial Results from the Hire Project." *Geological Survey of Finland, Special paper* 49: 49–58.

L'Heureux, E., B. Milkereit, and E. Adam. 2005. "3D Seismic Exploration for Mineral Deposits in Hardrock Environments." *CSEG Recorder* November: 36-39.

Large, R. 1992. "Australian Volcanic-Hosted Massive Sulfide Deposits; Features, Styles, and Genetic Models." *Economic Geology* 87 (3): 471-510.

Large, R., J. McPhie, B. Gemmell, W. Herrmann, and G. Davidson. 2001. "The Spectrum of Ore Deposit Types, Volcanic Environments, Alteration Halos, and Related Exploration Vectors in Submarine Volcanic Successions: Some Examples from Australia." *Economic Geology* 96 (5): 913-938. doi: 10.2113/gsecongeo.96.5.913.

Laznicka, P. 2006. "Proterozoic Intracratonic Orogens and Basins: Extension, Sedimentation, Magmatism." *Giant Metallic Deposits: Future Sources of Industrial Metals*: 367-423.

Leach, D., R. Taylor, D. Fey, S. Diehl, and R. Saltus. 2010. *A Deposit Model for Mississippi Valley-Type Lead-Zinc Ores: Chapter a in Mineral Deposit Models for Resource Assessment*. Reston, VA: U.S.G. Survey. USGS Publications Warehouse. http://pubs.er.usgs.gov/publication/sir20105070A.

Lehmann, B. 2008. "Uranium Ore Deposits." *Rev. Econ. Geol. AMS Online* 2008: 16-26.

Lindqvist, T. 2014. "3D Characterization of Brittle Fracture Zones in Kevitsa Open Pit Excavation, Northern Finland." University of Helsinki.

Liner, C., C.-F. Li, A. Gersztenkorn, and J. Smythe. 2004. "Spice: A New General Seismic Attribute" *2004 SEG Annual Meeting*: Society of Exploration Geophysicists.

Lines, L., and R. Newrick. 2004. *Fundamentals of Geophysical Interpretation*: Society of Exploration Geophysicists Tulsa, OK, USA.

Loukola-Ruskeeniemi, K., and P. Sorjonen-Ward. 1997. *Ore Deposits in Eastern Finland*: Geological Survey of Finland.

Ludwig, J., J. Nafe, and C. Drake. 1970. "Seismic Refraction." In *The Sea*, ed. A.E. Maxwell, 53-84.

Lydon, J. 1984. "Ore Deposit Models-8. Volcanogenic Massive Sulphide Deposits Part I: A Descriptive Model." *Geoscience Canada* 11 (4): 195–202.

Mahotkin, I., and E. Skinner. 1998. "Kimberlites from the Arkhangelsk Region — a Rock Type Transitional between Kimberlites, Melnoites and Lamproites. ." In *7th International Kimberlite Conference Cape Town, South Africa*, 532–535.

Mair, J., and A. Green. 1981. "High-Resolution Seismic Reflection Profiles Reveal Fracture Zones within a "Homogeneous" Granite Batholith." *Nature* 294 (5840): 439-442.

Malehmir, A., C. Schmelzbach, E. Bongajum, G. Bellefleur, C. Juhlin, and A. Tryggvason. 2009. "3D Constraints on a Possible Deep> 2.5 Km Massive Sulphide Mineralization from 2D Crooked-Line Seismic Reflection Data in the Kristineberg Mining Area, Northern Sweden." *Tectonophysics* 479 (3): 223-240.

Malehmir, A., and G. Bellefleur. 2009. "3D Seismic Reflection Imaging of Volcanic-Hosted Massive Sulfide Deposits: Insights from Reprocessing Halfmile Lake Data, New Brunswick, Canada." *Geophysics* 74 (6): B209-B219.

Malehmir, A., C. Juhlin, C. Wijns, M. Urosevic, P. Valasti, and E. Koivisto. 2012a. "3D Reflection Seismic Imaging for Open-Pit Mine Planning and Deep Exploration in the Kevitsa Ni-Cu-PGE Deposit, Northern Finland." *Geophysics* 77 (5): WC95-WC108. doi: 10.1190/GEO2011-0468.1.

Malehmir, A., R. Durrheim, G. Bellefleur, M. Urosevic, C. Juhlin, D.J. White, B. Milkereit, and G. Campbell. 2012b. "Seismic Methods in Mineral Exploration and Mine Planning: A General Overview of Past and Present Case Histories and a Look into the Future." *Geophysics* 77 (5): WC173–WC190. doi: 10.1190/GEO2012-0028.1.

Malehmir, A., M. Andersson, M. Lebedev, M. Urosevic, and V. Mikhaltsevitch. 2013. "Experimental Estimation of Velocities and Anisotropy of a Series of Swedish Crystalline Rocks and Ores." *Geophysical prospecting* 61 (1): 153-167.

Malehmir, A., E. Koivisto, M. Manzi, S. Cheraghi, R. Durrheim, G. Bellefleur, C. Wijns, K. Hein, and N. King. 2014. "A Review of Reflection Seismic Investigations in Three Major Metallogenic Regions: The Kevitsa Ni-Cu-PGE District (Finland), Witwatersrand Goldfields (South Africa), and the Bathurst Mining Camp (Canada)." *Ore Geology Reviews* 56: 423-441. doi: 10.1016/j.oregeorev.2013.01.003.

Manzi, M., M. Gibson, K. Hein, N. King, and R. Durrheim. 2012a. "Application of 3D Seismic Techniques to Evaluate Ore Resources in the West Wits Line Goldfield and Portions of the West Rand Goldfield, South Africa." *Geophysics* 77 (5): WC163-WC171.

Manzi, M., R. Durrheim, K. Hein, and N. King. 2012b. "3D Edge Detection Seismic Attributes Used to Map Potential Conduits for Water and Methane in Deep Gold Mines in the Witwatersrand Basin, South Africa." *Geophysics* 77 (5): WC133-WC147.

Manzi, M., K. Hein, R. Durrheim, and N. King. 2013. "Seismic Attribute Analysis to Enhance Detection of Thin Gold-Bearing Reefs: South Deep Gold Mine, Witwatersrand Basin, South Africa." *Journal of Applied Geophysics* 98: 212-228. doi: 10.1016/j.jappgeo.2013.08.017.

Manzi, M., G. Cooper, A. Malehmir, R. Durrheim, and Z. Nkosi. 2015. "Integrated Interpretation of 3D Seismic Data to Enhance the Detection of the Gold-Bearing Reef: Mponeng Gold Mine, Witwatersrand Basin (South Africa)." *Geophysical Prospecting* 63 (4): 881-902.

Manzi, M. 2015. "Seismic Exploration of the World's Deepest Gold and Platinum Orebodies in South Africa–Overview of the Past, Present and a Look into the Future." *ASEG Extended Abstracts* 2015 (1): 1-1.

Marsh, A., A. Furniss, and G. Kidd. 2000. "3D Seismic Visualization Using Multiple Volume Data Sets" *27th Annual Convention Proceedings*: Indonesian Petroleum Association.

Matthews, L. 2002. "Base Metal Exploration: Looking Deeper and Adding Value with Seismic Data." *Canadian Society of Exploration Geophysicists Recorder* 27: 37−43.

McCuaig, T., R. Kerrich, D. Groves, and N. Archer. 1993. "The Nature and Dimensions of Regional and Local Gold-Related Hydrothermal Alteration in Tholeiitic Metabasalts in the Norseman Goldfields: The Missing Link in a Crustal Continuum of Gold Deposits?" *Mineralium Deposita* 28 (6): 420-435.

McKay, A., Y. Miezitis, K. Porritt, A. Britt, D. Champion, S. Cadman, R. Towner *et al.* 2014. *Australia's Identified Mineral Resources 2013*. Canberra, Australia. http://dx.doi.org/10.11636/1327-1466.2013.

McQueen, K. 2005. "Ore Deposit Types and Their Primary Expressions." *Regolith Expression of Australian Ore Systems: a Compilation of Exploration Case Histories with Conceptual Dispersion, Process and Exploration Models, Butt, CRM, Robertson, IDM, Scott, KM, Cornelius, M.(eds). CRC LEME: Perth, WA*: 1-14.

Micklethwaite, S. 2009. "Mechanisms of Faulting and Permeability Enhancement During Epithermal Mineralisation: Cracow Goldfield, Australia." *Journal of Structural Geology* 31 (3): 288-300.

Milkereit, B., D. Eaton, J. Wu, G. Perron, M. Salisbury, E. Berrer, and G. Morrison. 1996. "Seismic Imaging of Massive Sulphide Deposits: Part Ii. Reflection Seismic Profiling." *Economic geology* 91: 829−834.

Milkereit, B., E. Berrer, A. King, A. Watts, B. Roberts, E. Adam, D. Eaton, J. Wu, and M. Salisbury. 2000a. "Development of 3−D Seismic Exploration Technology for Deep Nickel-Copper Deposits-a Case History from the Sudbury Basin, Canada." *Geophysics* 65: 1890-1899.

Milkereit, B., E. Berrer, A.R. King, A.H. Watts, B. Roberts, E. Adam, D.W. Eaton, J. Wu, and M.H. Salisbury. 2000b. "Development of 3-D Seismic Exploration Technology for Deep Nickel-Copper Deposits-a Case History from the Sudbury Basin, Canada." *Geophysics* 65 (6): 1890-1899.

Morris, R. 1993. "Genetic Modelling for Banded Iron-Formation of the Hamersley Group, Pilbara Craton, Western Australia." *Precambrian Research* 60 (1): 243-286.

Mutanen, T., R. Törnroos, and B. Johanson. 1988. "The Significance of Cumulus Chlorapatite and High-Temperature Dashkesanite to the Genesis of PGE Mineralization in the Koitelainen and Keivitsa-Satovaara Complexes, Northern Finland." In *Geo-Platinum 87*, 159-160. Springer.

Mutanen, T. 1997. "Geology and Ore Petrology of the Akanvaara and Koitelainen Mafic Layered Intrusions and the Keivitsa-Satovaara Layered Complex, Northern Finland." *Bulletin - Geological Survey of Finland* 395. http://www.scopus.com/inward/record.url?eid=2-s2.0-0030831479&partnerID=40&md5=b373150093a50b46d2b39cd9e0a73e8d.

Mutanen, T., and H. Huhma. 2001. "U-Pb Geochronology of the Koitelainen, Akanvaara and Keivitsa Layered Intrusions and Related Rocks." *Special Paper - Geological Survey of Finland* 33: 229-246.

Nafe, J., and C. Drake. 1957. "Variation with Depth in Shallow and Deep Water Marine Sediments of Porosity, and the Velocities of Compressional and Shear Waves." *Geophysics* 186: 523–552.

Neidell, N., and M. Taner. 1971. "Semblance and Other Coherency Measures for Multichannel Data." *Geophysics* 36 (3): 482-497. doi: doi:10.1190/1.1440186.

Niiranen, T., I. Lahti, V. Nykänen, and W.D. Maier. 2015. "The Orogenic Gold Potential of the Central Lapland Greenstone Belt, Northern Fennoscandian Shield." 2015.

Noponen, I., P. Heikkinen, and S. Mehrotra. 1979. "Applicability of Seismic Reflection Sounding in Regions of Precambrian Geology." *Geoexploration* 17 (1): 1–9.

O'Brien, H., and M. Tyni. 1999. "Mineralogy and Geochemistry of Kimberlites and Related Rocks from Finland." *Proceedings of the 7th International Kimberlite Conference (Vol. 2, pp. 625–636)*, *Cape Town, South Africa.*: Red Roof Design cc.

Page, R., G. Plafker, G. Fuis, W. Nokleberg, E. Ambos, W. Mooney, and D. Campbell. 1986. "Accretion and Subduction Tectonics in the Chugach Mountains and Copper River Basin, Alaska: Initial Results of the Trans-Alaska Crustal Transect." *Geology* 14 (6): 501-505.

Paradis, S., P. Hannigan, and K. Dewing. 2005. "Mineral Deposits of Canada Mississippi Valley-Type Lead-Zinc Deposits (Mvt)." *Natural Resources Canada-http://gsc. nrcan. gc. ca/mindep/synth_dep/mvt*.

Paradis, S., P. Hannigan, and K. Dewing. 2007. "Mississippi Valley-Type Lead-Zinc Deposits." In *Mineral Deposits of Canada: A Synthesis of Major Deposit-Types, District Metallogeny, the Evolution of Geological Provinces, and Exploration Methods*, ed. W.D. Goodfellow, 185–203. Geological Association of Canada, Mineral Deposits Division, Special Publication.

Peltola, E. 1978. "Origin of Precambrian Copper Sulfides of the Outokumpu District, Finland." *Economic geology* 73 (4): 461–477.

Perez, A. 2014. *Minerals Yearbook 2012: The Mineral Industry of Finland*: U.S. Department of Interior & U.S. Geological Survey.

Piercey, S., J. Peter, and R. Herrington. 2010. "Zn-Rich Volcanogenic Massive Sulphide (Vms) Deposits."

Pirajno, F., and L. Bagas. 2008. "A Review of Australia's Proterozoic Mineral Systems and Genetic Models." *Precambrian Research* 166 (1): 54–80.

Pitcairn, I., D. Teagle, D. Craw, G. Olivo, R. Kerrich, and T. Brewer. 2006. "Sources of Metals and Fluids in Orogenic Gold Deposits: Insights from the Otago and Alpine Schists, New Zealand." *Economic Geology* 101 (8): 1525-1546.

Polito, P., K. Kyser, D. Thomas, J. Marlatt, and G. Drever. 2005. "Re-Evaluation of the Petrogenesis of the Proterozoic Jabiluka Unconformity-Related Uranium Deposit, Northern Territory, Australia." *Mineralium Deposita* 40 (3): 257-288.

Posth, R., O. Konhauser, and A. Kappler. 2011. "Banded Iron Formations." In *Encyclopedia of Geobiology*, eds J. Reitner and V. Thiel, 92–103. Springer Netherlands.

Pretorius, C., W. Steenkamp, and R. Smith. 1994. "Developments in Data Acquisition, Processing, and Interpretation over Ten Years of Deep Vibroseismic Surveying in South Africa" *Proceedings XVth CMMI Congress*: South African Institute of Mining and Metallurgy

Raffensperger, J., and G. Garven. 1995. "The Formation of Unconformity-Type Uranium Ore Deposits; 2, Coupled Hydrochemical Modeling." *American Journal of Science* 295 (6): 639-696.

Rajesh, H. 2008. "Mapping Proterozoic Unconformity-Related Uranium Deposits in the Rockhole Area, Northern Territory, Australia Using Landsat Etm+." *Ore Geology Reviews* 33 (3): 382-396.

Randen, T., E. Monsen, C. Signer, A. Abrahamsen, J.O. Hansen, T. Sæter, J. Schlaf, and L. Sønneland. 2000. "Three-Dimensional Texture Attributes for Seismic Data Analysis" *70th Annual International Meeting, Society of Exploration Geophysics Expanded Abstracts, Calgary, Canada*,

Rao, D., and S. Naqvi. 1997. "Geological Setting, Mineralogy, Geochemistry and Genesis of the Middle Archaean Kalyadi Copper Deposit, Western Dharwar Craton, Southern India." *Mineralium Deposita* 32 (3): 230-242.

Rasanen, J., H. Huhma, J. Risinen, and H. Huhma. 2001. "U-Pb Datings in the Sodankyla Schist Area, Central Finnish Lapland." *Special Paper – Geological Survey of Finland*: 153–188.

Räsänen, J., E. Hanski, H. Juopperi, V. Kortelainen, E. Lanne, M. Lehtonen, T. Manninen, P. Rastas, and J. Väänänen. 1996. "New Stratigraphical Map of Central Finnish Lapland." In *The 22nd Nordic Geological Winter Meeting*, *Turku-Åbo, Finland,* edited by T. Kohonen and B. Lindberg, 8-11.

Raymond, O. 2003. "Yorke Peninsula (Moonta Subdomain) Pre–Neoproterozoic Geology: 1:250000 Scale Map (2nd Edition)." Geoscience Australia, Canberra.

Reed, K. 1993. *Seismic Reflection Surveying for Mining Exploration Applications, a Review of Practice Past and Current with an Outlook for the Future*.

Rex Minerals Ltd. 2015. *Annual Report*. http://www.asx.com.au/asxpdf/ 20150909/ pdf/4316jzmjpyjj2f.pdf.

Roberts, D. 1998. "Voxel Technology." In *Offshore Technology Conference, Houston*, 167–168.

Rudnick, R., and D. Fountain. 1995. "Nature and Composition of the Continental Crust: A Lower Crustal Perspective." *Reviews of Geophysics* 33 (3): 267–309.

Runnegar, B. 1979. "Ecology of Eurydesma and the Eurydesma Fauna, Permian of Eastern Australia." *Alcheringa: An Australasian Journal of Palaeontology* 3 (4): 261–285. doi: 10.1080/03115517908527798.

Salisbury, M., B. Milkereitz, and W. Bleeker. 1996. "Seismic Imaging of Massive Sulfide Deposits: Part I Rock Properties." *Economic Geology* 91: 821–828.

Salisbury, M., C. Harvey, and L. Matthews. 2003. "The Acoustic Properties of Ores and Host Rocks in Hardrock Terranes." eds D.W. Eaton, B. Milkereit, M.H. Salisbury and G. Society of Exploration. Tulsa, Oklahoma: Society of Exploration Geophysicists.

Salisbury, M., and D. Snyder. 2007. "Application of Seismic Methods to Mineral Exploration." In *Mineral Deposits of Canada: A Synthesis of Major Deposit-Types, District Metallogeny, the Evolution of Geological Provinces, and Exploration Methods*, edited by W.D. Goodfellow, 971–982. Geological Association of Canada, Mineral Deposits Division, Special Publication No. 5.

Schlumberger. 2014. *2014 Petrel Fundamentals: Training and Exercise Guide*: Copyright © 1998-2014 Schlumberger. All rights reserved. Schlumberger Private - Customer Use.

Schlumberger. 2015. Petrel 2015: Better Integration, Deep Science, and Productivity. Accessed 01/11/2015, https://www.software.slb.com/products/petrel/petrel-2015.

Schodde, R. 2011. "Recent Trends in Australian Exploration." presented at the AMEC 2011 National Mining Congress. Perth. http://www.minexconsulting.com/publications/jun2011.html.

Schodde, R. 2012. What's the Future for Mineral Exploration in Australia? …. And Why We Need Smart Geoscientists Now! Presentation to the Geological Society of Australia – Victoria Division, Monash. Accessed 20/10/2015, http://www.minexconsulting.com/publications/oct2012.html.

Schodde, R., and P. Guj. 2012. "Where Are Australia's Mines of Tomorrow." *Centre for Exploration Targeting, University of Western Australia, September*.

Scott, S. 2001. "Deep Ocean Mining." *Geoscience Canada* 28 (2).

Sheriff, R. 1993. "Vertical and Lateral Seismic Resolution and Attenuation: Part 7. Geophysical Methods." In *Development Geology Reference Manual*, eds D. Morton-Thompson and A.M. Woods. AAPG.

Sillitoe, R. 2010. "Porphyry Copper Systems." *Economic Geology* 105 (1): 3-41.

Skirrow, R., D. Huston, T. Mernagh, J. Thorne, H. Duffer, and A. Senior. 2013. *Critical Commodities for a High-Tech World: Australia's Potential to Supply Global Demand*.

Subrahmanyam, D., and P. Rao. 2008. "Seismic Attributes-a Review" *7th International Conference and Exposition on Petroleum Geophysics*, Hyderabad, India

Taner, M. 2001. "Seismic Attributes." *Canadian Society of Exploration Geophysicists Recorder*: 48–56.

Taylor, S., and S. McLennan. 1985. *The Continental Crust: Its Composition and Evolution*. United States: Blackwell Scientific Publications.

Tertyshnikov, K. 2014. "Seismic Imaging in Hard Rock Environments." Exploration Geophysics, Curtin University, Perth, WA. http://link.library.curtin.edu.au/p?cur_digitool_dc199685.

Thompson, T., M. Lamont, C. Bevilacqua, and N. Hendrick. 2011. "Fit for Purpose Seismic Reservoir Characterisation" *Petroleum Geology Conference and Exhibition 2011*, *Kuala Lumpur*: http://www.dugeo.com/images/uploads/PGCE_2011_technical_poster.pdf.

Törmänen, T., and M. Iljina. 2007. "Stop 2 the Kevitsa Intrusion and Associated Ni-Cu-Pge Deposit." In *Geologian tutkimuskeskus*, Guide 54. Geological Survey of Finland.

Tornos, F. 2006. "Environment of Formation and Styles of Volcanogenic Massive Sulfides: The Iberian Pyrite Belt." *Ore Geology Reviews* 28 (3): 259-307. doi: 10.1016/j.oregeorev.2004.12.005.

Tucker, P., and H. Yorston. 1973. *Pitfalls in Seismic Interpretation*: Society of Exploration Geophysicists Books.

Turner, G. 2014. "Finding Gold - Time for a Seismic Shift in Exportation Thinking." In *Gold14@Kalgoorlie – International Symposium*, *Kalgoorlie, WA*. http://www.hiseis.com.au/publications/finding_gold.pdf.

Tuusjärvi, M., I. Mäenpää, S. Vuori, P. Eilu, S. Kihlman, and S. Koskela. 2014. "Metal Mining Industry in Finland – Development Scenarios to 2030." *Journal of Cleaner Production* 84: 271–280. doi: http://dx.doi.org/10.1016/j.jclepro.2014.03.038.

Urosevic, M., E. Stoltz, and S. Massey. 2005. "Seismic Exploration for Gold in a Hard Rock Environment—Yilgarn Craton, Western Australia." *67th Annual International Conference and Exhibition, EAGE, Extended Abstracts* G009.

Urosevic, M., A. Kepic, E. Stolz, and C. Juhlin. 2007. "Seismic Exploration of Ore Deposits in Western Australia" *Proceedings of Exploration 07: Fifth Decennial International Conference on Mineral Exploration*,

Urosevic, M., and A. Kepic. 2008. "Nickel Exploration with 3D Seismic – Lake Lefroy, Kambalda, Wa." In *SEG Las Vegas 2008 Annual Meeting*

Urosevic, M., G. Bhat, and M.H. Grochau. 2012. "Targeting Nickel Sulphide Deposits from 3D Seismic Reflection Data at Kambalda, Australia." *Geophysics* 77 (5): WC123–WC132. doi: 10.1190/geo2011-0514.1.

Wang, C., J. Deng, S. Zhang, and L. Yang. 2010. "Metallogenic Province and Large Scale Mineralization of Volcanogenic Massive Sulfide Deposits in China." *Resource Geology* 60 (4): 404-413.

Whitaker, W., P. Murphy, and R. Rollason. 1974. "Geology of the Mundubbera 1:250 000 Sheet Area."

White, D., D. Secord, and M. Malinowski. 2012. "3D Seismic Imaging of Volcanogenic Massive Sulfide Deposits in the Flin Flon Mining Camp, Canada: Part 1—Seismic Results." *Geophysics* 77 (5): WC47-WC58.

Widess, M. 1973. "How Thin Is a Thin Bed?" *Geophysics* 38 (6): 1176-1180.

Williams, P., M. Barton, D. Johnson, L. Fontboté, A. De Haller, G. Mark, N. Oliver, and R. Marschik. 2005. "Iron Oxide Copper-Gold Deposits: Geology, Space-Time Distribution, and Possible Modes of Origin." *Economic Geology* 100 (2): 371–405.

Wilson, A., and M. Cervantes. 2013. "Survey of Mining Companies 2012/2013." Fraser Institute.

Witt, W., and F. Vanderhor. 1998. "Diversity within a Unified Model for Archaean Gold Mineralization in the Yilgarn Craton of Western Australia: An Overview of the Late-Orogenic, Structurally-Controlled Gold Deposits." *Ore Geology Reviews* 13 (1): 29–64.

Wolfe, R., and C. Liu. 1988. "Interactive Visualization of 3D Seismic Data: A Volumetric Method." *IEEE Computer Graphics and Applications* 8 (4): 24–30.

Wyss, T., M. Baumann, and E. Klingelé. 1993. *Estimation of Rheological Parameters by Combined Satellite-Gravity Gradiometric and Seismic Data*: Swiss Federal Institute of Technology, Institute of Geodesy and Photogrammetry.

Yavuz, S., J. Kinkela, A. Dzunic, M. Penney, R. Neto, V. Araújo, S. Ziramov, R. Pevzner, and M. Urosevic. 2015. "Physical Property Analysis and Preserved Relative Amplitude Processed Seismic Imaging of Volcanogenic Massive Sulfides—a Case Study from Neves–Corvo, Portugal." *Geophysical Prospecting* 63 (4): 798-812.

Yilmaz, O. 1987. *Seismic Data Processing: Society of Exploration Geophysiscists*: Tulsa, OK.

Yilmaz, O. 2001. *Seismic Data Analysis: Processing, Inversion, and Interpretation of Seismic Data*. Edited by S.M. Doherty. Tulsa, Oklahoma: Society of Exploration Geophysicists.

Zaccarini, F., and G. Garuti. 2008. "Mineralogy and Chemical Composition of Vms Deposits of Northern Apennine Ophiolites, Italy: Evidence for the Influence of Country Rock Type on Ore Composition." *Mineralogy and Petrology* 94 (1-2): 61-83.

Zhou, J., Z. Huang, M. Zhou, X. Li, and Z. Jin. 2013. "Constraints of C–O–S–Pb Isotope Compositions and Rb–Sr Isotopic Age on the Origin of the Tianqiao Carbonate-Hosted Pb–Zn Deposit, Sw China." *Ore Geology Reviews* 53: 77-92.

Zhou, P., and B. Gu. 2005. "Extraction of Oxidized and Reduced Forms of Uranium from Contaminated Soils: Effects of Carbonate Concentration and Ph." *Environmental science & technology* 39 (12): 4435-4440.

Ziramov, S., A. Dzunic, and M. Urosevic. 2015. "Kevitsa Ni–Cu–PGE Deposit, North Finland: A Seismic Case Study." In *24th International Geophysical Conference and Exhibition*, 1–4. ASEG–PESA 2015. doi: http://dx.doi.org/10.1071/ASEG2015ab122.

Appendices

Appendix I

Copyright consent

SEG Copyright Information

Open Access Papers

The Society of Economic Geologists, Inc., has in place a Gold Open Access (OA) policy that allows free access to papers for which the author has paid a fee in advance of publication. Under Creative Commons CC-BY licensing, this policy applies to final papers published in the journal *Economic Geology* that have been reviewed, copyedited, and typeset. The principles of fair use and attribution apply; duplicate or redundant publication of the full paper is not permitted at any time.

Papers that fall in this category are labeled with the OA padlock logo. In reusing the figures or other parts of the article, the user must acknowledge the author and the source of the material. If the new article uses more than 25% of an OA article or if more than 25% of the article comes from an OA article, it will judged to constitute duplicate publication and be in contravention of normal publishing ethics.

For additional information, please refer to the SEG Open Access publishing policy.

Permissions

Other than for papers licensed under Open Access, SEG holds the copyright on all its publications, although certain works by government employees may be an exception. It is the author's responsibility to make this determination.

Fair Use Permission

Use of up to three figures, a brief paragraph (up to 300 words), or a single table from an SEG publication is considered to be fair usage, and no formal permission is needed. If formal permission is required, please make your request as indicated below. Fees will be assessed. We expect the SEG publication to be cited with appropriate credit, i.e., fully and prominently.

Copying and Use in the Classroom

To reproduce SEG materials, please check with the Copyright Clearance Center (CCC) in the USA or equivalent in other countries. You will be charged a fee for reproduction and distribution within a classroom.

Other Use

If your usage does **not** fall within the above categories, please write us at the following address:

Copyright Permissions
subscriptions@segweb.org
7811 Shaffer Parkway
Littleton, CO 80127
Fax: +1 (720) 981-7874

Complete the Permissions Form and stipulate the following:

- What material you wish to use.
- The title of the publication in which you will use the material, and the publisher's name.
- At what price the publication will be sold or if there will be no charge.
- Whether the material will be modified, and a general statement about the extent of the modification.

Usage Fees

For all uses requiring written approval of the SEG, fees will be assessed, with a base fee of **US$50.00**. Extent and purpose of use will be considered in assessing additional fees. Fees are **not** waived for SEG members and must be paid prior to use of the material or the permission is void. Formal invoices will be issued only upon request

Electronic Usage

Electronic use of complete SEG publications, including individual articles, is typically discouraged because it competes with SEG distribution of print and electronic matter.

Posting on a Website

Posting on a website of material covered by SEG copyright is prohibited without specific permission from SEG, with one exception: an author or group of authors may post without further permission, on their own personal or organizational website(s) the **title, authors, and full abstract** of their paper(s), providing the posting cites the SEG publication in which the material appears and the citation includes the address line:

Society of Economic Geologists
7811 Shaffer Parkway
Littleton, CO 80127
USA

The SEG building will be closed for the holidays (December 25 - January 1).
Please allow for delayed e-mail responses.

Permissions

SEG publishes journals, books, and digital works with the primary aim of disseminating research in and theory and applications of applied geophysics. Consistent with this objective, the Society provides mechanisms for those who seek to reuse or republish material from SEG publications while protecting the viability of the SEG publications program. Any further questions about permissions can be sent via email to the SEG publications department at permissions@seg.org.

Fair use
Authors and publishers may present or republish up to two figures or tables per SEG article or per SEG book without seeking written permission from SEG, provided that full acknowledgment of the source is provided in the new work. If SEG has cited a publication for which it is not the publisher, rights should be obtained from that publisher. SEG considers this fair use. There are no fees associated with this permission. Authors who need documentation that SEG is extending this permission are encouraged to print this message and present it to their publishers. Those who require further documentation should contact the SEG publications director. Requests to use any portion of "Seismic Data Analysis: Processing, Inversion, and Interpretation of Seismic Data" should be directed to the SEG publications director.

Permission granting
Those seeking permission to republish more material than described above should contact the SEG publications director. Such requests should include complete citations of works for which permission to republish is sought. If permission for specific figures or tables is sought, please provide figure and table numbers. Requests should include a description of the work in which the SEG material would be republished. Information about the audience and the intended distribution also should be included. The requests should be prepared on institutional letterhead if the requesting party is representing an institution. License fees are assessed only when the request is for a large amount of material or when the proposed usage is commercial in nature or would limit SEG's market. If a license fee is assessed, it must be paid prior to use or the permission is void.

Purchase redistribution rights online
Those seeking to redistribute SEG publications or portions thereof in print, by fax, or online may purchase permission to do so online. SEG publications are registered with the Copyright Clearance Center, and licenses to redistribute SEG articles and portions of books are obtained through this nonprofit agency. Special pricing is available for university professors, including license to distribute SEG material through electronic course packs. Licenses also are available for distribution of journal articles and expanded abstracts via email or posting on Intranets and Extranets for limited time periods.

Authors' right to redistribute
Authors of articles in GEOPHYSICS, INTERPRETATION, THE LEADING EDGE, and the Technical Program *Expanded Abstracts* may post their own articles on their personal Web sites or the Web sites of their institutions without obtaining further permission from SEG. Authors of journal articles and *Expanded Abstracts* retain similar rights for print redistribution. If an author or an author's institution redistributes an author's article online or in print, the original publication venue encompassed in a complete citation and including SEG's status as publisher must be identified. Authors of SEG books, or portions of SEG books, must seek permission from the SEG publications director to redistribute these works in any form. Such permission will not be withheld if SEG's investment in the original publication of the works is not threatened. Questions should be directed to the publications director.

ELSEVIER LICENSE
TERMS AND CONDITIONS

Jan 01, 2016

This is a License Agreement between Muhammad S Hossain ("You") and Elsevier ("Elsevier") provided by Copyright Clearance Center ("CCC"). The license consists of your order details, the terms and conditions provided by Elsevier, and the payment terms and conditions.

All payments must be made in full to CCC. For payment instructions, please see information listed at the bottom of this form.

Supplier	Elsevier Limited The Boulevard,Langford Lane Kidlington,Oxford,OX5 1GB,UK
Registered Company Number	1982084
Customer name	Muhammad S Hossain
Customer address	Department of Exploration Geophysics Perth, Western Australia 6151
License number	3780170530719
License date	Jan 01, 2016
Licensed content publisher	Elsevier
Licensed content publication	Ore Geology Reviews
Licensed content title	External sulphur in IOCG mineralization: Implications on definition and classification of the IOCG clan
Licensed content author	Huayong Chen
Licensed content date	June 2013
Licensed content volume number	51
Licensed content issue number	n/a
Number of pages	5
Start Page	74
End Page	78
Type of Use	reuse in a thesis/dissertation
Portion	figures/tables/illustrations
Number of figures/tables /illustrations	1
Format	both print and electronic
Are you the author of this Elsevier article?	No
Will you be translating?	No
Original figure numbers	Figure 1
Title of your thesis/dissertation	Volumetric Interpretation of 3D Hard Rock Seismic Data

Expected completion date	Jan 2016
Estimated size (number of pages)	125
Customer Tax ID	AU344913680
Elsevier VAT number	GB 494 6272 12
Permissions price	0.00 AUD
VAT/Local Sales Tax	0.00 AUD / 0.00 GBP
Total	0.00 AUD
Terms and Conditions	

INTRODUCTION

1. The publisher for this copyrighted material is Elsevier. By clicking "accept" in connection with completing this licensing transaction, you agree that the following terms and conditions apply to this transaction (along with the Billing and Payment terms and conditions established by Copyright Clearance Center, Inc. ("CCC"), at the time that you opened your Rightslink account and that are available at any time at http://myaccount.copyright.com).

GENERAL TERMS

2. Elsevier hereby grants you permission to reproduce the aforementioned material subject to the terms and conditions indicated.
3. Acknowledgement: If any part of the material to be used (for example, figures) has appeared in our publication with credit or acknowledgement to another source, permission must also be sought from that source. If such permission is not obtained then that material may not be included in your publication/copies. Suitable acknowledgement to the source must be made, either as a footnote or in a reference list at the end of your publication, as follows:
"Reprinted from Publication title, Vol /edition number, Author(s), Title of article / title of chapter, Pages No., Copyright (Year), with permission from Elsevier [OR APPLICABLE SOCIETY COPYRIGHT OWNER]." Also Lancet special credit - "Reprinted from The Lancet, Vol. number, Author(s), Title of article, Pages No., Copyright (Year), with permission from Elsevier."
4. Reproduction of this material is confined to the purpose and/or media for which permission is hereby given.
5. Altering/Modifying Material: Not Permitted. However figures and illustrations may be altered/adapted minimally to serve your work. Any other abbreviations, additions, deletions and/or any other alterations shall be made only with prior written authorization of Elsevier Ltd. (Please contact Elsevier at permissions@elsevier.com)
6. If the permission fee for the requested use of our material is waived in this instance, please be advised that your future requests for Elsevier materials may attract a fee.
7. Reservation of Rights: Publisher reserves all rights not specifically granted in the combination of (i) the license details provided by you and accepted in the course of this licensing transaction, (ii) these terms and conditions and (iii) CCC's Billing and Payment terms and conditions.
8. License Contingent Upon Payment: While you may exercise the rights licensed immediately upon issuance of the license at the end of the licensing process for the transaction, provided that you have disclosed complete and accurate details of your proposed use, no license is finally effective unless and until full payment is received from you (either by publisher or by CCC) as provided in CCC's Billing and Payment terms and conditions. If full payment is not received on a timely basis, then any license preliminarily granted shall be deemed automatically revoked and shall be void as if never granted. Further, in the event

Title: External sulphur in IOCG mineralization: Implications on definition and classification of the IOCG clan

Author: Huayong Chen

Publication: Ore Geology Reviews

Publisher: Elsevier

Date: June 2013

Order Completed

Thank you very much for your order.

This is a License Agreement between Muhammad S Hossain ("You") and Elsevier ("Elsevier"). The license consists of your order details, the terms and conditions provided by Elsevier, and the payment terms and conditions.

Get the printable license.

License Number	3780170530719
License date	Jan 01, 2016
Licensed content publisher	Elsevier
Licensed content publication	Ore Geology Reviews
Licensed content title	External sulphur in IOCG mineralization: Implications on definition and classification of the IOCG clan
Licensed content author	Huayong Chen
Licensed content date	June 2013
Licensed content volume number	51
Licensed content issue number	n/a
Number of pages	5
Type of Use	reuse in a thesis/dissertation
Portion	figures/tables/illustrations
Number of figures/tables /illustrations	1
Format	both print and electronic
Are you the author of this Elsevier article?	No
Will you be translating?	No
Original figure numbers	Figure 1
Title of your thesis/dissertation	Volumetric Interpretation of 3D Hard Rock Seismic Data
Expected completion date	Jan 2016
Estimated size (number of pages)	125
Elsevier VAT number	GB 494 6272 12
Customer Tax ID	AU344913680
Permissions price	0.00 AUD
VAT/Local Sales Tax	0.00 AUD / 0.00 GBP
Total	0.00 AUD

ORDER MORE... CLOSE WINDOW

ELSEVIER LICENSE
TERMS AND CONDITIONS

Jan 01, 2016

This is a License Agreement between Muhammad S Hossain ("You") and Elsevier ("Elsevier") provided by Copyright Clearance Center ("CCC"). The license consists of your order details, the terms and conditions provided by Elsevier, and the payment terms and conditions.

All payments must be made in full to CCC. For payment instructions, please see information listed at the bottom of this form.

Supplier	Elsevier Limited The Boulevard,Langford Lane Kidlington,Oxford,OX5 1GB,UK
Registered Company Number	1982084
Customer name	Muhammad S Hossain
Customer address	Department of Exploration Geophysics Perth, Western Australia 6151
License number	3780170966526
License date	Jan 01, 2016
Licensed content publisher	Elsevier
Licensed content publication	Ore Geology Reviews
Licensed content title	Orogenic gold and geologic time: a global synthesis
Licensed content author	R.J Goldfarb,D.I Groves,S Gardoll
Licensed content date	April 2001
Licensed content volume number	18
Licensed content issue number	1-2
Number of pages	75
Start Page	1
End Page	75
Type of Use	reuse in a thesis/dissertation
Intended publisher of new work	other
Portion	figures/tables/illustrations
Number of figures/tables /illustrations	1
Format	both print and electronic
Are you the author of this Elsevier article?	No
Will you be translating?	No
Original figure numbers	Figure 10

Print This Page

Title:	Orogenic gold and geologic time: a global synthesis
Author:	R.J Goldfarb,D.I Groves,S Gardoll
Publication:	Ore Geology Reviews
Publisher:	Elsevier
Date:	April 2001

Order Completed

Thank you very much for your order.

This is a License Agreement between Muhammad S Hossain ("You") and Elsevier ("Elsevier"). The license consists of your order details, the terms and conditions provided by Elsevier, and the payment terms and conditions.

Get the printable license.

License Number	3780170966526
License date	Jan 01, 2016
Licensed content publisher	Elsevier
Licensed content publication	Ore Geology Reviews
Licensed content title	Orogenic gold and geologic time: a global synthesis
Licensed content author	R.J Goldfarb,D.I Groves,S Gardoll
Licensed content date	April 2001
Licensed content volume number	18
Licensed content issue number	1-2
Number of pages	75
Type of Use	reuse in a thesis/dissertation
Portion	figures/tables/illustrations
Number of figures/tables /illustrations	1
Format	both print and electronic
Are you the author of this Elsevier article?	No
Will you be translating?	No
Original figure numbers	Figure 10
Title of your thesis/dissertation	Volumetric Interpretation of 3D Hard Rock Seismic Data
Expected completion date	Jan 2016
Estimated size (number of pages)	125
Elsevier VAT number	GB 494 6272 12
Customer Tax ID	AU344913680
Permissions price	0.00 AUD
VAT/Local Sales Tax	0.00 AUD / 0.00 GBP
Total	0.00 AUD

ORDER MORE... CLOSE WINDOW

ELSEVIER LICENSE
TERMS AND CONDITIONS

Jan 01, 2016

This is a License Agreement between Muhammad S Hossain ("You") and Elsevier ("Elsevier") provided by Copyright Clearance Center ("CCC"). The license consists of your order details, the terms and conditions provided by Elsevier, and the payment terms and conditions.

All payments must be made in full to CCC. For payment instructions, please see information listed at the bottom of this form.

Supplier	Elsevier Limited The Boulevard,Langford Lane Kidlington,Oxford,OX5 1GB,UK
Registered Company Number	1982084
Customer name	Muhammad S Hossain
Customer address	Department of Exploration Geophysics Perth, Western Australia 6151
License number	3780171440422
License date	Jan 01, 2016
Licensed content publisher	Elsevier
Licensed content publication	Precambrian Research
Licensed content title	Geological characteristics and tectonic setting of proterozoic iron oxide (Cu□U□Au□REE) deposits
Licensed content author	Murray W. Hitzman,Naomi Oreskes,Marco T. Einaudi
Licensed content date	October 1992
Licensed content volume number	58
Licensed content issue number	1-4
Number of pages	47
Start Page	241
End Page	287
Type of Use	reuse in a thesis/dissertation
Intended publisher of new work	other
Portion	figures/tables/illustrations
Number of figures/tables /illustrations	1
Format	both print and electronic
Are you the author of this Elsevier article?	No
Will you be translating?	No
Original figure numbers	Figure 1

Title of your thesis/dissertation	Volumetric Interpretation of 3D Hard Rock Seismic Data
Expected completion date	Jan 2016
Estimated size (number of pages)	125
Customer Tax ID	AU344913680
Elsevier VAT number	GB 494 6272 12
Permissions price	0.00 AUD
VAT/Local Sales Tax	0.00 AUD / 0.00 GBP
Total	0.00 AUD
Terms and Conditions	

INTRODUCTION

1. The publisher for this copyrighted material is Elsevier. By clicking "accept" in connection with completing this licensing transaction, you agree that the following terms and conditions apply to this transaction (along with the Billing and Payment terms and conditions established by Copyright Clearance Center, Inc. ("CCC"), at the time that you opened your Rightslink account and that are available at any time at http://myaccount.copyright.com).

GENERAL TERMS

2. Elsevier hereby grants you permission to reproduce the aforementioned material subject to the terms and conditions indicated.
3. Acknowledgement: If any part of the material to be used (for example, figures) has appeared in our publication with credit or acknowledgement to another source, permission must also be sought from that source. If such permission is not obtained then that material may not be included in your publication/copies. Suitable acknowledgement to the source must be made, either as a footnote or in a reference list at the end of your publication, as follows:
"Reprinted from Publication title, Vol /edition number, Author(s), Title of article / title of chapter, Pages No., Copyright (Year), with permission from Elsevier [OR APPLICABLE SOCIETY COPYRIGHT OWNER]." Also Lancet special credit - "Reprinted from The Lancet, Vol. number, Author(s), Title of article, Pages No., Copyright (Year), with permission from Elsevier."
4. Reproduction of this material is confined to the purpose and/or media for which permission is hereby given.
5. Altering/Modifying Material: Not Permitted. However figures and illustrations may be altered/adapted minimally to serve your work. Any other abbreviations, additions, deletions and/or any other alterations shall be made only with prior written authorization of Elsevier Ltd. (Please contact Elsevier at permissions@elsevier.com)
6. If the permission fee for the requested use of our material is waived in this instance, please be advised that your future requests for Elsevier materials may attract a fee.
7. Reservation of Rights: Publisher reserves all rights not specifically granted in the combination of (i) the license details provided by you and accepted in the course of this licensing transaction, (ii) these terms and conditions and (iii) CCC's Billing and Payment terms and conditions.
8. License Contingent Upon Payment: While you may exercise the rights licensed immediately upon issuance of the license at the end of the licensing process for the transaction, provided that you have disclosed complete and accurate details of your proposed use, no license is finally effective unless and until full payment is received from you (either by publisher or by CCC) as provided in CCC's Billing and Payment terms and conditions. If

Order Completed

Thank you very much for your order.

This is a License Agreement between Muhammad S Hossain ("You") and Springer ("Springer"). The license consists of your order details, the terms and conditions provided by Springer, and the payment terms and conditions.

Get the printable license.

License Number	3780181449153
License date	Jan 01, 2016
Licensed content publisher	Springer
Licensed content publication	Springer eBook
Licensed content title	Volcanogenic Massive Sulfides
Licensed content author	John W. Jamieson
Licensed content date	Jan 1, 2014
Type of Use	Thesis/Dissertation
Portion	Figures/tables/illustrations
Number of figures/tables /illustrations	2
Author of this Springer article	No
Original figure numbers	Figures 1 and 2
Title of your thesis / dissertation	Volumetric Interpretation of 3D Hard Rock Seismic Data
Expected completion date	Jan 2016
Estimated size(pages)	125
Customer VAT ID	AU344913680
Total	0.00 USD

CLOSE WINDOW

SPRINGER LICENSE
TERMS AND CONDITIONS

Jan 01, 2016

This is a License Agreement between Muhammad S Hossain ("You") and Springer ("Springer") provided by Copyright Clearance Center ("CCC"). The license consists of your order details, the terms and conditions provided by Springer, and the payment terms and conditions.

All payments must be made in full to CCC. For payment instructions, please see information listed at the bottom of this form.

License Number	3780181449153
License date	Jan 01, 2016
Licensed content publisher	Springer
Licensed content publication	Springer eBook
Licensed content title	Volcanogenic Massive Sulfides
Licensed content author	John W. Jamieson
Licensed content date	Jan 1, 2014
Type of Use	Thesis/Dissertation
Portion	Figures/tables/illustrations
Number of figures/tables /illustrations	2
Author of this Springer article	No
Order reference number	None
Original figure numbers	Figures 1 and 2
Title of your thesis / dissertation	Volumetric Interpretation of 3D Hard Rock Seismic Data
Expected completion date	Jan 2016
Estimated size(pages)	125
Customer VAT ID	AU344913680
Total	0.00 USD
Terms and Conditions	

Introduction

The publisher for this copyrighted material is Springer. By clicking "accept" in connection with completing this licensing transaction, you agree that the following terms and conditions apply to this transaction (along with the Billing and Payment terms and conditions established by Copyright Clearance Center, Inc. ("CCC"), at the time that you opened your Rightslink account and that are available at any time at http://myaccount.copyright.com).

Limited License

With reference to your request to reuse material on which Springer controls the copyright, permission is granted for the use indicated in your enquiry under the following conditions:

- Licenses are for one-time use only with a maximum distribution equal to the number stated in your request.

ELSEVIER LICENSE
TERMS AND CONDITIONS

Jan 01, 2016

This is a License Agreement between Muhammad S Hossain ("You") and Elsevier ("Elsevier") provided by Copyright Clearance Center ("CCC"). The license consists of your order details, the terms and conditions provided by Elsevier, and the payment terms and conditions.

All payments must be made in full to CCC. For payment instructions, please see information listed at the bottom of this form.

Supplier	Elsevier Limited The Boulevard,Langford Lane Kidlington,Oxford,OX5 1GB,UK
Registered Company Number	1982084
Customer name	Muhammad S Hossain
Customer address	Department of Exploration Geophysics Perth, Western Australia 6151
License number	3780171215338
License date	Jan 01, 2016
Licensed content publisher	Elsevier
Licensed content publication	Ore Geology Reviews
Licensed content title	A review of reflection seismic investigations in three major metallogenic regions: The Kevitsa Ni–Cu–PGE district (Finland), Witwatersrand goldfields (South Africa), and the Bathurst Mining Camp (Canada)
Licensed content author	Alireza Malehmir,Emilia Koivisto,Musa Manzi,Saeid Cheraghi,Raymond J. Durrheim,Gilles Bellefleur,Chris Wijns,Kim A.A. Hein,Nick King
Licensed content date	January 2014
Licensed content volume number	56
Licensed content issue number	n/a
Number of pages	19
Start Page	423
End Page	441
Type of Use	reuse in a thesis/dissertation
Intended publisher of new work	other
Portion	figures/tables/illustrations
Number of figures/tables /illustrations	1
Format	both print and electronic
Are you the author of this Elsevier article?	No

Will you be translating?	No
Original figure numbers	Figure 4
Title of your thesis/dissertation	Volumetric Interpretation of 3D Hard Rock Seismic Data
Expected completion date	Jan 2016
Estimated size (number of pages)	125
Customer Tax ID	AU344913680
Elsevier VAT number	GB 494 6272 12
Permissions price	0.00 AUD
VAT/Local Sales Tax	0.00 AUD / 0.00 GBP
Total	0.00 AUD
Terms and Conditions	

INTRODUCTION

1. The publisher for this copyrighted material is Elsevier. By clicking "accept" in connection with completing this licensing transaction, you agree that the following terms and conditions apply to this transaction (along with the Billing and Payment terms and conditions established by Copyright Clearance Center, Inc. ("CCC"), at the time that you opened your Rightslink account and that are available at any time at http://myaccount.copyright.com).

GENERAL TERMS

2. Elsevier hereby grants you permission to reproduce the aforementioned material subject to the terms and conditions indicated.
3. Acknowledgement: If any part of the material to be used (for example, figures) has appeared in our publication with credit or acknowledgement to another source, permission must also be sought from that source. If such permission is not obtained then that material may not be included in your publication/copies. Suitable acknowledgement to the source must be made, either as a footnote or in a reference list at the end of your publication, as follows:
"Reprinted from Publication title, Vol /edition number, Author(s), Title of article / title of chapter, Pages No., Copyright (Year), with permission from Elsevier [OR APPLICABLE SOCIETY COPYRIGHT OWNER]." Also Lancet special credit - "Reprinted from The Lancet, Vol. number, Author(s), Title of article, Pages No., Copyright (Year), with permission from Elsevier."
4. Reproduction of this material is confined to the purpose and/or media for which permission is hereby given.
5. Altering/Modifying Material: Not Permitted. However figures and illustrations may be altered/adapted minimally to serve your work. Any other abbreviations, additions, deletions and/or any other alterations shall be made only with prior written authorization of Elsevier Ltd. (Please contact Elsevier at permissions@elsevier.com)
6. If the permission fee for the requested use of our material is waived in this instance, please be advised that your future requests for Elsevier materials may attract a fee.
7. Reservation of Rights: Publisher reserves all rights not specifically granted in the combination of (i) the license details provided by you and accepted in the course of this licensing transaction, (ii) these terms and conditions and (iii) CCC's Billing and Payment terms and conditions.
8. License Contingent Upon Payment: While you may exercise the rights licensed immediately upon issuance of the license at the end of the licensing process for the

Order Completed

Thank you very much for your order.

This is a License Agreement between Muhammad S Hossain ("You") and Springer ("Springer"). The license consists of your order details, the terms and conditions provided by Springer, and the payment terms and conditions.

Get the printable license.

License Number	3780181026066
License date	Jan 01, 2016
Licensed content publisher	Springer
Licensed content publication	Springer eBook
Licensed content title	Banded Iron Formations
Licensed content author	Nicole R. Posth
Licensed content date	Jan 1, 2011
Type of Use	Thesis/Dissertation
Portion	Figures/tables/illustrations
Number of figures/tables /illustrations	1
Author of this Springer article	No
Original figure numbers	Figure 4
Title of your thesis / dissertation	Volumetric Interpretation of 3D Hard Rock Seismic Data
Expected completion date	Jan 2016
Estimated size(pages)	125
Customer VAT ID	AU344913680
Total	0.00 USD

CLOSE WINDOW

Title: Mechanisms of faulting and permeability enhancement during epithermal mineralisation: Cracow goldfield, Australia

Author: Steven Micklethwaite

Publication: Journal of Structural Geology

Publisher: Elsevier

Date: March 2009

Order Completed

Thank you very much for your order.

This is a License Agreement between Muhammad S Hossain ("You") and Elsevier ("Elsevier"). The license consists of your order details, the terms and conditions provided by Elsevier, and the payment terms and conditions.

Get the printable license.

License Number	3811841441043
License date	Feb 18, 2016
Licensed content publisher	Elsevier
Licensed content publication	Journal of Structural Geology
Licensed content title	Mechanisms of faulting and permeability enhancement during epithermal mineralisation: Cracow goldfield, Australia
Licensed content author	Steven Micklethwaite
Licensed content date	March 2009
Licensed content volume number	31
Licensed content issue number	3
Number of pages	13
Type of Use	reuse in a thesis/dissertation
Portion	figures/tables/illustrations
Number of figures/tables /illustrations	1
Format	both print and electronic
Are you the author of this Elsevier article?	No
Will you be translating?	No
Original figure numbers	Figure 1
Title of your thesis/dissertation	Volumetric Interpretation of 3D Hard Rock Seismic Data
Expected completion date	Jan 2016
Estimated size (number of pages)	125
Elsevier VAT number	GB 494 6272 12
Customer Tax ID	AU344913680
Permissions price	0.00 AUD
VAT/Local Sales Tax	0.00 AUD / 0.00 GBP
Total	0.00 AUD

ORDER MORE... CLOSE WINDOW

SPRINGER LICENSE
TERMS AND CONDITIONS

Jan 01, 2016

This is a License Agreement between Muhammad S Hossain ("You") and Springer ("Springer") provided by Copyright Clearance Center ("CCC"). The license consists of your order details, the terms and conditions provided by Springer, and the payment terms and conditions.

All payments must be made in full to CCC. For payment instructions, please see information listed at the bottom of this form.

License Number	3780181026066
License date	Jan 01, 2016
Licensed content publisher	Springer
Licensed content publication	Springer eBook
Licensed content title	Banded Iron Formations
Licensed content author	Nicole R. Posth
Licensed content date	Jan 1, 2011
Type of Use	Thesis/Dissertation
Portion	Figures/tables/illustrations
Number of figures/tables /illustrations	1
Author of this Springer article	No
Order reference number	None
Original figure numbers	Figure 4
Title of your thesis / dissertation	Volumetric Interpretation of 3D Hard Rock Seismic Data
Expected completion date	Jan 2016
Estimated size(pages)	125
Customer VAT ID	AU344913680
Total	0.00 USD
Terms and Conditions	

Introduction

The publisher for this copyrighted material is Springer. By clicking "accept" in connection with completing this licensing transaction, you agree that the following terms and conditions apply to this transaction (along with the Billing and Payment terms and conditions established by Copyright Clearance Center, Inc. ("CCC"), at the time that you opened your Rightslink account and that are available at any time at http://myaccount.copyright.com).

Limited License

With reference to your request to reuse material on which Springer controls the copyright, permission is granted for the use indicated in your enquiry under the following conditions:

- Licenses are for one-time use only with a maximum distribution equal to the number stated in your request.

Disclaimer – Read this first

LEGAL NOTICE

By accessing and using the WWW pages of the Fennoscandian Ore Deposit Database (FODD) in the Internet pages of Geological Survey of Finland (GTK), you agree to the following terms and conditions. You must not access these pages if you do not agree to all of the following terms.

Use this Internet information at your own risk.

Copyright notice

In the FODD Internet pages, GTK owns all rights to the Finnish geological data set and the information in it and likewise Geological Survey of Norway (NGU) owns all rights to the Norwegian, Geological Survey of Sweden (SGU) owns all rights to the Swedish and The Federal Agency of Use of Mineral Resources of the Ministry of Natural Resources of the Russian Federation (MNRRF) to the Russian data sets and information contained in them, respectively. The organisations mentioned above are below jointly called as the "Data Owners". All material including text, images and audiovisual elements is protected by copyright laws.

Special terms of reproduction

The Data Owners encourage the readers to use the FODD Internet data for their research, academic and professional or personal purposes. When reproducing the data, always add the following acknowledgement: "Reproduced with the permission of "name of the Data Owner" All rights reserved."

The Data Owners consent to you storing on your computer or printing copies of extracts from these pages for any non-profit use. We do not allow this data to be sold to third parties.

For more detailed information and permission for extended licence to use the FODD Internet data, we urge you to contact the particular Data Owner to arrange necessary permission or copyright licence.

No Warranties or Representations

Although the Data Owners have used a considerable effort in preparing the information in this site, the Data Owners do not warrant the accuracy. All information published on these Internet pages is provided "as is" without warranties of any kind either expressed or implied made in relation to the correctness, reliability, timeliness, completeness, or accuracy of the information on these pages. The Data Owners do not warrant that its pages or the server are free of viruses or other harmful components.

Any documentation may include technical inaccuracies or typographical errors. **The resource categorisation does not follow the present international standards (for example, the JORC or the NI 43-101 codes).** Changes and additions may be made by the Data Owners to any information contained herein. The Data Owners reserve the right to revise the pages or withdraw access to them at any time. The Data Owners assume no responsibility for material created or published by third parties that the FODD Internet pages contain a link to.

IN NO EVENT WILL DATA OWNERS BE LIABLE TO ANY PARTY FOR ANY DAMAGES WHETHER DIRECT, INDIRECT, SPECIAL, CONSEQUENTIAL OR OTHER FOR ANY USE OR INABILITY TO USE OF THIS WEB SITE OR ITS CONTENTS, OR OF ANY OTHER HYPERLINKED WEB SITE, INCLUDING, WITHOUT LIMITATION, ANY DAMAGES FOR LOST PROFITS, BUSINESS INTERRUPTION, LOSS OF PROGRAMS OR OTHER DATA ON YOUR INFORMATION HANDLING SYSTEM OR OTHERWISE, EVEN IF WE ARE EXPRESSLY ADVISED OF THE POSSIBILITY OF SUCH DAMAGES.

The Data Owners make no warranties and/or representations whatsoever about any other web site, which you may access through this one. Such links are provided only as a convenience and does not mean that Data Owners endorse or accept any responsibility for the contents or the use of such web site.

Comments, questions and suggestions

The Data Owners do not want to receive confidential or proprietary information from you through our web site. Please note that any information, unsolicited suggestions, ideas or other submissions will be deemed to be non-confidential and non-proprietary. By sending the Data Owners any information or material, you grant the Data Owners a royalty free, unrestricted, irrevocable license to use, reproduce, display, perform, modify, transmit and distribute those materials or information, and to sublicense such rights, and you also agree to that the Data Owners are free to use any ideas, concepts, know-how or techniques that you send us for any purpose. Specific software available on the web site, any software that may be made available to download from this web site (the "Software") is the copyrighted work of the Data Owners and/or their suppliers. Use of the Software is governed by the terms of the end user license agreement, if any, which accompanies or is included with the Software ("License Agreement"). An end user will be unable to install any Software that is accompanied by or includes a License Agreement, unless the end user first agrees to the License Agreement terms. The Software is made available for downloading solely for use by end users according to the License Agreement. Any reproduction or redistribution of the Software not in accordance with the License Agreement may result in civil and/or criminal penalties.

WITHOUT LIMITING THE FOREGOING, COPYING OR REPRODUCTION OF THE SOFTWARE TO ANY OTHER SERVER OR LOCATION FOR FURTHER REPRODUCTION OR REDISTRIBUTION IS EXPRESSLY PROHIBITED.

THE SOFTWARE IS WARRANTED, IF AT ALL, ONLY ACCORDING TO THE TERMS OF THE LICENSE AGREEMENT. EXCEPT AS WARRANTED IN THE LICENSE AGREEMENT, THE DATA OWNERS HEREBY DISCLAIM ALL WARRANTIES AND CONDITIONS

WITH REGARD TO THE SOFTWARE, INCLUDING ALL IMPLIED WARRANTIES AND CONDITIONS OF MERCHANTABILITY, FITNESS FOR A PARTICULAR PURPOSE, TITLE AND NON-INFRINGEMENT.

DATA

Metallogenic areas of the Fennoscandian Shield
Download from Hakku service

Metallic mineral deposits of the Fennoscandian Shield
Download from Hakku service

Industrial mineral deposits of the Fennoscandian Shield
Download from Hakku service

MAPS

By clicking the Download button you agree to the disclaimer

Metallogenic map of the Fennoscandian Shield 1:2 000 000
http://tupa.gtk.fi/kartta/erikoiskartta/ek_080_300dpi.pdf

Metallic mineral deposit map of the Fennoscandian Shield 1:2 000 000
http://tupa.gtk.fi/kartta/erikoiskartta/ek_085_100dpi.pdf
http://tupa.gtk.fi/kartta/erikoiskartta/ek_085_300dpi.pdf
Download KMZ file (kmz 1.1 MB)

Industrial mineral deposit map of the Fennoscandian Shield 1:2 000 000
http://tupa.gtk.fi/kartta/erikoiskartta/ek_092_100dpi.pdf
http://tupa.gtk.fi/kartta/erikoiskartta/ek_092_300dpi.pdf
Download KMZ file (kmz 0.3 MB)

Gmail by Google

Muhammad Hossain <msh2124@gmail.com>

Copyright permission

Richard Schodde <richard@minexconsulting.com> Sat, Jan 2, 2016 at 6:16 AM
To: Muhammad Hossain <muhammad.hossain@postgrad.curtin.edu.au>

Muhammad,

Thanks for the note. You have my permission to use the two nominated charts in your PhD Thesis.

Attached are high-resolution copies of the charts.

Regards

Richard Schodde
Managing Director
MinEx Consulting Pty Ltd
49 Surrey Road
South Yarra
Victoria 3141
Australia

Mobile Phone +61 418909769
Email: Richard@MinExConsulting.com
Web: www.MinExConsulting.com
Providing strategic advice on mineral economics & exploration

From: msh2124@gmail.com [mailto:msh2124@gmail.com] **On Behalf Of** Muhammad Hossain
Sent: Saturday, 2 January 2016 2:42 AM
To: Richard Schodde
Subject: Copyright permission

Dear Mr Schodde,

I am a PhD student at the Department of Exploration Geophysics of Curtin University, Perth, Western Australia. In my doctoral thesis entitled "Volumetric Interpretation of 3D Hard Rock Seismic Data", I would like to include Figure 6 and Figure 20 from the following publication:

"Schodde, R.C., and P. Guj. 2012. "Where Are Australia's Mines of Tomorrow." Centre for Exploration Targeting, University of Western Australia, September 2012."

Once completed, the thesis will be made available in the hard-copy format at Curtin Library and

digital format on the website: http://library.curtin.edu.au/find-books-and-resources/theses.cfm . The material will be provided strictly for educational purposes and on a non-commercial basis.

I would be grateful to you for your consent to the copying and republishing of the above-mentioned figures. I would be willing to use a specific form of acknowledgement that you may require and to communicate any conditions related to the use of this material.

If you are not the copyright owner of the referred material, I would be grateful for any information you can provide as to who is likely to hold the copyright. I look forward to hearing from you and thank you in advance for your consideration of my request.

Kind regards,

Muhammad Shahadat Hossain

Muhammad Shahadat Hossain | *PhD Candidate*

Department of Exploration Geophysics | Western Australian School of Mines

[**Postal Address**: GPO Box U1987, Perth, Western Australia, 6845] [Bld 613, Rm 4H23]

[**Street Address**: ARRC/CSIRO Building, H Block, Level 4, 26 Dick Perry Avenue, Kensington 6151, Western Australia]

Tel | +61 8 9266 3521

Mob | +61 4 31 448 629

Fax | +61 8 9266 3407

Email | muhammad.hossain@student.curtin.edu.au

Web | http://student.curtin.edu.au/~15295817

2 attachments

CET Paper - Figure 20.emf
8101K

CET Paper - Figure 6.emf
1070K

Gmail by Google

Muhammad Hossain <msh2124@gmail.com>

Copyright permission

Mike Porter <mike.porter@portergeo.com.au> Sun, Jan 10, 2016 at 8:09 AM
To: Muhammad Hossain <muhammad.hossain@student.curtin.edu.au>

Dear Muhammad,

I have no problem with you using these diagrams/images. I own the the copyright, which was transferred to PGC Publishing as a condition of publication.

Please acknowledge as “Reproduced with the permission of PGC Publishing www.portergeo.com.au/publishing”

Good luck with your research. I look forward to reading your thesis in due course.

Regards,
Mike

T. M. (Mike) Porter – Porter GeoConsultancy Pty Ltd,
6 Beatty Street, LINDEN PARK, SA., 5065, Australia
Ph & Fax: +61 8 8379 7397
E-mail: mike.porter@portergeo.com.au
Web: http://www.portergeo.com.au

> On 2 Jan 2016, at 2:28 am, Muhammad Hossain <muhammad.hossain@student.curtin.edu.au> wrote:
>
> Dear Dr Porter,
>
> I am a PhD student at the Department of Exploration Geophysics of Curtin University, Perth, Western Australia. In my doctoral thesis entitled “Volumetric Interpretation of 3D Hard Rock Seismic Data”, I would like to include figures 12, 13 and a modified/cropped version of Figure 6 from the following article:
>
> ***"Conor, C., O. Raymond, T. Baker, G. Teale, P. Say, and G. Lowe. 2010. "Alteration and Mineralisation in the Moonta-Wallaroo Copper-Gold Mining Field Region, Olympic Domain, South Australia." In 2010 Hydrothermal Iron Oxide Copper-Gold and Related Deposits: A Global Perspective, ed. T.M. Porter, 147–170. PGC Publishing, Adelaide."***
>
> Once completed, the thesis will be made available in the hard-copy format at Curtin Library and digital format on the website: http://library.curtin.edu.au/find-books-and-resources/theses.cfm . The material will be provided strictly for educational purposes and on a non-commercial basis.
>
> I would be grateful to you for your consent to the copying and republishing of the above-mentioned figures. I would be willing to use a specific form of acknowledgement that you may require and to communicate any conditions related to the use of this material.
>
> If you are not the copyright owner of the referred material, I would be grateful for any information you can

provide as to who is likely to hold the copyright. I look forward to hearing from you and thank you in advance for your consideration of my request.

Kind regards,

Muhammad Shahadat Hossain

Muhammad Shahadat Hossain | *PhD Candidate*
Department of Exploration Geophysics | Western Australian School of Mines
[**Postal Address**: GPO Box U1987, Perth, Western Australia, 6845] [Bld 613, Rm 4H23]
[**Street Address**: ARRC/CSIRO Building, H Block, Level 4, 26 Dick Perry Avenue, Kensington 6151, Western Australia]
Tel | +61 8 9266 3521
Mob | +61 4 31 448 629
Fax | +61 8 9266 3407

Email | muhammad.hossain@student.curtin.edu.au
Web | http://student.curtin.edu.au/~15295817

<image001.png>

Gmail by Google

Muhammad Hossain <msh2124@gmail.com>

Copyright permission

Muhammad Hossain <muhammad.hossain@student.curtin.edu.au> Sat, Jan 2, 2016 at 12:16 AM

To: Karen Dawe <kfmdawe@mun.ca>

Dear Ms Dawe,

I am a PhD student at the Department of Exploration Geophysics of Curtin University, Perth, Western Australia. In my doctoral thesis entitled “Volumetric Interpretation of 3D Hard Rock Seismic Data”, I would like to include Figure 1 on page 186 with proper citation from the following publication:

"Paradis, S., P. Hannigan, and K. Dewing. 2007. "Mississippi Valley-Type Lead-Zinc Deposits." In Mineral Deposits of Canada: A Synthesis of Major Deposit-Types, District Metallogeny, the Evolution of Geological Provinces, and Exploration Methods, ed. W.D. Goodfellow, 185–203. Geological Association of Canada, Mineral Deposits Division, Special Publication."

Once completed, the thesis will be made available in the hard-copy format at Curtin Library and digital format on the website: http://library.curtin.edu.au/find-books-and-resources/theses.cfm . The material will be provided strictly for educational purposes and on a non-commercial basis.

I would be grateful to you for your consent to the copying and republishing of the above-mentioned figures. I would be willing to use a specific form of acknowledgement that you may require and to communicate any conditions related to the use of this material.

If you are not the copyright owner of the referred material, I would be grateful for any information you can provide as to who is likely to hold the copyright. I look forward to hearing from you and thank you in advance for your consideration of my request.

Kind regards,

Muhammad Shahadat Hossain

Muhammad Shahadat Hossain | *PhD Candidate*
Department of Exploration Geophysics | Western Australian School of Mines
[**Postal Address**: GPO Box U1987, Perth, Western Australia, 6845] [Bld 613, Rm 4H23]
[**Street Address**: ARRC/CSIRO Building, H Block, Level 4, 26 Dick Perry Avenue, Kensington 6151, Western Australia]
Tel | +61 8 9266 3521
Mob | +61 4 31 448 629
Fax | +61 8 9266 3407

Email | muhammad.hossain@student.curtin.edu.au

Web | http://student.curtin.edu.au/~15295817

Curtin University

Gmail by Google

Muhammad Hossain <msh2124@gmail.com>

permission to use figure

Steve Hill <SteveH@pennwell.com> Fri, Jan 15, 2016 at 5:26 AM
To: "msh2124@gmail.com" <msh2124@gmail.com>

Muhammed,

I recently received your request to reproduce fig 1-2, dip shooting, from “Applied Seismology,” by Gadallah and Fisher.

We grant you permission to reproduce this figure for your thesis. Please give the appropriate source credit for this figure: PennWell Publishing.

Best regards,

Stephen Hill

Acquisitions Editor

Professional Education Products

PennWell Publishing

1421 S. Sheridan Road

Tulsa OK 74112

(O) 918-831-9491

(M) 918-284-9028

Gmail by Google

Muhammad Hossain <msh2124@gmail.com>

Copyright permission

Muhammad Hossain <muhammad.hossain@student.curtin.edu.au> Wed, Jan 13, 2016 at 2:59 AM

To: Carla Flores <Carla.Flores@csiro.au>

Dear Ms Flores,

I am a PhD student at the Department of Exploration Geophysics of Curtin University, Perth, Western Australia. In my doctoral thesis entitled "Volumetric Interpretation of 3D Hard Rock Seismic Data", I would like to reproduce texts and figures from the following extended abstracts that I have submitted for the ASEG-PESA annual conferences in 2013 and 2015.

- Hossain, M., M. Urosevic, and A. Kepic. 2013. "Volumetric Interpretation of 3D Hard Rock Seismic Data." ASEG Extended Abstracts 2013 (1): 1-3. doi: 10.1071/ASEG2013ab088
- Hossain, M.S., M. Urosevic, and A. Kepic. 2015a. "Interpretation of 3D High-Resolution Seismic Data Collected over an IOCG Deposit in South Australia." ASEG Extended Abstracts 2015 (1): 1-5. doi: 10.1071/ASEG2015ab210.
- Hossain, M.S., M. Urosevic, and C. Wijns. 2015. "Seismic Volumetric Interpretation of a Disseminated Copper System in Kevitsa, Northern Finland." ASEG Extended Abstracts 2015 (1): 1–4. doi: 10.1071/ASEG2015ab097.

Once completed, the thesis will be made available in the hard-copy format at Curtin Library and digital format on the website: http://library.curtin.edu.au/find-books-and-resources/theses.cfm . The material will be provided strictly for educational purposes and on a non-commercial basis.

I would be grateful to you for your consent to the copying and republishing of the above-mentioned articles with proper citations. I would be willing to use a specific form of acknowledgement that you may require and to communicate any conditions related to the use of this material.

If you are not the copyright owner of the referred material, I would be grateful for any information you can provide as to who is likely to hold the copyright. I look forward to hearing from you and thank you in advance for your consideration of my request.

Kind regards,

Muhammad Shahadat Hossain

Muhammad Shahadat Hossain | *PhD Candidate*
Department of Exploration Geophysics | Western Australian School of Mines
[**Postal Address**: GPO Box U1987, Perth, Western Australia, 6845] [Bld 613, Rm 4H23]
[**Street Address**: ARRC/CSIRO Building, H Block, Level 4, 26 Dick Perry Avenue, Kensington 6151, Western Australia]

Tel | +61 8 9266 3521
Mob | +61 4 31 448 629
Fax | +61 8 9266 3407

Email | muhammad.hossain@student.curtin.edu.au
Web | http://student.curtin.edu.au/~15295817

Curtin University

Appendix II

Physical property measurements of the core samples from the hillside copper-gold mining project

Hole ID	Depth (m)	Vp (m/s)	Vs (m/s)	Density (kg/m^3)	Magnetic Susceptibility (SI)	General Lithology
HDD-009	70.0	5206	3213	2743	1.33E-04	Gabbro
HDD-009	101.0	5199	3572	2708	2.17E-01	Gabbro
HDD-009	119.4	6099	3571	2723	2.60E-04	Metasediment
HDD-009	119.4	6253	3659	2723	2.60E-04	Metasediment
HDD-009	132.0	6083	3418	2704	8.10E-05	Metasediment
HDD-009	145.7	5211	3531	2681	1.47E-04	Metasediment
HDD-009	199.5	6159	3482	2741	5.89E-04	Metasediment
HDD-009	199.5	6159	3541	2741	5.89E-04	Metasediment
HDD-009	227.6	5757	3338	2648	1.35E-04	Metasediment
HDD-009	254.2	5593	3119	3244	7.07E-02	Mineralisation
HDD-009	292.4	6115	3484	2784	1.27E-02	Metasediment
HDD-009	301.7	5819	3452	2704	3.24E-03	Metasediment
HDD-009	301.7	5900	3595	2704	3.24E-03	Metasediment
HDD-009	313.8	6186	3575	2798	4.44E-03	Metasediment
HDD-009	313.8	6251	3556	2798	4.44E-03	Metasediment
HDD-009	320.8	6398	3706	2896	8.86E-04	Metasediment
HDD-009	332.2	6231	3771	2695	2.56E-04	Metasediment
HDD-009	345.7	5060	2970	2929	3.20E-03	Metasediment
HDD-009	350.5	5571	3115	3206	1.14E-03	Mineralisation
HDD-009	359.9	5889	3154	3494	1.60E-02	Mineralisation
HDD-009	371.2	5767	3317	2795	1.25E-02	Gabbro
HDD-009	371.2	5783	3231	2795	1.25E-02	Gabbro
HDD-009	384.5	6265	4151	2669	1.10E-04	Granite
HDD-009	384.5	6493	4461	2669	1.10E-04	Granite
HDD-009	384.5	6685	4198	2669	1.10E-04	Granite
HDD-009	389.0	5858	3373	2811	1.60E-02	Gabbro
HDD-009	389.0	6132	3439	2811	1.60E-02	Gabbro
HDD-009	401.7	6303	3583	2842	4.10E-02	Gabbro
HDD-009	406.4	6167	3868	2618	2.75E-04	Granite
HDD-009	406.4	6319	4085	2618	2.75E-04	Granite
HDD-009	410.0	5955	3373	2852	7.15E-02	Gabbro
HDD-009	419.5	5206	3206	2748	1.37E-03	Gabbro
HDD-009	419.5	5678	3318	2748	1.37E-03	Gabbro
HDD-009	425.3	5985	3335	2614	2.44E-04	Granite
HDD-009	432.7	5971	3438	2863	2.49E-02	Gabbro
HDD-009	455.5	6003	3382	2865	1.13E-02	Gabbro
HDD-009	455.5	6110	3460	2865	1.13E-02	Gabbro

Hole ID	Depth (m)	Vp (m/s)	Vs (m/s)	Density (kg/m^3)	Magnetic Susceptibility (SI)	General Lithology
HDD-009	463.5	6263	3589	2861	1.37E-02	Gabbro
HDD-009	483.6	5191	3590	2913	4.85E-03	Gabbro
HDD-009	504.9	6496	3696	2859	4.53E-03	Gabbro
HDD-060	110.1	6291	3422	2715	1.35E-03	Metasediment
HDD-060	110.1	6357	3650	2715	1.35E-03	Metasediment
HDD-060	128.8	5961	3334	2691	4.37E-03	Metasediment
HDD-060	148.8	6152	3476	2695	6.18E-03	Metasediment
HDD-060	167.2	5530	3270	2722	5.62E-03	Metasediment
HDD-060	167.2	5668	3201	2722	5.62E-03	Metasediment
HDD-060	176.0	6293	3580	2739	2.16E-03	Metasediment
HDD-060	186.5	6483	3811	2711	2.31E-04	Metasediment
HDD-060	197.1	6030	3346	2789	2.64E-03	Metasediment
HDD-060	197.1	6082	3421	2789	2.64E-03	Metasediment
HDD-060	212.5	6403	3727	2627	3.70E-04	Granite
HDD-060	221.5	6194	3799	2646	2.06E-03	Granite
HDD-060	221.5	6581	3976	2646	2.06E-03	Granite
HDD-060	242.2	6126	3605	2791	4.12E-04	Gabbro
HDD-060	248.5	5890	3408	2711	3.21E-05	Metasediment
HDD-060	248.5	5928	3426	2711	3.21E-05	Metasediment
HDD-060	259.2	6503	3818	3632	6.97E-02	Mineralisation
HDD-060	259.2	6519	3791	3632	6.97E-02	Mineralisation
HDD-060	264.3	6283	3545	2855	8.18E-02	Gabbro
HDD-060	267.5	6330	3891	2629	3.83E-04	Granite
HDD-060	274.0	6357	3714	2604	3.56E-04	Granite
HDD-060	287.4	5884	3442	2671	5.05E-04	Metasediment
HDD-060	297.1	4640	3183	2733	4.19E-04	Metasediment
HDD-060	297.1	5693	3753	2733	4.19E-04	Metasediment
HDD-060	297.1	5953	3643	2733	4.19E-04	Metasediment
HDD-060	304.8	6548	3771	2650	2.04E-02	Granite
HDD-060	314.8	6336	3694	2636	1.17E-03	Granite
HDD-060	328.3	6100	3411	2867	2.82E-02	Gabbro
HDD-060	342.2	5314	3142	2780	1.08E-02	Gabbro
HDD-060	350.7	6077	3337	2694	5.08E-04	Gabbro
HDD-060	366.1	6730	4154	2814	2.07E-04	Metasediment
HDD-060	375.0	6821	4023	3232	1.37E-02	Mineralisation
HDD-060	378.9	6702	4042	3126	4.92E-02	Mineralisation
HDD-060	378.9	7359	4185	3126	4.92E-02	Mineralisation
HDD-060	395.8	6396	3960	3235	8.99E-02	Mineralisation
HDD-060	397.6	6613	3721	3717	2.42E-01	Mineralisation
HDD-060	403.7	6315	3635	2852	5.12E-02	Metasediment
HDD-060	428.1	6310	3740	2635	2.72E-03	Granite
HDD-060	428.1	6486	3624	2635	2.72E-03	Granite
HDD-060	432.7	6722	3713	3257	2.49E-02	Mineralisation

Hole ID	Depth (m)	Vp (m/s)	Vs (m/s)	Density (kg/m^3)	Magnetic Susceptibility (SI)	General Lithology
HDD-060	446.5	5970	3542	2615	8.41E-04	Granite
HDD-060	470.0	6048	3715	2643	5.41E-04	Granite
HDD-062	84.2	4766	3071	2895	3.35E-02	Gabbro
HDD-062	84.2	4892	3219	2895	3.35E-02	Gabbro
HDD-062	84.2	5472	3247	2895	3.35E-02	Gabbro
HDD-062	89.2	6233	3549	2789	5.85E-02	Gabbro
HDD-062	89.2	6252	3602	2789	5.85E-02	Gabbro
HDD-062	100.4	5742	3352	2802	2.41E-02	Gabbro
HDD-062	100.4	5885	3363	2802	2.41E-02	Gabbro
HDD-062	110.4	6388	3673	2639	1.01E-03	Granite
HDD-062	110.4	6443	3618	2639	1.01E-03	Granite
HDD-062	114.4	6339	3364	2911	8.35E-02	Gabbro
HDD-062	121.2	6011	3389	2712	2.34E-03	Gabbro
HDD-062	128.2	6231	3548	2697	7.82E-04	Gabbro
HDD-062	128.2	6302	3525	2697	7.82E-04	Gabbro
HDD-062	132.0	6255	3661	2653	9.48E-04	Granite
HDD-062	132.0	6488	3655	2653	9.48E-04	Granite
HDD-062	157.0	6225	3694	2629	5.78E-04	Granite
HDD-062	170.2	6786	3814	2625	7.72E-04	Granite
HDD-062	185.7	6285	3602	2657	8.40E-04	Metasediment
HDD-062	199.9	5774	3194	2799	3.44E-03	Gabbro
HDD-062	199.9	5815	3336	2799	3.44E-03	Gabbro
HDD-062	203.0	6480	3670	2620	7.91E-04	Granite
HDD-064	76.8	5624	3519	2739	3.85E-04	Gabbro
HDD-064	93.5	5933	3430	2670	7.69E-04	Gabbro
HDD-064	93.5	6141	3482	2670	7.69E-04	Gabbro
HDD-064	101.0	5513	3340	2842	2.09E-02	Gabbro
HDD-064	108.2	6486	3712	2898	3.15E-02	Gabbro
HDD-064	118.0	6005	3581	2877	3.84E-02	Gabbro
HDD-064	118.0	6221	3564	2877	3.84E-02	Gabbro
HDD-064	126.5	5911	3391	2845	3.78E-02	Gabbro
HDD-064	136.1	6244	3585	2626	5.73E-04	Granite
HDD-064	147.0	7241	4169	3119	3.99E-03	Gabbro
HDD-064	148.7	6506	3725	2897	2.92E-02	Gabbro
HDD-064	153.5	7168	3932	2909	1.68E-02	Gabbro
HDD-064	157.6	5912	3358	2862	5.17E-03	Gabbro
HDD-064	170.7	6570	3832	2921	1.93E-02	Gabbro
HDD-064	170.7	6708	3822	2921	1.93E-02	Gabbro
HDD-064	186.4	6227	3659	2826	6.74E-03	Gabbro
HDD-064	186.4	6515	3732	2826	6.74E-03	Gabbro
HDD-064	201.1	5936	3338	2816	3.73E-02	Gabbro
HDD-064	205.5	5814	3292	2842	7.16E-03	Gabbro
HDD-064	207.1	5989	3261	2675	2.78E-03	Granite

Hole ID	Depth (m)	Vp (m/s)	Vs (m/s)	Density (kg/m^3)	Magnetic Susceptibility (SI)	General Lithology
HDD-064	207.1	6081	3373	2675	2.78E-03	Granite
HDD-064	215.0	5287	3124	2791	5.30E-03	Gabbro
HDD-064	215.0	5682	3195	2791	5.30E-03	Gabbro
HDD-064	215.0	5725	3288	2791	5.30E-03	Gabbro
HDD-064	220.6	6373	3652	2649	6.74E-04	Granite
HDD-064	223.0	6216	3622	2631	7.17E-04	Granite
HDD-064	223.0	6413	3647	2631	7.17E-04	Granite
HDD-064	230.0	6138	3432	2784	9.27E-03	Gabbro
HDD-064	233.7	5000	2980	2824	3.02E-02	Gabbro
HDD-064	233.7	5278	3065	2824	3.02E-02	Gabbro
HDD-064	237.8	5605	3170	2824	9.36E-03	Gabbro
HDD-064	237.8	5624	3328	2824	9.36E-03	Gabbro
HDD-064	240.0	5772	3395	2805	6.56E-03	Gabbro
HDD-064	245.2	5565	3260	2784	1.42E-02	Gabbro
HDD-064	245.2	5739	3309	2784	1.42E-02	Gabbro
HDD-064	250.6	5918	3296	2859	1.08E-02	Gabbro
HDD-064	253.8	6210	3453	2859	1.61E-03	Gabbro
HDD-064	255.0	6606	4020	2825	6.70E-04	Granite
HDD-064	255.0	6833	4124	2825	6.70E-04	Granite
HDD-064	257.0	6148	3617	2680	1.33E-03	Metasediment
HDD-064	257.0	6208	3632	2680	1.33E-03	Metasediment
HDD-064	259.0	5597	3067	2747	4.84E-03	Metasediment
HDD-064	259.0	5791	3364	2747	4.84E-03	Metasediment
HDD-064	259.0	6000	3461	2747	4.84E-03	Metasediment
HDD-064	263.0	6292	3660	2625	5.33E-04	Granite
HDD-064	264.0	6322	3545	2726	2.67E-02	Gabbro
HDD-064	264.0	6626	3647	2726	2.67E-02	Gabbro
HDD-064	266.7	6453	3649	2637	2.40E-03	Granite
HDD-064	272.0	5453	3284	2878	6.95E-02	Gabbro
HDD-064	272.0	5472	3093	2878	6.95E-02	Gabbro
HDD-064	275.4	7063	3900	3103	4.27E-03	Gabbro
HDD-064	281.7	6491	3717	2648	5.50E-03	Granite
HDD-064	285.4	6571	3737	2967	1.46E-01	Gabbro
HDD-064	289.1	6002	3468	2904	3.13E-02	Gabbro
HDD-064	289.1	6514	3834	2904	3.13E-02	Gabbro
HDD-064	297.7	6226	3687	2646	3.41E-03	Granite
HDD-064	306.3	6253	3584	2900	9.50E-02	Gabbro
HDD-064	313.9	6428	3484	3668	1.83E-01	Mineralisation
HDD-064	314.0	6178	3252	3115	1.25E-02	Gabbro
HDD-064	314.0	6418	3457	3115	1.25E-02	Gabbro
HDD-064	316.7	6943	3604	4069	6.55E-01	Mineralisation
HDD-064	318.1	6556	3853	3218	7.92E-02	Mineralisation
HDD-064	322.6	6564	3727	3737	5.50E-01	Mineralisation

Hole ID	Depth (m)	Vp (m/s)	Vs (m/s)	Density (kg/m^3)	Magnetic Susceptibility (SI)	General Lithology
HDD-064	331.7	5656	3522	3225	8.70E-04	Gabbro
HDD-064	331.7	6106	3810	3225	8.70E-04	Gabbro
HDD-064	337.5	6964	4136	3372	1.04E-03	Gabbro
HDD-064	337.5	7328	4238	3372	1.04E-03	Gabbro
HDD-064	342.7	5448	3517	3332	2.07E-03	Gabbro
HDD-064	346.5	4458	2634	2867	4.50E-03	Gabbro
HDD-064	346.5	5067	3120	2867	4.50E-03	Gabbro
HDD-064	349.4	6106	3664	2612	8.29E-04	Granite
HDD-064	361.0	6485	3585	2640	9.65E-04	Granite
HDD-064	364.8	6336	3733	2611	5.70E-04	Granite
HDD-064	372.1	6238	3322	2693	8.48E-04	Granite
HDD-064	372.1	6749	3502	2693	8.48E-04	Granite
HDD-064	377.5	6287	3470	2695	7.93E-04	Granite
HDD-064	384.0	7003	3335	2637	8.29E-04	Granite
HDD-064	399.9	6066	3580	2658	7.06E-04	Granite
HDD-064	401.8	5794	2992	3579	4.33E-02	Mineralisation
HDD-064	401.8	5840	3016	3579	4.33E-02	Mineralisation
HDD-064	403.8	5982	3340	2724	6.69E-04	Metasediment
HDD-064	403.8	6029	3318	2724	6.69E-04	Metasediment
HDD-064	406.0	6209	3491	2728	5.39E-04	Metasediment
HDD-064	406.0	6507	3575	2728	5.39E-04	Metasediment
HDD-064	411.1	6210	3576	2678	2.65E-03	Metasediment
HDD-064	411.1	6210	3618	2678	2.65E-03	Metasediment
HDD-064	411.1	6755	3902	2678	2.65E-03	Metasediment
HDD-064	412.9	6498	3691	2869	6.32E-04	Metasediment
HDD-064	412.9	7159	4107	2869	6.32E-04	Metasediment
HDD-064	415.3	6612	3797	2892	7.72E-03	Metasediment
HDD-064	419.7	6073	3463	2707	1.00E-03	Metasediment
HDD-064	419.7	6168	3478	2707	1.00E-03	Metasediment
HDD-064	425.1	6208	3519	2667	1.62E-03	Metasediment
HDD-064	425.1	6382	3606	2667	1.62E-03	Metasediment
HDD-064	427.0	6318	3692	2706	1.10E-03	Metasediment
HDD-064	431.7	6576	3822	3270	7.91E-03	Metasediment
HDD-064	431.7	7347	4195	3270	7.91E-03	Metasediment
HDD-064	435.0	5927	3760	2889	2.04E-02	Metasediment
HDD-064	442.1	6469	3673	2906	3.11E-03	Metasediment
HDD-064	442.1	6620	3711	2906	3.11E-03	Metasediment
HDD-064	451.0	6174	3931	2651	8.70E-05	Granite
HDD-064	464.0	6137	3573	2648	9.99E-04	Granite
HDD-064	464.0	6730	3523	2648	9.99E-04	Granite
HDD-064	466.2	6211	3548	3118	1.34E-02	Metasediment
HDD-064	466.2	6402	3618	3118	1.34E-02	Metasediment
HDD-064	471.0	6389	3419	2751	6.75E-03	Granite

Hole ID	Depth (m)	Vp (m/s)	Vs (m/s)	Density (kg/m^3)	Magnetic Susceptibility (SI)	General Lithology
HDD-064	484.0	7768	4992	2645	1.22E-04	Granite
HDD-064	491.1	6775	3986	3127	3.45E-02	Mineralisation
HDD-064	491.4	6684	3541	4877	5.95E-01	Mineralisation
HDD-167	95.2	6159	3455	2646	5.30E-04	Gabbro
HDD-167	109.1	6714	3933	2598	5.53E-04	Metasediment
HDD-167	113.0	6271	3491	2623	1.52E-03	Metasediment
HDD-167	160.4	5907	3531	2628	5.43E-04	Metasediment
HDD-167	186.8	6035	3799	2997	2.08E-02	Mineralisation
HDD-167	186.8	6086	3902	2997	2.08E-02	Mineralisation
HDD-167	190.0	5833	3673	3247	1.10E-03	Mineralisation
HDD-167	190.0	6239	3730	3247	1.10E-03	Mineralisation
HDD-167	192.8	6133	3474	2776	2.37E-02	Metasediment
HDD-167	195.5	5559	3263	3008	3.69E-02	Mineralisation
HDD-167	195.5	5734	3225	3008	3.69E-02	Mineralisation
HDD-167	197.5	5969	3680	2853	3.51E-02	Metasediment
HDD-167	197.5	6127	3443	2853	3.51E-02	Metasediment
HDD-167	202.3	6179	3451	3502	5.21E-01	Mineralisation
HDD-167	202.3	6420	3350	3502	5.21E-01	Mineralisation
HDD-167	204.6	6694	3509	2603	1.12E-03	Granite
HDD-167	214.2	5378	3237	2986	3.21E-02	Gabbro
HDD-167	214.2	5462	3621	2986	3.21E-02	Gabbro
HDD-167	217.9	6522	3671	2631	4.35E-05	Granite
HDD-167	217.9	6676	3709	2631	4.35E-05	Granite
HDD-167	226.2	6244	3740	2606	8.49E-04	Granite
HDD-167	226.2	6631	3876	2606	8.49E-04	Granite
HDD-167	236.0	6267	3684	2592	4.85E-04	Granite
HDD-167	236.0	6322	3722	2592	4.85E-04	Granite
HDD-167	259.9	6375	3746	2718	9.69E-03	Gabbro
HDD-167	265.8	6025	3483	2733	8.39E-02	Gabbro
HDD-167	265.8	6073	3491	2733	8.39E-02	Gabbro
HDD-167	276.5	6125	3647	3631	7.21E-01	Gabbro
HDD-167	276.5	6125	3715	3631	7.21E-01	Gabbro
HDD-167	284.0	6200	3504	2847	1.28E-02	Metasediment
HDD-167	301.0	5382	3226	2879	5.60E-03	Gabbro
HDD-167	324.6	6932	3923	2938	5.62E-03	Gabbro
HDD-167	343.8	6212	4002	2645	1.75E-04	Granite
HDD-167	343.8	6257	4525	2645	1.75E-04	Granite
HDD-167	355.5	6389	3758	2606	1.50E-04	Granite
HDD-441	60.2	5166	3023	2762	7.18E-03	Metasediment
HDD-441	60.2	5307	3091	2762	7.18E-03	Metasediment
HDD-441	66.3	5957	3916	2667	7.81E-04	Metasediment
HDD-441	97.5	5024	3113	2671	6.39E-04	Metasediment
HDD-441	97.5	5311	3153	2671	6.39E-04	Metasediment

Hole ID	Depth (m)	Vp (m/s)	Vs (m/s)	Density (kg/m^3)	Magnetic Susceptibility (SI)	General Lithology
HDD-441	107.4	6048	3467	2704	7.86E-04	Metasediment
HDD-441	107.4	6100	3467	2704	7.86E-04	Metasediment
HDD-441	118.8	5944	3517	2762	2.68E-03	Metasediment
HDD-441	118.8	5993	3587	2762	2.68E-03	Metasediment
HDD-441	122.6	5934	3529	2738	2.95E-03	Metasediment
HDD-441	122.6	6186	3728	2738	2.95E-03	Metasediment
HDD-441	124.9	5474	3183	2968	1.18E-03	Metasediment
HDD-441	124.9	5741	3381	2968	1.18E-03	Metasediment
HDD-441	136.3	6017	3711	2715	1.65E-03	Metasediment
HDD-441	142.0	5795	3589	2706	3.60E-02	Metasediment
HDD-441	145.9	5758	3574	2687	5.70E-04	Metasediment
HDD-441	153.5	5811	3526	2743	6.30E-04	Metasediment
HDD-441	169.0	5826	3269	2733	6.90E-04	Metasediment
HDD-441	169.0	5872	3240	2733	6.90E-04	Metasediment
HDD-441	174.8	5912	3414	2714	5.02E-04	Metasediment
HDD-441	174.8	6050	3580	2714	5.02E-04	Metasediment
HDD-441	182.0	5808	3220	2642	5.62E-04	Metasediment
HDD-441	188.8	5710	3336	2969	5.35E-03	Metasediment
HDD-441	202.0	6182	2894	2933	4.15E-03	Gabbro
HDD-441	203.0	5039	2931	2661	2.61E-04	Gabbro
HDD-441	203.0	5450	3198	2661	2.61E-04	Gabbro
HDD-441	212.0	5068	2989	2791	1.30E-02	Gabbro
HDD-441	217.6	6178	3507	2868	3.28E-03	Gabbro
HDD-441	217.6	6231	3393	2868	3.28E-03	Gabbro
HDD-441	217.6	6452	3612	2868	3.28E-03	Gabbro
HDD-441	220.9	5466	3240	2859	2.07E-02	Gabbro
HDD-441	231.6	5171	3223	2807	1.40E-02	Gabbro
HDD-441	240.3	6021	3594	2651	4.83E-04	Gabbro
HDD-441	241.0	6085	3559	2682	1.09E-03	Gabbro
HDD-441	241.1	5899	3505	2692	2.46E-03	Gabbro
HDD-441	244.6	6176	3496	2779	1.01E-02	Gabbro
HDD-441	247.0	6179	3897	2780	6.15E-04	Gabbro
HDD-441	248.7	4639	3030	2751	5.43E-04	Gabbro
HDD-441	257.3	6339	3592	2861	8.78E-04	Gabbro
HDD-441	279.5	6888	3977	2888	2.26E-02	Gabbro
HDD-441	283.2	6784	3833	2916	7.70E-02	Gabbro
HDD-441	289.3	6631	3828	2873	9.32E-02	Gabbro